U.PORTO

FEUP FACULDADE DE ENGENHARIA
UNIVERSIDADE DO PORTO

Universitat de Girona

Mechanics of deformation and failure of fibre hybrid composites

Rodrigo Paiva Tavares

Doctoral Thesis under
co-supervision between the
University of Porto
and the
University of Girona

January 2020

U.PORTO

FEUP FACULDADE DE ENGENHARIA
UNIVERSIDADE DO PORTO

Universitat de Girona

Mechanics of deformation and failure of fibre hybrid composites

Rodrigo Paiva Tavares

Supervisors:
Prof. Dr. Pedro P. Camanho
Prof. Dr. Albert Turon

University of Porto - Doctoral Program in Mechanical Engineering

University of Girona - Doctoral Program in Technology

January 2020

Abstract

The concept of fibre hybridization consists in using more than one type of fibre in the same fibre reinforced composite material. This strategy, if well applied, can result in improved composite properties and performance, since it affects the materials properties and changes the damage mechanisms that lead to failure. Fibre hybridization can be used to tailor the properties of the composite material for a given application and synergies between its constituents can lead to improved material behaviour.

The objective of this work is to analyse and understand the mechanics of deformation and failure of fibre hybrid composites, with focus on fibre dominated failure. To better understand the behaviour of hybrid composites, a combined approach is taken: the development of numerical models to predict the longitudinal failure and the experimental study of the effects of interply and intratow hybridization techniques on the damage mechanisms that control longitudinal failure.

Due to the challenging complexity of modelling longitudinal tensile failure of composite materials, sophisticated micromechanical models that account for the different behaviour of its constituents are used. In this work, a 3D finite element micromechanical framework is developed, taking into account the non-linear elastic behaviour of the fibres and its stochastic strength distribution, matrix plasticity and damage, and interface decohesion. The developed framework is used to analyse simple micromechanical tests such as single fibre fragmentation and fibre push-out tests. The damage mechanisms that control failure in these tests are shown to be accurately represented using the proposed modelling methodology. Analyses on both hybrid and non-hybrid composites are also performed to understand the failure process of these materials. Additionally, the effect of hydrostatic pressure on the tensile failure of fibre reinforced composites is addressed and the generalized strength reduction with increased pressure is shown to be well captured by the models.

The presented 3D modelling strategy is capable of capturing the complex failure mechanisms of composite materials, however, its computational complexity and cost limit its usability. To circumvent this issue the Spring Element Model is proposed. This model considers a random fibre arrangement of more than one type of fibre, so it can be used to simulate hybrid and non-hybrid composites. A more complex version of the model that accounts for the dynamics of fibre failure is also proposed and shown to accurately capture the dynamic transient effects that occur when fibres fracture. The Spring Element Model is used to study fibre fracture and cluster

formation on non-hybrid materials, however, the numerical results are shown to differ from the experiments as higher fibre break densities at failure are generally predicted. The model is also used to investigate the effect of the microstructure on hybrid composite materials. A high dependence on the fibre dispersion is observed.

Alongside the development of the numerical tools to predict failure of hybrid composites, two experimental campaigns on fibre hybrid composites are performed, both on interply and intratow hybrid materials. The interply hybrid materials, resulting from the combination of thin-ply HR40 and T800 layers, show a notch insensitive behaviour with high strength in the presence of stress concentrations. This behaviour is shown to be related with the appearance of additional failure mechanisms due to fibre hybridization.

In this work, a strategy to manufacture intratow hybrid materials is also developed and implemented based on the spread-tow technology. The produced materials exhibited a lower fibre dispersion than expected, however, due to constraints in the manufacturing process, higher dispersions could not be attained. The manufactured materials are used to study the effects of intratow hybridization on the strength and toughness of these materials. The hybrid materials are shown to have a lower unnotched strength compared to the baseline non-hybrid materials and no increase in fracture toughness is observed, since no additional failure mechanics apart from fibre failure are promoted by the hybridization. Nonetheless, the intratow technology is considered to be a powerful manufacturing technique to produce hybrid composites with improved properties, if higher fibre dispersions can be achieved.

With this work more insight on the fracture behaviour of hybrid composites was gained and the potential of this technology reinforced. Not only due to the increased of design space, but also due to the improved ductility and toughness these materials exhibit when designed to trigger specific damage mechanisms. Nevertheless, more study on the optimization of these materials system is required, focusing not only on the fibres used but also on the optimal material microstructure, which was seen to be a key parameter controlling the material behaviour.

Resumo

A hibridização de materiais compósitos consiste no uso de vários tipos de fibras no mesmo material. Esta estratégia, quando bem concebida, pode levar a um material compósito com melhores propriedades, dado a hibridização afetar não só as propriedades do material mas também os mecanismos de dano que levam à sua rotura. A hibridização pode ser usada para melhor otimizar as propriedades dos materiais compósitos para uma aplicação específica e, em alguns casos, podem ser explorados efeitos sinergéticos, resultando na melhoria do comportamento do material.

O objetivo deste trabalho é analisar e compreender os mecanismos de deformação e rotura em materiais compósitos híbridos, com ênfase em casos de carregamento dominados por rutura de fibras. Para atingir este objetivo, foi usada uma estratégia que combina o desenvolvimento de modelos numéricos, para prever a rotura destes materiais, com estudos experimentais em diversos materiais híbridos, para compreender os mecanismos de dano que controlam a rotura longitudinal dos materiais compósitos.

Devido à elevada complexidade dos mecanismos de rotura de materiais compósitos sujeitos a tensão na direção das fibras, é necessário recorrer a modelos micromecânicos sofisticados que consideram os distintos comportamentos dos constituintes destes materiais. Deste modo, foi desenvolvido um modelo de elementos finitos micromecânico 3D que tem em conta a natureza estocástica da tensão de rotura das fibras e o seu comportamento não linear elástico, a plasticidade e dano na matriz, e a descoesão da interface fibra-matriz. Esta estratégia de modelação foi usada para analisar testes micromecânicos simples, como o *single fibre fragmentation test* e o *fibre push-out test*, e foi demonstrado que os mecanismos de dano que controlam a falha neste tipo de ensaios são devidamente representados pelos modelos desenvolvidos. Foram também realizadas análises em compósitos híbridos e não-híbridos para compreender os mecanismos de rotura nestes materiais. Adicionalmente, o efeito da pressão hidrostática na rotura longitudinal foi estudado e concluiu-se que o modelo é capaz de prever a redução da tensão de rotura com o aumento da pressão. O modelo desenvolvido é capaz de capturar os mecanismos de dano que levam a rotura dos materiais compósitos, no entanto, a sua complexidade e o seu elevado custo computacional levam a que o seu uso seja limitado. Para contornar este problema, o *Spring Element Model* (SEM) é proposto. Este modelo considera uma distribuição aleatória de fibras e pode ser usado tanto para compósitos híbridos como não-híbridos. Uma versão mais complexa deste modelo, que tem em conta os efeitos dinâmicos presentes na rotura de fibras, foi também proposto

para capturar os efeitos transientes que ocorrem no processo de rotura. O SEM é usado para estudar a rotura e a formação de clusters de fibras partidas em compósitos não-híbridos, tendo sido verificado que existem algumas discrepâncias entre os resultados numéricos e os experimentais, dado que a densidade de fibras fraturadas prevista é maior do que a observada experimentalmente. Este modelo foi ainda usado para estudar o efeito da microestrutura no comportamento dos compósitos híbridos tendo sido verificado que existe uma elevada dependência do comportamento destes materiais com a dispersão das fibras.

Paralelamente ao desenvolvimento dos modelos numéricos, foram realizados dois estudos experimentais em materiais compósitos híbridos: híbridização ao nível da camada (*intratow*) e camada a camada (*interply*), onde a hibridização é feita com camadas de diferentes materiais. Os materiais *interply* resultaram da combinação de camadas ultra-finas de fibras de carbono T800 e HR40. Estes materiais demonstraram um comportamento insensível ao entalhe com elevadas tensões de roturas na presença de concentração de tensões. Verificou-se ainda que este comportamento está relacionado com os mecanismos de dano promovidos pela combinação dos dois tipos de fibras.

Adicionalmente, uma estratégia baseada na tecnologia de *spread-tow* foi desenvolvida para o fabrico de híbridos *intratow*, onde as fibras de carbono HR40 e T800 são combinadas na mesma camada. Os materiais fabricados apresentaram uma dispersão de fibras mais reduzida que o esperado, no entanto, devido a limitações no processo de fabrico não foi possível obter materiais com maior dispersão. Os híbridos desenvolvidos foram usados para analisar o efeito deste tipo de hibridização na tensão de rutura e na tenacidade destes materiais. Verificou-se que os materiais híbridos apresentam uma redução tanto da tensão de rutura como da tenacidade quando comparado com o material não-híbrido de referência. A redução na tenacidade do material é justificada pelo facto da hibridização não promover outros mecanismos de dano com a exceção de rutura de fibras. Apesar dos resultados obtidos, a hibridização *intratow* demonstra potencial para a obtenção de materiais com melhor desempenho, caso seja for possível fabricar materiais com maior dispersão de fibras, sendo necessário aperfeiçoar o seu processo de fabrico.

Este trabalho permitiu obter uma visão mais pormenorizada do comportamento de rotura dos materiais híbridos e o potencial desta tecnologia foi reforçado, não só devido à maior flexibilidade no seu projeto, bem como devido ao potencial de aumentar a sua ductilidade e tenacidade, quando projetados para promover os mecanismos de dano corretos. No entanto, são necessários estudos adicionais de otimização deste tipo de materiais, focando-se não só na correta escolha das fibras a usar, bem como no design da sua microestrutura, que se verificou crucial no comportamento mecânico destes materiais.

Resum

El concepto de hibridación de fibras consiste en utilizar varios tipos de fibra en un mismo composite. Si se aplica bien, el composite resultante puede presentar un mejor comportamiento mecánico, pues no se afectan las propiedades elásticas de los constituyentes, pero si el desarrollo de los diferentes procesos de disipación que conducen a la falla. Así, la hibridación de fibra se puede utilizar para diseñar un material composite con las propiedades óptimas para una aplicación determinada.

El objetivo de este trabajo es analizar y comprender la mecánica de deformación y falla de composites híbridos reforzados con diferentes tipos de fibras, poniendo énfasis en el fallo dominado por la fibra. Para entender mejor el comportamiento de los composites híbridos, se realizan dos tareas diferenciadas: (i) el desarrollo de modelos numéricos para predecir la falla longitudinal y (ii) el estudio experimental de los efectos de dos estrategias de hibridación, capa a capa (*interply*) y hibridización a nivel de capa (*intratow*), sobre los mecanismos de daño que controlan la falla longitudinal.

La complejidad de la modelización de la falla a tracción longitudinal de los composites, hace que se utilicen modelos micromecánicos sofisticados que contemplan el comportamiento mecánico de los diferentes componentes (fibra, matriz e interfase fibra / matriz). En esta línea, en este trabajo se desarrolla un modelo Micromecánico 3D de elementos finitos, que tiene en cuenta el comportamiento elástico no lineal de las fibras y su distribución estocástica de resistencia, plasticidad y daño de la matriz y pérdida de adhesión de la interfaz. El modelo desarrollado se utiliza para analizar ensayos micromecánicos simples, tales como la fragmentación de una sola fibra (*single fibre fragmentation test*) y el ensayo de extracción de una fibra por presión (*fibre push-out test*). Se demuestra que los mecanismos de daño que controlan la falla en estas pruebas se representan con precisión con el modelo propuesto. También se realizan análisis sobre composites híbridos y no híbridos para comprender el proceso de fallo de estos materiales. Además, se aborda el efecto de la presión hidrostática sobre la falla a tracción de los composites reforzados con fibra y se demuestra que la reducción de resistencia debido a la presión hidrostática es bien capturada por los modelos.

La estrategia de modelado 3D presentada es capaz de capturar los diferente y complejos mecanismos de falla de los composites, sin embargo, su complejidad y su coste computacional limitan su aplicabilidad. Para evitar este problema, se propone el *Spring Element Model* (SEM). Este modelo considera una disposición de

fibras aleatoria de más de un tipo de fibra, por lo que se puede utilizar para simular composites híbridos y no híbridos. También se propone y muestra una versión más compleja del modelo capaz de capturar con precisión los efectos dinámicos transitorios que se producen cuando se rompen las fibras. El SEM se utiliza para estudiar la fractura de fibras y la formación de clústeres en materiales no híbridos, aún así, se muestra que los resultados numéricos difieren de los experimentos ya que generalmente se prevén densidades de ruptura de fibra más altas. El modelo SEM también se utiliza para investigar el efecto de la microestructura sobre materiales compuestos híbridos. Se observa una alta dependencia de la dispersión de fibras.

Paralelamente al desarrollo de herramientas numéricas para predecir la falla de los composites híbridos, se han realizado dos campañas experimentales, una sobre composites híbridos capa a capa y otra sobre híbridos a nivel de capa. Los materiales híbridos capa a capa, resultantes de la combinación de capas HR40 de capas delgadas y T800, muestran un comportamiento poco sensible a la presencia de zonas de concentraciones de tensiones. Se demuestra que este comportamiento está relacionado con la aparición de mecanismos adicionales de falla resultante de la presencia de diferentes tipos de fibras.

Respecto a los híbridos a nivel de capa, se ha desarrollado una estrategia para fabricarlos. Se ha hecho uso de la tecnología de dispersión del haz de fibras (*tow-spread techonology*) para realizar la hibridización. Los materiales producidos presentan una dispersión de fibra inferior a la prevista. Debido a restricciones en el proceso de fabricación, no se pudieron conseguir dispersiones más elevadas. Sin embargo, los materiales fabricados se han utilizado para estudiar los efectos de la hibridación intra-capa sobre la resistencia y la tenacidad. Se observa que los materiales híbridos ensayados presentan una resistencia más baja en comparación con los materiales de base y no se observa un aumento de la resistencia a la fractura, ya que no hay ninguna mecánica de falla adicional aparte de la falla de fibra. Sin embargo, se considera que la tecnología de dispersión del haz de fibras es una técnica a considerar y que se podrán producir compuestos con propiedades mejoradas si se consiguen dispersiones de fibra más altas.

Con este estudio, se ha alcanzado un conocimiento más profundo del comportamiento a fractura de los composites híbridos y el potencial de esta tecnología. No solo se ve incrementado el espacio de diseño, además se pueden mejorar propiedades como la ductilidad y la tenacidad diseñando el composite de manera que los diferentes mecanismos de daño se desarrollen de la manera deseada. Sin embargo, se necesitan de mas estudios de optimización de este material, no solo por lo que se refiere al tipo de fibras a utilizar, sino también para un diseño óptimo de la microestructura, pues, como se ha visto, es el parámetro clave que controla el comportamiento mecánico del material.

Resumen

El concepte d'hibridació de fibres consisteix a fer servir varis tipus de fibra en un mateix compòsit. Si s'aplica bé, el compòsit resultant pot presentar un millor comportament mecànic, doncs no s'afecten les propietats elàstiques dels constituents però si el desenvolupament dels diferents processos dissipatius que condueixen a la falla. Així, la hibridació de fibra es pot utilitzar per a dissenyar un material compòsit amb les propietats òptimes per a una aplicació determinada.

L'objectiu d'aquest treball és analitzar i comprendre la mecànica de deformació i falla de compòsits híbrids reforçats amb diferents tipus de fibres, posant èmfasi en la fallada dominada per la fibra. Per entendre millor el comportament dels compòsits híbrids, es realitzen dues tasques diferenciades: (i) el desenvolupament de models numèrics per predir la falla longitudinal i (ii) l'estudi experimental dels efectes de dues estratègies d'hibridació, capa a capa (*interply*) i hibridització a nivell de capa (*intratow*), sobre els mecanismes de dany que controlen la falla longitudinal.

La complexitat de la modelització de la falla a tracció longitudinal dels compòsits, fa que s'utilitzin models micromecànics sofisticats que contemplen el comportament mecànic dels diferent components (fibra, matriu i interfase fibra/matriu). En aquesta línia, en aquest treball es desenvolupa un model micromecànic 3D d'elements finits, que té en compte el comportament elàstic no lineal de les fibres i la seva distribució estocàstica de resistència, plasticitat i dany de la matriu i pèrdua d'adhesió de la interfície. El model desenvolupat s'utilitza per analitzar assajos micromecànics simples, com ara la fragmentació d'una sola fibra (*single fibre fragmentation test*) i l'assaig d'extracció una fibra per pressió (push-out test). Es demostra que els mecanismes de dany que controlen la falla en aquestes proves es representen amb precisió amb el model proposat. També es realitzen anàlisis sobre compòsits híbrids i no híbrids per comprendre el procés de fallada d'aquests materials. A més, s'aborda l'efecte de la pressió hidrostàtica sobre la falla a tracció dels compòsits reforçats amb fibra i es demostra que la reducció de resistència degut a la pressió hidrostàtica és ben capturada pels models.

L'estratègia de modelat 3D presentada és capaç de capturar els diferent i complexos mecanismes de falla dels compòsits, però, la seva complexitat i el seu cost computacional en limiten la seva utilitat. Per evitar aquest problema es proposa el Model de el *Spring Element Model* (SEM). Aquest model considera una disposició de fibra aleatòria de més d'un tipus de fibra, per la qual cosa es pot utilitzar per simular compòsits híbrids i no híbrids. També es proposa i mostra una versió més

complexa del model capaç de capturar amb precisió els efectes transitoris dinàmics que es produeixen quan es trenquen les fibres. El SEM s'utilitza per estudiar la fractura de fibres i la formació de clústers en materials no híbrids, tot i així, es mostra que els resultats numèrics difereixen dels experiments ja que generalment es preveuen densitats de ruptura de fibra més altes. El model SEM també s'utilitza per investigar l'efecte de la microestructura sobre materials compòsits híbrids. S'observa una alta dependència de la dispersió de fibres.

Paral · lelament al desenvolupament d'eines numèriques per predir la falla dels compòsits híbrids, s'han realitzat dues campanyes experimentals, una sobre compòsits híbrids capa a capa sobre híbrids a nivell de capa. Els materials híbrids capa a capa, resultants de la combinació de capes HR40 de capes primes i T800, mostren un comportament poc sensible a la presencia de zones de concentracions de tensions. Es demostra que aquest comportament està relacionat amb l'aparició de mecanismes addicionals de falla resultant de la presencia de diferents tipus de fibres.

Respecte els híbrids a nivell de capa, s'ha desenvolupat una estratègia per fabricarlos. S'ha fet ús de la tecnologia de dispersió del feix de fibres (*spread-tow technology*) per a realitzar la hibridització. Els materials produïts presenten una dispersió de fibra inferior a la prevista. A causa de restriccions en el procés de fabricació, no es van poder aconseguir dispersions més elevades. Tot i això, els materials fabricats s'han utilitzat per estudiar els efectes de la hibridació intra-capa sobre la resistència i la tenacitat. Es demostra que els materials híbrids presenten una resistència més baixa en comparació amb els materials de base i no s'observa un augment de la resistència a la fractura, ja que no hi ha cap mecànica de falla addicional a part de la falla de fibra. Tot i això, es considera que la tecnologia de dispersió del feix de fibres és una tècnica a considerar i que es podran produir compòsits amb propietats millorades si s'aconsegueixen dispersions de fibra més altes.

Amb aquest estudi, s'ha aconseguit un coneixement més profund del comportament a fractura dels compòsits híbrids i el potencial d'aquesta tecnologia. No només per l'increment en l'espai de disseny, sinó també per la millora en propietats com la ductilitat i la tenacitat que s'aconsegueix si es dissenyen de manera que els diferents mecanismes de dany es desenvolupin de la manera desitjada. Nogensmenys, calen més estudis d'optimització d'aquests material, no només pel que fa als tipus de fibres a utilitzar, sinó també pel que fa al disseny òptim de la microestructura que, com s'ha vist, és el paràmetre clau que controla el comportament mecànic del material.

Acknowledgements

First of all , I wish to express my gratitude to my supervisors Prof. Pedro P. Camanho and Prof. Albert Turon for granting me the opportunity and providing all the necessary conditions for me to finish my PhD.

I gratefully acknowledge the financial support provided by the Portuguese Government's Fundação para a Ciência e a Tecnologia, under grant SFRH/BD/115872/2016 and the project PTDC/EMS-PRO/4732/2014. I would also like to acknowledge the institutional support of INEGI, AMADE, LAETA and IAMAT.

Furthermore, I would like to thank Airbus Group Innovations (Munich, Germany) and Dr. Christian Weimer, Christian Metzner and Dr. Daniel Gzik for all the help and support on the development of the work on intratow hybrid composites.

I would also like to thank Dr. Fermin Otero, Dr. Joan Baiges, Dr. Miguel Bessa and Dr. António Melro for the invaluable help on the development of the numerical part of this work, as well as to Prof. Josep Costa and Prof. Joan Andreu Mayugo for supporting the work done in Girona.

This thesis would not be completed without acknowledging my colleagues and friends in Porto, Carolina Furtado, Dr. Albertino Arteiro, Dr. Giuseppe Catalanotti, Dr. Ricardo Pinto, Luis Pereira, Giuseppe Corrado and Martim Salgado. Everyone that I met in the Girona, Dr. Aravind Sasikumar, Sergio Medina, Jordi Llobet, Javi Gómez, Dr. Santiago Garcia, Adriá Quintanas, José Guerrero and Dr. Laura Carreras. And all the people from the different parts of this world that somehow ended up in Porto, Dr. Jérémy Chevalier, Dr. Albert Soto, Tobias Laux, Dr. Fujian Zhuang and Dr. Federico Danzi. To everyone that in some way or another was part of this journey and I forgot to mention, thank you for the support and friendship.

Last, but not least, I must thank Rita, my parents and my family.

Contents

List of symbols

Chapter 2

$\boldsymbol{B}^N$	Deformation matrix of the constituent N
d_m	Fibre spacing
E_N	Young's modulus of the constituent N
$\boldsymbol{f}$	Vector of applied forces
$f(\varepsilon)$	Gaussian probability density function
G_m	Matrix shear modulus
K	Stress concentration factor
$\boldsymbol{K}^N$	Stiffness matrix of the constituent N
L	Gauge length
L_0	Characteristic length for the Weibull parameters
m,m_1,m_2	Weibull shape parameters
$P(\sigma)$	Failure probability at the applied stress σ
R	Fibre radius
R_{hyb}	Hybrid effect
S	Standard deviation of the Gaussian distribution
S_N	Cross section area of the constituent N
$S_f\left(\sigma^f\right)$	Survival probability of a fibre subjected to a remote stress σ^f
t_m	Matrix thickness
u	Displacement vector
V	Volume associated with the gauge length L
V_0	Volume associated with the characteristic length L_0
V_N	Volume fraction of the constituent N
X_N^t	Tensile strength of the constituent N
α	Length dependency parameter
δ	Ineffective length
ε	Strain
ε^∞	Remote strain
ε_d	pseudo-ductile strain
$\langle\varepsilon\rangle$	Average fibre failure strain
μ	Mean of the Gaussian distribution
ϕ_f	Fibre diameter
ρ	Ratio of normalized stiffness of the hybridized fibres
σ	Stress

σ_0, σ_{01}, σ_{02}	Weibull scale parameters
σ^∞	Remote stress
ξ	load recovery percentage do define ineffective length
τ_{SL}	shear strength for the shear lag model

Chapter 3

A_n	Internal parameter for the material model
$\boldsymbol{C_f}$	Stiffness tensor of the fibre material
$\boldsymbol{C_f^0}$	Undamaged stiffness tensor of the fibre material
d_f	Damage variable of the fibre material
$\boldsymbol{D_f}$	Fibre stiffness tensor
$\boldsymbol{D}^e$	Elasticity tensor
E_i	Elastic modulus in the i-direction
E_f	Fibre longitudinal elastic modulus
E_0	Fibre longitudinal elastic modulus at zero applied strain
F_n^d	Damage activation function for the fibre model
G_{ff}	Fracture energy release rate of the fibre material in mode I
G_i	Shear modulus in the i-direction
$\mathscr{G}_n$	Complementary free energy density
G_{fm}	Fracture energy release rate of the matrix material
G_{iC}	Fracture energy release rate of the fibre-matrix interface
$\boldsymbol{H_f}$	Compliance tensor of the fibre material
$\boldsymbol{H_f^0}$	Compliance tensor for the undamaged fibre material
I_i	i^{th} invariant of the stress tensor
J_i	i^{th} invariant of the deviatoric stress tensor
L	Gauge length
L_0	Characteristic length for the Weibull parameters m and σ_0
l^e	Characteristic element length
m	Weibull shape parameter
$P(\sigma)$	Failure probability at the applied stress σ
r_n	Internal damage variable for the material n
$\boldsymbol{R}$	Residual
$\boldsymbol{S}$	Deviatoric stress tensor
S_{11}, S_{111}, S_{1111}	First, second and third order compliance coefficients
V_N	Volume fraction of the constituent N
X	Random number between 0 and 1
X_n^m	Strength of the material n in the load case m
Y_f	Associated thermodynamic force in the fibre model
W^*	Complementary free energy density
α_L	Longitudinal thermal expansion coefficient
α_T	Transverse thermal expansion coefficient
α_n^m	Rate dependence parameter for the matrix model
β_n^m	Temperature dependence parameter for the matrix model
δ_m^n	Separation at the state n under mixed mode conditions
$\delta\varepsilon_1$	Non-linear parameter for the fibre elastic modulus
η	Mixed-mode interaction parameter for the B-K law

$\boldsymbol{\varepsilon}$	Strain tensor
μ_τ	Friction at the fibre-matrix interface
ν_i	Poisson ratio in the i-direction
ν_p	Plastic Poisson ratio
$\boldsymbol{\sigma}$	Stress tensor
σ_{Yc}, σ_{Yt}	Compressive and tensile yield strengths
$\tilde{\boldsymbol{\sigma}}$	Effective stress tensor
σ_0	Weibull scale parameter
σ_{vm}	von Mises equivalent stress
τ^i	Fibre-matrix interfacial stress i-direction
τ_i^0	Fibre-matrix interfacial strength in the i-direction
ϕ_n^d	Loading function for the material model
Ψ_f	Energy dissipated per volume unit for the fibre model

Chapter 4

A_i^e	Area associated with the element e of type i
$\mathbf{B}_i$	Strain-displacement transformation matrix of the elements of type i
$\mathbf{C}_n^e$	Damping matrix of the element e of the type n
d	Distance between two adjacent fibres
$D_{p,q}$	Damage variable in the element of the fibre q at the plane p
DD	Dispersion Degree
E_f^e	Fibre elastic modulus of the element e
f_m	Shear force on the cross section in a matrix shear element
$\mathbf{f}^{\text{ext}}$	External force vector
$\mathbf{f}^{\text{int}}$	Internal force vector
G_m	Matrix shear modulus
$H_{p,c}$	Multiplier correction factor for the ineffective length of the fibre p, c
$\mathbf{K}_i$	Stiffness matrix of the elements of type i
L	Gauge length
L_0	Characteristic length for the Weibull parameters m and σ_0
l^z	Fibre element's length
$L_{p,q}^{\text{in}}$	Ineffective length of the element of the fibre q at the plane p
$\mathbf{M}_n^e$	Mass matrix of the element e of the type n
n_i	Number of matrix elements connected to the fibre i
N_i	Total number of elements of type i
N_f^b	Total number of broken fibre elements
$n_{p,c}$	Number of broken fibres in the p, c
$\boldsymbol{\mathcal{N}}_n$	Shape function of the element type n
$P(\sigma)$	Failure probability of a fibre element at the applied stress σ
R_i	Radius of the fibre i
R^{inf}	Radius of influence of a single or a cluster of broken fibres
$SCF_{p,q}$	Stress concentration factor in the element of the fibre q at the plane p
t_i, Δt_i	Time and time increment
$\mathbf{u}$, $\dot{\mathbf{u}}$, $\ddot{\mathbf{u}}$	Longitudinal displacement, velocity and acceleration vectors

V_f	Fibre volume fraction
X_T	Failure strength
X_T^e	Fibre tensile strength of the element e
α_m	Parameter that controls shear stiffness reduction of the matrix elements
α	Length scaling parameter for the modified Weibull distributions
α_d, β_d	Mass- and stiffness-proportional damping coefficients
$\delta_{(q-j)}$	Function that characterizes the evolution of the SCF in the in-plane direction
ε, Δ_ε	Strain and strain increment
ε_f	Failure strain
ε_d	Pseudo-ductile strain
$\lambda_{(p-i)}$	Function that characterizes the evolution of the SCF in the out-of-plane direction
ρ	Weibull shape parameter
ρ_n^e	Density of the element e of the material n
σ_0	Weibull scale parameter
σ_f^e	Stress in a fibre element e
$\sigma_{p,q}$	Stress in the element of the fibre q at the plane p
τ^u	Yield stress of the matrix elements

Chapter 5

E_i	Elastic modulus on the i-direction
E_f	Fibre elastic modulus
G_i	Shear modulus on the i-direction
K	Stress intensity factor
L	Gauge length
L_0	Characteristic length for the Weibull parameters m and σ_0
l_{fpz}	Length of the fracture process zone
R_0	Steady state fracture toughness
R_f	Fibre radius
R	Notch radius
T	Specimen thickness
X_n	Longitudinal strength for the load case n; L superscript refers to laminate properties
Y_n	Transverse strength for the load case n
W	Specimen width
α	Length scaling parameter for the modified Weibull distributions
β, γ	$\mathcal{R}$-curve parameters
ν_i	Poisson's ratio on the i-direction
ρ	Weibull shape parameter
σ_0	Weibull scale parameter
$\bar{\sigma}$	Failure stress; ∞ superscript refers to remote stress; N underscript refers to normalized stress
$\bar{\sigma}_S$	Notch sensitive normalized strength
$\bar{\sigma}_{IS}$	Notch insensitive normalized strength

Chapter 6

a_0	Notch length
E_i	Elastic modulus in the i-direction
$\acute{E}$	Equivalent elastic modulus
G_i	Shear modulus on the i-direction
$\mathcal{G}_I$	Driving force curve
$\mathcal{K}_I$	Stress intensity factor
L	Specimen length
l_{fpz}	Length of the fracture process zone
$\mathcal{R}$	$\mathcal{R}$-curve
$\mathcal{R}_{ss}$	Laminate steady state fracture toughness
$\mathcal{R}_0$	Steady state fracture toughness of the 0^{deg} plies
V_f	fibre volume fraction
X_t	Tensile strength
$2w$	Specimen width
β, γ	$\mathcal{R}$-curve parameters
ε_f	Failure strain
ν_i	Poisson's ratio on the i-direction

List of acronyms

1D/2D/3D	One, Two and Tree Dimensional
Avg.	Average
BFRP	Basalt Fibre Reinforced Plastic
CFRP	Carbon Fibre Reinforced Plastic
CTE	Coefficient of Thermal Expansion
DENT	Double Edge Notched Tension
FE/FEM	Finite Element/ Finite Element Method
FBM	Fibre Bundle Model
FRP	Fibre Reinforced Plastic
GFRP	Glass Fibre Reinforced Plastic
GLS	Global Load Sharing
HE	High Elongation
LE	Low Elongation
LLS	Local Load Sharing
MPI	Message Passing Interface
OHC	Open-Hole Compression
OHT	Open-Hole Tension
PLAW	Power-law Accelerated Weibull
PFM	Progressive Failure Model
PSC	Plain Strength Compression
PST	Plain Strength ension
RVE	Representative Volume Element
SCF	Stress Concentration Factor
SEM	Spring Element Model
STDV	Standard Deviation
UC	Unit Cell
UD	Unidirectional
WLT	Weakest Link Theory
WOW	Weibull of Weibulls

List of Figures

List of Tables

Part I

Introduction

Chapter 1

Introduction

A composite is a material that arises of the combination of two or more macroscopic components, resulting in a new material with superior properties than the constituents themselves. Composite materials are materials composed of a high stiffness and resistance reinforcing component - long fibres, short fibres or particles-, which are involved in a matrix, typically with weaker properties, that binds and protects the reinforcing material.

Composite materials are considered state-of-the-art materials, however, they are widely available in the nature and have been used by humans since the beginning of civilization. The muscles in the human body are an example of a fibrous material. The arrangement of muscular fibres with different orientations allows the creation of a very adaptable material with outstanding properties in a preferential direction. Another example of a composite material is wood, whose arrangement of cellulose fibres provides the necessary strength while the matrix (lignin) connects the fibres increasing its compressive resistance.

Man-made composites have existed for a long time. The first evidences of a man-made composite appeared in the Egyptian era, where straw and mud were mixed and burnt together by Israelites to obtain tougher bricks for construction. Another example of composite materials from the Egyptian era is papyrus, where layers of stems of the papyrus plant were stacked in perpendicular directions to manufacture paper with enough resistance to be written on and handled, thus creating the first man-made laminate. Throughout the ages other examples of composite material usage can be found. Advanced composite materials, as they are known, only appeared in the 20^{th} century, with the emergence of the glass fibres. This material rapidly gained market share in the aeronautical industry, during World War II, and in the aerospace industry, with the beginning of the space era. During the second half of the 20^{th} century other types of fibres emerged, namely the widely used carbon fibres.

Nowadays composite materials are widely available and the advances in the aerospace industry have been transferred to other industries. The applicability of composite materials is wide, from non-structural, secondary applications to structural and highly demanding applications. The widespread use of composite materials

is mainly due to the wide range of material properties that can be achieved with a correct design of these materials. This design focuses not only on the component's shape and form, but also in selecting the composite's constituents and its manufacturing process. Advanced composite materials, used in structural applications, are known for their high specific properties (strength and stiffness), and good fatigue, ballistic, thermal, corrosion, and electro-magnetic properties.

The growth in usage of composite materials can also be related to the recent advances in the computational techniques. The ability to analyse the behaviour of a material or component, without having the need to manufacture and test it, helped reducing the cost and time of the design process, allowing the development of new and better materials, designed for specific applications.

Computational simulations can be performed at different scales. Macromechanical simulations allow the designer to simulate the behaviour of a full component and to study stresses and deformations, however the material is considered to be homogeneous, which is a simplification from the complex geometry of a composite material.

At a more detailed scale it is possible to perform mesomechanical simulations where the composite material is considered to be composed by several homogeneous plies (laminas) that are stacked together with different orientations. Although the laminas are still considered homogeneous, this type of simulations allows a more detailed analysis and the study of several mechanisms of failure such as delamination, therefore providing better insight on the behaviour of composite materials.

As the composite materials are constituted by more than one macroscopic material, to simulate their microstructure it is necessary to resort to micromechanical simulations. These simulations explicitly model each of the constituents of the composite and consider that the different they have distinct behaviours, requiring different constitutive models. Despite of being more computationally demanding, these simulations allow a deep understanding of the mechanics of deformation and failure of composite materials and allow the distinction of the effects of each constituent, and its properties, on the global material behaviour

Motivation

Fibre-reinforced composites play a fundamental role in aircraft structural applications, however their optimal use is still hampered partly due to the relatively low toughness they exhibit. The tensile failure of UD composites is a catastrophic process due to the propagation of a cluster of broken fibres and hybridization may change this behaviour by changing the failure mechanisms typically observed in composite materials, leading to non-brittle composites.

Hybridization in composite materials is the concept of using more than one type of reinforcement or matrix system on the same material. Although hybridization was a large field of study from the invention of carbon fibre until the late 80s, the

interest has since then faded away, mainly due to the price reduction of carbon fibres and development of accurate models to predict the failure of non-hybrid composites. In the last years, hybridization, especially fibre hybridization, has become a field of interest mainly due to the possibility of delaying and achieving a more gradual failure of composite materials by controlling the damage mechanisms. However, their behaviour and the mechanisms that drive failure are not yet fully understood. In addition, modelling their complex behaviour is extremely challenging due to the complex interaction between failure mechanisms.

Even though composite materials are generally composed by layers with different orientations, fibre failure in the 0° layers is typically associated with the catastrophic failure of the material. This makes understanding the failure mechanisms in the tensile failure of unidirectional composites and the effects of hybridization in the failure mechanisms essential, not only from an experimental standpoint but also numerically. In addition, the development of accurate and efficient numerical models for hybrid composites allows their usage in combination with optimization tools. This provides the framework necessary to design optimal hybrid materials, not only by selecting the correct fibre combination, but also by designing their optimal microstructure.

Objectives

This thesis aims to develop the knowledge on the mechanical behaviour of unidirectional composites under tensile loadings, focusing on the mechanisms that lead to the failure of these materials and on the effects of fibre hybridization in damage development of this materials.

The theme of hybridization of composite materials has recently become a field of focus due to the potential of these materials to promote a more ductile behaviour. The usage of hybrid composites expands the possible design space and allows the optimization of the microstructure for a given application, material behaviour or material property. In this workk, the main focus of hybridization is the increase of ductility and toughness of composite materials and understanding the fibre and matrix properties required to achieve this goal. The ultimate goal is to be able to design a composite material with increased toughness without sacrificing the properties of the non-hybrid material, such as stiffness and strength.

To tackle the main objective of the thesis, a combined numerical/experimental approach was used. On one hand, complex micromechanical numerical models are developed and used to understand the mechanisms and properties driving the hybrid material's behaviour and failure. On the other hand, detailed experimental campaigns on hybrid materials are performed, not only to increase the knowledge of the behaviour of this type of materials, but also guide the development of the numerical tools to predict their failure.

Layout

This thesis is organized in 7 chapters that address different topics connected to the main goal of understanding the tensile failure of UD hybrid and non-hybrid composites.

Chapter 2 presents the state-of-the-art review. Different topics are addressed, including the size effects in composite materials, critical cluster size and the effects of the matrix in the tensile failure. The different statistical distributions to characterize the tensile strength of the fibres, important in the formation of the cluster of broken fibres before failure, are also presented. This chapter also addresses the topic of modelling of the tensile failure of UD composites, where several models with different backgrounds are presented and analysed to better understand the controlling factors in the tensile failure of UD composites. In addition, the state-of-the-art in hybridization of composite materials, focusing in fibre hybrid composites, is presented. A brief analysis on the effects of hybridization on the different materials properties is done. The concepts of pseudo-ductility and ductile composites are introduced and several experimental studies that demonstrated the pseudo-ductile behaviour are presented. The models for the tensile failure of hybrid composite are also analysed.

Chapter 3 presents the micromechanical modelling and simulations of different micromechanical phenomena. A damage model for the fibre constitutive behaviour that is able to account for fibre strength variability and fibre nonlinearity is developed. Results for more simple micromechanical tests as the single fibre fragmentation and fibre pushout tests are shown. Micromechanical results for the tensile failure of hybrid and non-hybrid composites are also presented and the sequence of mechanisms that lead to the failure of these materials is analysed, with the addition of the effect of hydrostatic pressure on the tensile failure of non-hybrid polymer composites.

In Chapter 4 a computationally efficient model to predict the tensile failure of fibre reinforced composites is presented. The Spring Element Model was developed, as an extension of a previously developed model, to account for a random fibre microstructure and for hybrid composites. Additionally, the results of this model were used to understand the analytical formulations for stress redistribution available in the literature. Finally, based on the shortcomings of the developed model, which considers static equilibrium, the model was extended for the dynamic case. This model was not only used to study non-hybrid composites but also hybrid materials and the effects of the microstructure on their global response.

To complement the numerical models developed, an experimental campaign focused on the analysis of the effects of interply hybridization in multidirectional laminates in structural details is presented in Chapter 5. In this work the concept of ply-by-ply hybridization is used to create multidirectional laminates with the objective of improving the response of a composite material at the structural level, focusing on open-hole tensile and compressive cases.

The concept of hybridization is further explored in Chapter 6. In this chapter, the spred-tow technology is used to to commingle tows of different types of fibre to manufacture intratow hybrid composites. An experimental campaign focused on the fibre driven properties of the manufactured materials is done and the behaviour of the materials and the damage processes controlling failure are analysed.

Lastly, in Chapter 7, the main conclusions of the work carried out in this thesis and some follow-up research topics are proposed.

Part II

State-of-the-art review

Chapter 2

State-of-the-art review

2.1 Mechanisms of longitudinal fracture

Modelling of composite materials is a difficult task due to the complexity of its internal structure and interactions between constituents (interface). However, having models that are able to predict the behaviour of composite materials is essential to optimize their design.

The mechanisms of longitudinal failure of unidirectional (UD) composites under longitudinal loadings are well understood, and are based in two essential aspects: (1) fibres do not have a deterministic value for tensile strength [33] and (2), after a fibre fractures, the stress is redistributed among the intact fibres in a complex way [34]. The failure sequence is considered to be as follows: the increase in applied strain leads to the failure of the weakest fibre, which means that, locally, it is no longer able to carry stress. As the matrix is loaded, it transfer the load back to the broken fibre, making it able to carry stress away from the point of fracture. The stress is redistributed to the remaining intact fibres by the matrix, which leads to stress concentrations in the intact fibres, increasing their probability of failure. At low applied stresses the fibres break appear in random locations and there is nearly no interaction between breaks. At later stages, the stress concentration in the intact fibres will cause their failure which leads to the creation of a cluster of broken fibres. These clusters will grow, when other fibres fail and, when a cluster reaches a certain critical size, it will propagate unstably leading to the failure of the composite. The tensile failure of a UD composite is, therefore, of statistical nature and function of the mechanics of load redistribution around broken fibres.

This chapter focuses on the tensile failure of non-hybrid composites.

2.1.1 Distributions for fibre strength

The tensile strength of a technical fibre cannot be represented by a single mean value. Due to their brittle behaviour the fibre tensile strength is governed by surface or volume flaws [33] and exhibits weak-link characteristics. There are several

statistical distributions that can be used to characterize the strength of fibres, being the most used the Weibull distribution, proposed by Weibull in 1951 [35].

2.1.1.1 Weibull distribution

The standard Weibull probability distribution can be written as:

$$P(\sigma) = 1 - \exp\left(-\left(\frac{L}{L_0}\right)\left(\frac{\sigma}{\sigma_0}\right)^m\right) , \tag{2.1}$$

where P is the failure probability at the applied stress σ, L is the characteristic gauge length, L_0 is the reference gauge length (these can also be characterised as volumes [36]), σ_0 the scale parameter and m the shape parameter or Weibull modulus [35].

This distribution usually leads to the overestimation of the fibre strength at short gauge lengths [2] and is very sensitive to the statistical parameters [37]. The discrepancy between the Weibull distribution and the experimental results for short gauge lengths can be attributed to variations in fibre diameter, variations of the Weibull distribution from fibre to fibre and presence of different flaw populations [2]. According Curtin [28] this distribution is not the most accurate to describe the strength of fibres, however is still the most used to characterize the tensile strength of technical fibres. One of the drawbacks of this distribution is that there is no threshold bellow which the failure probability is zero.

2.1.1.2 Modified Weibull distributions

Several authors found that the fibre strength is governed by more than one flaw population [38, 39] and therefore a bimodal Weibull distribution should be used:

$$P(\sigma) = 1 - \exp\left(-\left(\frac{L}{L_0}\right)\left(\frac{\sigma}{\sigma_{01}}\right)^{m_1} - \left(\frac{L}{L_0}\right)\left(\frac{\sigma}{\sigma_{02}}\right)^{m_2}\right) , \tag{2.2}$$

where σ_{01} and σ_{02} are the scale parameters and m_1 and m_2 the Weibull moduli for both populations of flaws. The usage of the traditional Weibull distribution indicates that there is no threshold stress below which the failure probability is zero, which is common in brittle materials like fibres, however if such threshold exists the bimodal distribution is able to capture that limit [1, 2].

As mentioned before, the traditional Weibull distribution fails to characterise the fibre strength at short gauge lengths, therefore a modified Weibull distribution that adds an exponent α to capture this dependency [40] was proposed:

$$P(\sigma_f) = 1 - \exp\left(-\left(\frac{L}{L_0}\right)^{\alpha}\left(\frac{\sigma}{\sigma_0}\right)^m\right) . \tag{2.3}$$

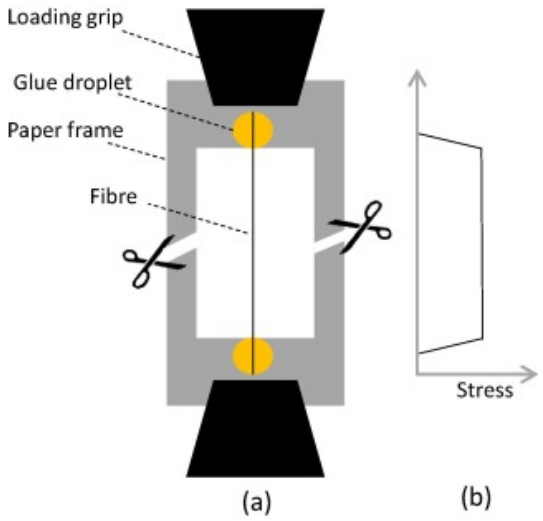

Figure 2.1: (a) Schematic illustration of a single fibre test; (b) stress profile in the tested fibre [1].

This equation leads to the traditional Weibull distribution when α equals 1. The α parameter, usually lower than 1, allows the strength distribution to be less sensitive to length scaling, therefore, reducing the overestimation usual of the traditional Weibull distribution at very short gauge lengths (usual of most composite strength models).

Curtin [28] proposed a model, entitled "Weibull of Weilbulls" that considers that the strength along a fibre follows a traditional Weibull distribution (Eq. (2.1)), therefore it is possible to calculated the characteristic strength for a fibre element of length L. Curtin also states that the characteristic strength of each fibre are different and follow another Weibull distribution, leading to the "Weibull of Weibulls" distribution of fibre strength. There is still no consensus whether traditional Weibull or the modified Weibull distributions better represent the fibre strength.

2.1.1.3 Issues with the determination of the fibre strength

The determination of the parameters necessary for the presented fibre strength distributions is not straightforward as large samples need to be tested in order to obtain representative parameters. As previously discussed, there are several distributions to characterize the failure probability of fibres, being the most used the traditional Weibull distribution (Equation 2.1).

The most used technique to determine the statistical strength distribution of the fibres is the single fibre test (Figure 2.1), that is described in several standards, such as BS ISO 11566 and ASTM C1557. The testing procedure is simple. It consists in extracting a fibre from a bundle and gluing it in a paper frame with the best alignment possible. Afterwards the frame is cut and a standard tensile test is performed.

By testing a large number of fibres and recording the strength, the Weibull distribution can be fitted to the data through a maximum likelihood estimation. Nonetheless, there are some issues with this type of testing. Firstly, it is necessary to test a high number of fibres to reduce the data dispersion, which may lead to wrong fibre properties, in particular the Weibull modulus. This makes sense, as measurement errors introduce scatters in the data, which widens the distribution and lowers the Weibull modulus [1, 41]. This test also runs into some problems with small gauge lengths due to an increased probability of having a misaligned fibre, which alters the results. This effect is also highlighted by the fact that in glued section of the fibre there is a stress build up through shear. This build up length is usually small, however, for short gauge lengths it may affect the results.

Other types of testing to determine the statistical strength distributions for the fibres are available, however, they are much less used, but may have some advantages over the single fibre tensile test. The fibre bundle test allows to test a large number of fibres simultaneously and has been used successfully in the determination of the Weibull parameters [36, 37]. This test allows the gathering of large amounts of data in a single test, however, it is usually necessary the determination of fibre fracture via acoustic emission and there is a small degree of interaction between the fibres in the bundle, which alters the fibre strength results. The fragmentation test, initially developed to determine the fibre-matrix interface properties, may also be used to determine the strength distribution [38, 42]. Similarly to the bundle test, it is possible to gather more than one data point in a single test, as there is multiple failure of the fibre. Another benefit of this test test is that it allows the determination of the statistical parameters for gauge lengths that are not easily accessible in the other tests [1] and it is performed within a matrix, which allows to gather the data in the system that will be used in the composite. There is also the loop test [43], which as some drawbacks, as only one fibre can be tested at a time and the non uniform stress in the fibre loop may lead to an overestimation of the fibre strength. The increase in definition in the synchrotron radiation computed tomography with the use of suitable fibre break algorithms may lead to a new type of fibre testing method, where a large number of fibres is tests simultaneously [1], however, this is still an ongoing subject.

Some parameters for the traditional Weibull distribution for carbon, glass and kevlar fibres are shown, respectively, in Tables 2.1, 2.2 and 2.3. It is also shown the mean failure strain $\langle \varepsilon \rangle$ of the fibres at a gauge length of 75 mm.

Table 2.1: Mechanical properties for carbon fibres.

Material	Reference	σ_0 (MPa)	L_0 (mm)	m	E (GPa)	R (μm)	$\langle\varepsilon\rangle$ @75mm (%)
HTS carbon	Beyerlein 1996 [44]	4493	19	4.8	230	3.5	1.34
X5 fibers	Nakatani 1999 [45]	2500	25	6.1	520	5.05	0.37
AS4 carbon	Curtin 1998 [21]	4275	12.7	10.7	234	3.5	1.48
T300	Curtin 1998 [21]	3170	25	5.1	232	3.5	1.01
T300	R Mili 1996 [46]	3200	30	5.5	232	3.5	1.08
T300-B4C	R Mili 1996 [46]	3150	30	5.4	232	3.5	1.06
700°C	Tanaka 2014 [27]	1400	10	11	55	3.3	2.02
1000°C	Tanaka 2014 [27]	4500	10	4.5	240	2.9	1.09
T800G	Tanaka 2014 [27]	6800	10	4.8	295	2.75	1.39
M30S	Tanaka 2014 [27]	6400	10	4.6	295	2.8	1.28
M40S	Tanaka 2014 [27]	4900	10	5.2	380	2.7	0.81
M50S	Tanaka 2014 [27]	4600	10	9	480	2.65	0.73

Table 2.2: Mechanical properties for glass fibres.

Material	Reference	σ_0 (MPa)	L_0 (mm)	m	E (GPa)	R (μm)	$\langle\varepsilon\rangle$ @75mm (%)
E-Glass	T.Okabe 2001 [29]	1550	24	6.34	76	6.5	1.59
E-Glass	Feih 2005 [47]	1649	20	3.09	66.9	7.8	1.44
E-Gkass	Pauchard 2002 [48]	2300	10	3.6	70	5	1.69
AR-HP	Foray 2012 [49]	1363	60	9.6	70	7	1.81
AR-HD	Foray 2012 [49]	876	60	4.8	70	7	1.09

Table 2.3: Mechanical properties for kevlar fibres.

Material	Reference	σ_0 (MPa)	L_0 (mm)	m	E (GPa)	R (μm)	$\langle\varepsilon\rangle$ @75mm (%)
Kevlar 29	Naito 2013 [50]	3445.8	25	11.8	85.3	6.895	3.52
Kevlar 49	Naito 2013 [50]	4083.3	25	8.2	149.1	5.135	2.26
Kevlar 119	Naito 2013 [50]	3101.2	25	11.8	61.4	5.46	4.41
Kevlar 129	Naito 2013 [50]	3433	25	10.3	99	5.79	2.97

2.1.2 Matrix and fibre-matrix interface properties

The tensile failure of composite materials is a fibre dominated phenomenon, however the matrix also plays an important role. The matrix allows the stress recovery of a broken fibre due to shear stress transfer [2] and its properties affect the stress concentration factors and failure mechanisms.

Several models consider the fibres and matrix to be perfectly bonded, which leads to a infinite stress concentration factor in the matrix around a fibre break. As the matrix and the interface are unable to support such a high stress three scenarios can occur: (1) the matrix yields, (2) the interface debonds and (3) the matrix cracks in the break plane [2]. A combination of these can also occur. Zeng et al. [51] studied the influence of interfacial damage in the stress redistribution in UD composites and concluded that the stress concentrations increased with increasing the strength of the interface. He also concluded that matrix shear yielding resulted in lower stress concentration factors in intact fibres. The matrix yield strength also affects the ineffective length significantly, the lower the shear yield stress, the larger the ineffective length [52]. Interfacial debonding tends to occur in composites with weak interfacial bonds, and has a similar effect as matrix yielding. Both matrix yielding and interfacial debonding have been extensively studied in the literature, unlike the matrix cracking failure mechanism.

Recently, Swolfs et al. [53] studied the influence of matrix cracks in both the SCF and the ineffective length in a composite with a random distribution of fibres. The authors concluded that the matrix cracking increases the ineffective length, drastically changing the stress recovery profile. As one can see in Figure 2.2, the stress in the broken fibre rapidly increases to 35% when there isn't a crack in the matrix, however, in the model with a crack, the stress slowly increases from zero, due to the presence of a crack in the matrix. Swolfs et al. [53] also showed that matrix cracks not only increases the ineffective length but, also the stress concentration factor, leading to an overall higher failure probability of the intact fibres.

According to Hobbiebrunken et al. [54] and Chevalier et al. [55] the matrix strength is size dependent, which means that the real strength of the matrix used in

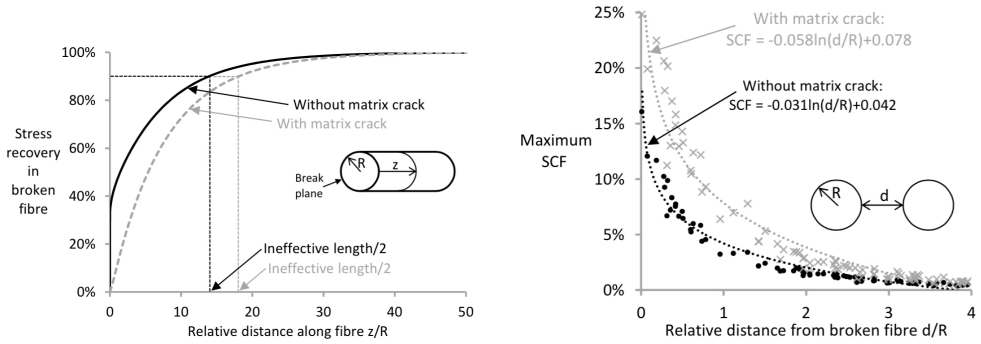

Figure 2.2: Effect of matrix cracks in the ineffective length (left) and the stress concentration factors (right) [2].

composite materials may differ from that tested in bulk [55]. In fibrous composites the matrix usually has a small thickness in the order of a few microns, thus having a strength higher than that of large test specimens. As the matrix strength affects the tensile behaviour of composites, not accounting for this size effect may lead less accurate results.

Morais [56] studied the effect of the matrix shear modulus in the range 1.2 – 1.6 GPa and he concluded that the tensile strength of the composite material is practically insensitive to this parameter. However, he concluded the matrix shear strength is an important factor in the composite tensile strength. His results showed that increasing the shear strength from 40 to 100 MPa increased the composite strength from 1300 to 1600 MPa for T300 carbon fibre and from 2400 to 3100 MPa for T800 carbon fibre. This changes can be attributed to modifications in the stress recovery profiles of the fibres. Similar conclusions have been reached by Pimenta and Pinho [7] using a different model.

Another aspect to take into account in matrix behaviour is the time dependency. This affects the composite behaviour as it is able to creep and fibre breaks may develop at constant applied load [1]. According to Foreman et al. [57] the increase in strain rate leads to a slightly shorter ineffective length and higher stress concentrations. This is due to the stiffening and strengthening of the matrix with the strain rate, which causes a localization of stresses in the fibre break plane, leading therefore to the formation of planar clusters.

Debonding between the matrix and the fibres occurs when a fibre breaks, which can be seen in single fibre fragmentation tests [17], however, this has not been seen experimentally in composite materials [1]. It is worth noting that debonding has been captured in micromechanical models [58]. The debonding is controlled by the fibre-matrix interface strength and strain energy release rate, the friction between the fibre and the matrix, the matrix yield strength and the fibre stiffness [1]. From these the interface strength is the most important parameter as it controls the ineffective length. A low interface shear strength leads to higher ineffective lengths, which causes stress concentrations in a larger region, which result in poor composite properties [1]. However, if the interface strength is too high, there is no debondonding which causes a high local stress concentrations that may lead to

premature failure. Therefore a intermediate value for the shear strength may lead to improved composite behaviour [59].

2.1.3 Size effects in composites

Size effects affect, not only the strength of individual fibres, but also influence the failure process and longitudinal strength of composite structures [3, 60, 61]. There are several factors that lead to this size effects, being that most authors agree that the statistics of fibre strength is the main one. Several authors have experimentally demonstrated this size scaling behaviour (see Figure 2.3).

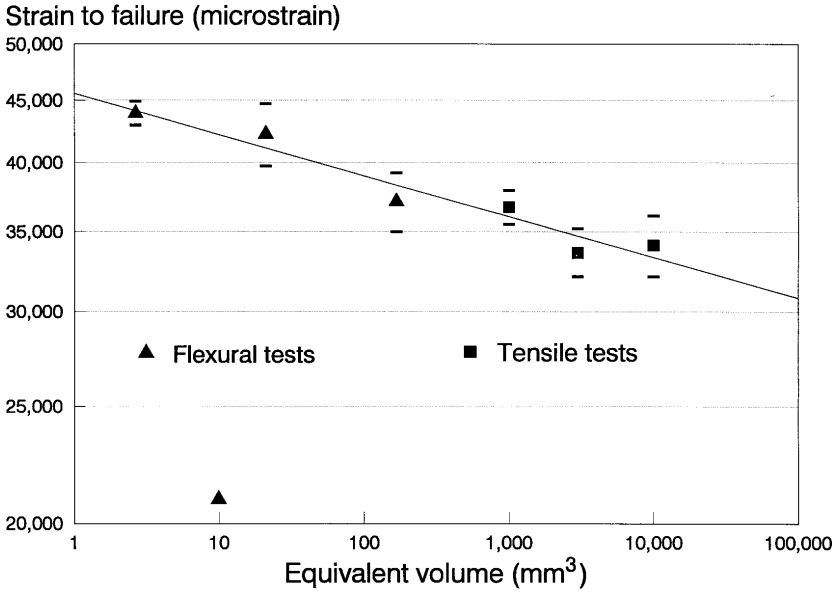

Figure 2.3: Size effects in glass/epoxy composites [3].

The longitudinal tensile strength of UD composites is characterized by strong size effects connected to both the length of the specimens and the total number of fibres. The size effect is not only affected by statistical aspects, but is also by deterministic factors, that include the effects of the damage process zone and the change of the failure modes [62]. There are other influencing factors, namely the influence of manufacturing and testing. This means that in order to achieve a good design of large composite structures based on coupon testing, one has to take into account that the coupons should be representative of the manufacturing process of the large scale component and that larger structures have lower strength due to the higher probability of the existence of a critical defect [3]. One of the factors that leads to size effect due to manufacturing is the fact have larger fibre waviness and overall defects present in larger components than in small coupons. Additionally to the experimental results validating size effects there have also been models able to capture this effect [7, 60, 63]. Okabe et al. [60] experimentally and numerically investigated the size effects on the ultimate tensile strength of unidirectional fibre reinforced composites and concluded that the simulation based on the traditional Weibull model overestimates the ultimate tensile strength. However, the authors

concluded that the predictions utilizing Curtin's Weibull of Weibull model [28] appears to agree well with the upper bounds of the experimental data.

2.1.4 Stress redistribution after fibre failure

The statistical distributions presented allow the determination of the strain at which a fibre will fracture. If a global load sharing rule is considered, then the stress that the fractured fibre previously carried is transferred equally to all the remaining intact fibres. This type of load sharing rule is able to predict the failure of lubricated tows, where the fibre interaction is low [36], but it's not accurate for composite materials where the fibres are bonded by a matrix and there is strong interaction between the fibres.

The interaction between the fibres and between the fibres and the matrix results in a non uniform stress redistribution to the intact fibres, which is highly dependent on the composite geometry [64]. The models that consider a non uniform stress redistribution are said to consider a local load sharing rule. For composite systems the redistribution of stresses is a complex process that depends on several parameters, including the strength and sliding resistance of the fibre/matrix interface, the fibre to matrix moduli ratio, the matrix cracking or yield stress, the regularity of the fibre spacing and debonding of the fibre-matrix interface [65]. This complex stress redistribution is often characterised by the stress concentration factor (SCF) and the ineffective length [2]. The SCF is the an adimensional parameter that is defined as the ratio between the longitudinal stress in an intact fibre after the failure of a neighbour fibre and the longitudinal stress in the absence of breaks. The stress in the absence of breaks is usually considered the stress in the intact fibre far from the plane of break, which simplifies the determination of this parameter. After a fibre breaks it locally looses the ability to carry stress, even so, away from the failure plane it is still able to carry loads, which means that a fibre doesn't fully loose the ability to carry stress after it breaks. The ineffective length is a measure of the stress recovery length of the fibre and can be defined, for instance, as twice the length at which the broken fibre can carry 90% of the applied stress [66]. These parameters are crucial in the modelling of composite materials as they will affect the stress redistribution and, therefore, the damage accumulation and the formation of clusters of broken fibres.

The redistribution of stress is closely related with the fibre packing. There are several types of fibre packings that one can consider when modelling the microstructure of a composite material, some are represented in Figure 2.4.

A 1D packing consists in a single row of fibres that can be equally spaced or randomly spaced. This type of packing is more common than 2D packings as it is easier to obtain, however it fails to give a accurate representation of the composite behaviour, and leads to an overestimation of the stress concentration factors, making 2D packings more accurate to describe the micro-structure of composite materials. Being so, 2D packings with random distribution of fibres are the models that most accurately represent the microstructure of a composite material, as they better relate with the real distribution of fibres in these materials [67]. The random distribution

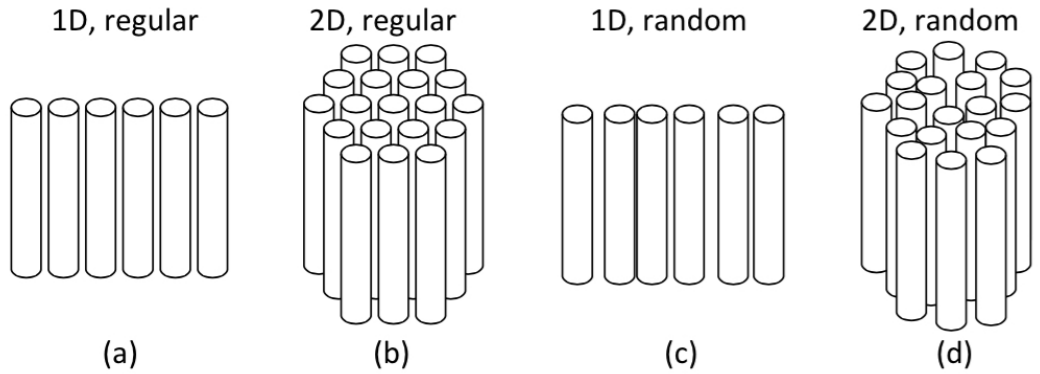

Figure 2.4: Schematic illustration of fibre packings: (a) 1D regular packing, (b) 2D regular packing (c) 1D random packing and 2D random packing [2].

of fibres instead of a regular packing, leads to a varying fibre spacing and, therefore, changes the stress distribution. Obtaining this random distributions is more difficult and computationally expensive than regular ones, however several random fibre generators capable of generating such microstructures are available in the literature [68–71]. Another problem of using random fibre packings in FE analysis is that the variations of fibre spacing lead to some problems with the meshing and the necessity of having a more refined mesh, which increases the computational load of the model. Nonetheless, if it is possible to use a random distribution, one should do so, as it translates better into the real microstructures and behaviour of fibrous composites. The randomness of the usual microstructure of the composite material as been shown by Swolfs et al. [34] to lead to higher stress concentration factors.

The fibre packing affects the stress redistribution around a broken fibre, however, the stress redistribution is also affect by other factors. Fibre breakage has the tendency to occur in clusters [72, 73] and this clustering has an effect on how the stress is redistributed into the surrounding fibres of a broken one. St-Pierre et al. [74] studied the effect of the number of broken fibres in a cluster on the stress redistribution around a broken fibre. The authors concluded that not only the maximum SCF increases with the number of fibres, but also does the ineffective length. The authors were able to derive analytical expressions for both the ineffective length and maximum SCF as a function of the number of broken fibres in a cluster.

Fibre breakage is a dynamic process [41, 58, 75–78] and the elastic energy previously stored in the fibre is converted into kinetic energy. This exchange causes stress waves to propagate in the fibres and, therefore, changes the stress fields over time. This dynamic transient effect leads to higher stress concentrations [75, 77–79, 79]. This dynamic effect can be essential in bridging the results mismatch between the state of the art models and the experimental results for fibre failure in longitudinal tension, nevertheless, most of the state of the art models ignore this fact.

2.1.5 Critical cluster size

As already mentioned, the failure of a UD composite under tensile loads is due to the unstable propagation of a cluster of broken fibres. The clusters are formed due to stress concentrations in the intact fibres that neighbour a broken one. This increase in SCF causes the stress in the intact fibres to increase, thus increasing their probability of failure, making it more probable that fibres will fail in clusters. When a cluster of broken fibres is large enough, it propagates in an unstable manner, leading to the composite failure. Critical cluster size is, therefore, an important topic in understanding the failure of UD composites.

Ibnabdeljalil and Curtin [80] studied this problem and derived an equation for the critical cluster size (n^{crit}):

$$n^{\text{crit}} = 403m^{-1.28} \,, \tag{2.4}$$

where m is the Weibull modulus. This equation was derived from numerical simulations using Green's function for stress redistribution, whose parameter Ω characterises the level of localization of the stress redistribution. The result presented in Equation 2.4 is for $\Omega = 0.001$, that represents a very local load sharing model ($\Omega \to \infty$ corresponds to global load sharing).

As the Weibull modulus presents some degree of dispersion, even for the same type of fibre, one can expect that, in a composite material, there are stronger and weaker regions [80], which will translate in variations of the critical cluster size and composite strength.

Although with some difficulties, the critical cluster size was also tackled in an experimental way. Using synchrotron computed tomography, Scott et al. [4] found a cluster size of 14 fibres (14-plet) prior to failure (Figure 2.5). This cluster was found at 94% of the failure strain, which means that the critical cluster size should be superior to 14.

More recently Swolfs et al. [73] used the synchrotron data from [4] in a more extensive way analysing the cluster initialization and development and compared those results with the ones from a numerical model. From these results it was verified that the final fibre failure density was very low, with less than 10% of the fibres failed in the last increment. Two types of clusters of broken fibres were defined, the co-planar and diffuse clusters. The first one was defined to occur if in the axial direction the failure of the two or more fibres occurred with a separation of less than a fibre radius and the latter otherwise. Experimentally it was verified that the number of co-planar clusters was higher than the number of diffuse. Around 70% of all clusters were co-planar, which contradicts the results from their model. The authors justify this phenomenon with two reasons: (1) the local very high stress gradients that occur at the tip of the matrix cracks were not accounted in the model due to the use of an average SCF in the fibre section; (2) the failure of the fibres is a dynamic process with very high transient stress concentrations that were not accounted in the model. The latter hypotheses is further verified due to the fact that, experimentally, the clusters that were found in a given increment did not grow

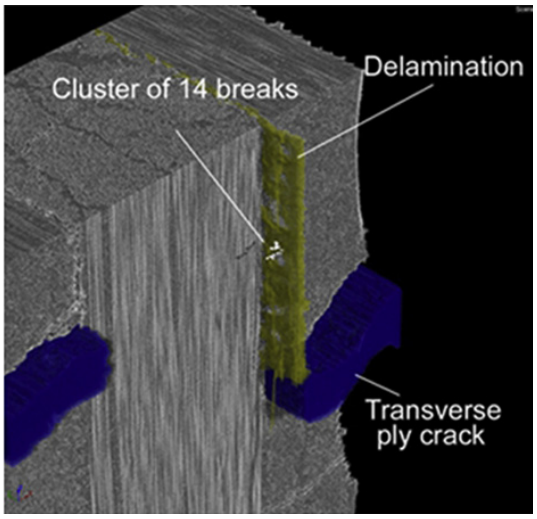

Figure 2.5: Cluster of 14 fibres observed by Scott et al. [4] using synchrotron computed tomography.

any further, justifying that the cluster formation is a dynamic process, which is not accounted in the model, where the clusters are considered to grow in a stable manner.

Other authors have done similar studies. For example Aroush et al. [81] found a critical cluster size in the range 9-33 for quartz fibre reinforced epoxy resin. Na et al. [82] used X-ray computed tomography to identify fibre breakage and clustering in CFRPs and observed that single isolated fibre fracture started at low applied loads, around 30% of maximum load. The authors also observed that clusters of broken fibres had the tendency to occur in proximity of each other, underlying the importance of stress concentration around the clusters of broken fibres. Additionally, it was observed that at increased the loads some clusters would be merged leading to the formation of a larger cluster, up to 25–35 fibres. Finally, the authors observed that the composite exhibited sudden catastrophic failure leaving larger multiple fracture clusters in the specimen.

2.1.6 Modelling the tensile failure of unidirectional composites

There are several models to predict the tensile failure strength of UD composites in the literature. Mishnaevsky and Brøndsted [83] consider four categories of models: analytical models, fibre bundle models, fracture mechanics models and continuum damage mechanics models. The latter models usually lead to complex simulations, being therefore limited in the size of the models.

In the next sections several models to predict the tensile failure of composites will be presented. The models are presented in five subsections. The first is about the deterministic rule of mixtures, the second presents the analytical fibre bundle models, the third presents the micromechanical models based on Monte-Carlo simulations, continuum damage mechanics based models and the last one presents a recent model

based on a hierarchical scaling law.

2.1.6.1 Deterministic rule of mixtures

The rule of mixtures is the simplest model to predict the tensile strength of UD composites. For the majority of composite materials the failure strain of the reinforcing fibres (ε_f) is lower than the failure strain of the matrix (ε_m), which means that the fibres will fail first. Usually composite materials have a fibre volume fraction (V_f) around 50 to 70% and, after the fibres fail, the matrix is not able to carry the stress. This means that the failure strain of the composite (ε_C) is equal to the failure strain of the fibres (ε_f). This assumptions translate into the following equation for the composite tensile strength (X_C^t):

$$X_C^t = V_f X_f^t + (1 - V_f)\,\frac{E_m}{E_f} X_f^t;, \tag{2.5}$$

where X_f^t is the fibres' tensile strength and E_f and E_m are, respectively, the fibre and matrix stiffness. According to the already reviewed influencing factors of the tensile strength, this model fails in two aspects. Firstly, it considers the fibre strength to be a deterministic one, which was already proven to not be realistic, as the tensile strength of fibres follow a statistical distribution. The second flaw is that the model doesn't consider the interaction between the fibres connected by the matrix and, therefore, it fails to accurately predict the tensile strength of UD composites.

More advanced and accurate models are presented in the next sections.

2.1.6.2 Analytical fibre bundle models

Fibre Bundle Models (FBMs) consider a bundle of parallel fibres with stochastic tensile strength, but with the same elastic properties and loaded under uniaxial tension [83]. When the remote stress is high enough to make the weakest fibre fracture it breaks and the stress is redistributed towards the remaining intact fibres. If the stress concentration, due to this stress redistribution, is enough to make another fibre fail, it will fail and the stress is redistributed again, if not the remote stress is increased. This process is repeated until all fibres fail or until the material cannot withstand further load increments. FBMs have been developed for dry bundles (with no matrix) and for composite materials, considering the influence of the matrix. The matrix acts as a connector between fibres and alters the stress redistribution, affecting the ineffective length and the stress concentrations in the neighbouring fibres of a broken one. According to the stress distribution rule this models can be divided into global load sharing (GLS) models and local load sharing (LLS) models. The GLS models are able to predict the failure of a dry bundle where the interaction between the fibres is low [36]. The LLS models consider that there isn't a uniform stress redistribution due to the presence of the matrix.

Global load sharing models The first fibre bundle model was developed by Daniels [84] and was later extended by several authors [66, 85]. This model considers a bundle composed of N fibres with a defined length (l_r), and the fibre strength is considered to follow a Weibull distribution (Equation 2.1). Daniels [84] determined the following law relating the stress in the bundle (σ^∞) with the applied strain (ε^∞):

$$\sigma^\infty = E_f \varepsilon^\infty \cdot S_f(\sigma^f) \,, \tag{2.6}$$

where E_f is the fibre longitudinal modulus, σ^f is the stress actuating in the intact fibres and $S_r^f(\sigma^f)$ represents survival probability under the stress σ^f of a fibre with length l_r. In this equation the contribution of the matrix to the load carrying capacity has been neglected. It was concluded that the tensile strength of a bundle with a large number of fibres can be represented by a normal distribution and the expected value for the strength of the bundle is given by:

$$X_r^b = \frac{\sigma_r^f}{m^{1/m} e^{1/m}} \qquad \text{where} \qquad \sigma_r^f = \sigma_0^f \left(\frac{l_r}{L_0}\right)^{-1/m} . \tag{2.7}$$

σ_0^f, m and l_0 are the characteristic parameters of the Weibull distribution and e is the base of the natural logarithm. As this model was developed for dry bundles it considers that a broken fibre is no longer able to carry load, which is not accurate in the presence of a matrix.

Rosen [66] considered the influence of the matrix trough a shear-lag model. This model considers that the stress is transferred, by the matrix, that is loaded in shear, back to the broken fibre. This means that there is a stress recovery in axial direction of the broken fibre. This leads to the definition of the ineffective length as the distance δ from the break where the fibre recovered the ability to carry a percentage ξ (e.g. 90%) of the remote stress. Based on these assumptions the following expression for the ineffective length δ was derived [66]:

$$\delta = \frac{\phi_f}{2} \sqrt{\frac{1-\sqrt{V_f}}{\sqrt{V_f}} \frac{E_f}{G_m}} \ln\left[\frac{1}{1-\xi}\right] \tag{2.8}$$

where ϕ_f is the fibre diameter and G_m is the matrix shear modulus.

Rosen [66] considered that a bundle with length l_r could be divided into a chain of bundles width lengths l_r/δ and that the longer bundle will fail as soon as one of the sub-bundles fails, according to the weakest link theory. As the strength distributions of the sub-bundles are given by Daniels' approach and, therefore, follow a normal distribution $F_\delta^b(\sigma^\infty)$. This assumptions mean that the bundle follows weakest link theory and the strength distribution for a bundle with length l_r can be calculated by:

$$F_r^b(\sigma^\infty) = 1 - \left[1 - F_\delta^b(\sigma^\infty)\right]^{l_r/\delta} . \tag{2.9}$$

For the particular case of a very large bundle, the standard deviation of the sub-bundle strength equal to zero and Weibull fibre strength distribution, the most likely failure strength of the bundle with length l_r is given by:

$$X_r^b = \frac{\sigma_r^f}{m^{1/m} e^{1/m}} \qquad \text{where} \qquad \sigma_r^f = \sigma_0^f \left(\frac{\delta}{L_0}\right)^{-1/m} . \tag{2.10}$$

This equation is similar to the one presented for Daniels' model (Equation 2.7), except for the length correction in the Weibul distribution. This means that while Daniels' model considers the full length of the bundle (l_r), Rosen's model considers only the ineffective length (δ). Equation 2.10 is a simplification of the general model (Equation 2.9) and represents a deterministic model based of the average fibre strength, and therefore isn't able to capture size effects [5].

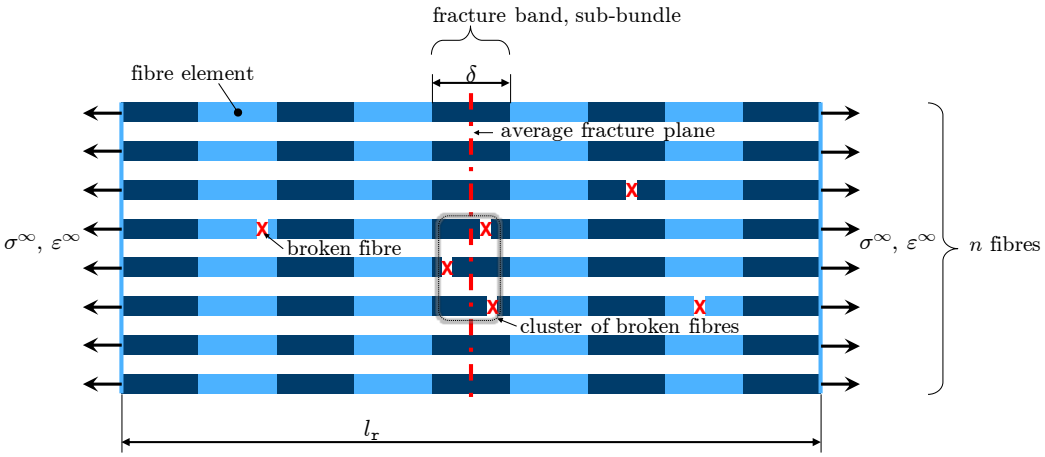

Figure 2.6: Diagram of a fibre bundle model [5].

Curtin [85] developed a fibre bundle model aimed for ceramic-matrix composites, that considers global redistribution of stress. This model considers a fracture band centred at the average plane of a bundle and for each remote stress σ^∞, a fraction of the bundle fibres χ are fractured at a random distance from the middle plane (see Figure 2.6). The fracture band as a length δ and each fracture is located at a distance l_{po} from the average plane. The broken fibres recover stress linearly, according to the shear lag model with a constant shear stress τ_{SL}. Being the undisturbed stress of a fibre σ^f, it is possible to define the fracture band length δ as:

$$\delta = \frac{\sigma^f \phi^f}{2\tau_{SL}} . \tag{2.11}$$

It is possible then to calculate the stress of a broken fibre at the average fracture plane (matrix crack) σ_{po}, which is given by:

$$\sigma_{po} = \frac{4 l_{po} \tau_{SL}}{\phi^f} . \tag{2.12}$$

With the Equations 2.11 and 2.12 one can relate the stress at the average fracture

plane with the undisturbed stress, resulting in:

$$\frac{\sigma_{po}}{\sigma_f} = \frac{2l_{po}}{\delta} \ . \tag{2.13}$$

Considering a random distribution of fracture within a band, the average pull-out length will be $\delta/_4$ resulting in a average pull-out stress equal to $\sigma^f/_2$. Curtin [85] assumed that the fraction of broken fibres within a bundle χ is given by a Weibull distribution (with parameters σ_0, l_0 and m), as follows:

$$\chi = \frac{\delta}{l_0}\left(\frac{\sigma^f}{\sigma_0}\right) \ , \tag{2.14}$$

which can be manipulated into

$$\chi = \left(\frac{\sigma^f}{\sigma_\delta^f}\right) \ , \qquad \text{where} \qquad \sigma_\delta^f = \left[\frac{2\left(\sigma_0\right)^m \tau_{SL} l_0}{\phi_f}\right]^{1/m+1} \ . \tag{2.15}$$

The parameter σ_δ^f is the key strength of the material. Considering the overall force equilibrium of the composite material and considering V_f as the fibre volume fraction, the composite tensile strength X_b^r results as:

$$X_r^b = V_f \sigma_\delta^f \frac{m+1}{m+2}\left(\frac{2}{m+2}\right)^{1/m+1} \ . \tag{2.16}$$

Curtin's model is an improvement over Rosen's model as it accounts the stress of broken fibres in the tensile strength and considers a characteristic length (δ) that isn't constant and scales with the applied stress [5].

The models presented in this section consider a global load sharing rule, which is considered not to be very accurate for composite materials and therefore limits the application of this models.

Local load sharing models The first person to address the non uniform redistribution of stress was Hedgpeth [75] in 1961. Considering a shear lag model and uniformly distributed parallel fibres the author calculated the stress concentration factor in the neighbouring fibres as a function of the number of broken fibres r, resulting in:

$$K_r = \frac{4 \cdot 6 \cdot 8 \cdot \ldots \cdot (2r+2)}{3 \cdot 5 \cdot 7 \cdot \ldots \cdot (2r+1)} \ . \tag{2.17}$$

Later, Hedgepeth and Dyke [86] extended this model to a 2D arrangement of fibres.

At this point here is no universally accepted rule, although there has been many publications about this subject using different approaches: shear-lag models, FE

analysis, variational mechanics, fracture mechanics. The stress redistribution, as already mentioned, affected by fibre packing, interaction between breaks, dynamic factors and others, and including a complex model for stress redistribution in a complex fibre strength model may lead to too complex models. Therefore, many models considers simplified stress redistribution models.

According to Pimenta [5] one of the most influential local load sharing fibre bundle model is the one developed by Harlow and Phoenix [87, 88]. This model considers a bundle composed of n fibres, with a length δ, in which the fibres strength is characterized by a Weibull distribution ($F^f(\sigma)$). They consider that the stress concentration due to a cluster of r broken fibres is $K_r = 1 + r/2$. The bundle probability failure ($F^b(\sigma)$) was obtained considering all the different sequences of fibre breaks leading to failure. Since the number of sequences is equal to 2^n, only bundles with less than nine fibres ($n < 9$) were considered. The main conclusions resulting from this model are:

- At high loads, the failure probability of the bundle follows the weakest link theory (WLT), leading to a Weibull distribution with same shape parameter as the fibre distribution: $f^b(\sigma) = 1 - \left[1 - F^f(\sigma)\right]^n$;
- At low loads, the failure probability follows a Weibull distribution with a higher shape parameter than the shape parameter for fibre distribution, resulting in less dispersion of the bundle strength: $m^b = n \cdot m^f$;
- As the bundle size increases, the asymptotic behaviours mentioned start governing the strength distributions;
- The size effects are lower in bundles with increasing number of fibres;
- The strength distribution for large bundles follows a Weibull distribution, within reasonable probabilities;
- It is possible to determine the equivalent single-fibre strength distribution through the WTL based on the strength distribution of a large number of fibres. The authors also noted that it is possible to estimate the strength of any large bundle with $n \geq 7$ following the WLT.

The results obtained by Harlow and Phoenix [87, 88] are exceptionally accurate and have been supported by more recent models and experimental results.

There are other LLS models that take into account other stress redistribution rules. One of this examples is the model developed by Ibnabdeljalil and Curtin [80] that considers the stress redistribution based on Green's function, whose parameters can be adjusted to consider a certain level of local load sharing.

2.1.6.3 Micromechanical models based on Monte-Carlo simulations

Monte-Carlo simulations of micromechanical models have been used to predict the tensile behaviour of UD composites, often assisted by finite element analysis. These

models consider a large number of fibres, that are divided in segments, to which is applied a probabilistic failure strength, normally based on a length scaling Weibull distribution. The models are based on different fibre strength realisations to simulate cluster formations and stress redistributions. Large number of simulations are done until there is enough data to fully characterise the material's behaviour.

There are some challenges when developing a Monte-Carlo simulations based model. Firstly, one needs to calculate the stress fields around broken fibres. Secondly, one needs to be able to do progressive failure analysis of cluster growth.

These models are usually grouped into three groups [5]:

- **Single-step Spring-based models**, that are models based on simplified shear-lag redistribution of stress and consider stochastical strength of fibres.
- **Combined field-superposition and fibre bundle simulations**, that consider a simple superposition method of the stress fields around broken fibres. These stress fields are obtained for a single fibre break and superposition of fields is imposed. This fields are included in Monte-Carlo simulations of fibre bundles.
- **Finite Element (FE) models**, which consider a macro model to be composed of several Unit Cells (UC). Using micromechanical simulations of the UCs, the stress fields with different number of fibre breaks are calculated. This stress fields are then used in the macro model using Monte-Carlo simulations.

2.1.6.4 Single-step spring-based models

Single-step spring-based models consider a lattice of nodes that are longitudinally connected by fibre springs and transversely by matrix springs (see Figure 2.7). The fibre springs can only support longitudinal load and their strength is stochastic. The matrix springs are considered to only being able to support shear stress. The movement of the nodes is limited to longitudinal displacement, which means that there is only one degree of freedom per node.

One of the most acknowledged single-step spring-based models is the one developed by Okabe et al. [29, 89] and is named Spring Element Model (SEM). The SEM considers a hexagonal arrangement of nodes (fibres), connected longitudinally by N^f linear elastic fibre spring elements with a random strength X^f, stiffness E^f and length l. It is then possible to calculate the longitudinal stiffness matrix $\boldsymbol{K}^f$ as a function of the area, length, stiffness of the fibres and nodal connectivities. In the transverse plane the nodes are connected by N^m linear elastic shear matrix springs, which can be arranged into the stiffness matrix $\boldsymbol{K}^m$, as function of the matrix properties, including the thickness. The nodes have only longitudinal displacements which can be arranged in the matrix $\boldsymbol{u}$.

A fibre fails when the applied stress is equal to its tensile strength (which is stochastic). If a fibre fracture, it recovers stress linearly according to the shear lag models with perfectly plastic matrix. At a given stress state there are N_b^f broken

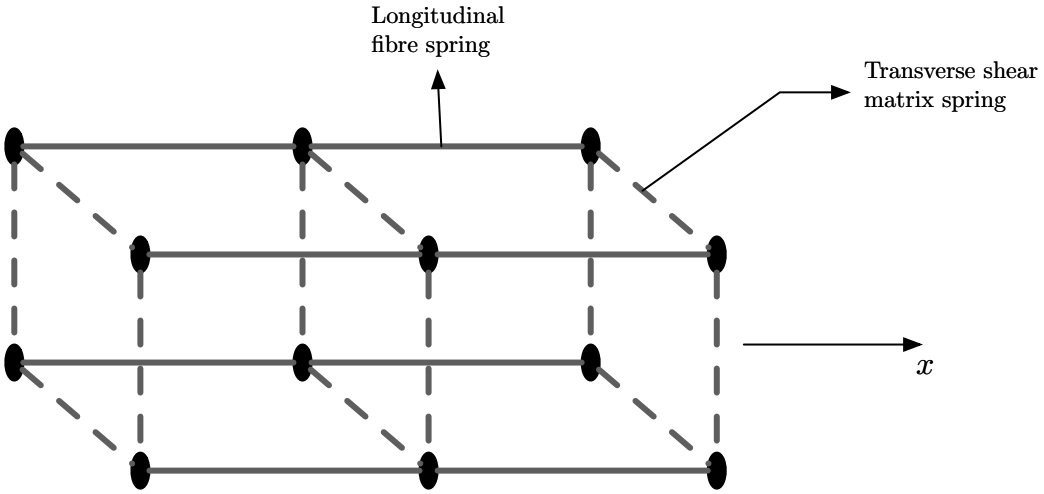

Figure 2.7: Representation of the node lattice of a single-step spring-based model.

fibre elements and N_{SL}^{f} fibre elements whose stress is lower than the applied stress due to a nearby break in that fibre. Therefore, the overall equilibrium for the model results in:

$$\left(\sum_{N_i^f} \boldsymbol{K}^f + \sum_{N^m} \boldsymbol{K}^m\right) .\boldsymbol{u} + \sum_{N_{SL}^f} A^f \int_{x_i}^{x_i+l} \boldsymbol{B}^{f\intercal} \sigma_{SL}\left(x\right)\, \mathrm{d}x = \boldsymbol{f}\ , \tag{2.18}$$

where N_i^f is the number of intact fibre elements in the model, $\boldsymbol{B}^f$ is the deformation matrix of the fibre elements and $\boldsymbol{f}$ is the matrix with the nodal applied forces. Equation 2.18 can be computed and at each increment of applied stress/strain there is the need to determine if any fibre fractures, if so a new equilibrium needs to be calculated. This process is repeated until there is failure of the composite.

2.1.6.5 Combined field super-position and fibre bundle simulations

Combined field super-position and fibre bundle simulations models derive from the basic fibre bundle models (section 2.1.6.2), but consider more accurate stress redistribution rules. This models are composed by three components:

- A deterministic model for stress redistribution to the neighbouring fibres after a fibre breaks;
- A super-position rule to account the effect of multiple fibre breaks in the stress redistribution;
- A Monte-Carlo simulation of the fibre bundle model. Due to the complexity of the stress redistribution this models aren't purely analytical as the ones referred in section 2.1.6.2.

Several models have been presented using this kind of analysis, but consider-

ing different stress concentration factors and different super-position techniques [63, 78, 90–92]. One of the most recent model was developed by Swolfs [2]. This model uses FE to determine the stress redistribution profiles around a broken fibre. The FE model consisted of a circular RVE with a broken fibre in the center, with the remaining fibres arranged in a random packing. The stress concentration factors were studied as a function of distance to the broken fibre. It was studied the effects of matrix cracks [53], volume fraction, fibre/matrix stiffness ratio, isotropic vs anisotropic fibres [34] and others. In his studies Swolfs [2] concluded that the stress concentrations depended mainly on the distance to the broken fibre and the other parameters only have a small influence.

The stress concentration profiles from FE were used to obtain trend-lines to be used in the FBM. The fibre bundle model considered a bi-modal Weibull fibre strength and a random fibre packing. The interaction between breaks was taken into account with a enhanced superposition method (Figure 2.8). This method firstly considers the linear superposition of stress fields due to the broken fibres, which doesn't guarantee the force equilibrium. In order to do so, the SCF that the broken fibres introduce in one another need to be redistributed. This redistribution is done proportionally to the original SCF in the linear superposition. Obtaining, therefore, a stress redistribution that guarantees the force equilibrium.

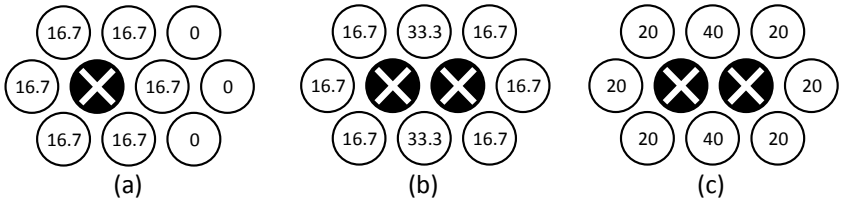

Figure 2.8: Schematics of the enhanced super-position stress redistribution: (a) stress concentration around a single break, (b) linear superposition results and (c) enhanced superposition [2].

The stress redistributions are used as inputs to the FBM, based on Rosen's chain of bundles approach [66] (Figure 2.9), that are used to predict the material behaviour, which is considered to fail when, at least, 10% of the fibres have failed in the same axial segment with length 35 μm. This model considers typically 2000 fibres and are 10 mm long, divided into 35 μm segments to which is attributed a strength based on a Weibull distribution, at the beginning of each Monte Carlo simulation. This model was developed with the objective of incorporating different types of fibres in a RVE in order to study hybrid composites and his able to do so due to its versatility. According to the author [2] the discrepancies to the experimental data of this model are due to: (1) errors in the Weibull distribution, (2) neglecting dynamic stress concentrations and (3) averaging of the SCFs over the entire cross section of the fibre. Nonetheless, this model was used to predict the tensile behaviour and cluster formation in different composite materials with good results.

Guerrero et al. [63] developed a modular FBM that can be used with different analytical formulations for both the in-plane SCFs and the ineffective length and

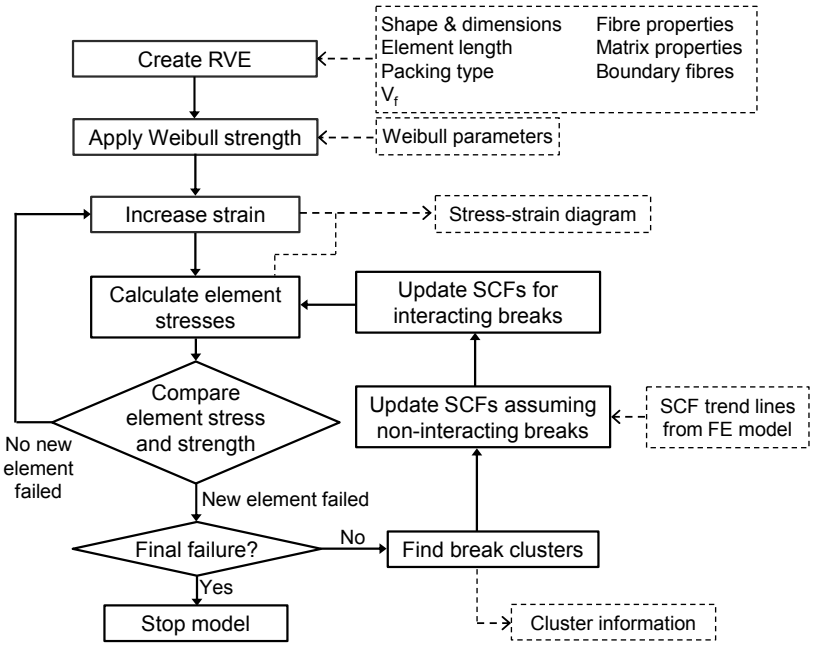

Figure 2.9: Flow chart of the model developed by Swolfs [2].

stress redistribution in the fibre longitudinal direction. The author compared different formulations for the stress distribution with experimental data for non-hybrid composites and used the model to predict the behaviour of a carbon-carbon hybrid composite.

Bullegas [78] developed a dynamic FBM to investigate the effects of dynamic stress concentrations on the bundle failure process and final strength. The author considered two steps in the stress redistribution, the first, immediately after fibre failure, where the dynamic phenomenon occurs, where the SCFs are scaled according to a factor (λ_{dyn}) to represent the increase in stress concentration due to the dynamic effects. The authors used a value of 2 for λ_{dyn}, as this is the maximum dynamic magnification factor for a spring-mass system without damping. The second step consists on reverting the SCFs to the standard static equilibrium values as to simulate the stabilization of the dynamic phenomenon into a static case. The author observed a 10% reduction in bundle strength when compared with the static case. Additionally, the author included a fracture mechanics failure criterion in the bundle model and observed that this model predicts lower bundle strengths and a negative trend for the strength of large bundles in agreement with experimental results.

2.1.6.6 FE models

Finite elements are extensively used in modelling composite materials, however, the prediction of micromechanical behaviour requires extremely refined meshes, making the models computationally costly. This fine mesh is required in order to accurately capture the stress redistribution, especially when a random packing is con-

sidered. This technique is useful to understand the mechanics dominating failure in composite materials, however, they are bound to small representative volume element sizes and large computational cost [58, 93]. St-Pierre et al. [74], used a combination of truss elements, for the fibres and 3D brick elements for the matrix to simulate longitudinal failure of a FRP. The authors observed that the Monte Carlo FE simulations slightly overestimate the experimentally measured survival probabilities of the fibres, for two different materials.

To avoid the use of such refined meshes in full scale models, coupled two-scale FE models have been developed [94, 95]. This separation of micro-macro scales allows the simulation of composites specimens with millions of fibres.

In the model developed by Thionnet et al. [95] the micro-scale model considers a Unit Cell (UC) with a length of 4 mm and 32 linear-elastic fibres arranged in a square packing. This UC are used to study the stress distribution due to different number of broken fibres (2,4,8 or 16 broken fibres). This micro-scales model are used to generate a library with the stiffness of the UC and the stress concentrations in the fibres for different damage states [5].

The macro-scale FE model is composed of several UCs with one integration point to which is attributed a fibre strength given by a Weibull distribution. The damage state of the UC is considered to evolve from no damage to 2, 4, 8, 16 and 32 broken fibres, and the library of micro-scale models is used to predict the stress concentrations and stiffness reduction as function of the damage.

It is considered that the specimen fails when there is a numerical instability, due to a rapid increase of the strain in constant stress. This model was used to predict the behaviour of UD composites under different loading conditions [95]. Also, it was considered the effect of time in the simulations, which lead the authors to conclude that time is an important factor due to visco-elastic behaviour of the matrix.

Monte-Carlo based models are extensively used in the literature, however they require a very fine mesh and large number of simulations in order to accurately capture the material response. Nonetheless, they are very versatile and allow to take into account several factors that most models aren't capable of.

2.1.6.7 Continuum damage mechanic based models

The failure mechanisms of UD composites can be described in the framework of continuum damage mechanics. This type of modelling uses simple definitions of internal damage variables, formulated in the framework of the thermodynamics of irreversible processes [83]. These damage variables are then used to alter the mechanical properties of the constituents, namely the reduction of stiffness.

This type of modelling has been tackled by several authors and can be divided into three stages: (1) definition of a suitable norm for the damage variable, (2) definition of a damage criterion and (3) definition of the evolution law for the damage variable [6]. Matzenmiller et al. [96] developed a model that relates the effective

elastic properties and the damage state of the composite material, and studied the influence of the material parameters in the stress-strain diagrams.

More recently, Turon et al. [6] developed a progressive damage model based on fibre fragmentation for UD composites. This model proposes a degradation of composite effective stiffness based on fibre fragmentation. The fibre fragmentation model considers that the fibre strength follows a Weibull distribution, and when the applied stress reaches the fibres tensile strength it will break. A broken fibre is still capable of carrying stress, according to a shear lag theory, and therefore it can fracture again at a certain distance from the original fracture. A fibre will fracture into shorter fragments until the shear stress transfer across the interface is no longer able to cause another fracture (Figure 2.10).

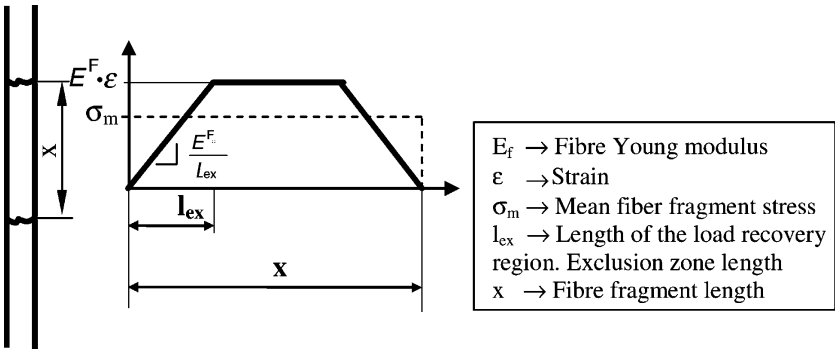

Figure 2.10: Stress profile in a fibre with multiple fractures, according to shear-lag model[6].

Based on the multiple fracture of the fibres, the authors formulate a damage model that considers a global load sharing rule and the influence of each component of the material is accounted for by using the rule of mixtures. The authors used this model, implemented in a FE model to study the effect of several parameters on the stress-strain curve and were able to accurately capture the stiffness loss in UD composites.

2.1.6.8 Hierarchical scaling law for the strength of composite fibre bundles

Pimenta and Pinho [7] developed a model that considers a scaling law for composite strength. They consider the composite to be composed of bundles with different levels, and that a bundle of the level $i+1$ is composed of two level-i bundles (see Figure 2.11). The level-0 bundle is composed of a singular fibre (embedded in the matrix), which means that a level-i bundle has number of fibres n^i equal to 2^i.

The model firstly considers a level-1 bundle of length l_r which is remotely loaded with a tensile stress σ^∞. When both fibres are intact their stress is considered equal and equal to σ^∞. The strength of the fibres is consider to follow a Weibull distribution. When the weakest fibre in the level-1 bundle fails, the broken fibre is assumed to follow a perfectly-plastic shear-lag formulation, with shear strength

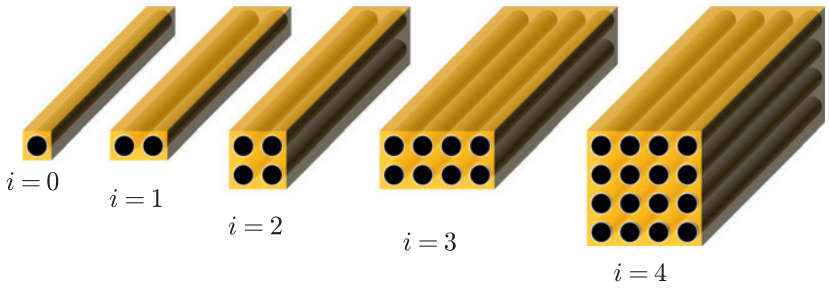

Figure 2.11: Hierarchical fibre bundles [7].

τ_{SL} and, therefore, the broken fibre linearly recovers its capacity to carry load (in the length l_e). Has the broken fibre locally looses its ability to carry stress, there is a stress concentration in the remaining intact fibre, increasing its probability of failure. A level-1 bundle is considered to fail if both fibres fail in nearby locations, close enough to promote complete yielding of the matrix. Is so possible to define a control region, where if the second fibre breaks leads to the failure of the bundle (see Figure 2.12). This region has a length $l_c = 2l_e$, where l_e is the fibre ineffective length.

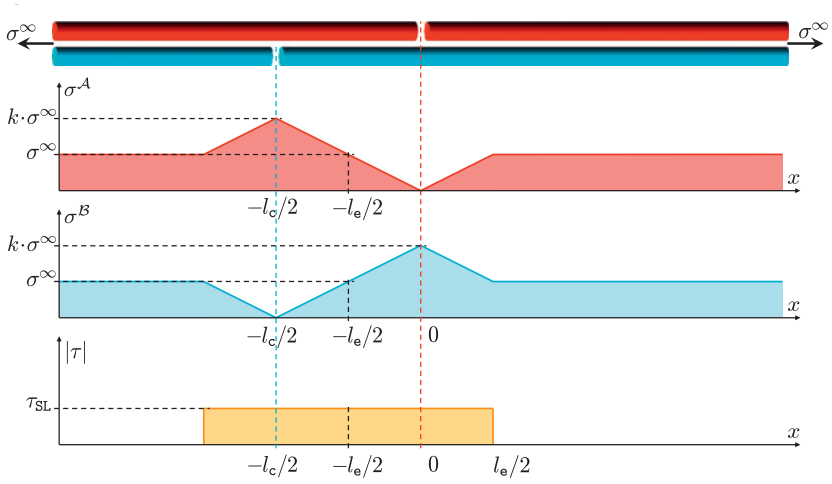

Figure 2.12: Definition of control region [7].

A level-1 bundle with length l_c survives an applied remote stress σ^∞ in the following situations:

- If the stress σ^∞ is lower than the strength of both fibres. This means that the four elements with length L_e remain intact. If the survival probability of a level-0 bundle is $S^0_{U,e}$, then the survival probability of the four regions is $\left[S^0_{U,e}\right]^4$;
- If the weakest fibre fails in the stress σ^∞ and the surviving fibre is able to support the stress concentration. The stress is the intact fibre (Figure 2.12) consists of half a length of constant stress and the other half with linear stress

concentrations. If the surviving probability of a element with length l_e under linear stress concentrations is $S^0_{K,e}$, the probability of the bundle to survive in this conditions is given by: $2\left[1-\left(S^0_{U,e}\right)^2\right]S^0_{U,e}S^0_{K,e}$.

Considering both events, the failure probability of a level-1 bundle with length l_c, under the stress σ^∞ can be expressed as

$$S^1_{U,c} = \left[S^0_{U,e}\right]^4 + 2\left[1-\left(S^0_{U,e}\right)^2\right]S^0_{U,e}S^0_{K,e}\ . \tag{2.19}$$

The authors consider a self-similar hierarchical failure process and generalise the failure events to higher order bundles, obtaining the following hierarchical scaling law:

$$S^{i+1}_{U,c} = \left[S^i_{U,e}\right]^4 + 2\left[1-\left(S^i_{U,e}\right)^2\right]S^i_{U,e}S^i_{K,e}\ , \tag{2.20}$$

where the probabilities with the superscript i refer to the failure modes of a level-i bundle, the same for the superscript $i+$. The subscript U refers to uniform stress in the bundle region and the subscript K to linear stress concentrations in that region.

The survival probability distributions $S^i_{U,e}$ and $S^i_{K,e}$ can be calculated analytically, taking into account that:

$$l^i_e = 2\frac{n^i A^f}{C^i \tau_{SL}\sigma^\infty} \qquad \text{and} \qquad l^i_c = l^{i-1}_e\ , \tag{2.21}$$

where C^i the shear-lag perimeter for a level-i bundle, τ_{SL} is the yielding strength of the matrix (or sliding resistance) and A^f is the area of a single fibre. It should be noted that the length of the damage zone increases, not only with the level of the bundle, but also with the applied stress. This means that the cluster of broken fibres has influence over a larger zone than a single fibre break.

This model is able to make predictions of tensile behaviour of composites with a large number of fibres in short amount of time, and is able to capture the size effects of composite materials, nevertheless, due to the nature of the model, the local stress concentrations are overpredicted by the model.

2.1.7 Conclusion

In this chapter several models for tensile behaviour of UD composites were presented, as well as the main influencing parameters in these materials' behaviour. It is well agreed that the failure of UD composites is a progressive one and that fibre will fracture progressively forming clusters that will grow until a critical size is reached. This, in turn, results in an unstable propagation leading to failure. This process in governed mainly by the fibre strength statistics and the micromechanical stress redistribution, which has been proven to be affected by several parameters, such as the elastic properties of the constituents, the fibre distribution and the fibre-matrix interface behaviour.

Several models, with different backgrounds and formulations, are able to accurately predict the behaviour of UD composites, however there are still improvements to be made. Most of the models don't include the increase in influence area of a cluster in relation that of a single broken fibre, which has been proven by experimental data [5]. Another aspect that most models fail to capture is the dynamic effects of the loading, which has been proven to affect the matrix properties. The dynamic effects are also present when a fibre fails, leading to dynamic stress concentrations that vary with time [75].

In the next chapter models for hybrid UD composites will be presented, and the main influencing factors in hybrid behaviour will be assessed.

2.2 Hybridization- State-of-the-art

The previous chapter focused in understanding the mechanisms of failure in unidirectional composites. It is important to do so as hybrid composites have more complex failure mechanisms than non-hybrids, nonetheless, the basic mechanics of the failure are present in both materials.

In this chapter, the state-of-the-art of hybrid composites will be reviewed, firstly focusing on the general aspects of hybrid composites, including the main effects of hybridization under different loadings. Later on, the models for tensile failure of UD hybrid composites will be reviewed and conclusions will be drawn regarding the most influential parameters of their behaviour.

2.2.1 Hybrid composites

Hybrid composites can be defined as a composite material that contains more than one of type of fibre and/or matrix system [97]. The main focus of this work will be in the hybrid composites with more than a single type of fibres, the so called fibre-hybrid composites. Hybridisation is a strategy that can lead to improved composite properties, namely fracture toughness and damage tolerance.

There are three main types of fibre-hybrid composites, defined according to the configurations of both fibre types:

- **Interlayer** or layer-by-layer hybrids have different types of fibres in different layers, being that each layer only has a single fibre type (Figure 2.13a);
- **Intralayer** or yarn-by-yarn hybrids have both types of fibres in a single layer (Figure 2.13b);
- **Intratow** or fibre-by-fibre hybrids have both fibre types in a single tow (Figure 2.13c). This type of configuration is the one that leads to a better dispersion of both fibre types.

The different types of hybridization will lead to different properties and different

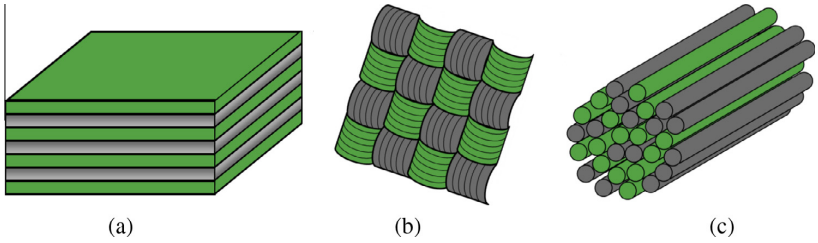

Figure 2.13: Hybrid configurations: (a) interlayer, (b) intralayer and (c) intratow configurations [8].

mechanisms of failure.

The study of hybrid composites started in the 70s. Due to the high price of the recently invented carbon fibres, cheaper fibres, like glass fibres, were added to the carbon fibre composites to reduce the material's price and still take advantage of the better properties of carbon fibres. Afterwards, and with the reduction of carbon fibre prices, hybridization of composite materials became a secondary topic and the focus became in modelling and understanding non-hybrid composites.

Nowadays the topic of hybridisation is growing in interest because it enables a wider design space for composite materials with more tailored properties for a specific application, ensuring that the material in usage can be optimized for a given application. This is valid in several loading cases, for instance, in flexural loadings it is advantageous changing the inner carbon layer for carbon fibres enables the reduction of the price of the material while maintaining its flexural properties [8].

In hybrid composite materials it is usual to refer the two types of fibres as: high elongation (HE) and low elongation (LE) fibres. The HE fibres are the ones that have the highest failure strain, while LE have the lowest. It should be noted that high and low are relative terms and that in a hybrid system fibres can be the HE fibres while in another they can be the LE fibres.

2.2.1.1 Hybrid effect

The hybrid effect was firstly defined by Hayashi [98], in 1972, when he found that the apparent failure strain of the carbon fibres in a carbon/glass hybrid was enhanced in relation to that of the non-hybrid carbon composite. This experimental observation lead to the creation of the first definition of hybrid effect, defined as the apparent failure strain enhancement of the LE fibres in a hybrid composite compared to the failure strain of the LE fibres in the non-hybrid reference composite (Figure 2.14a). The application of this definition requires an accurate determination of the failure strain of the reference non-hybrid composite as this is the baseline in the determination of the hybrid effect. The determination of the failure strain can be affected by the experimental set-up, namely the stress concentrations at the grips. These stress concentrations are usually higher for non-hybrids than for hybrid composites [8, 99], leading to a reduction of the baseline failure strain, which can

result in an overestimation of the hybrid effect.

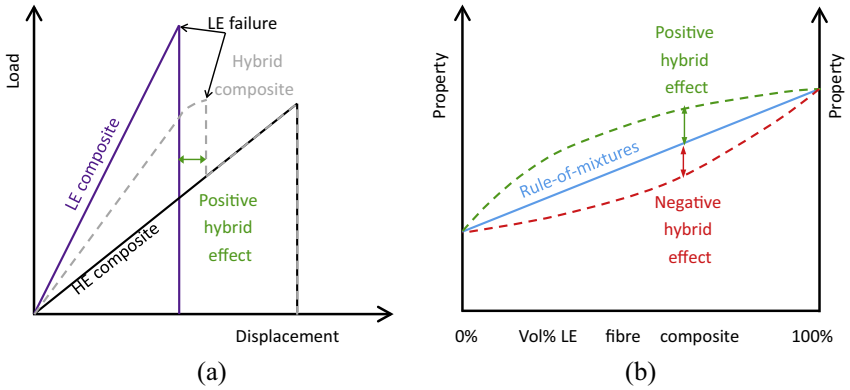

Figure 2.14: Diagrams for the definition of the hybrid effect: (a) first definition proposed by Hayashi and (b) general definition based on the rule-of-mixtures [8].

The definition proposed by Hayashi [98] for the hybrid effect refers only to the enhancement of apparent failure strain, however, hybridization introduces changes in other mechanical properties [100]. This lead to the necessity of a new, more general definition for the hybrid effect. Hybrid effect was then defined as a deviation from the rule of mixtures [101]. This definition is more general and allows it to be applied to several mechanical properties, also allowing the existence of positive or negative hybrid effect (Figure 2.14b) if there is, respectively, an improvement or a deterioration of the property in question.

Although the second definition for hybrid effect presents an improvement in relation to the first proposed by Hayashi [98], it still has some drawbacks. Firstly, the rule-of-mixtures is not always linear, for instance, for the tensile strength the rule-of-mixtures is a bilinear one [100, 102]. Secondly, as noted by several authors [100, 103], the definition of a good parameter to define the hybrid composition and to be applied in the rule-of-mixtures is essential. These authors noted that a good parameter would be the relative HE/LE volume fraction, however this parameter is not always easy to determine [8]. And finally, not all properties can be describe with a rule-of-mixtures. While tensile elastic properties relate well with a linear rule-of-mixtures [98, 100, 103], to determine the flexural modulus one should use a more complex approach, such as classical laminate theory.

Several authors [15, 100, 104] noted that one essential parameter in the influence of hybridization in the mechanical properties of the hybrid composite was the dispersion of both fibre types (Figure 2.15). Dispersion can be defined has the reciprocal of the length of the smallest repeat unit of the composite [104]. Dispersion is, therefore, a characterization of how well mixed both fibre types are.

Several authors [15, 100, 104] noted that increasing the dispersion lead to an improvement in the mechanical properties. This means that the use of intratow (Figure 2.13c) hybridization instead of interlayer (Figure 2.13a) or intralayer (Figure 2.13b) should lead to better mechanical properties.

Throughout the years several explanations for the occurrence of the hybrid effect

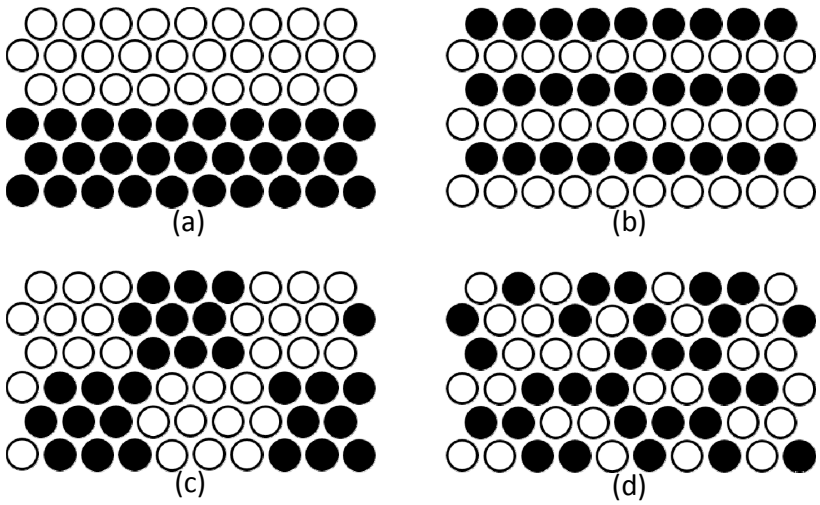

Figure 2.15: Dispersion in hybrid composites: the degree of dispersion increases from (a) to (d) [8].

were proposed. Currently there are three hypotheses for the hybrid effect [8]: (1) thermal residual stresses, (2) changes in the damage development leading to final failure of the hybrid composite and (3) dynamic stress concentrations. These hypotheses will be further explained in the following sections. Another influencing parameter in hybrid effect is the scatter in fibre strength, which will be explained later on.

Residual stresses

Hybrid composite materials are composed of different types of materials, whose Coefficients of Thermal Expansion (CTE) differ from each other. For instance, carbon fibres have a CTE ranging from -1 to $+1$ $10^{-6}\mathrm{K}^{-1}$ [2, 104], while in glass fibres it is around 5-10 $10^{-6}\mathrm{K}^{-1}$ [8, 104]. This difference of CTEs means that upon cooling the carbon fibres will remain almost the same size while glass fibres will tend to shrink. In a composite material, however, there is a third component, the matrix, that acts as a restraint to the free movement of the fibres. Therefore, the cooling stage of the fabrication of a hybrid composite material leads to residual stresses in the fibres. For instance, in a carbon/glass hybrid, the carbon fibres, whose CTE is close to zero, will be subjected to compressive residual stresses and the glass fibres will be subjected to tensile residual stresses, maintaining the overall force equilibrium in the material. The compressive residual stresses in the carbon fibres will alter their tensile behaviour and change the apparent failure strain of the carbon fibres.

These residual stresses contribute effectively to the hybrid effect, however they do not fully explain the hybrid effect [104, 105]. According to Zweben [105], in a carbon/graphite hybrid with epoxy resin the residual thermal stresses can account only for 10% of the increase in apparent failure strain of the carbon layers, which is

insufficient to explain the total hybrid effect and, therefore, there are other factors affecting the hybrid effect.

Damage development

As explained in the previous chapter (Ch. 2.1), failure of unidirectional composites is determined by the stochastic strength of fibres and the stress redistribution after fibre failure. Hybridizing a composite material significantly changes both these parameters.

As the composite is constituted by more than one type of fibres, their strengths will be represented by different distributions, meaning that the fibres may not fail at the same range of applied stress/strain which, by itself, strongly changes the behaviour of the composites.

For longitudinal tensile loadings, after a LE fibre fails, due to a lower failure strain, the stress that they previously carried has to be redistributed among the surrounding intact fibres. As the fibres have different elastic properties the stress distribution will be more complex than in non-hybrid composites [13, 34]. Hybridization not only changes the SCFs but also changes the ineffective lengths as the different type of fibres have different elastic properties, radius and different interface properties [105]. These changes in the stress redistribution will alter the cluster development and damage progression.

When loaded in the fibre direction, the LE fibres will probably fail first, however, as there are HE fibres mixed in the composite, there will be bridging points, provided by the HE fibres, that will hinder crack propagation and the cluster development, therefore, delaying the failure of the composite. The intact HE fibres among the broken LE fibres will increase the fragmentation process in the LE fibres, being that theses fibres will fragment multiple times [58]. Another aspect that can have effect in the damage development in hybrid materials are the size effects [3, 61].

Another aspect to take into account is that the strength of a fibre decreases with increasing the sample size. As hybrid effect is defined in comparison with a LE fibres non-hybrid composite, and in this material the volume of LE fibres is higher, the introduction of another fibre type (HE) in the material will cause an increase in the expected strength of the LE fibres, because their overall volume is lower and, therefore, making it less likely that there are fibres with major flaws, fact that may affect the hybrid effect [2].

Dynamic stress concentrations

Failure of a composite materials is a dynamic process. When a fibre breaks energy is released and the fibre acts as a spring, with a stress wave propagating in its axial direction. This phenomenon was first reported by Hedgepeth [75] and later confirmed by several authors [58, 77, 79, 106, 107]. Hedgepeth limited his study to

the dynamic stress concentrations in the fracture plane and reported an increase of 15 to 27% in relation to the static SCF, however he used a shear-lag model that has limitations in the study of dynamic phenomena [2]. Hedgepeth's model [75] was later extended by Xing et al. [77], that reached similar conclusions for the SCFs outside the plane of fracture.

Xia and Ruiz [106] studied the dynamic stress concentrations in carbon and glass composites and predicted that they were 20% higher for glass composites. This means that stress wave, that propagates axially in the intact fibres after another breaks, behaves differently according to the material. According to Xing et al. [77], the phase and amplitude of the stress wave are dependent on the elastic properties of the fibres, thus changing with the material.

Xing et al [108] extended this dynamic model to hybrid composites. With this theoretical model, the authors were able to capture two waves propagating in the LE and HE fibres. Since the waves in the different fibres are out-off-phase, the stress concentrations in the composite are lower and, therefore, improve the overall resistance of the material. Strictly from the point of view of dynamic stress concentrations the hybrid effect will always be positive as it always leads to lower SCFs [2].

These earlier models were able to give some insight off the dynamic effects in fibre composites and hybrid fibre composites, however more advanced dynamical models should be used to support these conclusions and further understand the mechanics behind this process.

2.2.2 Mechanical properties of hybrid composites

An brief review on the effects of hybridization on the mechanical properties of composites will be presented in the following sections.

2.2.2.1 Tensile properties

Tensile modulus

The longitudinal tensile modulus can be accurately predicted by a linear rule-of-mixtures:

$$E^* = E_{f1}V_{f1} + E_{f2}V_{f2} + E_mV_m \ , \tag{2.22}$$

where E_{f1} and E_{f2} are the longitudinal tensile modulus of both fibres, E_m the matrix elastic modulus, and V are the volume fractions of the respective component.

Since the longitudinal tensile modulus can be predicted by a linear rule-of-mixtures, hybrid effects are not expected for this property. In the transverse direction, however, hybrid effect may occur [109].

Failure strain

In regard to the failure strain, it is expected that hybrid effect can occur. In fact, the first definition of hybrid effect was done regarding failure strain enhancement [98]. This enhancement regards the failure strain of LE fibres in hybrid composites in comparison with non-hybrids. Kretsis [100] reviewed the mechanical properties of hybrid composites in 1987, later compiled by Swolfs et al. [8] which is shown in Figure 2.16. Depending on the hybrid system the failure strain enhancement may vary, but for failure strain the typical range for hybrid effect is 10-50%. According to Swolfs et al. [8] the values inside the red line in Figure 2.16 should be treated with care due to improper testing, definition of the reference failure strain or definition of the hybrid effect. One of the main issues in defining hybrid effect for failure strain is the definition of the reference failure strain as the system set-up can affect the results [99], therefore leading to wrong estimation of the hybrid effect.

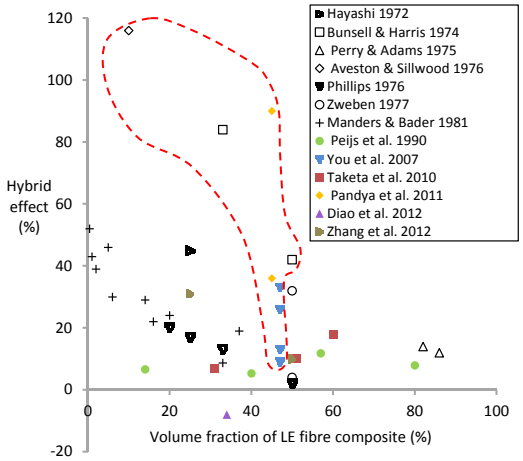

Figure 2.16: Hybrid effect for tensile failure strain. Information in Black was gathered by Kretsis and information in colour by Swolfs. The information inside the red line should be interpreted with care, due to errors [8].

Tensile strength

The hybrid effect for tensile strength should determined based on a bilinear rule-of-mixtures (Figure 2.17a). As tensile tests are usually performed under displacement control and LE fibres are the first to fail, if the HE fibre content is low the composite strength reaches its maximum when the LE fibres fail (Figure 2.17b). However, if the HE volume fraction is high enough the composite may still able to carry stress after the LE fibres fail and, therefore, the tensile strength is dominated by the HE fibres (Figure 2.17d).

Several authors have found a positive hybrid effect for tensile strength [8], concluding that the bilinear rule-of-mixtures does not accurately predict the effects of hybridization on the tensile strength, therefore, more accurate models are necessary to predict this property on hybrid composites.

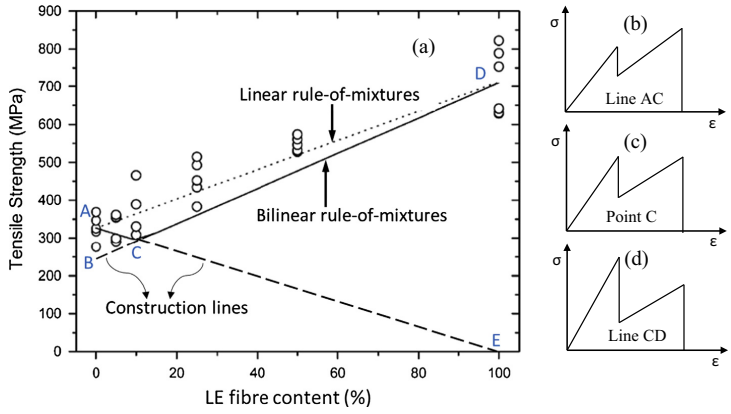

Figure 2.17: Bilinear rule-of-mixtures for tensile strength. Experimental data for carbon/glass hybrids [8].

2.2.2.2 Flexural properties

The effect of hybridization in flexural properties cannot be determined based on the volume fraction of both fibre types since the layup configuration is essential. This is due to different stress states in different positions relatively to the neutral axis/plane, which makes the prediction of the flexural hybrid effect harder than for tensile properties. The hybrid effect in flexural properties is due to different material behaviour in tension and in compression, for instance, glass fibres have a tensile to compressive strength ratio of 0.73, while for carbon is 0.37 [110].

Dong et al. [9, 111] studied the effects of hybridizing carbon fibre composites with glass fibres, concluding that replacing the carbon fibres by glass fibres in the compressive side of the specimen would increase the flexural properties of the material (Figures 2.18 and 2.19).

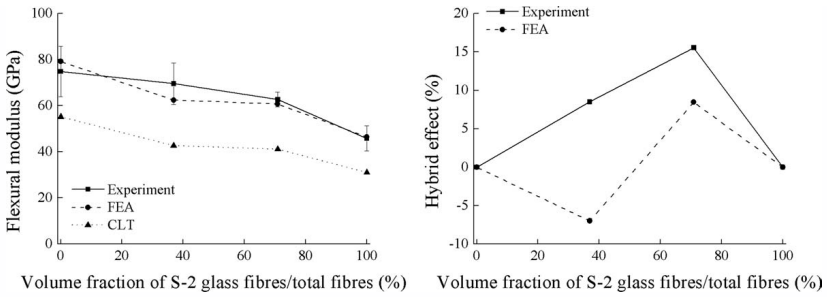

Figure 2.18: Effects in the flexural modulus of hybridizing carbon fibre composites with glass fibres in the compressive layers [9].

Dong et al. [9, 111] results show positive hybrid effects for flexural modulus and strength, which can not be accurately predicted by classical laminate theory nor by simple FE analysis. Other authors [112] reached similar conclusions in hybridizing carbon composites with glass fibres. These results mean that an symmetrical layup may not be optimal when there are flexural loads and that there is an optimal hybrid

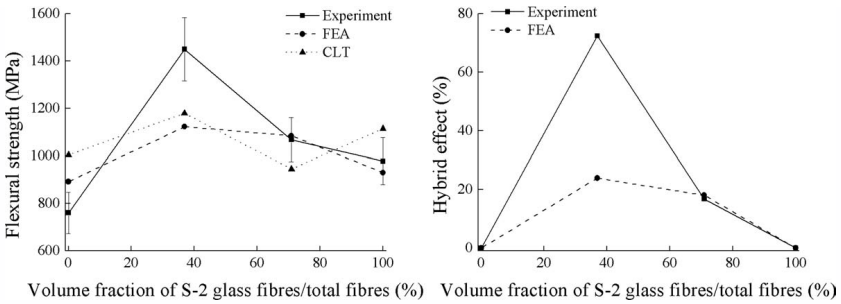

Figure 2.19: Effects in the flexural strength of hybridizing carbon fibre composites with glass fibres in the compressive layers [9].

ratio to improve flexural properties which, according to Dong et al.[111], is 12.5% of glass fibres.

2.2.2.3 Impact resistance

One of the main goals of hybridizing fibrous composites is improving the toughness of these materials, making impact resistance properties important, as they are related with the toughness of the material. Impact resistance can be characterized by three parameters: (1) energy absorbed during penetration impact, (2) damaged area after a non-penetrating impact and (3) post impact properties. These parameters are governed by different mechanisms and hybridization may affect differently each one of them [8]. In impact tests, the material behaviour is highly dependent on the ply configuration, as it is affect by the flexural properties of the material, and, therefore hybridizing different plies will have different influence in the impact resistance. Similarly to the other mechanical properties, the dispersion of both fibres types is important in impact resistance, in this case due to changes in the damage mechanisms [2].

For interlayer hybrids,the positioning of the layers is important because it not only changes the flexural properties (as seen in Section 2.2.2.2), but also the damage mechanisms to dissipate the impact energy.

Sayer et al. [113] tested asymmetric interlayer carbon/glass hybrids. With this asymmetric laminate it was possible to study the effect of having the LE in the impact side or in the other side of the laminate, which is subjected to tensile loadings. The authors found that if the carbon fibres (LE) were on the impacted side, the impact resistance was increased by 30%.

Jang et al. [114] studied several hybrid composites with different fibre types. For a two-layer carbon/aramid hybrid, the dependence of which layer is in the compressive side was reduced, fact that was attributed to similar impact behaviour of the aramid and carbon reference composites. However, replacing the carbon fibres with polyethylene (PE) resulted in different behaviours if the aramid fibres were on the compressive or tensile side of the impact. If the PE fibres (HE fibres) were on the compressive side, the impact resistance increase by 50% in comparison with the

aramid fibres in the compressive side, which suggests that HE preform better when in the tensile side of the impact. These results contradict the ones of Sayer et al. [113], however this can be attributed to differences in the damage mechanisms which are related to fibre and fibre/matrix interface properties [2].

Naik et al. [115] tested the impact behaviour and post-impact properties of carbon/glass symmetrical hybrids and reported that the compression-after-impact strength of the hybrid material was higher than that of both reference composites (non-hybrid).

From the previous results it becomes clear that, the positioning of the different plies affects the impact properties of the material however dispersion also influences these properties.

Sarasini et al. [116] tested glass/basalt hybrid composites and concluded that the well dispersed specimens showed smaller damaged area and higher post-impact flexural strength, which was attributed to the presence of high amount of small delamination in the well dispersed composites compared to extensive fibre breaks and delamination in the less dispersed ones. De Rosa et al. [117] got similar results for the same hybrid material.

Park and Jang [118] studied aramid/polyethylene hybrids and observed that the interlayer hybrids had a higher penetration impact resistance than the intralayer hybrids, which means that less dispersed composites had better impact resistance. In terms of damaged area it was found that intralayer hybrids presented a smaller damaged zone and therefore should have better post-impact properties (which were not determined).

Gonzales et al. [119] used two woven reinforcements, one glass and one carbon, and a third carbon UD material to manufacture different hybrid composites and different layups from the materials. Drop-weight impact and Compression After Impact (CAI) tests were performed. The authors observed a large influence on the position of the hybrid layers on both the impact and CAI results and argue that this results from differences in the sequence of initiation, growth and interaction of the failure mechanisms.

2.2.2.4 Fatigue resistance

Although fatigue resistance is an important property for many applications, the effects of hybridization in this property have not been extensively studied [8]. In principle, hybridization should lead to improved fatigue properties, as HE can act as bridging points in a crack and stop crack propagation.

Wu et al. [10] studied the fatigue properties of several materials, including hybrid composites.

As seen in Figure 2.20, for the the same conditions (same fraction of maximum and medium loads), the addition of carbon fibres, whose base behaviour is represented by CFRP, in a basalt composite (BFRP) increases the number of cycles to

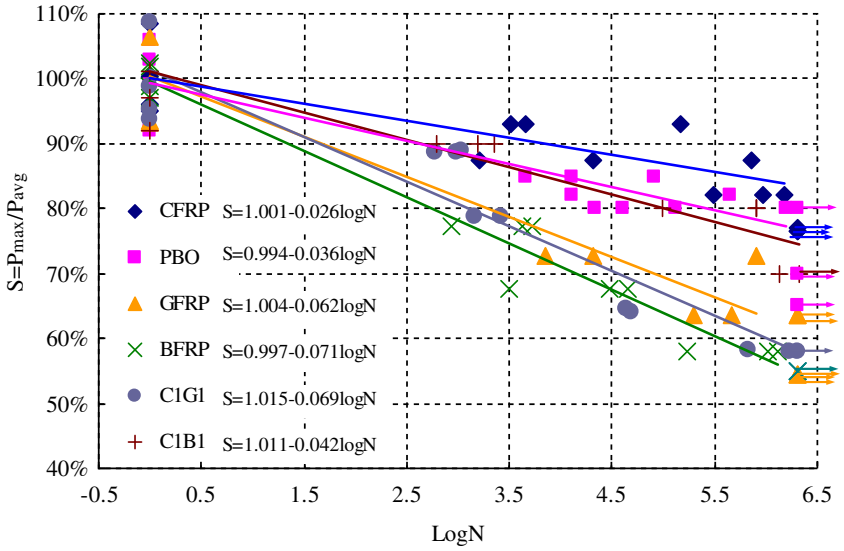

Figure 2.20: Fatigue response of several fibre reinforced composites [10].

rupture of the hybrid material (C1B1). Wu et al. [10] justified this increase with the reduction of the stress in the basalt fibres due to the addition of the carbon fibres, that have a higher modulus, improving the fatigue life of the basalt fibres. The addition of carbon to a glass composite (GFRP) didn't have the same effect as the previous material (see Figure 2.20-C1G1), which was attributed to the superficial properties of glass fibres.

Peijis and de Kok [120] studied the fatigue resistance of PE/carbon hybrids and found that hybridization resulted in flatter S-N curves, meaning that the fatigue life of the material was improved. They also reached the conclusion that hybrid composites have a less scattered fatigue life and that increasing the dispersion improves it.

2.2.2.5 Pseudo-ductile behaviour

The longitudinal failure of fibre-reinforced composites is catastrophic under longitudinal tension. Another problem is that the material can be damaged in its interior without it being noticeable in the outer layers. This can lead to mechanical properties lower than expected, leading to a premature failure of the component.

Hybridization can tackle some of these challenges by developing a more gradual failure of the material. The usual behaviour of a composite material is showed in Figure 2.21a, which represents a catastrophic failure. Hybridization leads to a diagram like the on in Figure 2.21b but, if the material is designed correctly, a pseudo-ductile behaviour can be achieved (Figure 2.21c), which is considered to be the ideal response of a hybrid composite [121] in terms of damage tolerance.

Pseudo-ductile behaviour can be characterized by the pseudo-ductile strain. Yu et al. [122], defined the pseudo-ductile strain (ε_d) as the difference between the

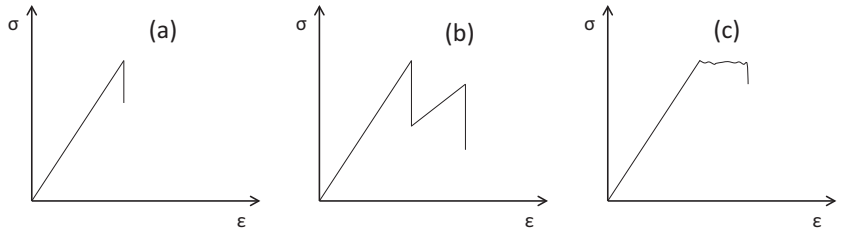

Figure 2.21: Schematic stress-strain diagrams for: (a) non hybrid composites, (b) typical hybrid composites and (c) pseudo-ductile hybrid composites [2].

strain at which the specimen looses is integrity ($\varepsilon_{\max}$) and the elastic strain (ε_{E0}), at the same stress level as $\varepsilon_{\max}$ but based on the initial young modulus (E_0), as illustrated in Figure 2.22.

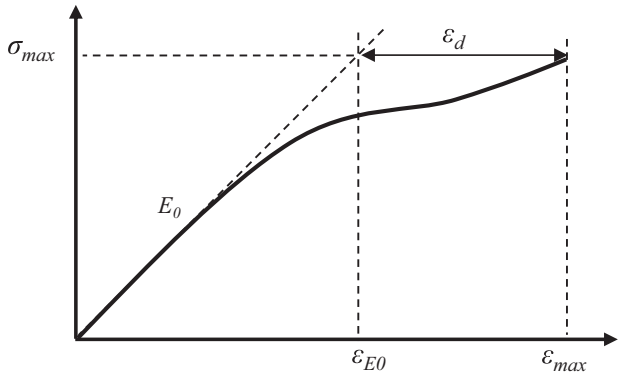

Figure 2.22: Diagram of pseudo-ductile strain.

ε_{E0} can be calculated as $\varepsilon_{E0} = \sigma_{\max}/E_0$, where E_0 can be estimated by the linear rule-of-mixtures as:

$$E_0 = V_{f1}E_{f1} + V_{f2}E_{f2} \; . \tag{2.23}$$

The increase in interest in a pseudo-ductile behaviour can be attributed to the high safety factors that are used in composite materials, which can be reduced if the materials showed a pseudo-ductile behaviour [2].

Czél et al. [123] and Jalalvand et al. [11] achieved a pseudo-ductile behaviour for carbon/glass hybrid thin-ply composites. The authors considered carbon/glass hybridization due to: the compatibility between materials, the existence of ultra-thin carbon prepregs, the difference in failure strain of the considered materials allows the alteration of the reference properties by hybridization and the transparency of the glass allows the detection of failure mechanisms in the ultra-thin carbon layer. The authors [11, 123] presented both experimental and numerical evidence of the pseudo-ductile behaviour. It was noted that the pseudo-ductile behaviour was closely connected with the failure mechanisms and that the total and relative thickness of the layers lead to different behaviours (see Figure 2.23).

It was noted that when there was multiple fragmentation of the carbon layer the material showed a pseudo-ductile behaviour [11, 123]. This multiple fragmentation

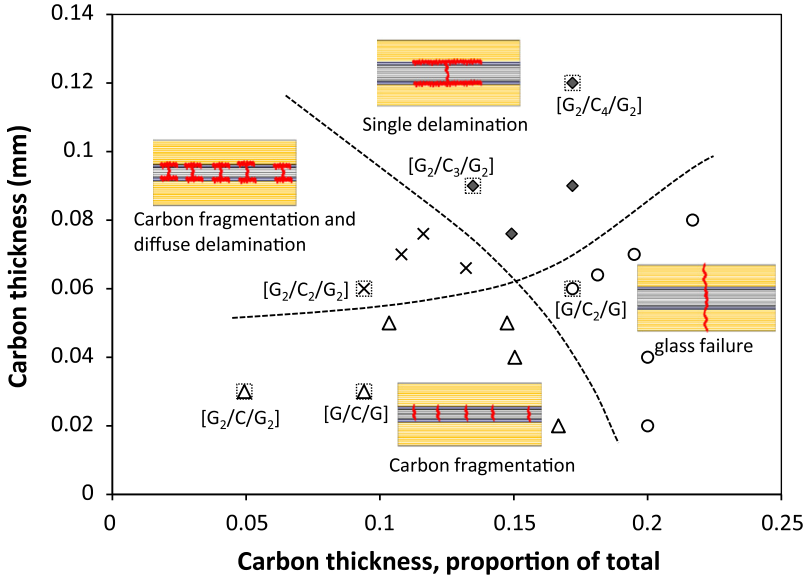

Figure 2.23: Failure modes as a function of absolute and relative layer thickness in carbon/glass hybrid composites [11].

could be achieved when the carbon layer thickness was small (see Figure 2.23). This model has been validated and has been used to create pseudo-ductile quasi-isotropic laminates by Fotouhi et al. [124].

Other authors have tackled the pseudo-ductile topic. Jones and Dibenedetto [121] demonstrated pseudo-ductile behaviour of carbon/glass and carbon /aramid composites when each carbon fibre was surrounded by carbon or aramid fibres, reducing the interaction between the carbon fibres. Liang et al. [125] demonstrated some degree of pseudo-ductility in carbon/glass rods when the glass fibres were all put in the core of the rod. However, the stress-strain diagram is more close to the one from Figure 2.21b than the pseudo-ductile one in Figure 2.21c. Czél et al. [126] demonstrated a pseudo-ductile behaviour in unidirectional discontinuous carbon/glass fibre composites and for composites with discontinuous carbon fibres and continuous glass fibres [127]. Swolfs et al. [128] also demonstrated that pseudo-ductility can be achieved by controlling the failure mechanisms in composites. This was done for carbon fibre and self-reinforced polypropylene composites and the pseudo-ductility was achieved when the carbon fibre layers were able to fracture in multiple locations before the failure of the composite. Yu et al. [122] also achieved a pseudo-ductile behaviour for hybrid carbon/glass composites with highly aligned discontinuous fibres. This hybridization was done at the ply level and each ply was constituted by both types of fibres (intralayer hybridization).

Recent works on pseudo-ductility have been focusing on achieved the pseudo-ductile behaviour using multiple techniques to control the failure mechanisms and damage propagation. Many of these using thin-ply composites. Fuller and Wisnom [129] have demonstrated the potential of non-hybrid angle-ply laminates in achieving pseudo-ductility. This was achieved using a combination of angle-plies $[\pm\theta]$ with thin-plies. This way fibre rotation was allowed due to matrix plasticity but damage

was suppressed due to the fact that thin plies were used. The authors also performed an analytical study on a $[0/\theta]$ hybrid carbon-carbon composite concluding that there is potential in such configuration to achieve pseudo-ductile behaviour [130]. Czél et al. [131] demonstrated that the pseudo-ductility in unidirectional hybrids can be transferred to multi-directional laminates, due to the fragmentation of the LE carbon fibre layers. The authors also concluded that the damage mechanisms promoted in the hybrid material in a open-hole tensile test lead to a reduced notch sensitivity. ar Amacher et al. [12] have used thin-ply hybrid composites to improve the translaminar toughness of the material system. This was done for both carbon-carbon and carbon-twaron hybrids. In this work the authors demonstrated the potential of hybrid composites to improve the properties of composite materials, with both hybrid composites tested having increased translaminar toughness, while maintaining the remaining properties within acceptable bounds. The carbon-carbon composite material also achieved a pseudo-ductile strain equal to 0.47%, this for a T800/HR40 [0/90] composite.

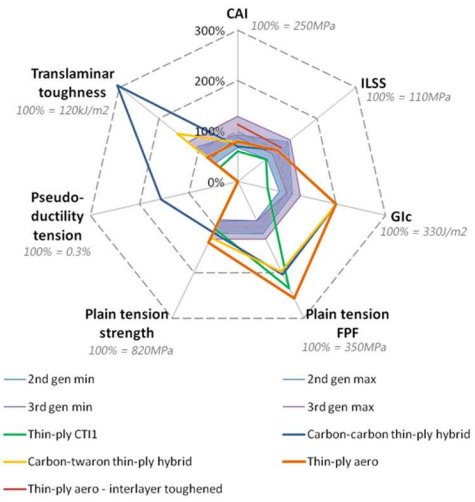

Figure 2.24: Comparison between different composite materials, including toughened epoxy system and carbon-carbon and carbon-twaron thin-ply composites [12].

Ortega et al. [132] studied the translaminar fracture properties of interply hybrid materials, for the same materials used in the impact study [119], with compact compression and compact tension tests, and observed a minimal influence on the stacking sequence on the fracture toughness of the materials. The authors also found that the damage mechanisms change for the different materials, which can explain the different measured apparent fracture toughness.

Overall, the pseudo-ductile behaviour has only been achieved for low fractions of LE fibres (e.g. carbon fibres) and therefore their mechanical properties are reduced. New strategies need to be developed to achieve this behaviour in higher LE fibre fractions [8]. Additionally, the usage of intratow hybrids should help improving pseudo-ductility and fracture toughness, however, the manufacturing of such material is very challenging.

2.2.3 Failure development and stress redistribution in UD hybrid composites

The failure development of hybrid composites follows the same principles of non-hybrid composites (presented in chapter 2.1): (1) the strength of the fibres is not deterministic and (2) the stress previously carried by a broken fibre is redistributed among the intact ones in a complex manner, taking into account that the broken fibre is still able to carry stress away from the fracture plane.

As in a hybrid composite, there is presence of two fibre types (HE and LE), the failure development will be more complex than in non-hybrid composites. As the LE fibres have a lower mean failure strain, they will break first, causing stress concentrations in the remaining fibres. The failure of the LE fibres also causes the initiation of cracks in the matrix, which will be extended with increasing applied stress. As the HE fibres have a higher failure strain, they will act as crack arresters, bridging the cracks formed by broken LE fibres [2, 121, 133]. This will lead to a delay in damage development and failure of hybrid composites. Nonetheless, the increase in applied strain/stress will cause the creation of clusters of broken fibres, constituted by LE and HE fibres. These clusters will grow and, when one reaches a critical size, unstable propagation will occur and, therefore, the composite will fail.

As previously stated for non-hybrid composites, the stress redistribution after a fibre breaks is crucial to understanding the behaviour of UD composites under tensile loadings. Swolfs et al. [13] did an extensive study of stress redistribution in hybrid composites. Using a 3D FE model with a random fibre packing with a broken LE fibre (in this case carbon) in the centre of the RVE, the authors were able to study the effects of several parameters in the stress redistribution in hybrid composites.

Firstly, Swolfs et al. [13] studied the effect of the having fibres with different radii in the SCFs and ineffective lengths (see Figure2.25). They considered the carbon to have a radius of 3.5 μm and the glass fibres to have a radius of 3.5 or 6 μm.

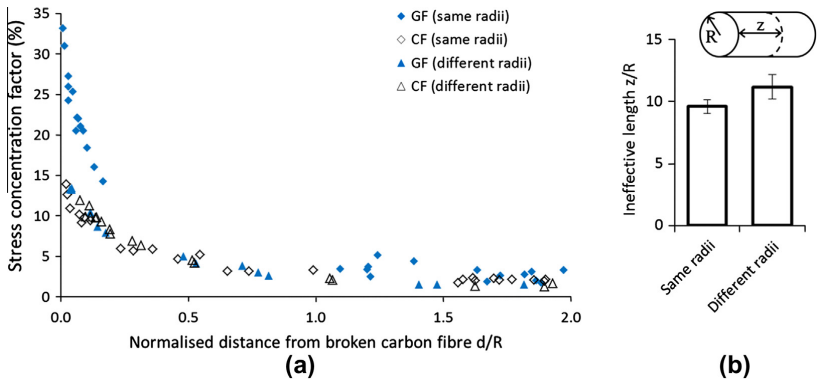

Figure 2.25: Stress redistribution in hybrid composites with 50% carbon and glass fibres: (a) SCFs in both fibre types, considering the same and different radii; (b) ineffective length of the broken carbon fibre considering fibres with the same and different radii [13].

The authors concluded that having fibres with different radius affects both the SCFs and the ineffective length. For the model with different fibre radii the SCFs, in the carbon and glass fibres follow the same trend-lines. This was attributed to the fact that considering glass fibres with higher diameter causes the SCFs to decrease due to an increase in cross section, compensating, therefore, the difference in the stiffness of the fibres. In terms of ineffective length, the authors attribute the increase of ineffective length in the model with fibres with different radii to the fact that, in packings with different radii, there is less fibrous material surrounding the broken fibre, reducing the homogenized shear stiffness of the material in this region of the composite. As the stress is transmitted to the broken fibre in shear, reducing the homogenized shear stiffness causes an increase of the ineffective length.

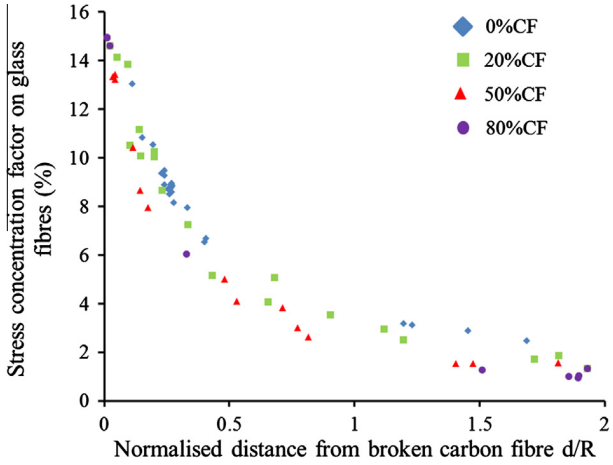

Figure 2.26: Stress concentration factors in glass fibres as a function of the distance from the broken fibre [13].

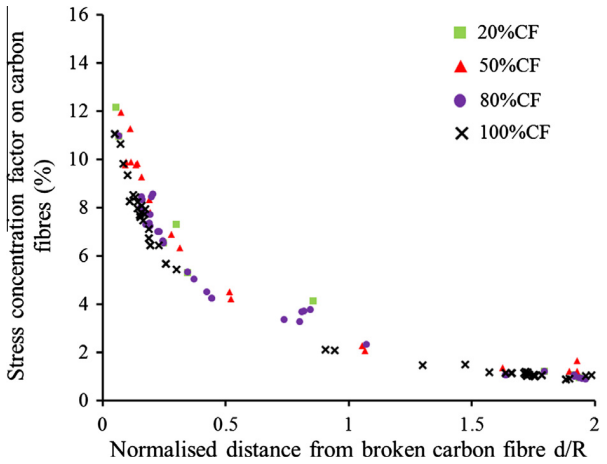

Figure 2.27: Stress concentration factors in carbon fibres as a function of the distance from the broken fibre [13].

Swolfs et al. [13] also studied the effect of hybrid volume fraction in the stress redistribution, for carbon/glass hybrids. Analysing Figure 2.26 and 2.27, the hybrid volume fraction has a low influence in the SCFs in both fibre types, however, increasing the volume of carbon fibres, slightly decreases the SCFs due to an increase in the composite longitudinal stiffness. The influence of the hybrid volume fraction in the ineffective length is similar to that in the SCFs (see Figure 2.28), the increase of the carbon volume content slightly decreases the ineffective length.

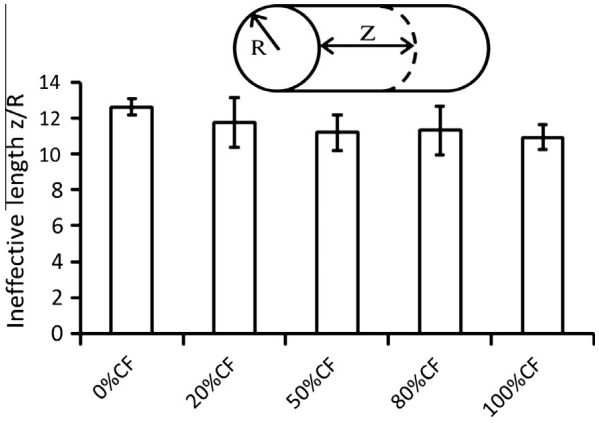

Figure 2.28: The ineffective length of carbon–glass hybrids for different hybrid volume fractions. The error bars indicates the 95% confidence interval based on five realisations[13].

Swolfs [2] also presented the results for SCF and ineffective length for carbon hybrids hybridized with HE fibres with different stiffnesses. The author concluded that increasing the stiffness of the HE fibres increased the SCF in these fibres. However, the effect is opposite in the SCFs in the carbon fibres, but this effect is reduced. The effect of the stiffness of HE fibres in the ineffective length can be seen in Figure 2.29: increasing the stiffness of the HE fibres slightly reduces the ineffective length of a broken carbon fibre, but increases that of a broken HE fibre.

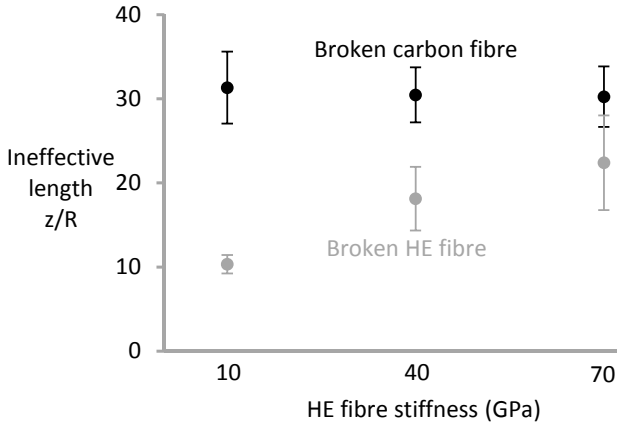

Figure 2.29: The ineffective length in carbon and HE fibres as a function of HE stiffness[2].

The cluster development in composite materials is affected by hybridization. Swolfs et al. [15] studied the how the hybrid ratio affected the cluster develop-

ment, concluding that, increasing the volume fraction of HE fibres would lead to an delay in the cluster formation. This means that to achieve the same level of clusters of broken fibres the applied strain needs to be higher. The authors also found a relation between the critical cluster size and the hybrid ratio, concluding that increasing the volume fraction of HE fibres leads to a reduction of the critical cluster size. With these results in the stress redistribution, Swolfs et al. [13] concluded that bridging of the broken carbon fibres by the intact hybridisation fibres has a major contribution to the hybrid effect.

Guerrero et al [134] also studied the local stress fields in hybrid composites and the effects of hybridization on the cluster development process. The authors concluded that the ductile hybrid composites presented a gradual and progressive increase of fibre break density, whereas an exponential increase was obtained for the brittle materials.

2.2.4 Modelling the tensile failure of UD hybrid composites

The first author to model the tensile failure of hybrid composites was Zweben [105], in 1997, with the intention of predicting the hybrid effect for failure strain. Zweben extended a shear-lag model for UD hybrid composites and considered local-load-sharing for stress redistribution after a fibre break. This model considered a 1D fibre packing with alternating HE and LE fibres (Figure 2.30b) which represents a simplification of the complex geometry of hybrid composites. The hybrid composite behaviour was compared with the non-hybrid composite composed only with LE fibres (Figure 2.30a) to determine the hybrid effect.

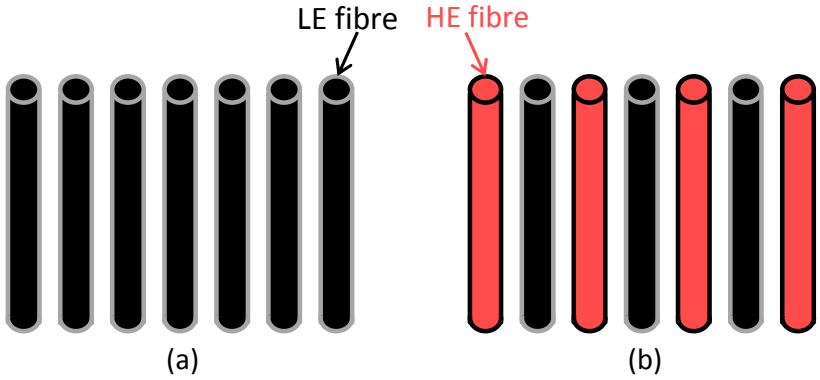

Figure 2.30: Representation of the fibre packings used in Zweben's model : (a) non-hybrid LE composite and (b) hybrid composite with alternating LE and HE fibres [2].

As the model considered fibres with different cross sections and elastic modulus, Zweben considered that when a LE fibre breaks the neighbouring HE fibres would be subjected to a strain concentration, rather than a stress concentration. The strain concentration factor can be defined as the ratio between the strain in a fibre next to a single broken fibre over the applied strain. Zweben also considered that after a fibre breaks there is a length at which the fibre is not capable of fully carry stress (ineffective length) and derived analytical expressions for both strain concentration

factors and ineffective length for hybrid and non hybrid composites. For non-hybrid composite, the strain concentration factor (k_{LE}) is equal to 1.293 and for hybrid composites the strain concentration factor (k_h) only depends on ρ, which is the ration of normalised stiffness of both fibres:

$$\rho = \frac{E_{LE}S_{LE}}{E_{HE}S_{HE}} \ , \tag{2.24}$$

where E_{LE} and E_{HE} are the Young's modulus of the low elongation (LE) and high elongation (HE) fibres, and S_{LE} and S_{HE} are the cross-sectional areas of both fibre types.

The ineffective lengths for the non-hybrid (δ_{LE}) and hybrid composite (δ_h) can be determined as:

$$\delta = N\left(\frac{E_{LE}S_{LE}d_m}{G_m t_m}\right)^{1/2} \ , \tag{2.25}$$

where G_m is the matrix shear modulus, t_m and d_m are, respectively the matrix thickness and the fibre spacing. the factor N is equal to 1.531 for non-hybrid composites and is a function of ρ for the hybrid ones.

Zweben considered that the hybrid composite fails when the first HE fibre breaks, resulting in a lower bound for composite strength [105]. Zweben assumed that the failure of a HE fibre would trigger the unstable failure of all the other LE fibres, therefore, the failure strain used to determine the hybrid effect is according to the definition of hybrid effect presented by Hayashi [98] and explained in Section 2.2.1.1. Combining the equations for ineffective length, strain concentration factors and the Weibull distributions for fibre strain, Zweben derived the following expression for the hybrid effect (R_{hyb}):

$$R_{hyb} = \sqrt{\frac{\varepsilon_{HE}}{\varepsilon_{LE}}}\left[\frac{\delta_h\left(k_h^m - 1\right)}{2\delta_{LE}\left(k_{LE} - 1\right)}\right]^{-1/2m} \ , \tag{2.26}$$

where ε_{LE} and ε_{HE} are the mean failure strains of the LE and HE fibres at the considered gauge length and m is the Weibull modulus of the fibres, which was considered to be equal in both fibre types.

According to Swolfs [2] the main conclusions to draw from this model are:

- The strain concentration factor depends only on the normalised stiffness ratio of the two fibres (ρ), which means that in the case of a hybrid composite with both fibres with the same factor $[E \times A]$, the stress concentration in the hybrid and non-hybrid composite will be the same;
- The most influential parameter in Zweben's model is the ratio of failure strains, meaning that hybrid effect should be more effective with fibres with very high failure elongation;
- As the Weibull modulus are usually over 5, the exponent $-1/(2m)$ will be small, meaning that the strain concentration factors and ineffective lengths have a small influence in the hybrid effect;

- Fibres with small Weibull modulus (high strength/strain dispersion) should lead to higher hybrid effects as comproved by Fukunaga et al. [135].

In 1984 Fukuda [136] modified the model developed by Zweben [105] according to three flaws he encountered in that model. Firstly, Fukuda considered that the first failure of a HE fibre, which was the failure criteria used by Zweben, is not an accurate failure criteria for hybrid composites and it is not in accordance with the hybrid effect definition proposed by Hayashi [98]. Secondly, Zweben focused on the failure of a HE fibre next to a broken LE fibre and said that represented the lower bound for composite failure strain. According to Fukuda [136], that will represent the lower bound for non-hybrid composites but may not be true for hybrid ones, because, after a LE fibre breaks, it is expected that the nearest LE fibre will break next, instead of the HE fibre in the middle of those, due to the difference in failure strains. The failure of the two LE fibres causes an higher stress concentration in the HE fibre that is in the middle of the broken LE fibres than the one predicted by Zweben. Lastly, Fukuda [136] considered that the SCFs and the ineffective lengths used in Zweben's model were not accurate as, in a non-hybrid composites, the model predicted smaller SCFs than the ones of Hedgpeth shear-lag model [75].

Taking into account these three shortcomings of Zweben's model [105], Fukuda [136], proposed the following equation for the hybrid effect:

$$R_{hyb} = \left[\frac{\delta_h \left(k_h^m - 1\right)}{2\delta_{LE}\left(k_{LE} - 1\right)}\right]^{-1/2m} . \tag{2.27}$$

This equation is very similar to the one of Zweben's model (Equation 2.26), however it was developed using more accurate values for the SCFs. Comparing equations (2.27) and (2.26) it is observed that in Fukuda's model the failure strain ratio of both fibre types doesn't affect the hybrid effect, as proposed in Zweben's model.

Zweben [105] did experimental work to determine the hybrid effect in a carbon/aramid hybrid composite and concluded that the hybrid effect for this material was 4%. For this material Zweben's model [105] predicted a hybrid effect of 22% and Fukuda's model [136] predicted a hybrid effect of 13%, which is closer to the experimental value. Both authors compared their results with a multi-directional composite material, however, these 1D models may not be accurate to predict the complex failure of multi-directional composites.

According to Swolfs [2], there are others limitations of Zweben's model. Firstly, the 1D fibre packing is a simplification of the complex 2D micro-structure of the hybrid composite materials and leads to a overestimation of the SCFs in the fibres [13]. Secondly, the dispersion of both fibre types is maximized in the alternating HE and LE fibres for a hybrid ratio of 50%. Lastly, Zweben's model does not allow the study of the hybrid ratio, which has been proved to affect the hybrid effect [100].

More recently, Mishnaevsky and Dai [137] developed a 2D numerical fibre bundle model with a random fibre packing. Using Monte-Carlo method, random properties

are given to the fibres according to a Weibull distribution. The authors used this model to study the failure of a carbon/glass hybrid, and concluded that fibre mixing had a negative effect on the critical stress of the composite. However they considered that the critical stress occurred when the composite stiffness was reduced by 50% and considered a fibre volume fraction of 25%.

Pimenta and Robinson [14] extended the hierarchical bundle model, previously developed [7], to hybrid composites. This model was the first 2D shear-lag model for hybrid composites and considers a square arrangement of fibres with stochastic strength values. The model is able to study the effect of dispersion and hybridization ratio (N^B) by changing the construction parameters of the unit cells (see Figure 2.31)

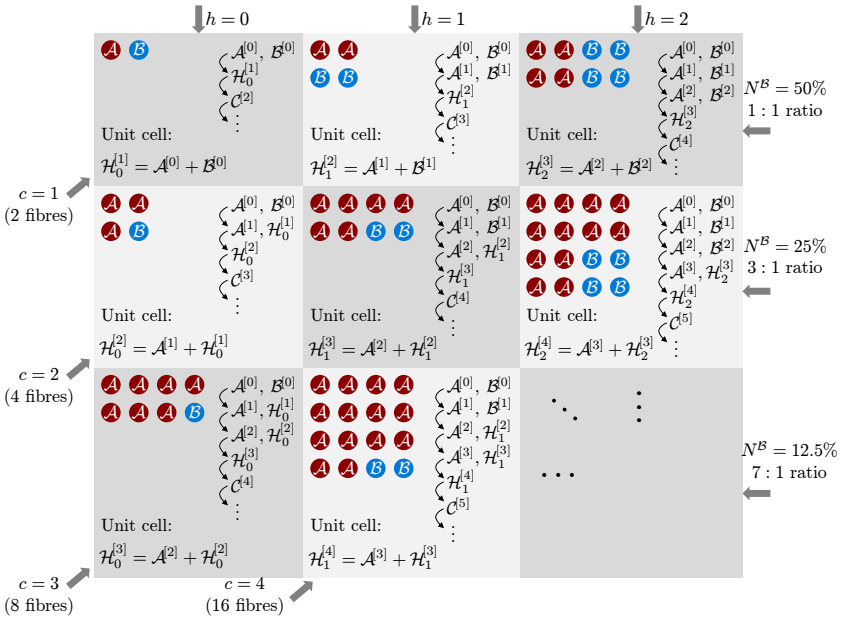

Figure 2.31: Hybrid unit-cells with different hybridization ratios (N^B) and hybridization degrees [14].

With this model, Pimenta and Robinson [14] were able to demonstrate the influence of the carbon/glass fibre volume ratio and the effect of dispersion in the hybrid effect, which increases with increasing dispersion. According to Swolfs [2] the main drawback in this model is the stress concentrations that were considered are unrealistic and, therefore, so are the predictions of failure development.

Swolfs [2] extended his model, presented in section 2.1.6.5, to hybrid composites. Some adaptations were made from the original model. Firstly, the hybrid model considers an hexagonal arrangement of fibres instead of a random one which, according to the author, was done to allow the study of dispersion of both fibre types in hybrid composites. The stress redistribution around a broken fibre was also altered to consider a very local load sharing, which means that the stress, previously carried by a broken fibre, is redistributed only to the six closest fibres (Figure 2.32), fibres that were considered to have de same radius.

In figure 2.32 it is observed that the SCFs in both fibre types. The difference

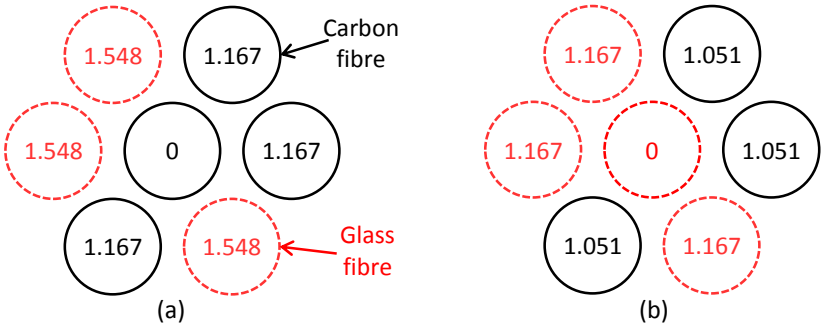

Figure 2.32: Stress concentration factors, according to very local load sharing, around (a) a broken carbon fibre and (b) a broken glass fibre [2].

in SCFs is due to the difference in stiffness of both fibres. If the broken fibre is a carbon fibre, the nearest carbon fibres have a SCF of 7/6 and the glass fibres have a SCF equal to $1 + 1/6 \cdot 230/70 = 1.548$ where 70 and 230 GPa are the Young's moduli of the glass and carbon fibres, respectively. The same strategy is used for a broken glass fibre, where the nearby glass fibres have a SCF equal to 7/6 and the carbon fibres equal to $1 + 1/6 \cdot 70/230 = 1.051$. To further simplify the original model, the stress recovery in a broken fibre is assumed to be linear. The ineffective lengths were determined using FE analysis.

The model considers 2000 breakable fibres and 250 boundary fibres (unable to break), to which is attributed a strength according to a Weibull distribution. This model was used to study the hybrid effect and cluster formation of carbon/glass hybrids.

Tavares et al. [58] developed different modelling strategies with increasing level of complexity to understand the effects of hybridization on the tensile failure of composite materials. The authors developed two semi-analytical models to predict the tensile failure of hybrid composites. The first is based on the statistics of fibre strength and can be used to predict failure of bundles of fibres that are not connect by a matrix. Secondly, the authors developed a progressive damage model based on fibre fragmentation phenomenon to access the effects of hybridization, now considering a composite material. Nevertheless, the developed model considers a global load sharing rule and, therefore leads to an overprediction of the strength of the materials in study. Finally, the authors used a 3D finite element model that considers a random fibre dispersion and the main mechanisms of failure in composite materials, such as fibre failure, matrix plasticity and cracking and fibre-matrix debonding. The authors used the latter model to validate the study performed with the simpler models and observed that the simpler models were able to capture the main effects of the fibre strength distributions on the tensile behaviour of hybrid composites.

Guerrero et al. [63] use the developed FBM to study the effects of hybridization. The authors used the model not only to study the stress-strain behaviour of hybrid composites at different hybrid volume fractions but also to study fibre fracture and cluster development for hybrid composites. Additionally, the authors compared the developed FB model with the 3D FE model developed by [58] and found a good

agreement between the models.

2.2.5 Influencing parameters in the strength of hybrid composites

The models for predicting the failure of hybrid UD composites were presented, however, the most influencing parameters in the hybrid composite behaviour haven't yet been accessed. There is a large number of parameters that can influence the behaviour of hybrid composites and some will be presented in this section. As most authors focus their attention on the parameters that influence the failure strain enhancement of the LE fibres (hybrid effect), most of this data will be related to that effect.

2.2.5.1 Failure strain ratio

As presented in Section 2.2.4, Zweben's model [105] considers the ratio of the failure strains of both fibres to be the most influential parameters in the hybrid effect. Fukuda [136] contradicted the results of Zweben's model and considered that the failure strain ratio has no influence on the hybrid effect. This difference is due to the models considering different failure definitions for the hybrid composite. More recently, Swolfs [2] addressed this issue and concluded that the failure strain ratio affects the hybrid effect, however, for failure strain ratios above 2 this influence is reduced (see Figure 2.33). These results were obtained for the same LE fibres.

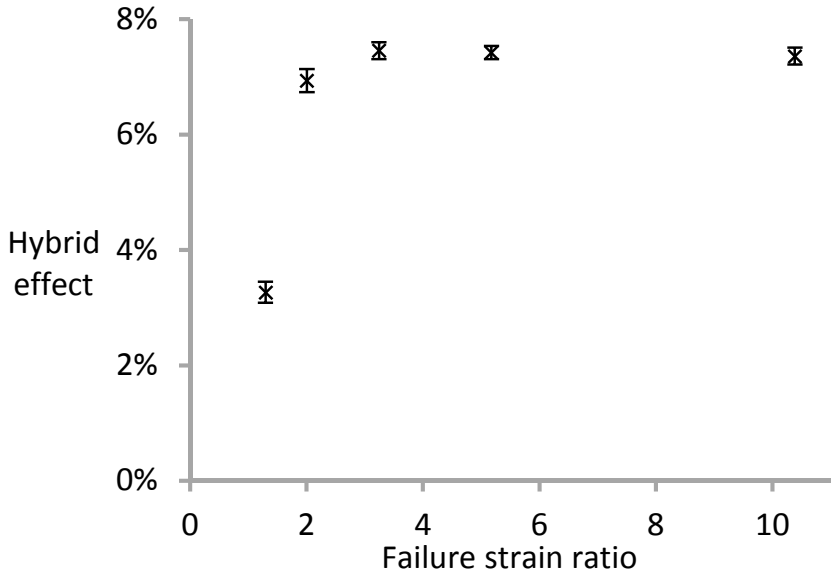

Figure 2.33: Influence of failure strain ratio in the hybrid effect, for a hybrid composite with 50% of each fibre type [2].

Swolfs [2] attributed these results to the delay of HE fibre breaks, delaying the development of clusters of broken fibres. Nonetheless, the author stated that there

are three limitations to his conclusions. Firstly, the model assumes that the failure occurs when a critical cluster of broken LE fibres is developed. In this situation, most of the HE fibres are still intact and able to carry load, which means that, especially for high contents of HE fibres, the composite may not fail at this point. Secondly, the model considers the elastic properties of the HE fibres remain the same with increasing their failure strain, which may not be accurate since higher failure strain is usually associated with higher compliance. Thirdly, the author considers that the threshold of failure strain ratios of 2 may be affected by the Weibull modulus of both fibre types.

Although the model developed by Swolfs [2] isn't able to consider the residual load carrying capabilities of the HE fibres, it is considered that this may be an important factor in the behaviour of hybrid composites.

2.2.5.2 Hybrid volume fraction

Hybrid volume fraction represents the relative amount of both fibre types in the material and has been shown to have a large effect in the hybrid composite behaviour [2, 100]. Increasing the volume content of HE fibres was shown to increase the hybrid effect [100]. The earlier models for hybrid composites were not able to study this effect due to the limitations in fibre packing. Recent models [2, 14, 121] have been able to do so, concluding that increasing HE fibre content increases the hybrid effect. Swolfs [2] reported that, for carbon/glass fibres, increasing the HE fibre content lead to a delay of the development of clusters of broken fibres. On the other hand, it was found that increasing the volume fraction of HE fibres reduced the critical cluster size (size of a cluster of broken fibres that leads to failure of the composite), which will counteract, in part, the delay in cluster development, as the composite will fail when a smaller critical cluster develops. This parameter was also shown to have a large influence on the type of failure developed under tensile loadings [58, 63, 134].

2.2.5.3 Elastic properties of the fibres

The elastic properties of the fibres are important in the stress distribution in the hybrid composite. They affect the three hypotheses for hybrid effect [2], as they affect the static SCFs [13, 105, 136], the dynamic stress concentrations [108], the ineffective lengths [2, 13] and the residual thermal stresses. According to the results presented by Swolfs [2], increasing the stiffness of the HE fibres (maintaining same properties for the LE fibres) leads to a small increase of the hybrid effect, which is attributed to a decrease in the SCFs in the LE fibres with the increase of the HE fibres' stiffness. Guerrero et al. [134] also showed that the combination of the elastic properties of both hybridized fibres has a large influence on the stress redistribution and damage development and failure of hybrid composites.

2.2.5.4 Fibre strength distribution

Both Zweben's [105] and Fukunga's [136] models consider the fibre strength distribution to have a large influence on the hybrid effect and concluded that, increasing the dispersion of the strength of the fibres, by decreasing the Weibull modulus, increases the hybrid effect. Swolfs [2] addressed this issue and reached the same conclusions as the previous authors, stating that reducing the Weibull modulus from 4.8 to 3 doubled the hybrid effect. These conclusions are important because, lower quality fibres, may have a higher potential for hybrid effects. Manders [138] even stated that "the hybrid effect arises from a failure to realise the full potential strength of the fibres in all-carbon fibre composites, rather than from an enhancement of their strength in the hybrids", which means that if the fibres had a deterministic strength, their full potential would already be realised in non-hybrid composites and the hybrid effect wouldn't exist. Nevertheless, this is a property that is difficult to control, as it depends directly on the fibre type and manufacturing process, making it only possible to change the type of fibres to be hybridized and not controlling directly the strength distributions

2.2.5.5 Fibre dispersion

Fibre dispersion is a measure of how well mixed the fibres are in a hybrid composite. Several authors have, experimentally demonstrated that this is an important factor in the behaviour of hybrid composites [104, 139].

The earlier models that considered 1D arrangements of fibres were not capable of addressing this topic. Recently, Mishnaevsky and Dai [137] addressed this topic and reported that increasing dispersion lead to to slower internal damage development for displacement-controlled models but faster damage development for load-controlled models. Pimenta and Robinson [14] reported that clustering the carbon fibres decreased both the failure strength and strain of the hybrid composites (for the same hybrid fibre ratio), which means that dispersing the LE fibres in the HE fibres leads to better properties.

Swolfs et al. [15] extensively studied this topic. The authors considered a RVE with around 2000 breakable fibres and considered three different types of mixing of both fibre types: in bundles (Figure 2.34a), in layer (Figure 2.34b) and random dispersion.

In this study, the authors concluded that increasing dispersion, by either reducing bundle size or reducing layer thickness, increased the hybrid effect. However, the authors found that layer-by-layer dispersion with layers of 1 fibre thickness, lead to the maximum hybrid effect, even higher than random dispersion (for a hybrid volume fraction of 50%). This was attributed to a reduced number of possible paths for a crack to grow in the LE fibre layers. Random dispersion, however, showed higher hybrid effect than that possible with bundle-by-bundle dispersion, but the authors didn't study the limit case of bundles with just one fibre. The authors also reported that dispersion had a small influence in the critical cluster size. It

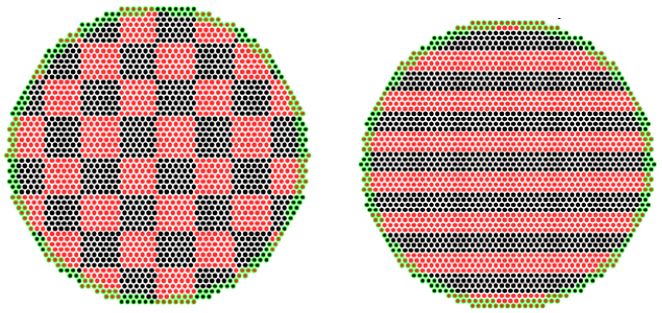

(a) (b)

Figure 2.34: Illustration of the (a) bundle-by-bundle and (b) layer-by-layer dispersion considered by Swolfs et al. (Adapted from[15]).

should be noted that controlling the microstructure to such an extent is currently technologically impossible, therefore, the limit configuration of a single fibre layer impractical. Nevertheless, this shows that ultra-thin laminas have potential to be used for hybridization purposes.

2.2.5.6 Matrix properties

Similarly to non-hybrid composites, the matrix properties are only expected to have a secondary effect in the composite properties, by influencing the SCFs and the ineffective lengths. The matrix shear modulus has an influence on the ineffective length, however its effect on the SCFs is usually not represented in the models due to shear-lag assumptions.

2.2.6 Conclusion

Hybrid composites are attracting an ever growing attention from both academia and industry, due to their potential to increase the design space. The interactions between the constituents in hybrid composites are hard to predict, however hybrid composites may lead to better properties that those of the non-hybrid composites of reference, leading to the existence of positive hybrid effects. These hybrid effects have been reported under several loading conditions, and in several hybrid materials.

Modelling the tensile behaviour of hybrid composites has been shown to be a difficult task. The earliest model to do so was Zweben's model [105], which considered a 1D packing of fibres. This model was able to predict the existence of hybrid effect, but due to its simplicity wasn't able to fully predict the full composite's behaviour, nor to fully justify the hybrid effect. Other models have since then been presented, which helped increase the level of knowledge on hybrid composites and can guide the creation of new material systems.

The modelling and the experimental work done in hybrid composites enabled

the identification of the main influencing parameters in the behaviour of hybrid composites, being the most important the dispersion of the fibres, the hybrid volume fraction and the fibre strength distributions, factor controlled by the fibres chosen to be hybridized.

Part III

Numerical modelling of the longitudinal failure of composite materials

Chapter 3

3D micromechanical models

To study and understand longitudinal failure of composite materials it is necessary to develop micromechanical models that are able to take into account the damage mechanisms that occur for this type of loading condition. These models need to be able to correctly represent the behaviour of each of the individual constituents in the composite, being the two main constituents of the composite the fibres and the matrix. These two materials have very different behaviours: the matrix has a plastic behaviour before failure while the fibres are purely elastic or non-linear elastic up to failure and are brittle. This requires the use of two different material models, one for each of the constituents. In a composite, the matrix and the fibres are not perfectly bonded, they have a damageable interface that connects them, therefore, it is also necessary to account for its behaviour. The interface has a large influence on the behaviour of the composite material as the interfacial separation is one important failure mechanism in longitudinal failure of composite materials.

In this chapter a micromechanical numerical framework is presented to study the longitudinal failure of fibre reinforced composite materials.

3.1 RVE generation

As previously stated in Chapter 2.1, the fibre arrangement is an important factor in the composite's behaviour, as simplified square and hexagonal fibre arrangements usually lead to unrealistic results. To overcome this difficulty it is necessary to generate a Representative Volume Element (RVE) that is representative of the material, which means having a correct size and being able to represent the real microstructure of the composite material to accurately capture the material's behaviour.

The algorithm used to generate the random distribution of fibres is based on the algorithm developed by Melro et al. [68], with some changes to allow the RVE to have multiple types of fibres. The algorithm is composed of three steps, of which only one had major changes, the first step. The flowchart of the algorithm is shown in Figure 3.1. The variable N_i^{max} is the maximum allowed number of iterations of the overall algorithm and N_i is the current number of iterations.

The changes that were required to implement in the hard-core model (STEP 1) are related with the necessity of guaranteeing that the algorithm is able to generate fibres with different diameters and that it is able to achieve the specified volume fraction of each fibre. The flowchart of the modified hard-core model is shown in Figure 3.1. The variables V_f^{curr} and V_f^{req} define the current and required fibre volume fraction, and with the subscript 1 and 2 represent the volume fractions of each type of fibre in the hybrid composite. The variable N_g is the current number of iterations in this step and N_g^{max} is the maximum number of iterations before executing the step two of the algorithm.

The changes in this algorithm allowed the generation of a RVE with different fibre volume fractions and hybrid volume fractions, with fibres of different radii. This algorithm also guarantees material symmetry in order to correctly implement the boundary conditions to the RVE. Another important aspect is guaranteeing a minimum distance between fibres in order to inhibit poorly meshed regions in the RVE.

To correctly simulate the behaviour of UD composite materials under tensile loadings it is necessary to have a RVE with an adequate size to capture the mechanisms of failure of these materials, which leads to the necessity of having a large RVE. The dimensions of the RVE in the direction perpendicular to the fibres directly affect the number of fibres in the RVE. The in-plane dimensions of the RVE need to be such as it is possible to capture the damage mechanisms and cluster formation prior to the failure of the composite. Thefore, the number of fibres must be higher than the expected critical cluster size as this is the main mechanism of failure of UD composites. In terms of the size in the fibre direction, the RVE needs to be long enough to simulate the ineffective length of the fibres.

As the RVE needs to be representative of the material we are trying to model it is necessary to define correct boundary conditions. The characteristics of a composite material make it necessary to define periodic boundary conditions for the RVE. These boundary conditions define constraints in the displacements and rotations in the faces, edges and vertices that are opposed to each other [140]. As this type of boundary conditions is computationally very expensive, a simplified version of these boundary conditions was used by constraining the displacements of opposite faces in the RVE, using Abaqus [141] tie constraints.

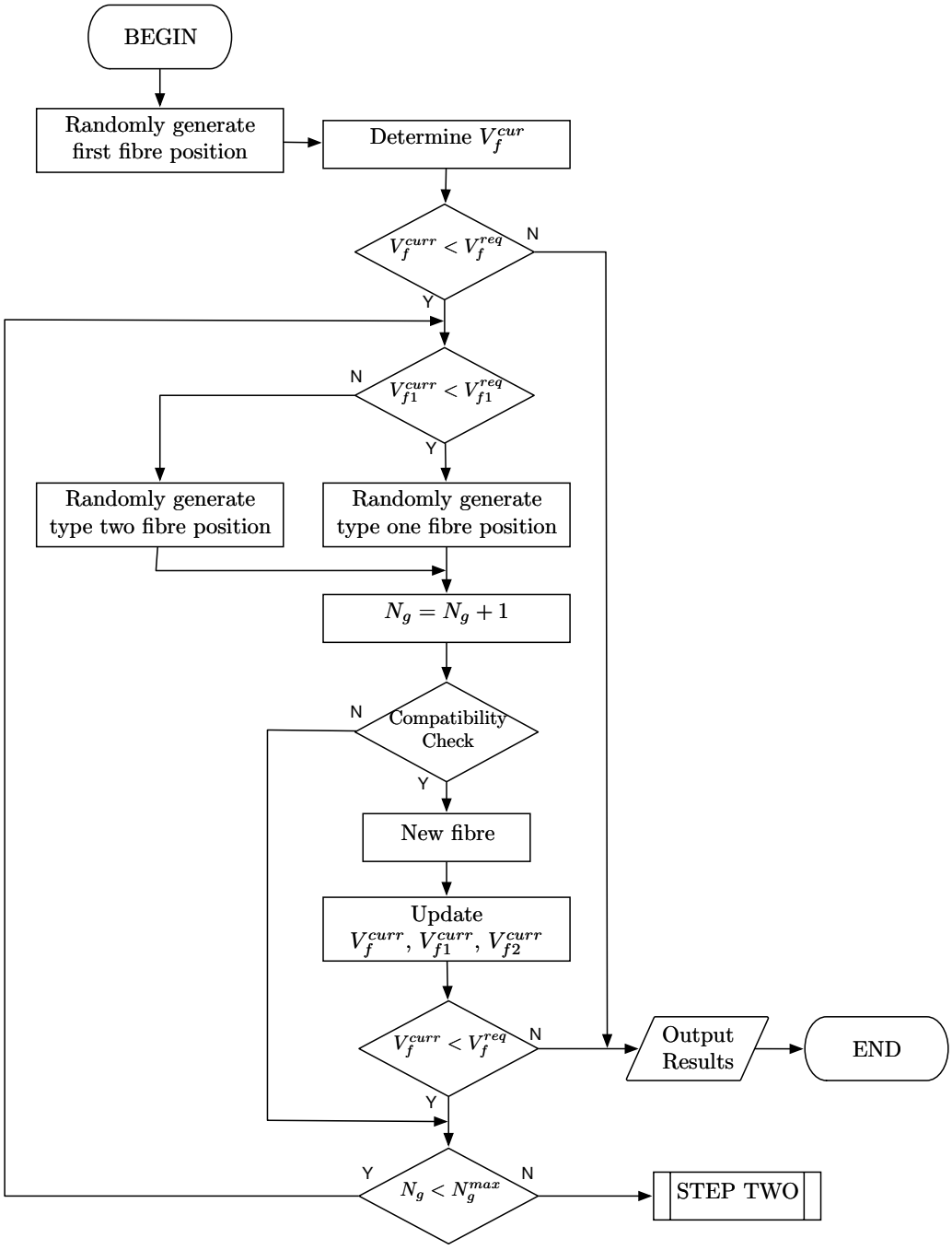

Figure 3.1: Flowchart of the hard-core model for the generation of the microstructure.

3.2 Material models

To simulate the micromechanical behaviour of composite materials it is necessary to develop material models that are able to represent the behaviour of its constituents. As the composite materials is constituted by two types of materials, the matrix and the fibres, it is necessary to develop two material models. Additionally, it is necessary to correctly model the fibre-matrix interface.

The material model used for the matrix is the one developed by Melro et al. [142], which is an isotropic damage model with plasticity based on a paraboloid yield criteria, able to capture the thermal and strain-rate dependency in the matrix behaviour [93].

3.2.1 Non-linear elastic and damage model for carbon fibres

Although being the main load carrying component in composite materials, the available models to predict fibre fracture do not account for all the relevant aspects of the mechanics of fibre fracture. Carbon fibres have been shown to have a non-linear behaviour, with increasing stiffness as function of the applied stress [16, 143–147]. The non-hookean stress-strain response of carbon fibres is reversible and it is unaffected by the cycles of loading and unloading up to at least 40% of the tensile strength. This suggests that the non-hookean stress-strain response of carbon fibres is not due to either partial destruction of the fibre structure or plastic deformation of the materials [147], and is usually attributed to the reorientation of the crystals in the carbon fibres with applied strain. As is expected from the mechanical anisotropy of graphite, the tensile modulus of carbon fibres strongly depends on the crystallite orientation. Generally, carbon fibres with a higher orientation of the carbon layers in the direction of the fibre axis develop a higher tensile modulus. The crystallite orientation of carbon fibres also changes with tensile stress applied to the fibres and increases with increasing tensile stress [147]. The stiffness of a carbon fibre is usually described as:

$$E_f = E_0 \left(1 + \delta\varepsilon_1\right) \ , \tag{3.1}$$

where E_0 is the elastic modulus at zero applied strain, δ is the non-linear parameter and ε_1 is the applied strain. In the literature there are other ways of expressing the increase in modulus of carbon fibres. For instance, based on the theory of nonlinear elasticity for unidirectional continuous carbon fibre polymer matrix composites, Ishikawa et al. [148] derived the following constitutive relation:

$$E_f = \frac{\mathrm{d}\sigma}{\mathrm{d}\varepsilon} = \frac{1}{S_{11} + 2S_{111}\sigma_1 + 3S_{1111}\sigma_1^2} \ , \tag{3.2}$$

where S_i are the first and higher order compliance coefficients, that can be estimated from the stress-strain behaviour in a tensile test.

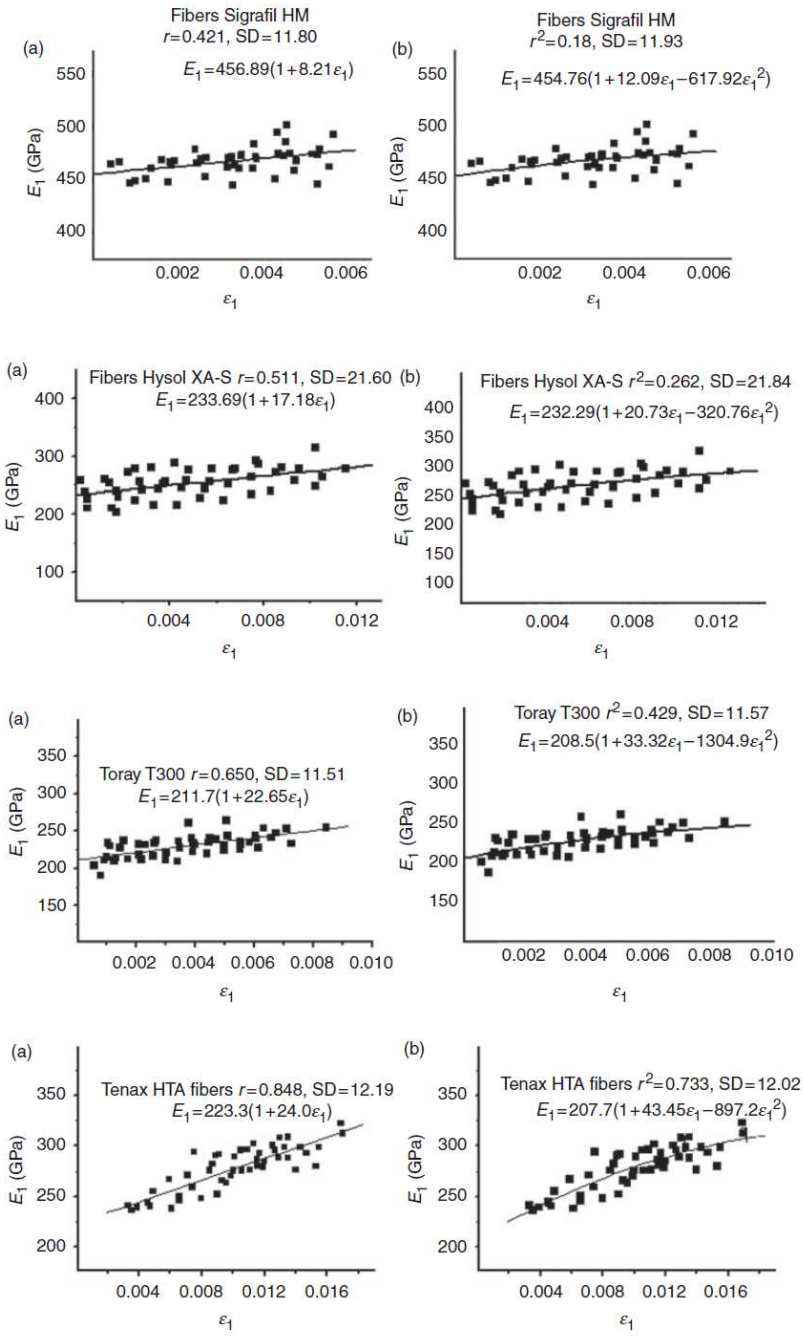

Figure 3.2: Modulus-Strain relation obtained by regression of $E-\varepsilon$: (a) linear regression; (b) square polynomial regression[16].

Djordjevic et al. [16] conducted an extensive experimental study on four different types of carbon fibres to characterise their tensile behaviour, for which the authors applied a linear and quadratic fit to the variation of the elastic modulus with the applied strain. The authors also measured the orientation distribution of graphene planes by X-ray analysis.

From comparing the orientation distribution in the carbon fibres and the degree on nonlinearity in the stress-strain relation, the authors concluded that higher nonlinearity was directly related with higher dispersion in orientation. This means that fibres with higher preferred orientation show less nonlinear behaviour.

3.2.1.1 Constitutive behaviour

To be able to capture the nonlinear behaviour of carbon fibres in micromechanical simulations and be able to predict their failure it is necessary to have a nonlinear elastic model coupled with damage.

The model proposed here considers the fibres transversely isotropic and nonlinear elastic up to failure, which is controlled by a maximum stress criterion and an exponential damage law is used to simulate the full process of fibre fracture.

To take into account the nonlinear behaviour of the carbon fibres it is necessary to change the complementary free energy density function from which the model is derived. Hahn et al. [149] develop a thermodynamically consistent nonlinear model for a composite laminae by considering terms of higher order (above two) in the definition of the complementary free energy function. Based on this work and based on the evidence of the nonlinearity of carbon fibres, a thermodynamically consistent damage model for carbon fibres was developed.

The fibres are considered to be nonlinear elastic up to failure and to have a transversely isotropic behaviour. The complementary free energy per unit volume is defined as:

$$W^* = \frac{\sigma_{11}^2}{2E_1\left(1-d_f\right)} + \frac{\sigma_{22}^2+\sigma_{33}^2}{2E_2\left(1-d_f\right)} + \frac{\nu_{12}}{E_1}\left(\sigma_{11}\sigma_{22}+\sigma_{11}\sigma_{33}\right) - \frac{\nu_{23}}{E_2}\left(\sigma_{22}\sigma_{33}\right) + \frac{\sigma_{12}^2+\sigma_{13}^2}{2G_{12}\left(1-d_f\right)} + \frac{\sigma_{23}^2}{2G_{23}\left(1-d_f\right)} + \frac{S_{111}}{3}\frac{\langle\sigma_{11}\rangle_+^3}{1-d_f}, \tag{3.3}$$

where $\langle x\rangle_+$ is the McCauley operator defined as $x = (x+|x|)/2$. E_1 and E_2 are the longitudinal and transverse Young's moduli, G_{12} and G_{23} the longitudinal and transverse shear moduli and d_f is the damage variable for the fibres. Using standard arguments, the strain tensor is defined as the partial derivative of the complementary free energy density with respect to the stress tensor:

$$\boldsymbol{\varepsilon} = \frac{\partial W^*}{\partial \boldsymbol{\sigma}} = \begin{bmatrix} \frac{\sigma_{11}}{E_1\left(1-d_f\right)} + \frac{S_{111}\langle\sigma_{11}\rangle_+^2}{\left(1-d_f\right)} - \frac{\nu_{12}}{E_1}\left(\sigma_{22}+\sigma_{33}\right) \\ \frac{\sigma_{22}}{E_2\left(1-d_f\right)} - \frac{\nu_{12}}{E_1}\sigma_{11} - \frac{\nu_{23}}{E_2}\sigma_{33} \\ \frac{\sigma_{33}}{E_2\left(1-d_f\right)} - \frac{\nu_{12}}{E_1}\sigma_{11} - \frac{\nu_{23}}{E_2}\sigma_{22} \\ \frac{\sigma_{12}}{G_{12}} \\ \frac{\sigma_{13}}{G_{12}} \\ \frac{\sigma_{23}}{G_{23}} \end{bmatrix}. \tag{3.4}$$

The compliance tensor ($\boldsymbol{H_f}$) is calculated as:

$$\boldsymbol{H_f} = \frac{\partial^2 W^*}{\partial \boldsymbol{\sigma}^2} = \begin{bmatrix} \frac{1}{E_1\left(1-d_f\right)} + \frac{2S_{111}\langle\sigma_{11}\rangle_+}{\left(1-d_f\right)} & -\frac{\nu_{12}}{E_1} & -\frac{\nu_{12}}{E_1} & 0 & 0 & 0 \\ -\frac{\nu_{12}}{E_1} & \frac{1}{E_2\left(1-d_f\right)} & -\frac{\nu_{23}}{E_2} & 0 & 0 & 0 \\ -\frac{\nu_{12}}{E_1} & \frac{\nu_{23}}{E_2} & \frac{1}{E_2\left(1-d_f\right)} & 0 & 0 & 0 \\ 0 & 0 & 0 & \frac{1}{G_{12}\left(1-d_f\right)} & 0 & 0 \\ 0 & 0 & 0 & 0 & \frac{1}{G_{12}\left(1-d_f\right)} & 0 \\ 0 & 0 & 0 & 0 & 0 & \frac{1}{G_{23}\left(1-d_f\right)} \end{bmatrix}. \tag{3.5}$$

Inverting the compliance tensor results in the stiffness tensor ($\boldsymbol{D_f}$):

$$\begin{aligned} \boldsymbol{D_f} &= \boldsymbol{H_f}^{-1} \\ &= \frac{1-d_f}{\Delta} \begin{bmatrix} (1-\beta)E_1^2 & E_1\nu_{12}(1-d_f) & E_1\nu_{12}(1-d_f) & 0 & 0 & 0 \\ E_1\nu_{12}(1-d_f) & \frac{E_2\left(E_1-\gamma\left(1-d_f\right)+2E_1^2S_{111}\langle\sigma_{11}\rangle_+\right)}{1+\beta} & \frac{E_2\left(1-d_f\right)\left(\gamma+\nu_{23}E_1\left(1+2E_1S_{111}\langle\sigma_{11}\rangle_+\right)\right)}{1+\beta} & 0 & 0 & 0 \\ E_1\nu_{12}(1-d_f) & \frac{E_2\left(1-d_f\right)\left(\gamma+\nu_{23}E_1\left(1+2E_1S_{111}\langle\sigma_{11}\rangle_+\right)\right)}{1+\beta} & \frac{E_2\left(E_1-\gamma\left(1-d_f\right)+2E_1^2S_{111}\langle\sigma_{11}\rangle_+\right)}{1+\beta} & 0 & 0 & 0 \\ 0 & 0 & 0 & G_{12}\Delta & 0 & 0 \\ 0 & 0 & 0 & 0 & G_{12}\Delta & 0 \\ 0 & 0 & 0 & 0 & 0 & G_{23}\Delta \end{bmatrix} \end{aligned} \tag{3.6}$$

where

$$\beta = \nu_{23}\left(1-d_f\right) \tag{3.7a}$$

$$\gamma = \nu_{12}^2 E_2\left(1-d_f\right) \tag{3.7b}$$

$$\Delta = -2\gamma\left(1-d_f\right) - E_1\beta + 2E_1^2S_{111}\langle\sigma_{11}\rangle_+\left(1-\beta\right) + E_1 \tag{3.7c}$$

To ensure the thermodynamical admissibility of the formulation, the following inequality must be satisfied:

$$\det\left(\frac{\partial^2 W^*}{\partial \boldsymbol{\sigma}^2}\right) > 0; \tag{3.8}$$

which results in the following constraint:

$$\sigma_{11} < -\frac{1}{2}\frac{2E_2\nu_{12}^2 + E_1\left(\nu_{23}-1\right)}{\left(\nu_{23}-1\right)S_{111}E_1^2}\,. \tag{3.9}$$

3.2.1.2 Stress updating with Newton-Raphson algorithm

Defining the residual:

$$\boldsymbol{R}(\boldsymbol{\sigma}) = \boldsymbol{\sigma} - \boldsymbol{D}(\boldsymbol{\sigma}) : \boldsymbol{\varepsilon}\,. \tag{3.10}$$

The linear approximation of the residual is given by:

$$\boldsymbol{R}(\boldsymbol{\sigma}_{n+1}) = \boldsymbol{R}(\boldsymbol{\sigma}_n) + D\boldsymbol{R}(\boldsymbol{\sigma}_n)\Delta\boldsymbol{\sigma}\,. \tag{3.11}$$

The value of $\boldsymbol{\sigma}$ that makes the residual null needs to be calculated:

$$\boldsymbol{R}(\boldsymbol{\sigma}_n) + D\boldsymbol{R}(\boldsymbol{\sigma}_n)\Delta\boldsymbol{\sigma} = 0 \; . \tag{3.12}$$

Solving this equation in order to $\Delta\boldsymbol{\sigma}$ results in:

$$\Delta\boldsymbol{\sigma} = -\left[D\boldsymbol{R}(\boldsymbol{\sigma}_n)\right]^{-1}\boldsymbol{R}(\boldsymbol{\sigma}_n) \tag{3.13}$$

The stress update expression is given by:

$$\boldsymbol{\sigma_{n+1}} = \boldsymbol{\sigma_n} - \Delta\boldsymbol{\sigma} \; . \tag{3.14}$$

$D\boldsymbol{R}(\boldsymbol{\sigma}_n)$ is matrix the whose components are the various partial derivative of the components of $\boldsymbol{R}$, given by:

$$D\boldsymbol{R}(\boldsymbol{\sigma}) = \frac{\partial \boldsymbol{R}}{\partial \boldsymbol{\sigma}} = \boldsymbol{I} - \frac{\partial \boldsymbol{D}(\boldsymbol{\sigma})}{\partial \boldsymbol{\sigma}} : \boldsymbol{\varepsilon} \; . \tag{3.15}$$

As the stiffness tensor $\boldsymbol{D}$ only depends on the stress component σ_{11}, then only the first column of $D\boldsymbol{R}(\boldsymbol{\sigma})$ is used:

$$\boldsymbol{I}_1 - \frac{\partial \boldsymbol{D}(\boldsymbol{\sigma})}{\partial \sigma_{11}}\varepsilon \tag{3.16}$$

where $\boldsymbol{I}_1$ is a column vector with the first component equal to one and the remaining null and $\frac{\partial \boldsymbol{D}(\boldsymbol{\sigma})}{\partial \sigma_{11}}$ is given as:

$$\frac{1}{\Delta^2}\begin{bmatrix} -2(1-d_f)^2E_1^4S_{111}(1-\beta)^2 & -2(1-d_f)^2\nu_{12}E_1^3S_{111}(1-\beta)E_2 & -2(1-d_f)^2\nu_{12}E_1^3S_{111}(1-\beta)E_2 & 0 & 0 & 0 \\ -2(1-d_f)^2\nu_{12}E_1^3S_{111}(1-\beta)E_2 & -\gamma S_{111}E_1^2E_2(1-d_f)^2 & -\gamma S_{111}E_1^2E_2(1-d_f)^2 & 0 & 0 & 0 \\ -2(1-d_f)^2\nu_{12}E_1^3S_{111}(1-\beta)E_2 & -\gamma S_{111}E_1^2E_2(1-d_f)^2 & -\gamma S_{111}E_1^2E_2(1-d_f)^2 & 0 & 0 & 0 \\ 0 & 0 & 0 & 0 & 0 & 0 \\ 0 & 0 & 0 & 0 & 0 & 0 \\ 0 & 0 & 0 & 0 & 0 & 0 \end{bmatrix} \tag{3.17}$$

With the definition of $D\boldsymbol{R}(\boldsymbol{\sigma}_n)$ the integration scheme is fully defined and can be implemented according to the algorithm shown in Table 3.1.

Table 3.1: Newton-Raphson algorithm implemented.

i	Determine the elasticity tensor before the strain increment $\boldsymbol{D}(\boldsymbol{\sigma}_0)$
ii	Determine the initial predictor for the stress-state $\boldsymbol{\sigma}_1 = \boldsymbol{\sigma}_0 + \boldsymbol{D}(\boldsymbol{\sigma}_0) : \boldsymbol{\varepsilon}$
iii	Determine the new elasticity tensor $\boldsymbol{D}(\boldsymbol{\sigma}_1)$
iv	Determine the residual $\boldsymbol{R} = \boldsymbol{\sigma}_1 - \boldsymbol{D}(\boldsymbol{\sigma}_1) : \Delta\boldsymbol{\varepsilon}$
v	Check for convergence IF $\lvert\boldsymbol{R}\rvert < tol$ END ELSE $\Delta\boldsymbol{\sigma} = -\left(\frac{\partial \boldsymbol{R}}{\partial \boldsymbol{\sigma}}\right)\boldsymbol{R}$ $\boldsymbol{\sigma}_1 = \boldsymbol{\sigma}_1 + \Delta\boldsymbol{\sigma}$ GOTO iii

3.2.1.3 Damage model

The damage activation function is defined as:

$$F_f^d = \phi_f^d - r_f \leq 0 \,, \tag{3.18}$$

where ϕ_f^d is the loading function defined as:

$$\phi_f^d = \frac{\tilde{\sigma}_{11}}{X_f^t} \,, \tag{3.19}$$

and r_f the internal variable

$$r_f = \max\left\{1, \max_{t\to\infty}\left\{\phi_{f,t}^d\right\}\right\} \,. \tag{3.20}$$

The loading function is function of the fibre tensile strength (X_f^t), which has a stochastic value and will vary from element to element. The loading function is also a function of the effective longitudinal stress $\tilde{\sigma}_{11}$, which is a component of the effective stress tensor given by:

$$\tilde{\boldsymbol{\sigma}} = \left(\boldsymbol{H_f^0}\right)^{-1} : \boldsymbol{\varepsilon} \,, \tag{3.21}$$

where $\boldsymbol{H_f^0}$ is the compliance tensor of the undamaged material.

To avoid mesh dependency issues and to ensure that there is a correct energy dissipation during the damage process energy regularization is preformed by controlling

the parameter A_f in the damage evolution law, defined as:

$$d_f = 1 - \frac{e^{A_f(1-r_f)}}{r_f} \ , \tag{3.22}$$

where the parameter A_f has to be determined for each element of the mesh as a function of the tensile strength and element length, ensuring that the dissipated energy in an element is

$$\Psi_f\left(A_f\right) = \frac{G_{ff}}{l^e} \ , \tag{3.23}$$

where G_{ff} is the fracture toughness of the fibres in mode I, l^e the element's characteristic length.

As the tensile strength of the fibres is a stochastic parameter a random strength is assigned to each element that represents the fibre. This is done by using one of the statistical distributions for fibre strength shown in Section 2.1.

Equation (3.9) limits the applicability of the nonlinear model, by defining a maximum allowed stress. Another issue is that close to this limit the nonlinearity of the model is very high, due to the increased stiffness, which can cause numerical convergence problems. To improve the applicability of the model up to fibre tensile strengths close to the limit in Equation (3.9) and, as there is the need to determine the elastic trial stress to calculate the damage variable, it is considered that the material has a constant stiffness if $\tilde{\sigma}_{11}$ is higher than X_f^t. This translates into the following limit of applicability of the model:

$$X_f^t < -\frac{1}{2}\frac{2E_2\nu_{12}^2 + E_1\left(\nu_{23}-1\right)}{\left(\nu_{23}-1\right)S_{111}E_1^2} \ , \tag{3.24}$$

being that for higher elastic stresses the material is considered linear elastic, ensuring stress and stiffness continuity. This is done by forcing the σ_{11} variable in the stiffness matrix $\boldsymbol{D}$ is equal to X_f^t if $\tilde{\sigma}_{11} > X_f^t$. This behaviour can be seen in Figure 3.3, where both the real stress and the trial elastic stress are shown. In this figure it is possible to see that the trial elastic stress evolves linearly after the failure strength has been reached.

3.2.1.4 Determination of the A_f parameter

The A_f parameter is used to regularise the energy dissipation during the damage process, ensuring that:

$$\Psi_f\left(A_f\right) = \frac{G_{ff}}{l^e} \ . \tag{3.25}$$

Solving this equation allows the determination of the damage parameter A_f. To do so, a numerical iterative procedure to solve non-linear equations is required. The procedure used is the secant method.

The dissipated energy $\Psi_f\left(A_f\right)$ is determined by numerically integrating the stress-strain curve for a purely tensile load. As A_f only affects the softening part of

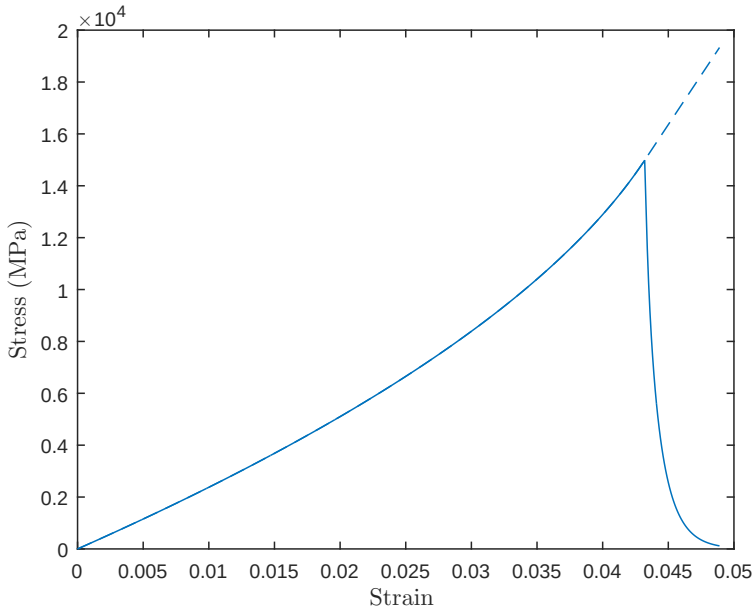

Figure 3.3: Typical stress-strain curve of the nonlinear model: real stress in full and trial elastic stress in dashed.

the material behaviour and not the elastic part, the energy dissipated in the elastic domain is determined a priori as a function only of the tensile strength. Due to the low value of the fracture toughness of the fibres, and to avoid using extremely refined meshes, the fracture toughness of the fibres may have to be changed as a function of the tensile strength to avoid snap back effects. Therefore, if the dissipated energy in the elastic domain (I_{elast}) is lower than $\frac{G_{ff}}{l^e}$, the actual fracture toughness of the fibres G_{ff} is increased to $1.05 I_{elast}$, ensuring that there is a smooth softening with no snap back.

To start the iterative process to determine A_f it is necessary to define two initial parameters, chosen according to [142, 150]:

$$A_f^1 = \frac{2 l^e {X_f^t}^2}{\left| 2 E_1 G_{ff} - l^e {X_f^t}^2 \right|} \qquad \text{and} \qquad A_f^2 = 0.5 A_f^1 \, . \tag{3.26}$$

As the parameter A_f must be positive, the following iterative procedure was followed:

$$\ln\left(A_f^{i+1}\right) = \ln\left(A_f^i\right) - \left[\ln\left(\Psi_f\left(A_f^i\right)\right) - \ln\left(\frac{G_f f}{l_e}\right)\right] \frac{\ln\left(A_f^i\right) - \ln\left(A_f^{i-1}\right)}{\ln\left(\Psi_f\left(A_f^i\right)\right) - \ln\left(\Psi_f\left(A_f^{i-1}\right)\right)} \tag{3.27}$$

The flowchart for the iterative process to determine A_f is shown in Figure 3.4.

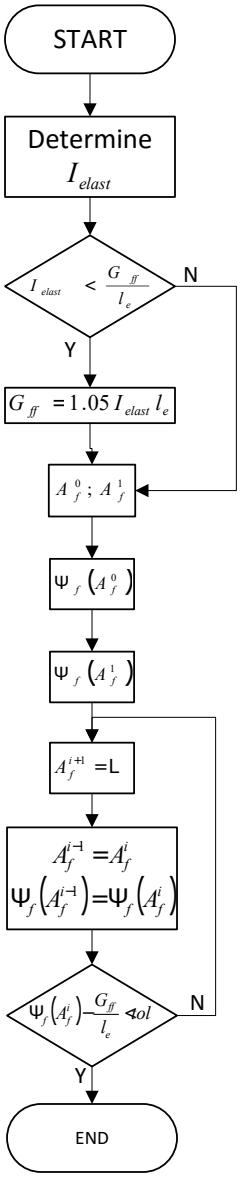

Figure 3.4: Flowchart of the iterative procedure to determine A_f.

3.2.1.5 Model implementation

Figure 3.5 shows the flowchart corresponding to the algorithm of the constitutive model implemented.

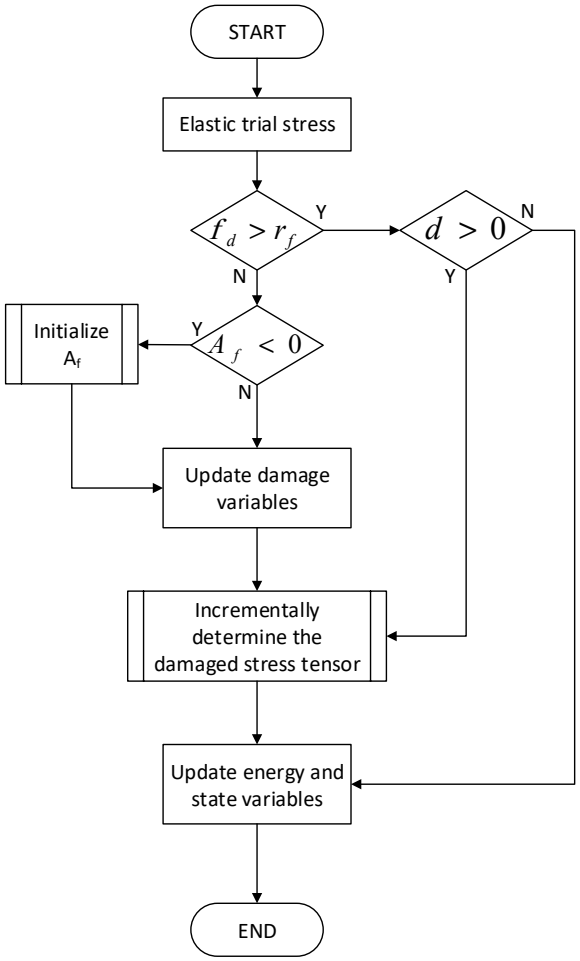

Figure 3.5: Model flowchart.

The parameter A_f is determined for each element when it starts to damage and is a function of both the element length and the tensile strength assigned to that respective element, with the process described in Section 3.2.1.4.

The elastic trial stress is determined based on the elastic stress of the previous increment, being saved in the form of a state variable. This procedure is done with the Newton-Raphson algorithm previously presented. After the trial stress is determined loading and unloading conditions are verified, if the loading is verified the damage variable is updated. Afterwards the damaged stress tensor is determined. Due to the nature of the model it is not possible to directly determine the damaged stress state based on the trial elastic stress state. To determine the damaged stress state a incremental procedure is performed considering the material to be damaged at the undeformed state ($d \neq 0$). This incremental procedure is done by considering

the material initially to be in the undeformed state and through incrementing the strain until equilibrium is achieved at the desired applied strain. Afterwards, the energy variables are updated as well as the state variables.

The nonlinearity present in the model only affects the tensile behaviour of the fibres, being that in compression the fibres have a transversely isotropic linear elastic behaviour up to failure. The behaviour of the fibres in compression or in cases that $S_{111} = 0$ reverts to the previous developed damage model [58]. This is implemented in the code by analysing if the trial elastic stress is positive or negative.

3.2.2 Matrix elasto-plastic damage model

Definition of the most appropriate constitutive model for the polymer resins is a challenging subject. In fact, polymer resins can exhibit a strong nonlinear response under general loading scenarios, which must be accurately captured to ensure that reliable analysis of its deformation can be performed. The plastic deformation in polymer resins has been often modelled using either the Drucker-Prager model or the Mohr-Coulomb model. However, experimental evidence reveals that neither of these models are able to properly capture the constitutive behaviour of epoxy resins [140, 142]. Hence, for an accurate representation of the nonlinear response of typical epoxy resins, an elasto-plastic constitutive model based on a paraboloidal yield criterion, developed by Melro et al. [142], is used.

Initially the matrix is considered linear elastic, being possible to relate the stress and strain tensors as:

$$\boldsymbol{\sigma} = \boldsymbol{D}^e : \boldsymbol{\varepsilon}^e \ , \tag{3.28}$$

where D^e is the elasticity tensor. The non-linear behaviour of the matrix controlled by a paraboloidal yield criterion, being the yield surface defined as:

$$\Phi\left(\boldsymbol{\sigma}, \sigma_{Yc}, \sigma_{Yt}\right) = 6J_2 + 2I_1\left(\sigma_{Yc} - \sigma_{Yt}\right) - 2\sigma_{Yc}\sigma_{Yt} \ , \tag{3.29}$$

where σ_{Yc} and σ_{Yt} are, respectively, the compressive and tensile yield strengths of the matrix material, J_2 is the second invariant of the deviatoric tensor $\boldsymbol{S}$ and I_1 the first invariant of the stress tensor.

For a correct definition of the volumetric deformation in plasticity, the paraboloidal yield criterion, defined as:

$$g = \sigma_{vm}^2 + \alpha p^2 \ , \tag{3.30}$$

where σ_{vm} is the von Mises equivalent stress, p the hydrostatic pressure and α is a material parameter defined by

$$\alpha = \frac{9}{2}\frac{1 - 2\nu_p}{1 + \nu_p} \ , \tag{3.31}$$

where ν_p is the plastic Poisson's ratio of the matrix. If this flow potential rule is applied to a metal, the plastic Poisson's ratio would be 0.5 and α null, reverting the flow potential to the standard von Mises flow potential. Having defined the flow

rule, it is possible to establish the increment of plastic strain, in tensorial notation, as:

$$\Delta\varepsilon^p = \Delta\gamma \left(3\boldsymbol{S} + \frac{2}{9}\alpha I_1 \boldsymbol{I}\right) , \tag{3.32}$$

where $\Delta\gamma$ is the increment of the plastic multiplier.

The hardening laws are defined as dependent of the equivalent plastic strain for the compressive and tensile yield strengths, as these are the only strengths needed to define the yield surface. The increment of equivalent plastic strain is defined as:

$$\Delta\varepsilon_e^p = \sqrt{k\Delta\boldsymbol{\varepsilon}^p : \Delta\boldsymbol{\varepsilon}^p} , \tag{3.33}$$

where k is a constant that varies with the yield criterion, defined ensuring that the equivalent plastic strain is equal to that obtained in a simple uniaxial test. A general return mapping algorithm with an elastic predictor/plastic corrector strategy is used for the numerical implementation of the model.

The model also takes into account strain-rate and temperature dependence. Having the hardening behaviour defined for the reference conditions, the following phenomenological scaling laws are proposed to account for the influence of temperature and strain-rate on the material response:

$$\sigma_{Y_n} = \sigma_{Y_n}^{\star} \left(1 + \alpha_n^m \ln \frac{\dot{\varepsilon}_e^p}{\dot{\varepsilon}_e^{p\star}}\right) + \beta_n^m \left(T - T^{\star}\right) , \tag{3.34}$$

where $\sigma_{Y_n}^{\star}$ are the reference yield strengths at the reference temperature $T^{\star}$ and strain-rate $\dot{\varepsilon}_e^{p\star}$, T and $\dot{\varepsilon}_e^p$ are the actual temperature and strain-rate and α_n and β_n are the strain-rate and temperature dependence parameters, that can be different for tension, shear and compression.

The model also considers isotropic damage for the matrix, using a single damage variable that affects the stiffness of the material. The complementary free energy is defined as:

$$\begin{aligned} \mathscr{G}_m =& \frac{\sigma_{11}^2 + \sigma_{22}^2 + \sigma_{33}^2}{2E_m\left(1 - d_m\right)} - \frac{\nu_m}{E_m}\left(\sigma_{11}\sigma_{22} + \sigma_{22}\sigma_{33} + \sigma_{33}\sigma_{11}\right) \\ &+ \frac{1 + \nu_m}{E_m\left(1 - d_m\right)}\left(\sigma_{12}^2 + \sigma_{13}^2 + \sigma_{23}^2\right) + \mathscr{G}_m^p , \end{aligned} \tag{3.35}$$

where d_m is the damage variable, E_m and ν_m are, respectively, the Young's modulus and Poisson coefficient of the matrix. $\mathscr{G}_m^p$ represents the contribution of the plastic flow to the stored energy. The damage activation is controlled by a paraboloidal surface similar to the one for yielding, but considering the tensile (X_m^t) and compressive (X_m^c) failure strengths instead of the yield strengths. The damage activation is defined as:

$$F_m^d = \phi_m^d - r_m \leq 0 , \tag{3.36}$$

where r_m is an internal variable controlled by a damage evolution law and ϕ_m^d is the loading function

$$\phi_m^d = \frac{3\tilde{J}_2}{X_m^c X_m^t} + \frac{\tilde{I}_1\left(X_m^c - X_m^t\right)}{X_m^c X_m^t} , \tag{3.37}$$

where $\tilde{J}_2$ and $\tilde{I}_1$ are the invariants of effective stress tensor ($\tilde{\boldsymbol{\sigma}}$).

The damage evolution can be measured by the rate of energy dissipation per unit volume:

$$\Xi = \frac{\partial \mathscr{G}_m}{\partial d_m}\dot{d}_m = Y_m \dot{d}_m \geq 0 \ , \tag{3.38}$$

where Y_m is the thermodynamic force that is always positive from the definition of complementary free energy, therefore, to guarantee the condition of irreversibility, the condition $\dot{d}_m \geq 0$ is sufficient. To distinguish loading and unloading situations Kuhn-Tucker conditions must be applied, that can be defined as function of the internal variable and damage activation function.

To avoid mesh dependency issues, Bažant's crack band model [151] was implemented. The computed dissipated energy is regularized by the element's characteristic length (l^e):

$$\Psi_m = \int_0^\infty Y_m \dot{d}_m \, \mathrm{d}t = \int_1^\infty \frac{\partial \mathscr{G}_m}{\partial d_m}\frac{\partial d_m}{\partial r_m} \, \mathrm{d}r_m = \frac{G_{fm}}{l^e} \ , \tag{3.39}$$

where G_{fm} is the energy release rate of the matrix material.

The damage evolution law considered can be defined as.

$$d_m = 1 - \frac{e^{A_m\left(3-\sqrt{7+2r_m^2}\right)}}{\sqrt{7+2r_m^2}-2} \ , \tag{3.40}$$

where A_m is a parameter that is computed by solving Equation (3.39) for each element as function of its characteristic length.

3.2.3 Fibre-matrix interface modelling

The interface between the fibre and the matrix plays a large role in the fracture processes of composite materials, however, despite its large importance, there is still no clear understanding of its properties. Nonetheless, it is usual to model this interface using a linear cohesive law [23, 24]. This cohesive behaviour is usually implemented either with cohesive elements or with the surface based cohesive behaviour provided by Abaqus [141]. In this work, the latter is used.

There are multiple criteria to define damage initiation in the interface. The most simple criterion is the maximum stress criterion:

$$\max\left\{\frac{\langle\tau_1\rangle}{\tau_1^0}, \frac{\tau_2}{\tau_2^0}, \frac{\tau_3}{\tau_3^0}\right\} = 1 \ , \tag{3.41}$$

where τ_i are the stresses in the interface and τ_i^0 the interface strengths. This is a non-interactive criterion. As an interactive criterion the quadratic criterion is usually considered:

$$\left\{\frac{\langle\tau_1\rangle}{\tau_1^0}\right\}^2 + \left\{\frac{\tau_2}{\tau_2^0}\right\}^2 + \left\{\frac{\tau_3}{\tau_3^0}\right\}^2 = 1 \ . \tag{3.42}$$

These are two very simple initiation criteria, however, due to the lack of knowledge of the interfacial behaviour, it is considered that more complex criteria are not necessary. Both presented initiation criteria are using in this, being referenced in each work which one is being used.

Damage evolution is based on an energetic criterion. In this case a linear damage evolution law is used, given by:

$$d = \frac{\delta_m^f \left(\delta_m - \delta_m^0\right)}{\delta_m \left(\delta_m^f - \delta_m^0\right)} , \tag{3.43}$$

where δ_m is the effective separation, δ_m^0 the effective separation at the point of damage initiation and δ_m^f is the effective separation at failure under mixed mode conditions, given by:

$$\delta_m^f = \frac{2G_c}{t^0}; , \tag{3.44}$$

where t^0 is effective traction at damage initiation. Mixed mode conditions are taken into account using the B-K law [152], which can be established in terms of the energy release rate as:

$$G_c = G_{Ic} + AB^\eta , \tag{3.45}$$

where $A = G_{IIc} - G_{Ic}$ and $B = \frac{G_{II}+G_{III}}{G_I+G_{II}+G_{III}}$. the cohesive behaviour is used in this work as a surface interaction using Abaqus' cohesive surfaces [141].

3.3 Single fibre fragmentation test

The single fibre fragmentation test is used to determine important properties used in micromechanical models, such as the fibre strength distribution and the interfacial strength. This test is useful not only to determine the probabilistic strength distribution for the fibre tested but also the matrix-fibre interface properties [17, 27, 38, 153]. This type of testing is useful in understanding the behaviour of composite materials in tension. Using the single fibre fragmentation test it is possible to see multiple fragmentation of a single fibre, study the ineffective and fibre-matrix decohesion lengths, as well as study the yielding of the matrix on the vicinity of a fibre fracture. Based on this phenomena different models have been developed to predict the tensile failure of composite materials [6, 85], and also to take into account the use of different types of fibres in hybrid composites [58, 128, 154]. These models are simplified global load sharing models that have as basis the fact that a broken fibre is still able to carry stress and are able to fracture in locations away from the initial crack plane.

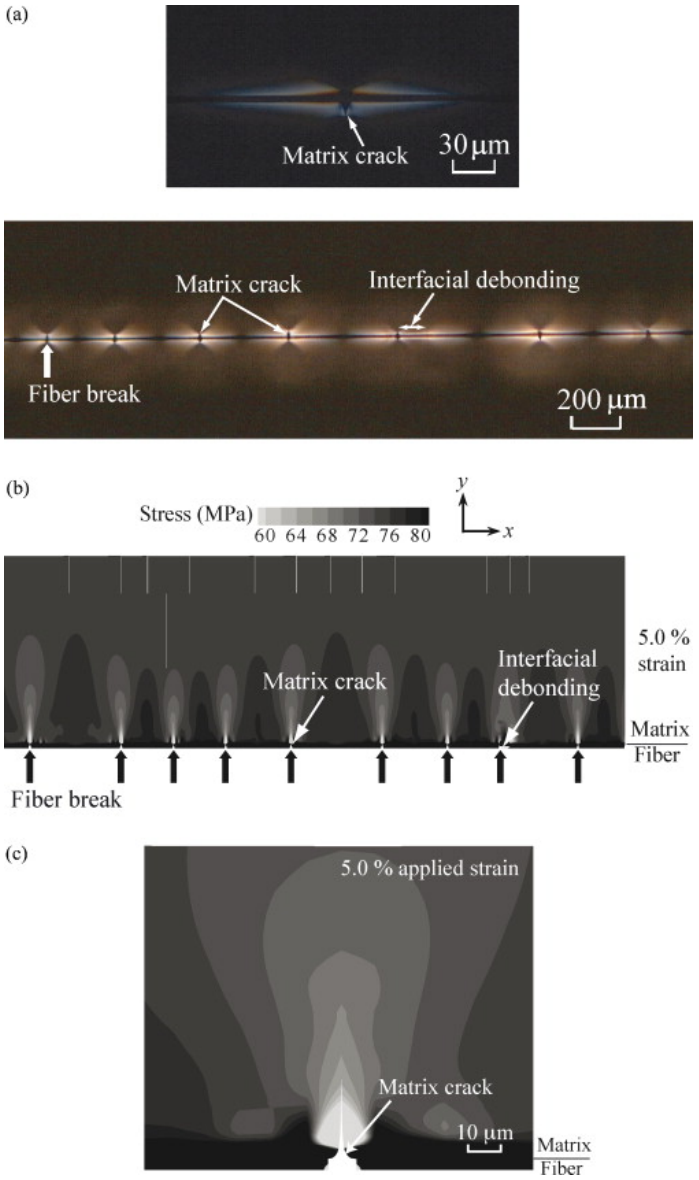

Figure 3.6: Microscopic damage in a single carbon-fibre epoxy composite: (a) experimental results ; (b) simulated result; (c) typical matrix cracking around a fibre break (magnified view of (b)) [17].

Figure 3.6 shows the microscopic damage mechanisms that can be found in single-fibre composites. It is shown that a single fibre breaks in multiple locations, justifying the fact that fibres do not fully lose the load carrying capabilities due to a single fracture. In the the fracture plane it is possible to see that a matrix crack develops. It is also possible to see some plastic region in the matrix in the neighbourhood of the fracture, as well as interfacial debonding. In the same figure it is also possible to see the results from the simulation performed by Nishikawa et al. [17], where the main damage mechanisms are captured

Modelling accurately this type of tests at a scale where the the damage mechanics

can be observed is not easy as it requires a large computational effort and correct constitutive models for the different constituents in the composite material. Nonetheless, there have been works to study this phenomenon [79, 107, 155, 156].

In this section a micromechanical model for this type of test is developed and the effects of the several important parameters are addressed.

3.3.1 Miromechanical model

The model to study the fibre fragmentation phenomenon in single fibre composites is a very simple one. As there is only one fibre, there is no need for a complex RVE generator. Nonetheless, it is necessary to guarantee that the model is able to capture the main damage mechanisms present in these tests: multiple fibre fracture, matrix cracking and fibre-matrix decohesion. The model developed is shown in Figure 3.7.

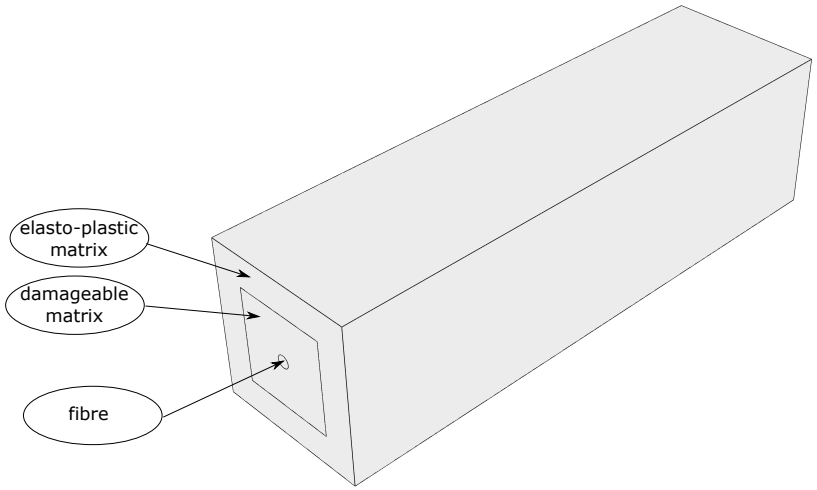

Figure 3.7: Model for the single fibre fragmentation test with the two types of matrix behaviour: elasto-plastic and elasto-plastic with damage.

This model is composed by three parts: the fibre and two matrix parts. The matrix part that surrounds the fibre is considered to have the constitutive behaviour given by the model in Section 3.2.2, which is a plasticity model with damage. The surrounding matrix is considered only to be elasto-plastic and no damage is considered. This was done to prevent having an excessively large RVE while avoiding the full separation of the model due to a matrix crack propagating through the section. The model is 87.5 μm in the transverse direction and has a length of 0.7 mm, and will be the base model used in the following sections.

3.3.2 Effect of the nonlinearity of carbon fibres in the fragmentation phenomenon

AS the developed fibre model is able to capture the nonlinear behaviour of the fibres, the evaluation of the effect of the nonlinearity in the fragmentation process is performed. For this study the T300 carbon fibre was used. It should be noted that all simulations where done with the same model without altering the fibre strength distribution, to avoid changes in the results due to the random fibre strength.

Table 3.2: T300 carbon fibre properties from [21, 22].

Material property	Value
Fibre diameter	
$2R$ (mm)	0.007
Longitudinal Elastic Modulus	
E_1 (MPa)	232000
E_0 (MPa)	222970
S_{111} (MPa^{-2})	-1.049×10^{-10}
Transverse Elastic modulus	
E_2 (MPa)	15000
Poisson's ratio	
ν_{12}	0.2
Shear moduli	
G_{12} (MPa)	15000
G_{23} (MPa)	7000
Coefficients of thermal expansion	
α_{11} (°C^{-1})	-0.7×10^{-6}
α_{22} (°C^{-1})	12×10^{-6}
Critical energy release rate	
G_{ff} (N/mm)	4×10^{-3}
Weibull parameters	
σ_0 (MPa)	3170
m	5.1
l_0 (mm)	25

The properties of the T300 carbon fibres are shown in Table 3.2. E_1 is the longitudinal elastic modulus if the fibres are considered linear and E_0 and S_{111} are the two parameters needed to defined the nonlinear behaviour of the carbon fibre. The matrix and fibre-matrix interface properties used are shown in Tables 3.3 and 3.4. In these simulations the maximum stress criterion was used as initiation criterion for damage in the interface.

Using the properties defined previously and randomly generating a value for the strength of each element within the fibre according to the Weibull parameters, the results in Figure 3.8 were obtained, considering both the fibre linear and nonlinear. In this figure the homogenized stress in the fibre is shown as a function of the applied strain.

It is observed that the results considering the fibres linear and nonlinear are very similar. This was expected due to the nonlinearity in the fibres being very low. Nonetheless, it is possible to see that the stiffness of the fibre is higher at the failure

Table 3.3: Epoxy matrix properties from [23–25].

Material property	Value
Young's modulus	
E_1 (MPa)	3760
Poisson's ratio	
ν	0.39
Coefficient of thermal expansion	
α ($°C^{-1}$)	-58×10^{-6}
Plastic Poisson's ratio	
ν_p	0.3
Critical energy release rate	
Gf_m (N/mm)	0.09
Strengths	
X_{Y_T} (MPa)	94.9
X_{Y_C} (MPa)	220

Table 3.4: Fibre-matrix interface properties from [23, 24, 26].

Material property	Value
Interface maximum strengths	
τ_1 (MPa)	50
τ_2 (MPa)	70
τ_3 (MPa)	70
Interface critical energy release rates	
G_{Ic} (N/mm)	0.002
G_{IIc} (N/mm)	0.006
G_{IIIc} (N/mm)	0.006
Mixed-mode interaction parameter	
η	1.45

point when we consider a nonlinear behaviour. As the results are very close in both models we will only analyse the failure mechanisms in the nonlinear model.

Figure 3.9 shows again the stress-strain behaviour of the nonlinear model, with the linear behaviour considering the initial elastic modulus (E_0) shown in grey. A few specific points of the curve are labelled and will be used to study the failure fragmentation phenomenon. In this figure it is possible to see that are two peaks, each of them representing a fibre fragmentation. In Figure 3.10 it is possible to see the fragmentation phenomenon. The region where the matrix is considered as non-damageable is not shown, only the damageable part is. It is possible to see that two fractures clearly appear in the fibre which causes two cracks in the matrix that grow towards the exterior of the RVE.

The failure of the fibres causes not only matrix cracking but also decohesion between the fibre and matrix, through damage of the interface. This has been observed experimentally (Figure 3.6) and can be captured in the proposed model (Figure 3.11). The decohesion starts in the location of the first fibre fracture (Figure 3.11a) and grows in the longitudinal direction as the loading continues (Figure 3.11b). This growing decohesion will change the stress profile in the fibre and, con-

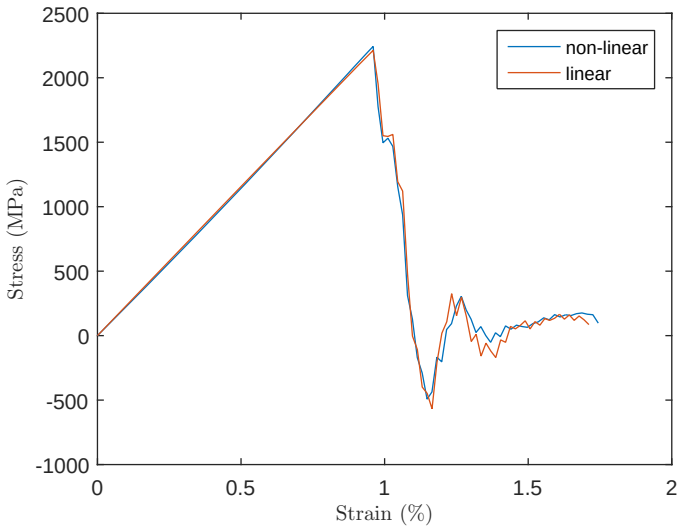

Figure 3.8: Homogenized stress-strain curve for the fibre: considering nonlinear behaviour in blue and linear behaviour in orange.

sequently, its ineffective length. In Figure 3.11c it is possible to see the second fibre fracture, which is the trigger for another decohesion zone. Similar to the first fracture the decohesion grows through time. In Figure 3.11d, that corresponds to point D in the stress-strain curve the fragment between both cracks is almost completely disconnected from the fibre, due to the interface damage. This prevents this part of the fibre from carrying load.

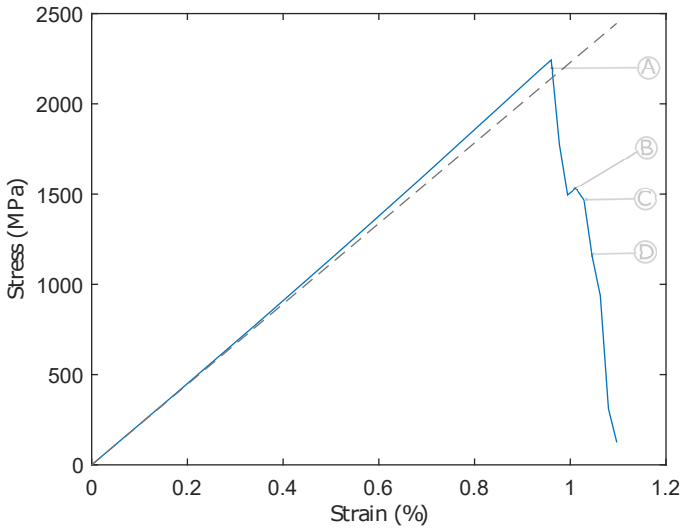

Figure 3.9: Homogenized stress-strain curve for the fibre for the full model.

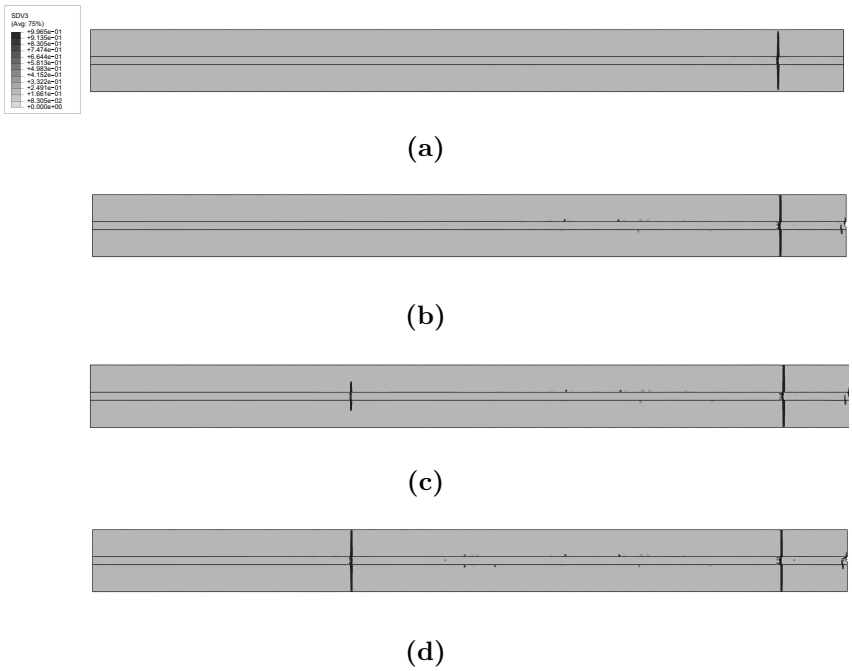

Figure 3.10: Fragmentation and matrix cracking in the full model: A, B, C and D correspond to the same points as in Figure 3.9.

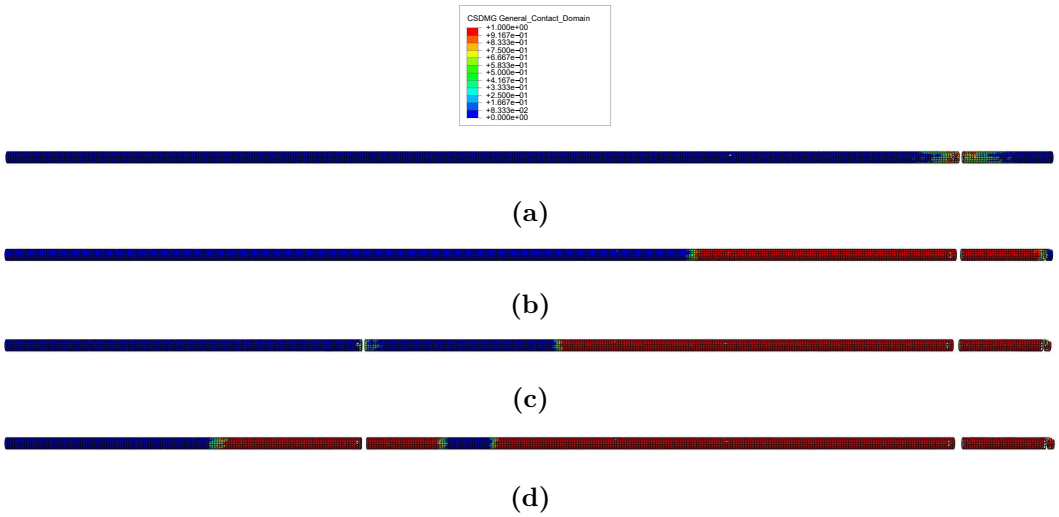

Figure 3.11: Evolution of the fibre-matrix interface damage in the fragmentation process: A, B, C and D correspond to the same points as in Figure 3.9.

Several models for fibre fragmentation [6, 7, 63, 73] are based on the fact that the fibres have an ineffective length where their ability to carry stress is hampered. This region is usually considered to be dependent, mainly, on the fibre-matrix interfacial shear strength. With the model developed here it is possible to determine the stress profile along the fibre direction during all fragmentation process, which was done by homogenizing the stress in all the elements in each fibre section. The stress profiles are shown in Figure 3.12 during different stages of the fragmentation process.

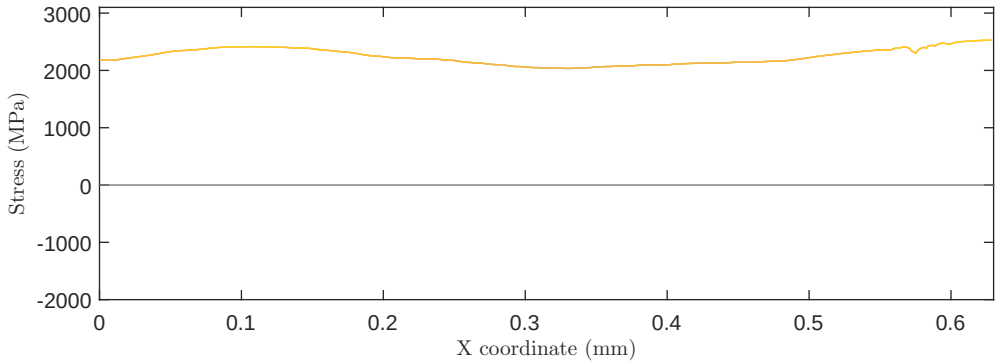

(a) Fibre stress profile prior to the first fracture.

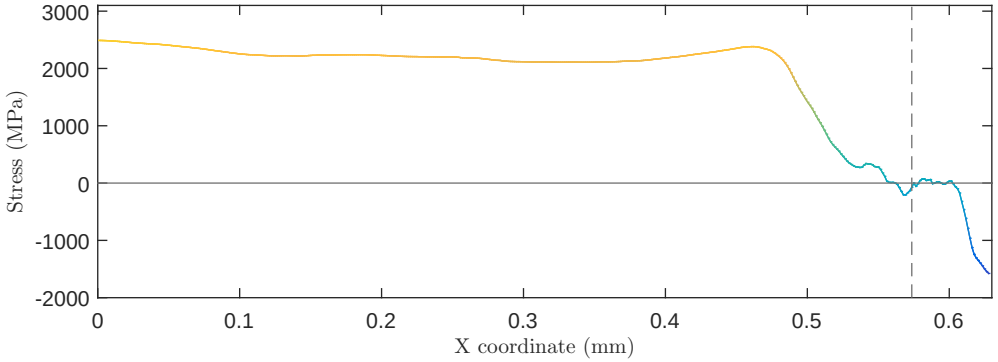

(b) Fibre stress profile after first fracture: point A.

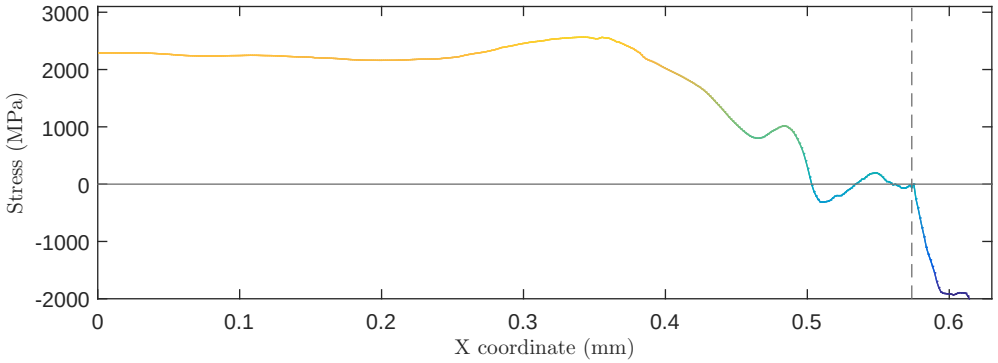

(c) Fibre stress profile after first fracture: between A and B.

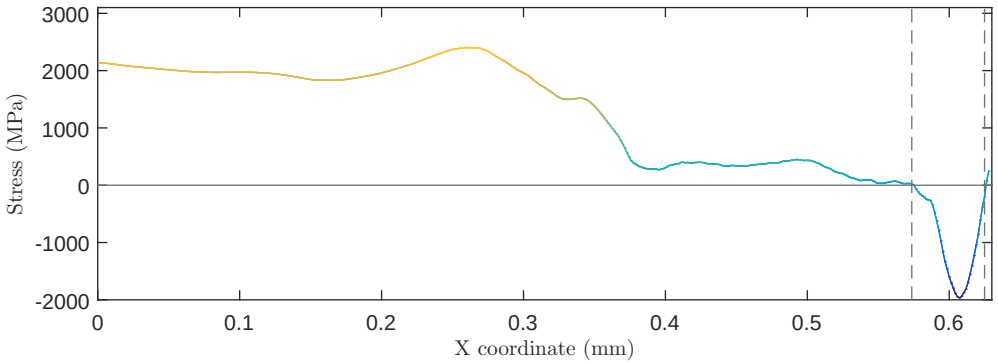

(d) Fibre stress profile after first fracture: point B.

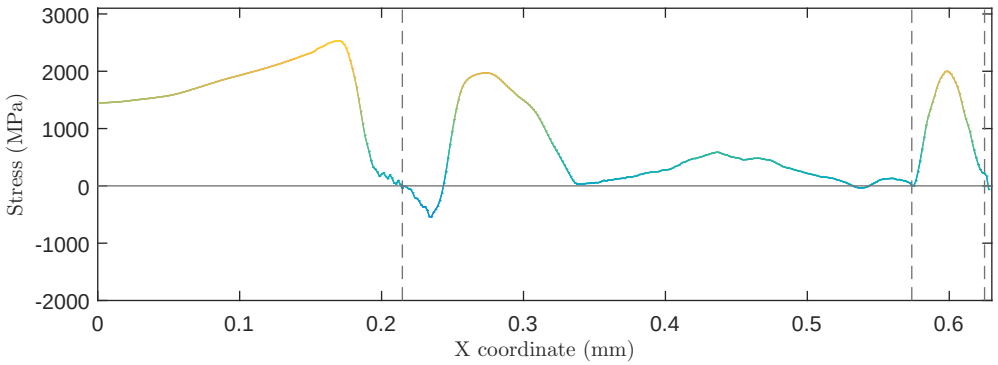

(e) Fibre stress profile after second fracture: point C.

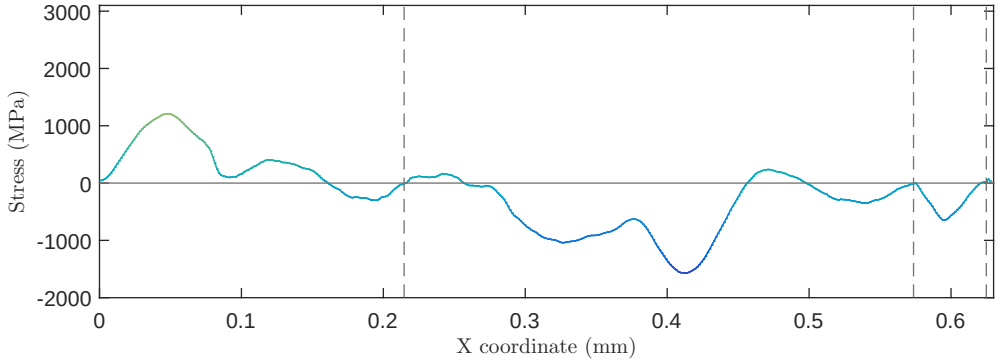

(f) Fibre stress profile after second fracture: point D.

Figure 3.12: Evolution of the fibre stress profile in the fragmentation process: A, B, C and D correspond to the same points as in Figure 3.9.

In Figure 3.12a it is possible to see the stress profile in the fibre immediately prior to the first fracture, which corresponds to the peak load. At $x = 0.58$ mm it is possible to see a small disturbance in the stress profile that corresponds to crack initiation that has not propagated through the section of the fibre. This eventually develops into a fibre fracture as seen in Figure 3.10a. The stress profile at this stage is shown in Figure 3.12b. It is possible to see that near the fracture the fibre loses its load carrying capacity, however, moving away from the fracture it regains this capacity. This stress recovery profile is seen to change due to the evolution of the fibre-matrix decohesion, which can be seen in Figure 3.12c, where the recovery length is higher than in Figure 3.12b. In Figure 3.12d a second crack forms near the boundary of the fibres, which causes a section of the fibre to bee loose and oscillate, however, this is a very small section near the boundary which does not affect the overall fibre behaviour. In Figure 3.12e it is possible to see the second fracture of the fibre developing, at $x = 0.22$ mm, which causes another recovery region, which will grow and connect with the one from the previous fracture causing the fibre to loose all the stress carrying capacity, at which the point we consider the fibre to be fully broken. With this analysis it is possible to conclude that the model is able to capture the main mechanics of the fibre fragmentation process, and that considering the nonlinear behaviour of carbon fibres does not have a large effect on the fragmentation process, at least for the carbon fibre in study, where the nonlinearity is low.

3.3.3 Effect of the fibre-matrix interface properties in the fragmentation process

In this section a comparison study on the effects of changing the interface properties in the fragmentation process is done. To make sure the results are comparable the same RVE with the same fibre strength distribution and fibre and matrix properties are used and different simulations are performed with different fibre-matrix interface properties. The homogenized stress vs strain curves of the fibre are shown

in Figure 3.13. Each of the shown curves represents one simulation with different fibre-matrix interface properties (Table 3.5). For these simulations new RVEs were generated, different from the ones in the previous section, but are all equal between each other, including the same fibre strength distribution.

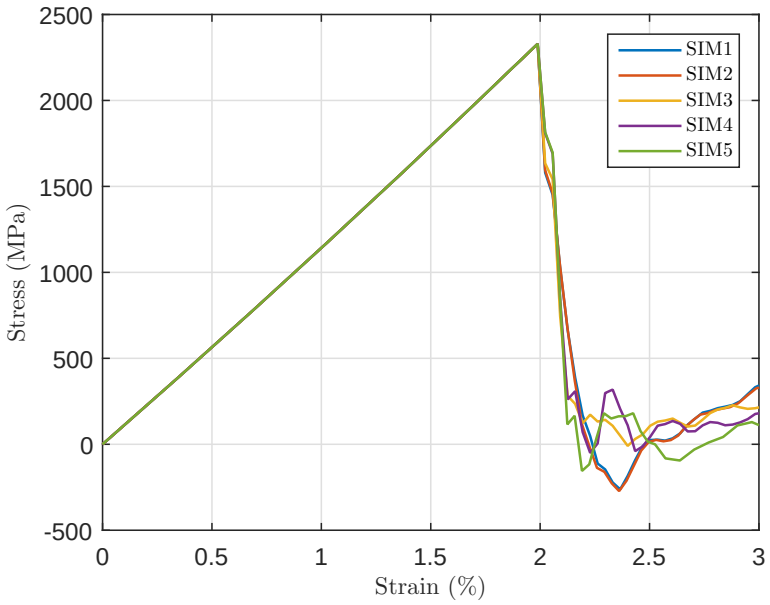

Figure 3.13: Homogenized stress in the fibre in the single fibre fragmentation simulations with different fibre-matrix interface properties (see Table).

Table 3.5: Fibre-matrix interface properties used in the single fibre fragmentation simulations.

Simulation	Initiation Criterion	τ_I (MPa)	τ_{II} (MPa)	G_{Ic} (N/mm)	G_{IIc} (N/mm)
SIM1	Maximum stress	50	70	0.002	0.006
SIM2	Quadratic stress	50	70	0.002	0.006
SIM3	Quadratic stress	50	70	0.002	0.012
SIM4	Quadratic stress	78.5	110	0.002	0.006
SIM5	Maximum stress	78.5	110	0.002	0.006

From the stress-strain curves shown it is possible to see that changing the interface properties changes the behaviour of the model, but, as expected, only after the first fibre fracture, as there is no damage initiation in the interface prior to the first fibre fracture.

In section 3.2.3 two different initiation criteria were presented, the maximum stress criterion and the quadratic criterion. The results on the previous section were obtained using the maximum stress criterion, therefore, it should be useful to understand if changing to the quadratic criterion affects the results. This is shown in simulations SIM1 and SIM2 for the baseline interfacial properties used in the previous section. As it is possible to see in Figure 3.14 the fibre-matrix separation is very similar in both cases for the same applied strain after the first fracture. This can be expected as in this process the interface is loaded almost purely in mode

II.

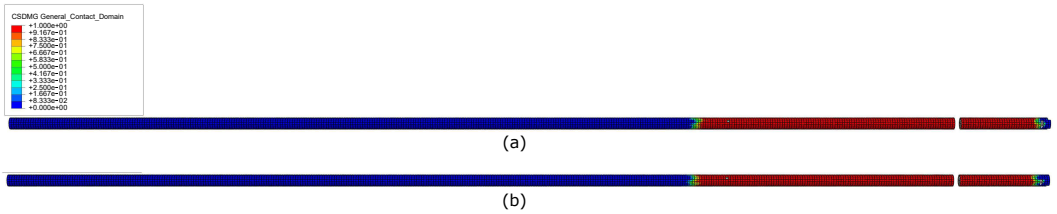

Figure 3.14: Comparison of the interfacial damage variable at the same applied strain using the maximum stress criterion (a) and the quadratic criterion (b).

In simulation SIM3 the G_{IIc} of the interface was doubled to see what was the effect on the fracture process. In Figure 3.15a) it is possible to see that increasing the critical energy release rate reduces the decohesion extent for the same applied strain (as in Figure 3.14), this causes the stress recovery length to be lower and the overall fibre-stress higher, allowing a second fracture to occur in the fibre, which was not verified in the first two simulations. Two new cracks appear in the fibre and afterwards the interfacial damage propagates throughout all the fibre causing the full separion between the fibre and the matrix.

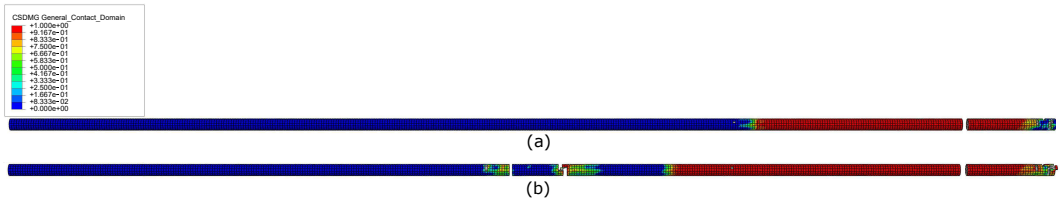

Figure 3.15: Comparison of the interfacial damage for simulation SIM3 at two applied strains: (a) same strain as in Figure 3.14; (b) at second fibre fracture.

Similarly to increasing the mode two energy release rate, increasing the shear strength also reduces the fibre recovery length and allows the fibre to break multiple times for simulations SIM4 and SIM5. In Figure 3.16 it is possible to see that there is a clear reduction in debonding length when compared to the baseline properties (Figure 3.14). In addition, and as previously stated, the differences between the maximum and quadratic stress criteria are reduced. Nevertheless, the fragmentation process is very similar to the one previously analysed, where after a second fibre fracture appears the decohesion propagates throughout the fibre, leading to the full separation of the fibre from the matrix.

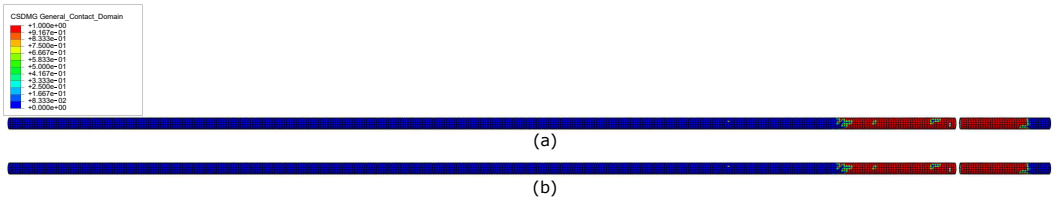

Figure 3.16: Comparison of the interfacial damage for simulations: (a)- SIM4 and (b)- SIM5; at the same applied strain as in Figure 3.14.

From the shown images it is possible to see that the decohesion profiles differ

from simulation to simulation, however, what determines the fracture process are the actual stresses in the fibre, which are affected by the interfacial debonding. The stress profile in the fibre after the first fracture (at the same applied strain) for all the simulations are shown in Figure 3.17. It is clear that for simulations SIM1, SIM2 and SIM3 the ineffective length of the fibre is higher than in SIM4 and SIM5, but are very similar between each other.

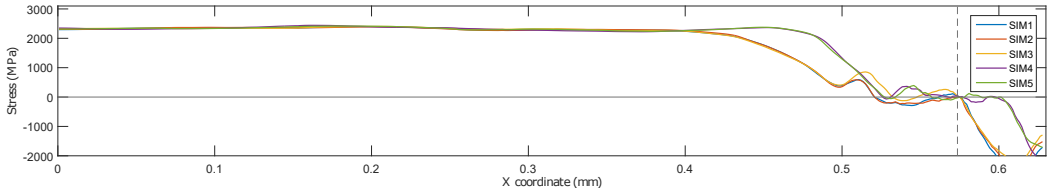

Figure 3.17: Comparison between the stress profile in the fibre for all the simulations at the same applied strain (post first fibre fracture).

After the first fracture the stress profiles for SIM1, SIM2 and SIM3 are very similar, as the interfacial failure strengths are the same, however, for SIM3 there is an increase in the mode II energy release rate, therefore, the propagation of the decohesion should differ. This is shown in Figure 3.18, which shows the stress profile prior to the appearance of the second fibre fracture (in the cases that it occurs). In this figure it is possible to see that SIM1 and SIM2, and SIM4 and SIM5, have very similar profiles between each other and that SIM3 has a stress profile in between both. This explains the fact that the threee latter simulations fractured more than once while the first two only fractured once.

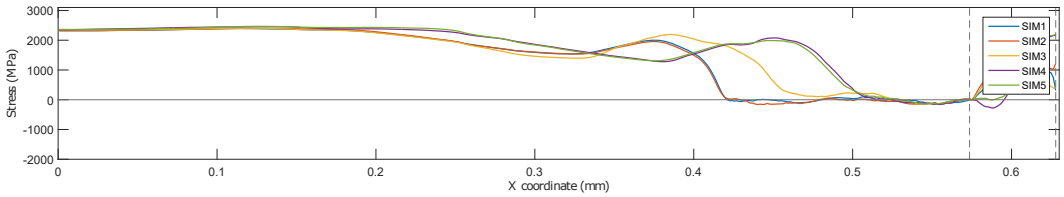

Figure 3.18: Comparison between the stress profile in the fibre for all the simulations at the same applied strain (before second fibre fracture).

From these results of the single fibre fragmentation process it is possible to conclude that the phenomena that occur in this process are captured in the simulations, including the debonding and its effect on the ineffective length. It was also shown that changing this properties clearly modifies the stress recovery profile in the fibre as well as the fragmentation process. This effect will likely also occur in multi-fibre composites, therefore, affecting the failure process.

3.4 Fibre pushout test

The single-fibre push-out test (see Figure 3.19) is a micromechanical test used characterize the fibre–matrix adhesion of composites. During a single-fibre push-out experiment an individual fibre within a thin composite sample (thickness below 100

μm), is loaded by a diamond indenter tip. With increasing load an evolution from crack-initiation, fibre–matrix debonding to fibre push-out occurs. The specimen is usually supported by a metallic grid, allowing the fibres to get pushed out. During the experiment, the force–displacement curve is recorded, which allows to extract values to quantify the fibre–matrix adhesion.

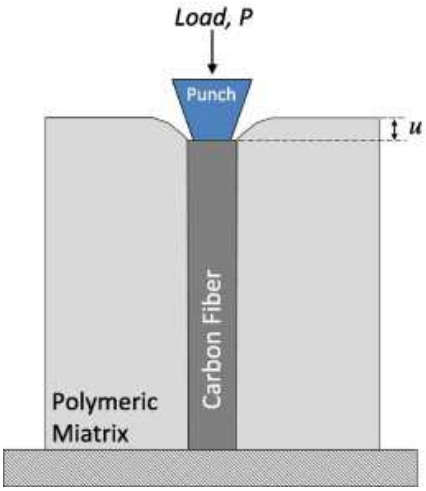

Figure 3.19: Schematic representation of the fibre pushout test (adapted from [18]).

Multiple authors have published work on obtaining the interface properties from the pushout test [18, 19, 157] using different techniques and modelling strategies. For polymer composites it is usually considered that the force-displacement is initially linear, but it becomes non-linear during the test. This is often interpreted as crack initiation followed by crack growth [18, 157], however, it has been shown that for some composites this is not due to crack growth but due to plasticity in the matrix before failure of the interface [19]. This complex mechanism affects the stress-distribution around the fibre and therefore the loading of the interface, which is not taken into account in most modelling strategies.

In this section a fully 3D simulation of the pushout test is done using the framework presented in the previous sections. In this type of tests there is an influence of the surrounding fibres in the stress state in the interface, therefore, it was considered that an random fibre distribution should be used. In addition, the matrix was modelled using the elasto-plastic damage model for epoxy matrices presented in Section 3.2.2. In this section we aim to simulate the pushout tests performed in RTM6 and to determine the best cohesive properties in that material system.

The experimental results shown here were performed in Université Catholique de Louvain-la-Neuve, Belgium. The tests were conducted in specimens with a thickness of 50 μm and 2 and 3mm in the remaining directions. These specimens are glued into a metallic grid with a grid size of 35μm that allows the fibres to be pushed out.

Figure 3.20 it is possible to see a post-mortem micrography of a pushed fibre. From analysing these images it is possible to see that the fibre is clearly separated

from the matrix and the separation as occurred in the interface, as there is no matrix adhered to the pushed fibre. In Figure 3.20a it is possible to see a small plastically deformed region of the matrix that surrounds the pushed fibre. This region is whiter than the remaining matrix material.

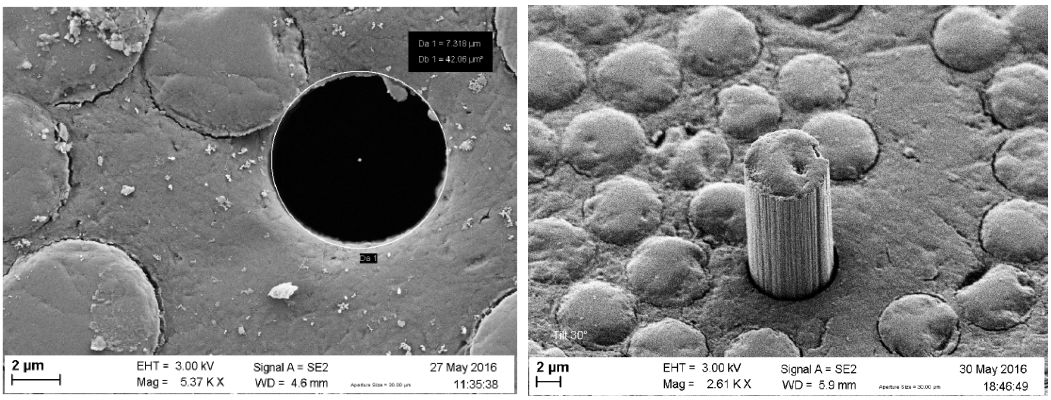

(a) **(b)**

Figure 3.20: Pushed out fibre using a nanoindenter: a) top view; b) bottom view (courtesy of Dr. Jérémy Chevalier).

Figure 3.21 shows different experimental results obtained for RTM6 pushout tests. The results shown in blue and in yellow were performed under load control, while the result in orange was obtained from Jagger et al. [19] using displacement controlled loading at a rate of 40 nm/s. These results will be used to calibrate the interface properties for an RTM6 carbon fibre material system, using a micromechanical model.

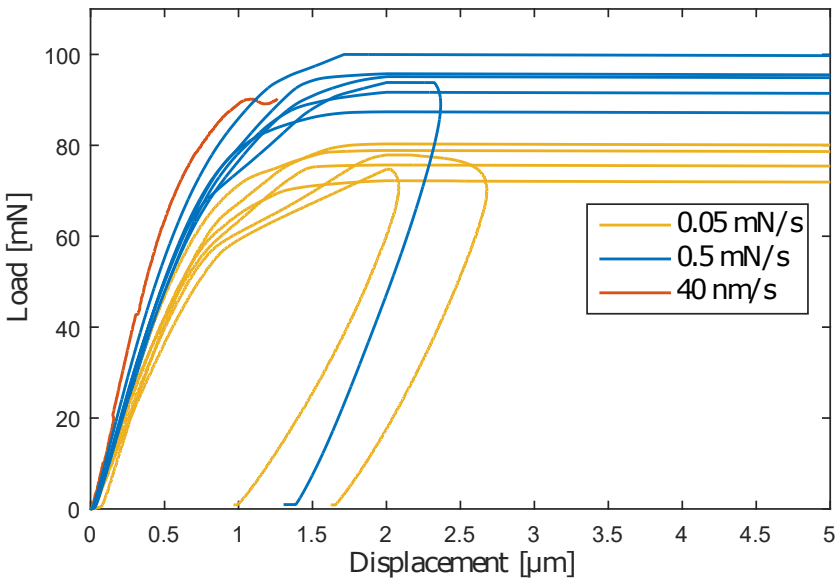

Figure 3.21: Experimental results of the fibre pushout tests: in blue and yellow - experimental results provided by Jeremy Chevalier at two force rates; in orange - experimental result from [19].

It should be noted that the tests were performed in load control and the plateaus seen in the graphs are not plasticity and signal the actual separation of the fibre from the matrix.

3.4.1 Micromechanical model

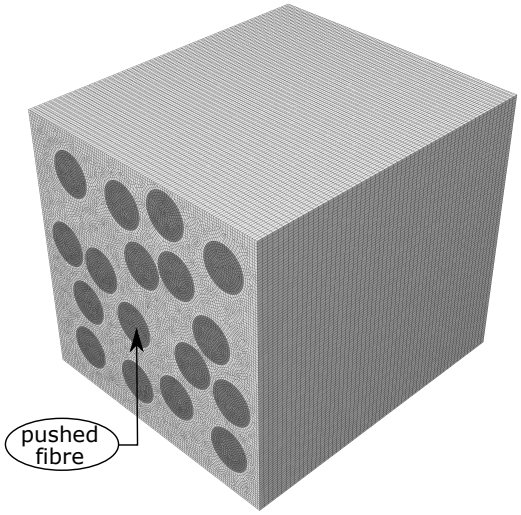

Figure 3.22: Micromechanical model of the pushout test with a random fibre distribution.

The simulation of the pushout test in conditions that are appropriate to calibrate a 3D cohesive law for the interface is performed. It was considered that the distance between fibres should impact the results and, therefore, a random fibre distribution with the desired volume fraction, in this case 40%, as used. The fibre closer to the middle of the RVE was chosen to be pushed, as shown in Figure 3.22. To push the fibre, the indenter was not explicitly modelled but a displacement/force was applied to the surface of the chosen fibre. The grid that supports the specimen was not modelled explicitly, nevertheless, adequate boundary conditions were applied to simulate its effect. The boundary conditions were applied in the side surfaces of the RVE. It was considered that in the surfaces there was no displacement in the fibre direction and neither in the direction perpendicular to the respective surface, therefore, approximating the effect of the grid (in the fibre direction) and the remaining part of the specimen in the transverse directions. A simulation was also performed with a homogenized part surrounding the RVE but the results did not change, therefore, the simplified model was considered.

The fibres were considered transversely isotropic linear elastic, with the properties shown in Table 3.6, as this is a matrix and fibre-matrix interface dominated phenomenon and no fibre failure is expected. The matrix was modelled using the model presented in Section 3.2.2, with properties shown in Table 3.7 , but no damage was considered, only plasticity, whose calibration curves are shown in Figure 3.23. The interface was modelled using Abaqus [141] surface-based cohesive behaviour, as presented in Section 3.2.3.

Table 3.6: Carbon fibre properties used in the pushout simulations.

Material property	Value
Fibre diameter	
$2R$ (mm)	0.007
Elastic moduli	
E_1 (MPa)	275000
E_2 (MPa)	19500
Poisson's ratio	
ν_{12}	0.28
Shear moduli	
G_{12} (MPa)	70000
G_{23} (MPa)	5740

Table 3.7: RTM6 epoxy matrix properties used in the pushout simulations.

Material property	Value
Young's modulus	
E_1 (MPa)	3000
Poisson's ratio	
ν	0.34
Plastic Poisson's ratio	
ν_p	0.3

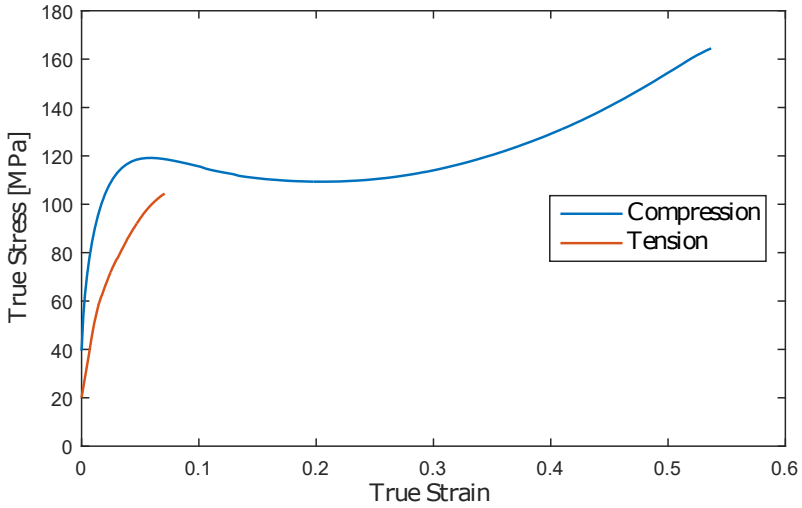

Figure 3.23: True stress versus true plastic strain curves used for the plasticity model for RTM6.

3.4.2 Simulation results

In this section the results of the simulations of the pushout test using the micromechanical model presented earlier are shown. The aim of this study was to address the fibre-matrix interface properties to have realistic values that can be used in the composite simulations. In Figure 3.24 the results of the several simulations, whose interface properties can be seen in Table 3.8, are shown.

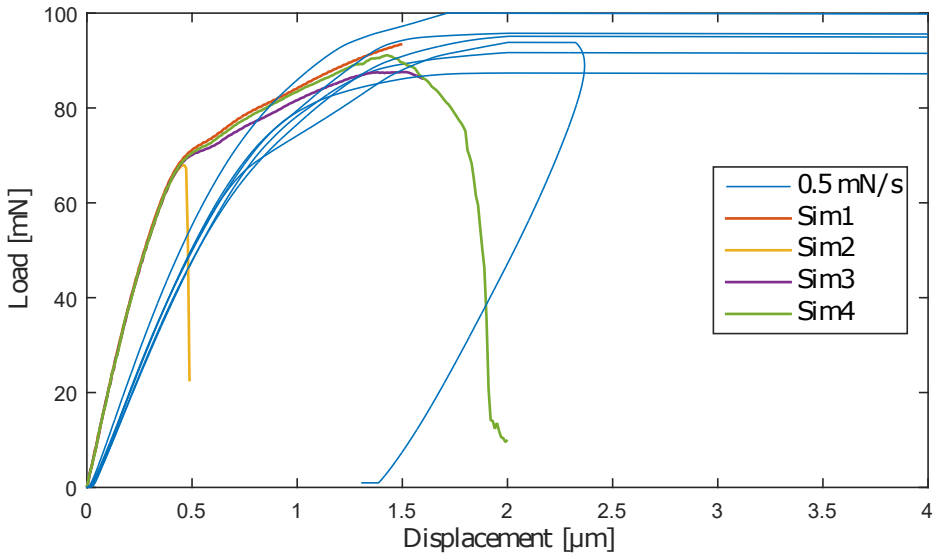

Figure 3.24: Comparison between the numerical simulations and the experimental results for the pushout test.

To establish a baseline result a simulation was performed with a perfect tie between the fibres and the matrix. The result from this simulation is shown in Figure 3.24 in orange (Sim1). It is possible to see that the overall shape of the curve is well captured, and that there is a high nonlinear behaviour due to plasticity in the matrix. Nonetheless, it is possible to see that there is a discrepancy between the model stiffness and the actual stiffness of the test. This was considered to be due to some issues in measuring the displacement in the nanoidentation machine, which is highly affected by temperature, as well as the compliance introduced in the system by the glue used to glue the specimen to the grid. Another issue that can help explaining the difference in stiffness is the displacements due to bending of the specimen, which are not captured in the simulations, as the model is smaller than the actual specimen. As the objective of this study is to address the interface properties, and the stress fields are very localized in the surrounding area of the pushed fibre (see Figure 3.25), it was considered that the difference in the stiffness would be disregarded.

Simulation 2 in yellow in Figure 3.24 uses the fibre-matrix interfaces properties typical of micromechanical simulations [23, 24, 58], which are normal failure stress equal to 50 MPa and shear failure stress equal to 70 MPa, being that the toughnesses are, respectively, 0.002 N/mm and 0.006 N/mm. From the analysis of the load-displacement curves it is seen that the initiation and propagation of the interfacial

Table 3.8: Fibre-matrix interface properties used in the fibre pushout simulations.

Simulation	Initiation Criterion	τ_I (MPa)	τ_{II} (MPa)	G_{Ic} (N/mm)	G_{IIc} (N/mm)
SIM1	Quadratic stress	∞	∞	-	-
SIM2	Quadratic stress	50	70	0.002	0.006
SIM3	Quadratic stress	50	110	0.002	0.0096
SIM4	Quadratic stress	78.5	110	0.002	0.006

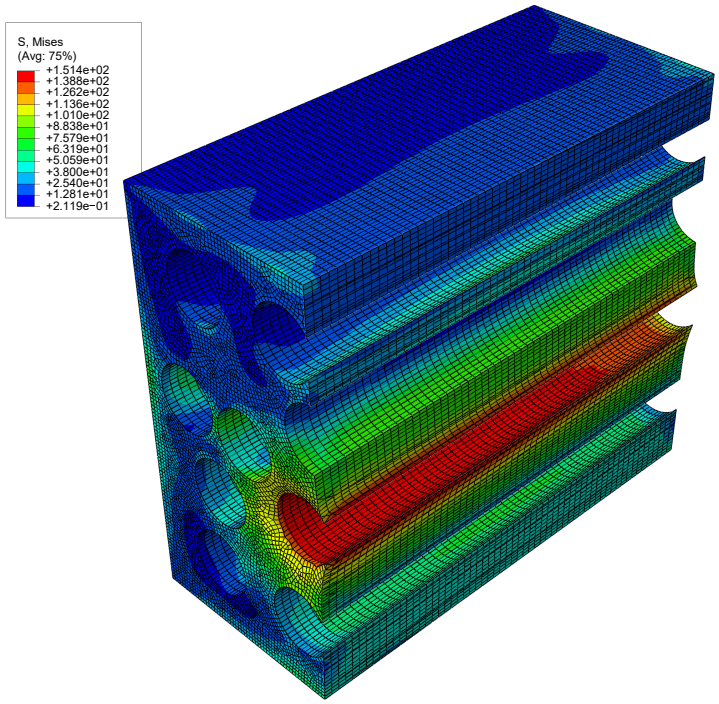

Figure 3.25: Von Mises stress in the matrix in the pushout test with no interface damage.

damage occur sooner than expected, making the results inaccurate. To tackle this early failure, both the shear failure stress and toughness were increased for 110 MPa and 0.0096 N/mm, respectively. The results with these properties are shown in purple in Figure 3.24. These results are closer to what the real failure load in the nanoindentation tests, however, no full separation of the fibre and matrix was observed (see Figure 3.26). This can be attributed to the higher toughness of the interface, which prevents the propagation of the decohesion. It was also observed that the damage initiation was too premature and was due to normal stresses in the lower part of the specimen.

With these results in mind a last simulation was performed, increasing the normal failure stress to 78.5 MPa and reducing the shear toughness to the original value. This simulation is shown in green in Figure 3.24. As it is possible to see the results are in the failure range seen in the experimental results and there is a full decohesion of the interface, as seen in the experiments. The damage still initiates in the bottom part of the specimen, however, when a critical load is achieved, a second decohesion starts in the top part of the specimen that grows and meets the one that started in the bottom leading to the full separation of the matrix from the fibre. The final

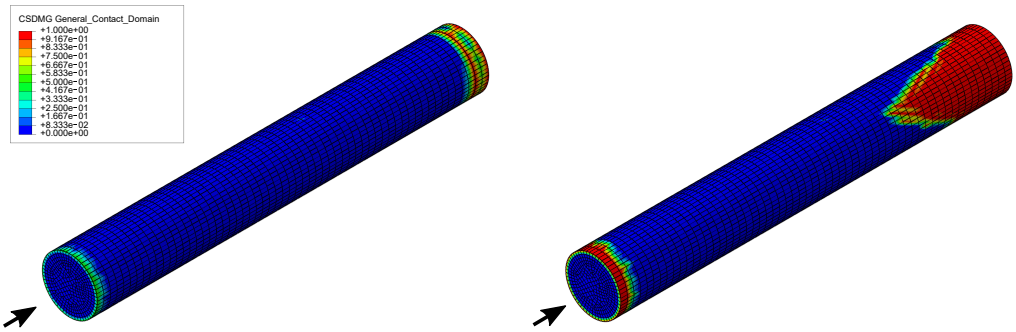

Figure 3.26: Interfacial damage at initiation on the left and at the end of the simulation on the right (pushing direction represented by the arrow).

deformed state of the region near the pushed fibre can be seen in Figure 3.27, where it is possible to see the full separation of the fibre and matrix

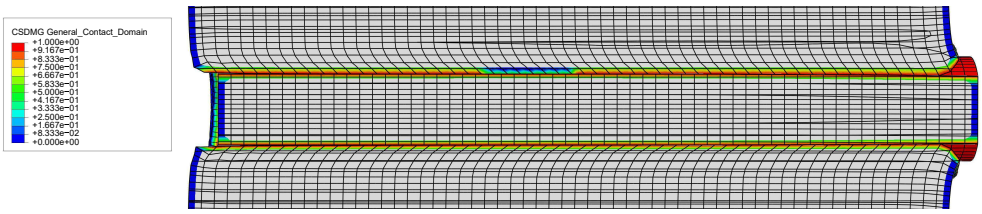

Figure 3.27: Interfacial damage and permanent deformation in the matrix near the pushed fibre at full separation.

3.5 Composite micromechanical simulations

In the previous sections studies were performed on specific phenomena that help in understanding the general failure of composite materials as well as validate the material models and calibrate material properties. Nevertheless, the focus is on understanding the tensile failure behaviour of composite materials and the effect of fibre hybridization in this behaviour. To do so, composite level micromechanical simulations have to be performed, which is the focus of this section.

3.5.1 Non-hybrid composites

3.5.1.1 AS4 non-hybrid composite

Table 3.9: AS4 carbon fibre properties from [21, 22, 27].

Material property	Value
Fibre diameter	
$2R$ (mm)	0.007
Young's moduli	
E_1 (MPa)	234000
E_2 (MPa)	15000
Poisson's ratio	
ν_{12}	0.2
Shear moduli	
G_{12} (MPa)	15000
G_{23} (MPa)	7000
Coefficients of thermal expansion	
α_{11} ($^{\circ}C^{-1}$)	-0.5×10^{-6}
α_{22} ($^{\circ}C^{-1}$)	15×10^{-6}
Critical energy release rate	
G_{ff} (N/mm)	4×10^{-3}
Weibull parameters	
σ_0 (MPa)	4275
m	10.7
l_0 (mm)	12.7

This section is dedicated to the study of the tensile failure of the non-hybrid composite composed of AS4 carbon fibres, whose properties are shown in Table 3.9.

The fibre strength determined for each element of the fibre is function of the length (L) considered, i.e, the length of the RVE in the fibre direction. To study the effect of the length on both the fibre strength and in the failure mechanisms, RVEs having the same fibre distribution but with different lengths were generated. Another RVE, with a length equal to 15 times the fibre radius, was generated without cohesive surfaces between the fibres and the matrix and, therefore, assuming a perfect bond between these. All these RVEs have dimensions in the direction perpendicular to the fibres equal to 15 times the fibre radius. The stress-strain curves of these non-hybrid RVE's subjected to tensile loadings in the fibre direction are shown in Figure 3.28.

From the presented results it is observed that the stress-strain curves are very similar for the RVEs with a length of 15 and 30 times the fibre radius. However, the RVE with a length of 45 times the fibre radius failed prematurely, which can be related with random events in the generation of the tensile strength of the elements. The RVE modelled without the cohesive surfaces at the fibre-matrix interface shows similar failure strength as those with cohesive surfaces, however, using cohesive surfaces represent more accurately the failure mechanisms as the decohesion of the fibre-matrix interface is more realistically captured. In the RVEs with cohesive

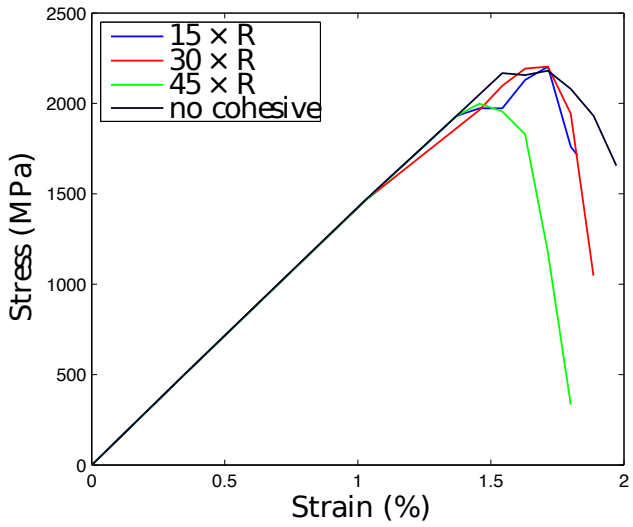

Figure 3.28: Comparison of the tensile behaviour of AS4 non-hybrid composite for different RVE's.

surfaces, the decohesion is observed causing the separation of the fibre from the matrix (Figure 3.29d). For the RVE without the cohesive surfaces, the matrix that surrounds a broken fibre is fully damaged, which creates a separation of both constituents, as the elements that are fully damaged are removed from the model. This, although leading to similar results, is inaccurate as the separation of the fibre from the matrix most often occurs not due to the cracking and failure of the matrix but due to failure of the interfaces. In Figure 3.29a the strength distribution of an AS4 fibre is presented. It can be observed that the tensile strength is randomly distributed simulating the presence of initial flaws or defects.

Analysing the failure locations in multiple simulations, it is observed that the main factor controlling the location of fibre failure is not stress concentrations but the location of the defects, that are simulated as elements with lower failure strength. This is seen not only to dominate first fibre failure but also the subsequent failures.

It has been observed that when a fibre fails, the fibre unloads suddenly causing a dynamic effect. The propagation of the stress wave after a fibre break can induce compression stresses in the fibres, which is captured by the model. This makes the fibre lose the load carrying capacity in some of its length, the ineffective length. This effect is captured by the model, as shown in Figure 3.29. After a fibre breaks a crack in the matrix surrounding this broken fibre can appear, as shown in Figure 3.30a. The crack progression is hampered by the intact surrounding fibres, that are affected by stress concentrations as shown in Figure 3.30b. These stress concentrations act in a small region surrounding the broken fibre.

The first fibre failure is proceeded by the failure of other fibres. As previously stated, the break location is determined by flaws in the fibres. From the performed analysis it is seen that the majority of the fibres did not fail in the same plane,

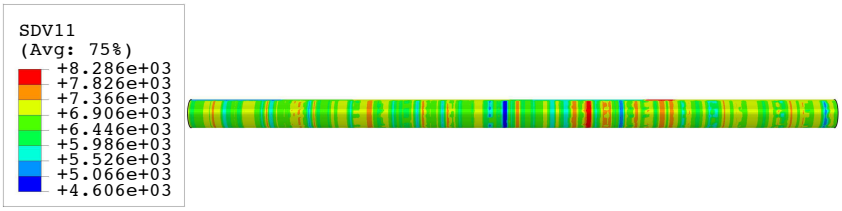

(a) Distribution of fibre strength

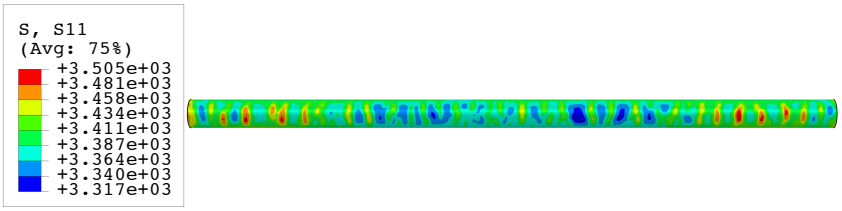

(b) Stress distribution prior to fibre failure

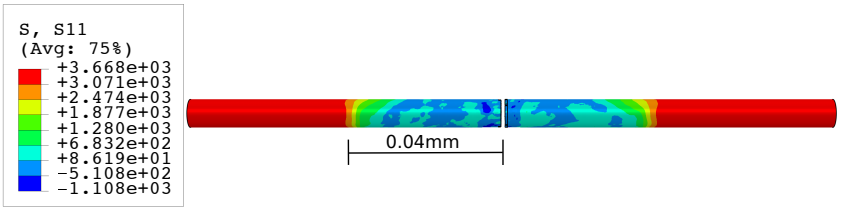

(c) Stress profile after fibre failure

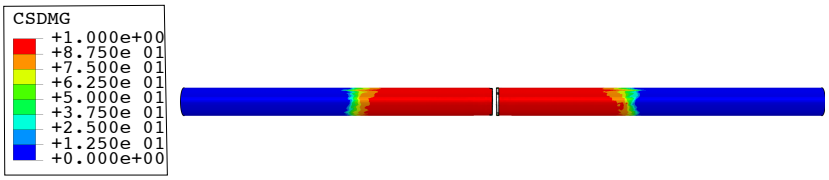

(d) Interfacial damage after fibre failure

Figure 3.29: Failure process in an AS4 carbon fibre.

leading to the formation of a disperse clusters instead of a co-planars. This type of cluster development has been reported previously in the literature [4, 73]. The locations of fibre breaks are represented in Figure 3.31 and it can be observed that many fibres are broken in multiple locations.

From the shown analysis it is argued that the model captures the main failure mechanisms of polymer composites in longitudinal tension reported in the literature.

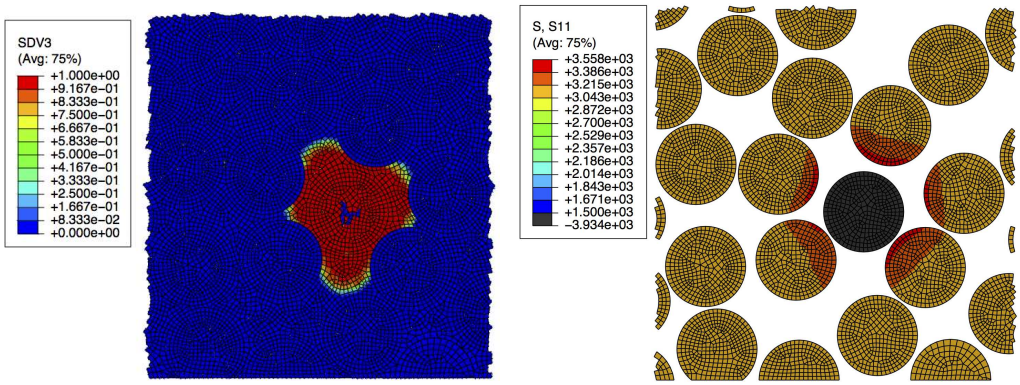

(a) **(b)**

Figure 3.30: **(a)** Matrix crack surrounding a broken fibre (red regions with SDV3 equal to 1); **(b)** Stress concentrations in intact fibres surrounding a broken one (in black).

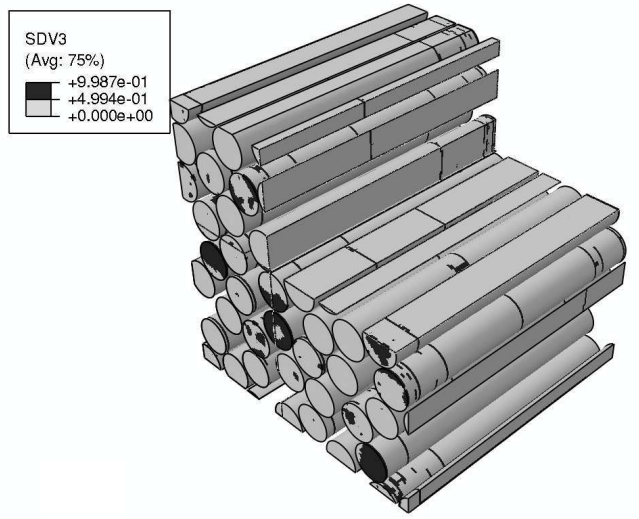

Figure 3.31: Location of fibre breaks after the failure of the composite: fracture zones represented in black.

3.5.1.2 Effect of the nonlinearity of carbon fibres for T300 carbon fibres

Similarly to what was done in Section 3.3, the influence of the nonlinearity of carbon fibres is studied, this time at the composite level. Due to the lack of information on the nonlinear behaviour of the AS4 carbon fibres, in this section the T300 carbon fibres, whose properties are shown in Table 3.2, will be used. In this section, three RVEs with different fibre and fibre strength distributions were created and used to with linear and non-linear behaviour, being that for each RVE the linear and nonlinear simulations were performed using the same exact fibre strength distribution.

In Figure 3.32 the results of the simulations of the three RVEs considering the fibres linear and nonlinear are shown. It is possible to see that the nonlinear models

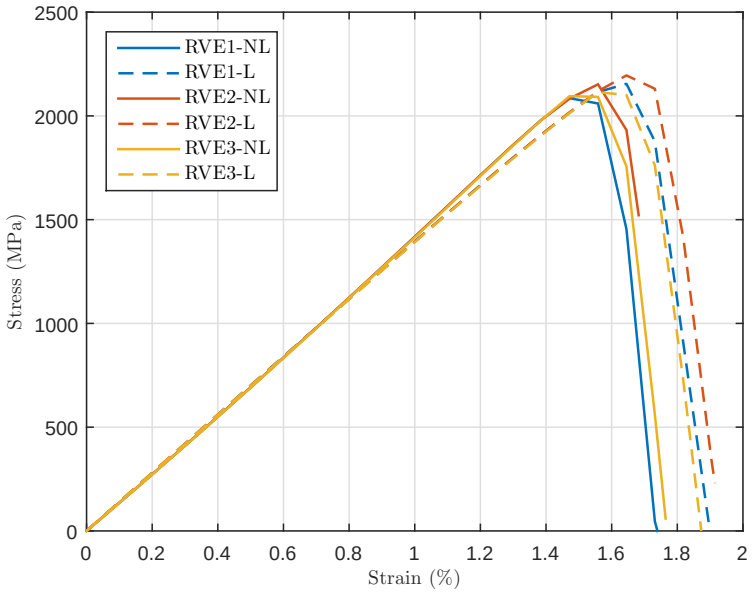

Figure 3.32: Comparison of the tensile behaviour of T300 non-hybrid composite for different RVEs, considering the fibres linear and nonlinear.

have a failure strain lower than their linear counterparts, but at very similar stress. This can be explained as the stress in the fibre, at the later stages of the simulations are higher for the nonlinear models than for the linear ones. Allied to this fact and since a maximum stress criterion is used to control the failure of the fibres, the fibres tend to fail at lower strains.

The difference in fibre fracture strains is easily seen if we plot, for the same strain, the broken fibres and the locations at which they break. This is shown in Figure 3.33 for the simulations of the RVE1. Analysing both figures it is possible to see that for the same strain more fibres are broken in the nonlinear model than in the linear one, which explains the failure at lower elongations when considering the nonlinear behaviour of carbon fibres.

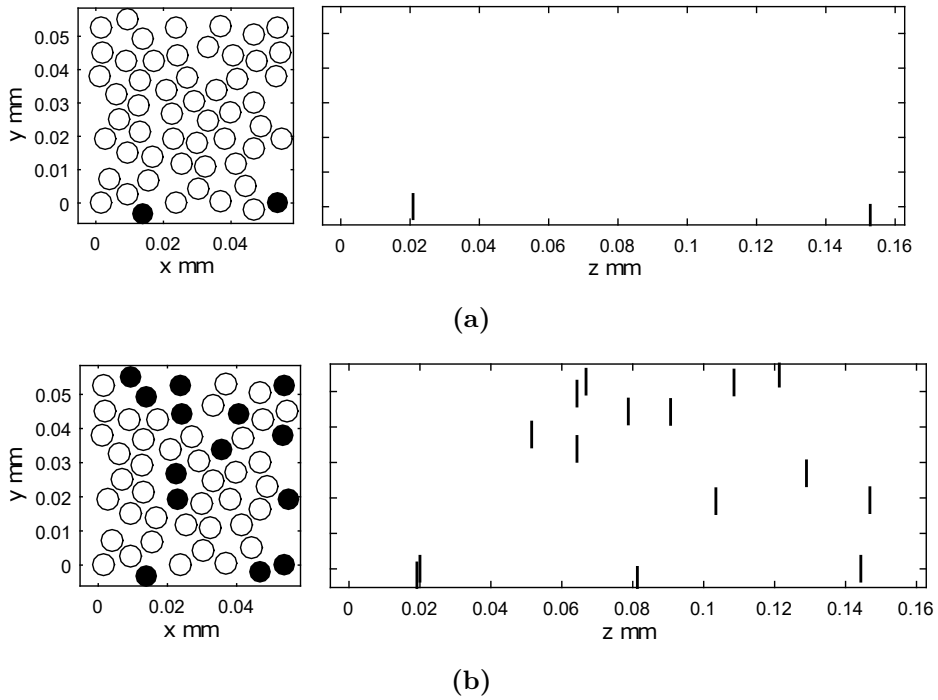

Figure 3.33: Fibre break locations at an applied strain of 1.55%: (a) for the linear RVE1; (b); for the nonlinear RVE1.

3.5.1.3 Effect of hydrostatic pressure

Unidirectional composites exhibit high mechanical properties when loaded along the fibre direction. However, a combined state of stress in the materials exists in most practical cases. One particularly interesting stress state is the combination of the simple unidirectional cases and superimposed hydrostatic pressure [158–164]. The combination of longitudinal tension with hydrostatic pressure is an important loading scenario as it has been shown that, not only the tensile strength of a composite materials, but also the failure mechanisms and fracture vary with the imposed pressure [159, 160, 163]. It is observed that at ambient pressure, longitudinal failure of composites is dominated by fibre fracture, generalized splitting and pullout, however, when an hydrostatic pressure is superimposed, the fracture surface changes and a clean break is observed. In addition, a generalized decrease in strength with the increase of the imposed hydrostatic pressure is observed [161, 163].

In this section, the developed micromechanical framework is used to study the effect of hydrostatic pressure in the failure of a carbon fibre reinforced composite. To do so, the RVEs generated for the previous section (for the T300 carbon fibres with non-linear behaviour) are used with the addition of the superimposed hydrostatic pressure to the model. The hydrostatic pressure was applied to the transverse faces of the RVE in a smooth step and was kept constant throughout the tensile loading. Different hydrostatic pressure were considered, ranging from 0 to 300 MPa.

The stress-strain behaviour of the RVEs for the different imposed pressures are

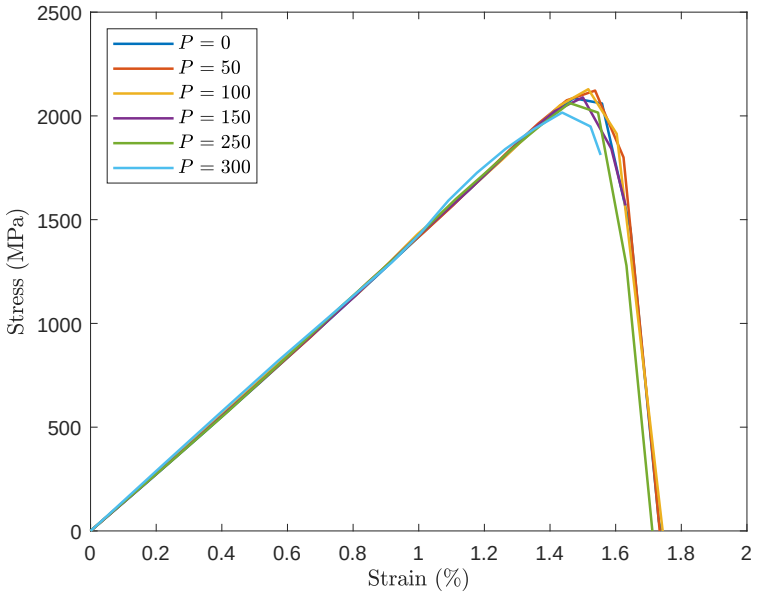

Figure 3.34: Stress-strain diagrams for a T300 non-hybrid composite subjected to different hydrostatic pressures.

shown in Figure 3.34. In addition, in Figure 3.35, the strength and failure strain of the material are shown as a function of the imposed pressure.

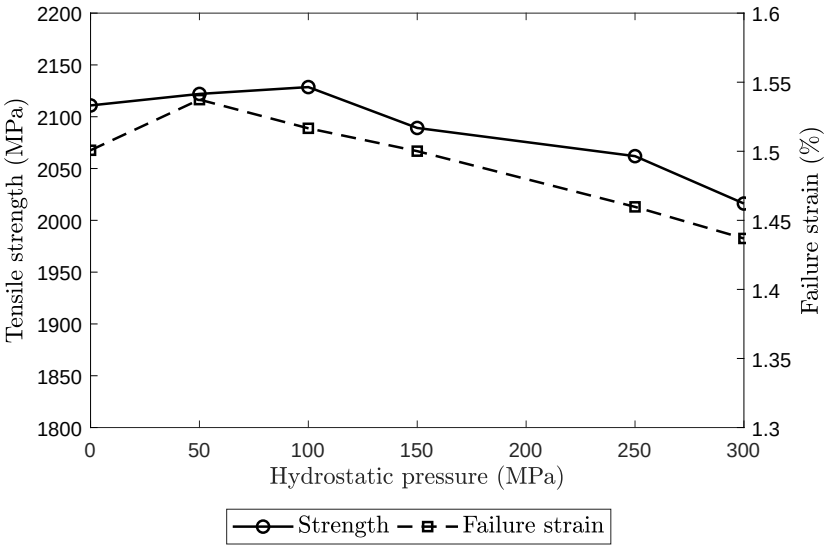

Figure 3.35: Strength and failure strain as a function of the applied hydrostatic pressure.

From the shown results it possible to see that for low hydrostatic pressures the strength of the material is very similar to that at ambient pressure, with a slight

increase in the strength up to 100 MPa of pressure. For higher hydrostatic pressures both the strength and failure strain are lower than with no pressure. The generalized decrease of the tensile strength has been observed experimentally by several authors [159, 160, 162, 163] for different fibre reinforced composites.

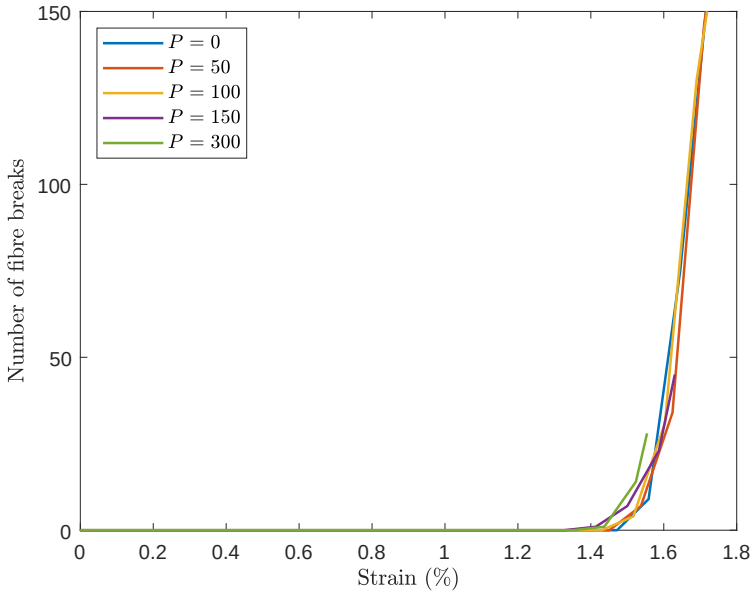

Figure 3.36: Number of fibre breaks in the RVE as a function of the strain for different applied hydrostatic pressures.

As mentioned before, the hydrostatic pressure not only changes the strength of the material but also the failure mechanisms and type of fracture that occurs. To better understand the failure process, the evolution of fibre breaks is shown in Figure 3.36. There are changes in the fracture process, being that for higher hydrostatic pressures fibre breaks occur earlier and grow more rapidly. However, no clear distinction in the fracture process and failure surface could be observed analysing the models. All the models analysed showed similar fracture patterns with multiple fibre fractures mainly in locations of fibre defects.

Although the micromechanical model developed here is able to capture the effect of hydrostatic pressure in the strength of the material, it is not possible to distinguish numerically the different fracture mechanics observed experimentally. One explanation is that the micromechanical models are too small to be able to capture these changes in the fracture process as these occur at a larger scale. In addition, the usage of larger RVEs reduces the effects of the fibre defects on the failure process, as one broken fibre has a lower impact on the overall material behaviour and might lead to the desired changes in the fracture process. Nevertheless, due to the high computation cost of these models, that required a very refined mesh to capture the local stress redistribution and complex material models, it is currently not feasible to simulate larger RVEs.

3.5.2 Hybrid composite simulations

The previous sections focused on the study of the tensile failure of composite when a single type of fibre was considered. The following sections focus on the more complex phenomenon of tensile failure of hybrid composites, where two types of fibres are combined in a single composite material with the objective of improving the mechanical response. In Chapter 2.2 hybrid composites were introduced and some of its advantages were studied. Here we focus only on intratow hybridization with two types of fibres and its effect on the tensile failure.

3.5.2.1 AS4-M50S carbon hybridization

This section focuses on the study of the hybridization between the AS4 and M50S carbon fibres. The properties of the AS4 carbon fibres are shown in Table 3.9. For the M50S carbon fibres, due to lack of information, the same fibre properties were used, with the exception of the longitudinal Young's modulus, Weibull parameters and fibre radius [27] shown in Table 3.10.

Table 3.10: M50S carbon fibre properties from [27].

Material property	Value
Fibre diameter	
$2R$ (mm)	0.0053
Young's moduli	
E_1 (MPa)	480000
Weibull parameters	
σ_0 (MPa)	4600
m	9
l_0 (mm)	10

Several RVEs were generated to study this hybridization. The tensile stress-strain curves are shown in Figure 3.37. All the RVEs studied had dimensions 15 times the radius of the fibre with higher diameter, leading to an RVE with a size equal to 52.5 μm. To study the effect of the fibre radius two types of RVEs were generated. The first consider both the AS4 and the M50S carbon fibres to have the same radius, equal to 3.5 μm; the corresponding results are shown in solid lines in Figure 3.37. The second type of RVEs considered the fibres to have the real fibre radii and, therefore, the AS4 and the M50S were modelled with different radii. The results for these RVEs are shown in Figure 3.37 in dashed lines. In this figure it is shown the tensile behaviour for hybrid composites with different volume fraction of each fibre type. Comparing the results for the RVE's with the same radii (solid line) and different radii (dashed line) it is observed that considering of the M50S to be equal to 2.65 μm, higher tensile strength is obtained, for all the hybrid volume fractions analysed. Varying the volume fraction of each fibre type drastically changes the response of the composite material. In all cases, there is no interaction in the failure of both fibre types, this is, all the LE fibres fail prior to the failure of any HE fibres. This causes the first load drop seen for all hybrid composites. However, as we increase the volume content of HE fibres the load drop is reduced, being minimum

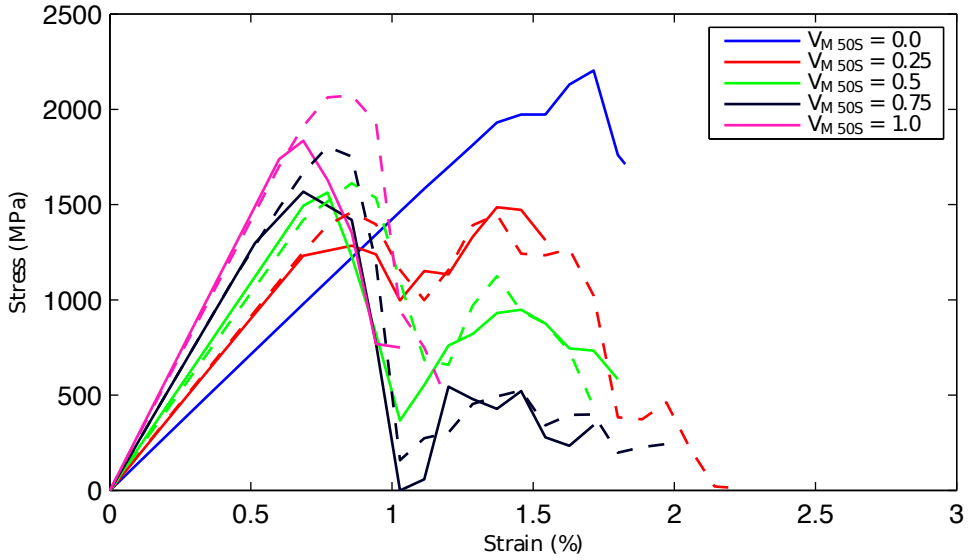

Figure 3.37: Stress-strain diagrams for AS4-M50S hybrid composites with various hybrid volume fractions: full - RVEs with all fibres with radius equal to 3.5 μm; dashed - RVE's with the M50S with radius equal to 2.65 μm.

for a volume fraction of M50S fibres equal to 0.25 (curves in red).

The stress-strain curves for the hybrid composite with a volume fraction of M50S fibres equal to 0.25 are again shown in Figure 3.38 alongside the microstructure of the RVE, where the circles in full represent broken fibres while the others represent intact fibres. Analysing the microstructures it is possible to note that all the LE fibres (M50S fibres) fail prior to the failure of a single high elongation fibre. This failure causes the first load drop seen in the curves. After the first load drop, as the HE fibres are still intact, the material is still able to carry stress which causes the increase in load after the first drop. At the second load peak, the failure strain of the HE has been reached which causes their failure and the failure of the material. Between both load peaks it is seen that, usually, the LE fibres keep on fracturing leading to the fragmentation of these fibres in multiple locations, which is responsible for the non-linearities seen between the failure of the LE and HE fibres. The tensile response for this hybridization is close to what is described as pseudo-ductility, for a volume fraction of M50S fibres equal to 0.25, however, there is a small load drop after the failure of the LE fibres and prior to the failure of the HE fibres, typical of hybrid composites.

3.5.2.2 AS4-T300 carbon hybridization

The tensile response for the hybridization of the AS4 carbon fibres and the T300 carbon fibres, whose properties are shown in Tables 3.9 and 3.2, respectively, is studied.

The T300 carbon fibres have a lower Weibull modulus and therefore a higher variability in fibre strength. Furthermore, the failure strain distribution of the T300

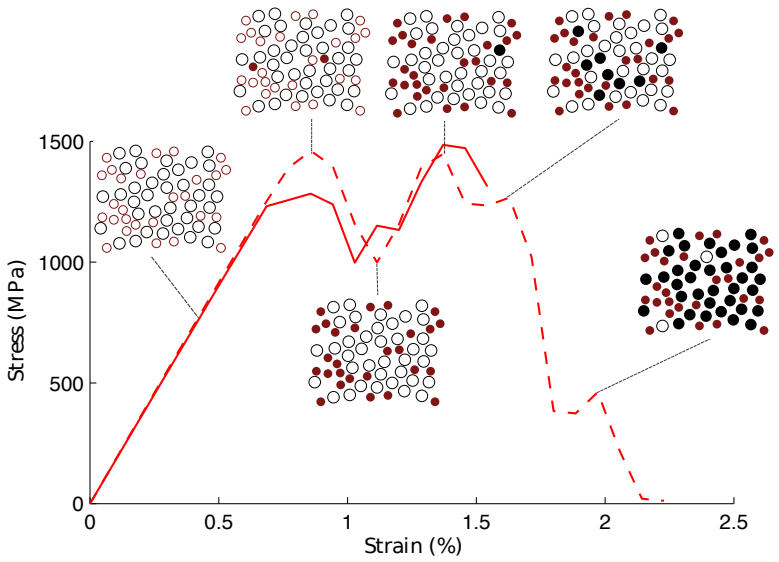

Figure 3.38: Stress-strain curves and microstructures for the hybrid composite with a volume fraction of M50S carbon fibres equal to 0.25: circles in full represent broken fibres.

carbon fibres is closer to that of the AS4 carbon fibres than that of the M50S fibres, which can reduce the load drop seen for the AS4-M50S hybrids. The same RVE's generated for the previous hybridization with all fibres with radius equal to 3.5 μm were used for this hybridization, leading to the results shown in Figure 3.39.

Analysing this figure it is possible to see that the results for the AS4-T300 hybridization are quite different from those obtained using AS4-M50S hybridization. This is in agreement with the results obtained from the analytical models previously described. The more interesting results are for the hybrid composites with a volume fraction of T300 fibres equal to 0.5 and 0.75. For these hybrids there is a delay in first fibre failure in comparison to the non-hybrid T300 composite, which occurs at a strain equal to 0.7%. This can be attributed to the reduction of the volume of T300 carbon fibres by replacing them with AS4 fibres, which reduces the probability of existence of a very severe defect in a fibre, causing the delay in first fibre failure. Nevertheless, it should be noted that only one simulation was performed for each configuration, and the randomness of both the fibre distribution and fibre strength might influence the results. It is also possible to see there is no major stress drop due to the failure of the LE fibres in these hybrid materials. This is attributed to the higher dispersion in fibre strength of the T300 carbon fibres, which causes them to fail at a wider strain range and, therefore, cause a more gradual failure. This can be seen in the microstructures shown in Figure 3.40 for the hybrid composite with a volume fraction of T300 fibres equal to 0.5. It is also possible to see that not all LE (T300) fibres fail before the HE (AS4) fibres start to fail, which leads to the gradual failure response shown. However, it should be noted that the fact that the increased strength dispersion of the T300 fibres increases the dispersion in the results, as they are quite dependent on the location and extension of the defects in the fibres.

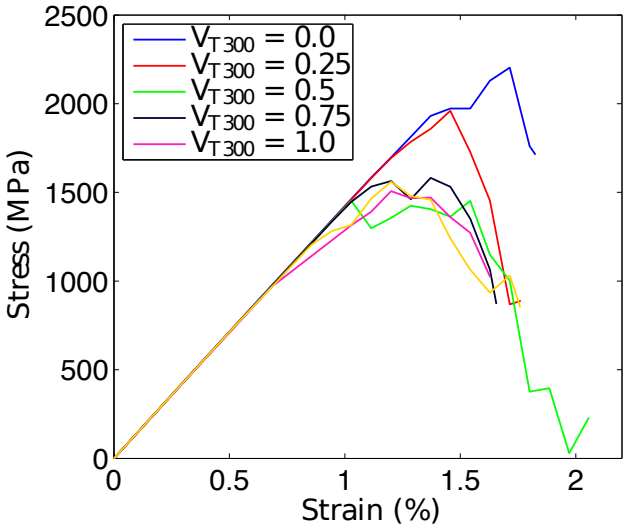

Figure 3.39: Stress-strain diagrams for AS4-T300 hybrid composites with various hybrid volume fractions.

Similar results are seen for the hybrid composite with a volume fraction of T300 carbon fibres equal to 0.75. The microstructures and stress-strain curves are shown in Figure 3.41. It is possible to see that the failure strain of the LE fibres differs from fibre to fibre due to the low Weibull modulus and high strength dispersion. Once again, there is the failure of HE fibres prior to the complete failure of the LE fibres.

It is possible to conclude that the fibre strength distributions play an important role to achieve pseudo-ductility and that the interaction between the failure of the LE and HE fibres is the key point for achieving pseudo-ductility. Nevertheless, the RVEs in study have a small number of fibres, which limits their representativeness. The models developed capture the distinct behaviours of hybrid composites for different hybrid ratios. In addition, insight on the fracture process in this materials can be gained.

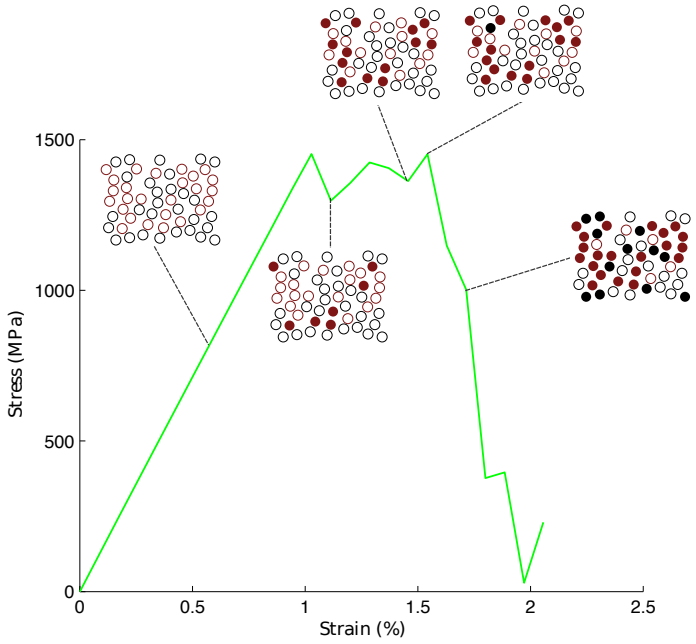

Figure 3.40: Stress-strain curve and microstructures for the hybrid composite with a volume fraction of T300 carbon fibres equal to 0.5: circles in full represent broken fibres.

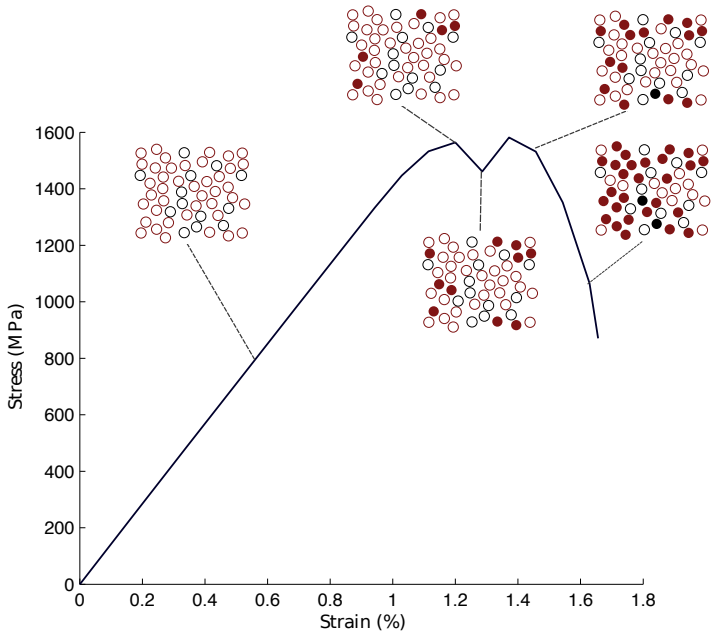

Figure 3.41: Stress-strain curve and microstructures for the hybrid composite with a volume fraction of T300 carbon fibres equal to 0.75: circles in full represent broken fibres.

3.6 Conclusions

This chapter was dedicated to the micromechanical modelling of different failure processes in fibre reinforced composite materials. Several analysis were preformed to understand, firstly the mechanisms of failure in UD non-hybrid composites and secondly the effects of hybridization in these mechanisms and in the tensile behaviour of the composite.

The analysis on the single fibre fragmentation and fibre pushout tests allowed not only to verify the material models, but also understand the effect of the interface properties on longitudinal tensile failure. It is noted that that for the RTM6 material system the properties used initially were too low and lead to premature failure of the interface.

The simulations of the non-hybrid composites allowed the analysis of the failure mechanism in the composites. It was shown that the fibre failure is phenomena dominated by flaws in the fibres and that the fibre failure rarely occurs in the same plane, usually failing in multiple plains according to the locations of these weaker regions. The failure of the first fibre can be preceded by matrix cracking if the failure strain of the matrix is lower than that of the fibres. Nonetheless, the fracture of the fibres leads to the development of cracks in the matrix and decohesion between the fibre-matrix interface. The failure of the fibres and the matrix cracks lead to stress concentrations in the intact fibres that surround a broken one. This intact fibres act as barriers to the propagation of the cracks in the matrix.

After its failure, a fibre is loaded in compression, acting as a spring, however this is a transient effect and after it stabilises it is possible to see that the fibre is loaded in a similar profile as the one from the shear-lag model. In the fracture plane the stress in the fibre is zero, however, moving away from the fracture plane the fibre regains its load carrying capability until it is fully able to carry stress. This makes it possible for the same fibre to break in multiple locations. The effect of fibre nonlinearity was also addressed, for which it was concluded that the effects were small, only affecting the composite failure strain, without any major differences in the failure process. In addition. the effect of superimposed hydrostatic pressure on the longitudinal tensile failure was addressed and, although the model captures its effects on the tensile strength, no changes in the failure mechanisms were observed, although this can be attributed to the limitations on the size of the RVEs.

Hybridization, by introducing two types of fibres in a single composite, drastically changes its tensile behaviour. For the AS4-M50S hybridization it is possible to see that the hybrid fibre volume content has a large effect in the composite's tensile behaviour. For a low LE fibre volume content the load drop after the failure of these fibres is reduced and the maximum stress is achieved after this point, something that does not occur for higher LE fibre volume contents. As the hybridized fibres have very different failure strains the LE and HE fibres fail in two very distinct moments. In-between the failure of both fibre types it is possible to see that the LE keep fracturing in multiple locations, leading to a non-linear behaviour and increasing the extent of matrix cracking. For the AS4-T300 hybridization it was concluded

that there is some pseudo-ductile behaviour, which was explained by the continuous failure of the HE and LE fibres, not allowing for large load drops as seen in the AS4-M50S hybridization.

The developed framework is able to capture the very complex failure and damage mechanisms of both non-hybrid and hybrid composites, withal, due to its computational cost, the RVEs modelled have reduced sizes. This limits the model's applicability and their ability to accurately predict cluster formation and propagation, as larger RVEs are required. Nevertheless, the studies performed provide important insights on the failure process of fibre reinforced composites subjected to longitudinal tensile loadings.

Chapter 4

Spring element model

The previous chapter focused on a high fidelity model to predict failure, and in the understanding of the mechanisms driving fibre dominated failure in composite materials. Although powerful, these models are computationally expensive, due to their 3D geometry and complex material models, limiting their usage. This limitation occurs not only in terms of number of simulations that can be performed, making parametric studies hard to execute, but also regarding the size of RVE that can be used, which is limited by the computational resources, as discussed in Chapter 3. This size restriction limits the understanding of one of the main phenomenon driving fibre dominated failure that is the formation of clusters of broken fibres.

In this chapter a simplified model to predict fibre dominated failure is presented and it is used to assess the mechanics that drive cluster formation and failure in composite materials. The chapter is divided in four sections. Firstly, the baseline model is presented with the necessary modifications to ensure that it accounts for a random fibre distribution and is capable of predicting failure in hybrid composites, i.e. fibres with different material and geometrical properties. Section 4.2 presents a comparison between the developed Spring Element Model (SEM) with other models present in the literature. Section 4.3 presents the extension of the model developed in Section 4.1 to a dynamic model, which can account for the transient dynamic effects that occur when a fibre breaks and that change the stress redistribution and, therefore, cluster formation. Finally, Section 4.4 presents a study on fracture and failure of hybrid composites and the effect of fibre dispersion on the cluster formation.

4.1 Static model

Modelling the longitudinal tensile failure of unidirectional (UD) composite materials is a challenging task due to the complex mechanisms that govern this type of failure. As the main load carrying component, the fibres play an important role in the failure process. It is understood that fibre strength is a stochastic property that is dominated by a distribution of flaws [33, 165], therefore an accurate characteriza-

tion of the random nature of fibre strength is necessary to develop proper composite models.

Another important factor in the failure process is the stress redistribution once a fibre is broken and the interaction between multiple fractures leading to the formation of clusters of broken fibres [5, 72, 73, 95]. If a cluster reaches a critical size it propagates unstably and causes the failure of the material. When a fibre breaks it does not fully lose its load carrying capability because the surrounding matrix is loaded in shear and transfers stress back onto the unbroken fibre part [34, 86, 166, 167]. A region along the fibre called ineffective length is created. In this region the fibre's load carrying capability is hampered, however, at a certain distance away from the breakage the fibre stress carrying capability is fully recovered. The well known Cox's shear-lag model can be used to estimate the ineffective length and stress distribution around the broken fibre [168]. However, shear yielding of the matrix at the tip of broken fibre will be initiated due to an intensive stress concentration state. To consider this phenomenon, Kelly and Tyson [169] proposed modelling the matrix behaviour within the ineffective length with a perfect-plasticity model, therefore, the ineffective length is calculated from the load balance between the fibre and matrix. Following this ideas, the Global Load Sharing (GLS) model was proposed by Curtin [85]. In this approach, the stress released from a broken fibre is equally distributed among the remaining unbroken fibres. GLS models do not take into account the interaction between the fibres and no local fields due to fibre fracture are considered. Local Load Sharing (LLS) models were developed to take into account fibre interaction in the longitudinal failure of UD composites [170]. Several analytical models to determine the stress concentration factor around a single broken fibre [171] or in the presence of multiple broken fibres [87, 172, 173] have been proposed. In addition, 3D Finite Element Models (3D FEM) have been used to fully model the microstructure of the composite [58, 174, 175]. These models are computationally expensive due to the refined meshes involved and the complex material models required, imposing a limitation in the number of fibres represented in the Representative Volume Element (RVE).

The Spring Element Model (SEM) was proposed by Okabe and co-workers as a low computational cost alternative to 3D FEM [89, 176]. The SEM takes into account local stress redistribution due to fibre failure. The model is based on the assembly of periodic packages of fibre and matrix spring elements. The periodic package or unit cell consists of one fibre surrounded by six other fibres connected through shear spring elements that represent the matrix behaviour. Therefore, the unit cell consists of fibre axial springs in the longitudinal direction and matrix shear springs in transverse direction. This modelling approach has the advantage of being computationally efficient, allowing the simulation of RVEs with a large number of fibres, while allowing to accurately capture the stress redistribution and fibre break interaction during the failure process of UD composites.

The objective of this work is to present a simple, yet accurate and computationally efficient model to predict the failure behaviour of composites using a random fibre distribution. The model should be able to capture the clustering process leading to the ultimate failure of UD composites and the influence of different material properties on the stress redistribution and the failure process zone of composites.

4.1.1 Spring element model for random distribution of different fibres

The model proposed in this section is an extension of the SEM approach to both random distribution of fibres and hybrid composites, where the fibres can have different geometrical and mechanical properties. The SEM consists of longitudinal spring elements, which represent the fibres, connected by transverse spring elements representing the matrix. The matrix contribution in the axial load, i.e. fibre direction, is disregarded in SEM, a commonly accepted hypothesis for UD polymer composites. Therefore, only the matrix shear contribution is represented through shear transverse elements. The stiffness matrices $\mathbf{K}$ of longitudinal and transverse spring elements, from fibre and matrix elements, are given by [89]:

$$\mathbf{K}_f = A_f \int_0^{l^z} {\mathbf{B}_f}^T E_f^e \mathbf{B}_f dz, \tag{4.1}$$

$$\mathbf{K}_m = A_m \int_0^{d} {\mathbf{B}_m}^T G_m \mathbf{B}_m dr, \tag{4.2}$$

where subscripts f and m denote fibre and matrix elements, E is Young's modulus of the fibre, G_m is the shear modulus of the matrix, $\mathbf{B}$ is the strain-displacement transformation matrix, A_f is the fibre cross section area, A_m is the associated area on the fibre surface of the matrix, l^z is the fibre element's length and d is the distance between surfaces of two adjacent fibres.

4.1.1.1 Micro-structure generation and finite element discretization

To obtain the geometric model necessary to represent the composite's micro-structure, a periodic 3D RVE is generated with a random fibre distribution, using the random generator developed by [68] with the necessary modifications. To guarantee that the RVE has a defined quadrangular geometry, the fibres that are divided by the boundary of the RVE are forced to have its centre at the edge, while ensuring geometric periodicity. With the centre of the fibres defined, ensuring the correct fibre volume fraction and that no fibre overlap occurs, a 2D Delaunay triangulation [177] algorithm is used to generate a 2D triangular mesh. Figure 4.1 shows an example of a mesh, where each circle represents a fibre and each line a matrix shear element. Finally, to generate the 3D RVE mesh the previously obtained 2D mesh is replicated with an offset distance of l^z , which is the predetermined length for fibre spring elements, until the final total desired length of the RVE in fibre direction is achieved. The generated sections are connected through longitudinal fibre spring elements.

Considering the shape functions of the fibre elements as:

$$\boldsymbol{\mathcal{N}}_f(z) = \begin{bmatrix} \mathcal{N}_1(z) & \mathcal{N}_2(z) \end{bmatrix} = \begin{bmatrix} 1 - \frac{z}{l^z} & \frac{z}{l^z} \end{bmatrix}, \tag{4.3}$$

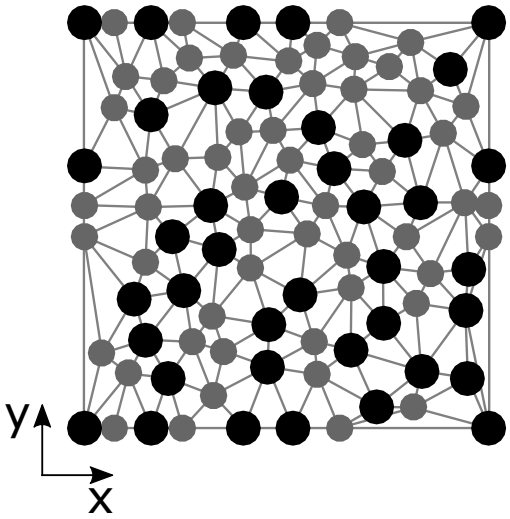

Figure 4.1: 2D mesh for a periodic RVE with a random fibre distribution.

the derivatives of the shape functions can be written as

$$\mathbf{B}_f = \frac{d\boldsymbol{\mathcal{N}}_f}{dz} = \begin{bmatrix} -1/l^z & 1/l^z \end{bmatrix} . \tag{4.4}$$

Considering that the cross section area (A_f^e) and the Young's modulus (E_f^e) of the fibre do not change along the spring element it is possible to compute the stiffness matrix of the fibre elements:

$$\mathbf{K}_f^e = A_f^e \int_0^{l^z} {\mathbf{B}_f}^T E_f^e \mathbf{B}_f dz = \frac{A_f^e E_f^e}{l^z} \begin{bmatrix} 1 & -1 \\ -1 & 1 \end{bmatrix}, \tag{4.5}$$

where the superscript e refers to element properties or parameters, which can be different for the different fibres involved.

Due to the random distribution of the fibres, two major changes occur with respect to the hexagonal packing used in the original SEM: firstly the distance between each fibre element differs and secondly not all fibre elements are connected to other six fibres, as in the hexagonal packing. The fibres can be connected to, depending on the fibre arrangement, from to three to ten fibres. Therefore, the stiffness of the matrix elements change from element to element, being therefore necessary to change the approach to obtain the stiffness matrix of the matrix shear elements.

Consider two fibres (1 and 2) with different radii (R_1 and R_2) that are connected to, respectively, n_1 and n_2 fibres, and are separated by a distance d. The associated area on each fibre of the transverse spring element representing the matrix that connects both fibres is, respectively:

$$A_m^{(1)} = \frac{2\pi R_1}{n_1} l^z \quad \text{and} \quad A_m^{(2)} = \frac{2\pi R_2}{n_2} l^z. \tag{4.6}$$

The area of the matrix element is considered to vary linearly between $A_m^{(1)}$ and $A_m^{(2)}$:

$$A_m(r) = A_m^{(1)} + \frac{\left(A_m^{(2)} - A_m^{(1)}\right)}{d} r \,. \tag{4.7}$$

A schematic representation of the fibres and the matrix shear element, which connects both fibres, is shown in Figure 4.2.

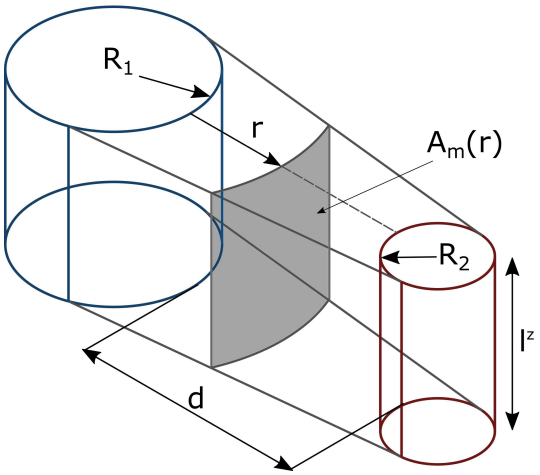

Figure 4.2: Matrix shear element connecting 2 fibres.

The shear force on a cross section (at position r) in the matrix shear element can be written as:

$$f_m(r) = G_m A_m(r) \frac{du}{dr}, \tag{4.8}$$

where u is the displacement in the longitudinal direction and r is the distance from the fibre 1 surface to the cross section, varying from 0 to d (see Figure 4.2). Imposing force equilibrium on a isolated portion of the matrix shear element of radial dimension dr yields:

$$\frac{df_m(r)}{dr} = 0 \quad \Rightarrow \quad \frac{d}{dr}\left(G_m A_m\left(r\right) \frac{du}{dr}\right) = 0. \tag{4.9}$$

The solution of Eq. (4.9) gives the relationship between the shear force on the matrix shear element and the relative displacement of the fibres

$$f_m = \frac{G_m \left(A_m^{(2)} - A_m^{(1)}\right)}{d \ln\left(A_m^{(2)}/A_m^{(1)}\right)} \left(u_2 - u_1\right). \tag{4.10}$$

Finally, using Eq. (4.10) the stiffness matrix for the matrix shear element reads:

$$\mathbf{K}_m = \frac{G_m \left(A_m^{(2)} - A_m^{(1)}\right)}{d \ln\left(A_m^{(2)}/A_m^{(1)}\right)} \begin{bmatrix} 1 & -1 \\ -1 & 1 \end{bmatrix}. \tag{4.11}$$

The previous matrix equation gives a general expression for the stiffness of a matrix shear element, which will be particularized in each case depending on the

connected fibres. For example, the stiffness matrix of the matrix shear element presented in the original SEM [89] is recovered from Eq. (4.11) by taking the limit when $A_m^{(1)} \to A_m^{(2)}$.

It is interesting to compare the previous result with that obtained using a linear Finite Element to estimate the stiffness matrix of the matrix shear element. Let us consider a node 1 in the fibre 1 and a node 2 in the fibre 2, then the shape functions are:

$$\boldsymbol{\mathcal{N}}_m(r) = \begin{bmatrix} \mathcal{N}_1(r) & \mathcal{N}_2(r) \end{bmatrix} = \begin{bmatrix} 1 - \frac{r}{d} & \frac{r}{d} \end{bmatrix}, \tag{4.12}$$

and the stiffness matrix is obtained by:

$$\tilde{\mathbf{K}}_m = \int_0^d \frac{d\boldsymbol{\mathcal{N}}_m}{dr}^T G_m A_m \frac{d\boldsymbol{\mathcal{N}}_m}{dr} dr, \tag{4.13}$$

where A_m is given by Eq. (4.7). Solving Eq. (4.13) the stiffness matrix of the matrix shear element using a FEM approach is obtained:

$$\tilde{\mathbf{K}}_m = \frac{G_m \left(A_m^{(2)} + A_m^{(1)} \right)}{2d} \begin{bmatrix} 1 & -1 \\ -1 & 1 \end{bmatrix}. \tag{4.14}$$

Note that $\tilde{\mathbf{K}}_m$ can be seen as a linearisation of the stiffness matrix $\mathbf{K}_m$ obtained previously around the $A_m^{(1)} \to A_m^{(2)}$ point. If the associated areas ($A_m^{(1)}$ and $A_m^{(2)}$) on each fibre are not substantially different, Eq. (4.14) represents a good approximation of $\mathbf{K}_m$. In any case, Eq. (4.11) i.e. $\mathbf{K}_m$, will be used in this work to obtain the stiffness matrix for the matrix shear element.

As previously explained, the 3D RVE is generated by extruding the 2D mesh (see Figure 4.1) with fibre elements connecting each of the sections. Therefore, the virtual work of the total spring-element model is

$$\delta \mathbf{u}^T \left[\left(\sum_{e=1}^{N_f - N_f^b} \mathbf{K}_f^e + \sum_{e=1}^{N_m} \mathbf{K}_m^e \right) \mathbf{u} \right] = \delta \mathbf{u}^T \mathbf{f}^{\text{ext}}, \tag{4.15}$$

where N_f and N_m are the total number of fibre and matrix elements, $\mathbf{u}$ and $\mathbf{f}$ the displacement and force vectors and N_f^b is the number of broken fibre elements, respectively. $\mathbf{K}_f^e$ is given by expression shown in Eq. (4.5), while $\mathbf{K}_m^e$ is the stiffness matrix of the each individual matrix shear element (see Eq. (4.11)). Finally, the nodal displacements in the proposed modification of the SEM are obtained by solving

$$\mathbf{K}\mathbf{u} = \mathbf{f}^{\text{ext}}, \tag{4.16}$$

where $\mathbf{K}$ is the global stiffness matrix,

$$\mathbf{K} = \sum_{e=1}^{N_f - N_f^b} \mathbf{K}_f^e + \sum_{e=1}^{N_m} \mathbf{K}_m^e. \tag{4.17}$$

4.1.1.2 Failure modelling

For the fibre elements a failure criteria associated with the longitudinal failure mechanism is considered, which can be written in its general form as

$$\frac{\sigma_f}{X_T^e} - 1 < 0 \quad \text{if} \quad \sigma_f > 0, \tag{4.18}$$

where σ_f is the fibre stress and X_T^e is the tensile strength of the fibre element. As will be seen in the next section, the tensile strength of an element i.e. X_T^e will be randomly assigned recurring to one of the available statistical distributions to describe fibre's strength. In the present implementation a fibre element will be considered fully damaged if the failure criteria given by Eq. (4.18) is not satisfied. Therefore, when a fibre element does not verify Eq. (4.18) it is considered broken and N_f^b updated accordingly.

The matrix behaviour plays an important role in the tensile failure of composite materials, since this is the element that allows stress redistribution to occur after a fibre breaks. This stress-redistribution is affected by both matrix plasticity and damage, as well as fibre-matrix decohesion [17, 58]. The matrix was considered to be linear elastic and perfectly plastic. This behaviour was implemented in the model using a sequentially linear analysis [178, 179].

The sequentially linear approach approximates the constitutive stress-strain relationship using a series of saw-teeth that maintain a positive tangent stiffness. Linear analyses are repeated, each with a reduced positive stiffness, until the global analysis is complete. Thus, the negative or null tangent stiffness, which is characteristic of softening curves, that can be detrimental to convergence, is entirely avoided.

In a sequentially linear strategy, the stress-strain diagram can be reproduced by a consecutively reducing the shear stiffness (G_i) as well as changing the yield stress of each critical element (τ_i^u). The shear stiffness is reduced in a discrete manner according to:

$$G_{i+1} = \frac{G_i}{\alpha_m}\,, \tag{4.19}$$

where α_m is a parameter larger than one and that can be controlled by the user, ensuring a control in accuracy versus computational time. The behaviour of the matrix is dominated by an envelope that determines when each stiffness reduction occurs and the new yield stress of the material is defined. In this paper, the behaviour considered is a linear elastic perfectly plastic behaviour, characterized by a constant yield stress (τ^u). Both the accurate and the approximation using the sequentially linear analysis of the matrix behaviour considered are shown in Figure 4.3.

Although being used only to simulate elastic and perfect plastic model in this work, this is a versatile implementation that allows the behaviour to the matrix to be changed to consider any type of constitutive behaviour. It should be noted that, while there is a reduction of the stiffness of the matrix elements during the sequentially linear analysis procedure, the number of connections in each fibre (n_1 and n_2) is not changed.

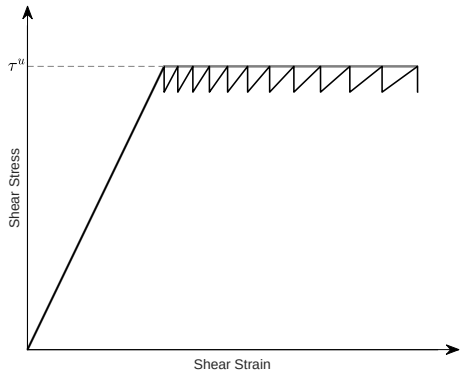

Figure 4.3: Saw-shape matrix behaviour using sequentially linear analysis, in black, and analytical behaviour in grey.

In this model the stresses on the fibre elements in the ineffective length are not imposed, but are obtained from the overall equilibrium of the system together with the failure criterion proposed for the matrix shear elements.

4.1.1.3 Numerical implementation

The flowchart of numerical implementation of the model proposed is shown in Figure 4.4. The model was implemented using the commercial software MATLAB®.

Firstly, the RVE geometry is generated with a 2D random fibre distribution, which is then extruded to generate the 3D periodic RVE. For all the fibre elements and according to an adequate fibre strength distribution a random strength is assigned to each of the fibre elements.

An evolutive strain incrementation procedure is considered to ensure that a strain increment only forces one fibre to fail, given generally by:

$$\Delta\varepsilon = \min\left(\frac{X_T^e - \sigma_f^e}{E_f^e}\right) , \tag{4.20}$$

where σ_f^e is the stress in the fibre element from the previous strain increment. The global stiffness matrix with the updated number of broken fibre elements and updated matrix shear stiffness is determined. Displacement control is considered in the model and the applied displacement is calculated based on the strain increment given in Eq. (4.20) and the RVE dimension. The external force vector f_j^i is obtained based on the current stiffness matrix and the applied displacement. Solving the system of equations (4.16) the unknown displacement vector is calculated. From the displacement vector the strains and stresses in all the elements are determined. Periodic Boundary Conditions (PBCs) [180] are considered when solving the system of equations, which is possible due to the material periodicity of the RVE. The implementation of the PBCs is done through the elimination of the redundant degrees of freedom on the RVE boundary.

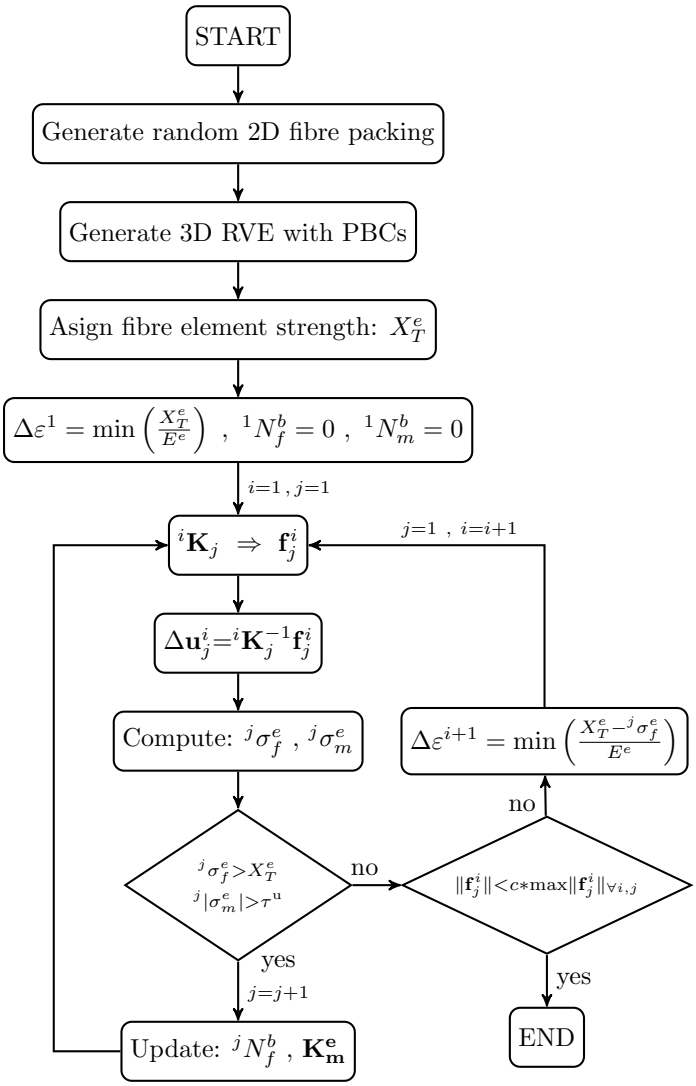

Figure 4.4: Flowchart of the the model implemented.

A failure criteria for the fibres as well as a elastic and perfectly plastic model for the matrix were implemented. If any of the fibre elements fail or if the shear stress in the matrix elements exceeds τ_i^u, the number of broken fibre elements is updated as well as the stiffness of the matrix elements. Then a new global stiffness matrix is computed and the system of equations is solved once more. This iterative process continues until no fibre or matrix element fail and equilibrium has been achieved. If equilibrium is achieved and the termination criterion is not met, a new strain increment is determined and the iterative process continues. If the termination criterion is met, then the simulation finishes. The termination criterion used stops the algorithm once the norm of the external force vector in the current iteration is lower than c times the maximum norm of the external force vector from all the previous increments, where c is a value between zero and one. The numerical results shown in this work are obtained using a value of c equal to 0.2.

4.1.2 Mechanisms of longitudinal failure

4.1.2.1 Local fields around a broken fibre

To verify if the model is capable of correctly capturing the stress profile of a broken fibre, several simulations were performed using an RVE with a transverse section of 87.5 × 87.5 μm composed of 132 fibres with a length of 350 μm. The fibres used for these simulations are the AS4 carbon fibres [90], whose properties are: $E_f = 234$ GPa, $R_f = 3.5$ μm.

The ineffective length of a broken fibre in this model is not only controlled by the shear modulus of the matrix (G) but also by the yield stress (τ^{u}). Figure 4.5 shows the influence of the matrix shear modulus and yield stress in the stress recovery profile of a broken fibre. For comparison purposes the Kelly-Tyson [169] and modified Cox [166] shear-lag models are shown, using a fibre-matrix interfacial strength of 70 MPa and a matrix shear modulus of 1 GPa. The results shown were obtained considering an applied strain of 2%.

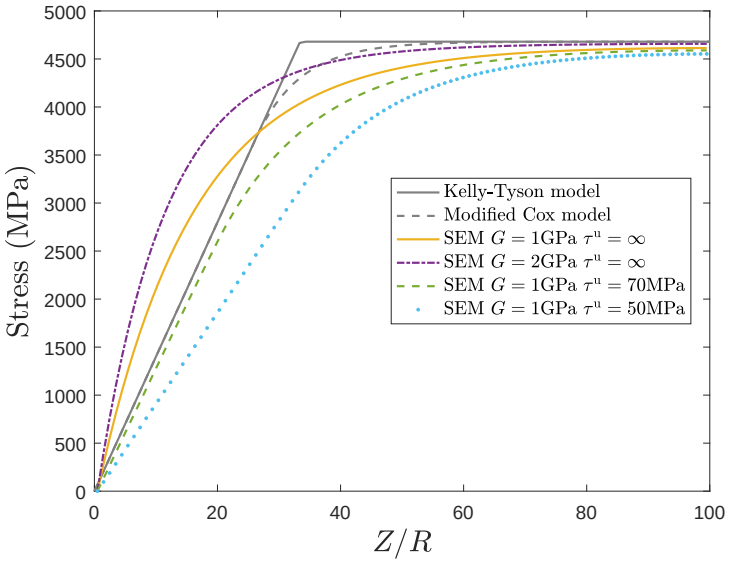

Figure 4.5: Influence of matrix properties on the stress recovery profile of a broken fibre.

It can be observed in Figure 4.5 that the stress recovery profile of a broken fibre is captured by the model, Z is the distance from the break plane in the longitudinal direction. While there are some differences between the stress profile obtained by the SEM and the simplified shear-lag models, the profile is considered to be accurate and therefore there is no need to superimpose the shear-lag profile in the modelling strategy. In this figure, it is also possible to see that limiting the maximum stress in the matrix shear elements affects the recovery profile and therefore the ineffective length, which is increased. This is discussed in more detail at the end of this section.

When a fibre breaks there is not only an ineffective length in the broken fibre,

but the stress previously carried by this fibre is redistributed among the surrounding intact fibres, increasing the stress carried by these fibres and thus increasing their failure probability. The increase of stress can be quantified by a Stress Concentration Factor (SCF), considered here to be the ratio of the actual stress in the fibre over the stress in the fibre if there were no breaks, given by $E_f\varepsilon$, where ε is the applied strain. This SCF is affected by the matrix and fibre properties as well as by the fibre arrangement. Figure 4.6 shows the SCF as a function of the distance between the centre of a given fibre and the centre of the broken fibre (d), in the fracture plane. The results are shown for matrix shear modulus of 1 GPa, with $\tau^{\mathrm{u}} = \infty$, $\tau^{\mathrm{u}} = 70$ MPa and $\tau^{\mathrm{u}} = 50$ MPa and 2 GPa with $\tau^{\mathrm{u}} = \infty$.

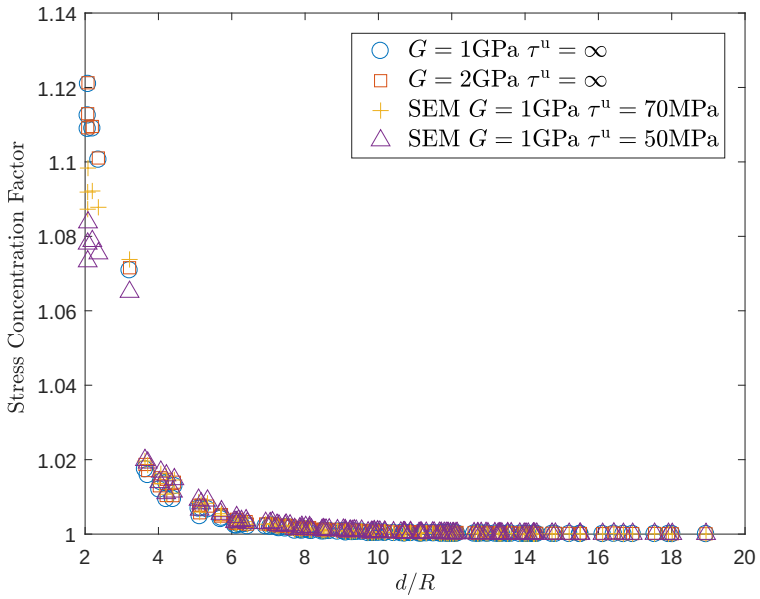

Figure 4.6: Stress concentrations as a function of the distance to the broken fibre.

The SCF decreases away from the broken fibre, being this decrease continuous if no matrix yield stress is considered, i.e., the matrix is considered linear elastic. If matrix yield stress is considered the stress redistribution is more complex as there is a maximum matrix shear stress in the matrix shear elements, causing the stress redistribution to be less uniform and more dependent on the actual fibre arrangement. To better visualize this stress redistribution the stress concentration factor in each intact fibre that surrounds the broken one is plotted in Figure 4.7. Figures 4.7a and Figure 4.7b show the predictions for different values of the matrix stiffness, maintaining $\tau^{\mathrm{u}} = \infty$. It is observed that the stress concentrations are higher in the surrounding fibres for the higher shear stiffness of the matrix. When a matrix limit stress is considered the analysis of the stress redistribution becomes more complex (Figures 4.7c and 4.7d): for the fibres closer to the broken one the SCF is reduced, while for the remaining ones the SCF increases to maintain the equilibrium. Therefore, the in-plane stress recovery region is increased while the maximum SCF is decreased. This stress redistribution is not trivial to predict, not only on the fracture plane but along the broken fibre's ineffective length, being this dependent on the matrix properties as well as on the fibre distribution. Nonetheless, this stress

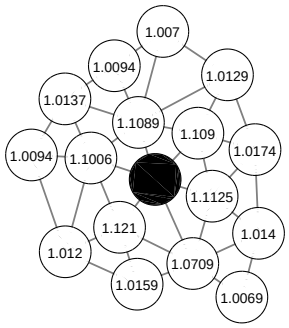

(a) $G = 1$GPa and $\tau^{u} = \infty$.

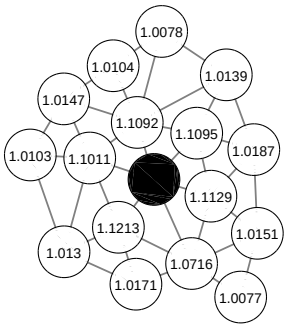

(b) $G = 2$GPa and $\tau^{u} = \infty$.

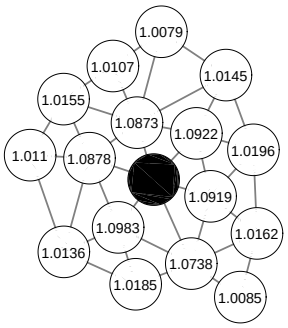

(c) $G = 1$GPa and $\tau^{u} = 70$MPa.

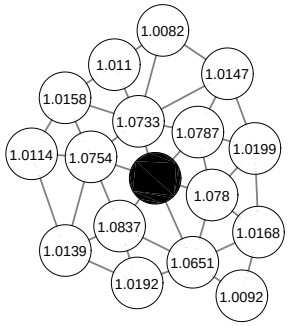

(d) $G = 1$GPa and $\tau^{u} = 50$MPa.

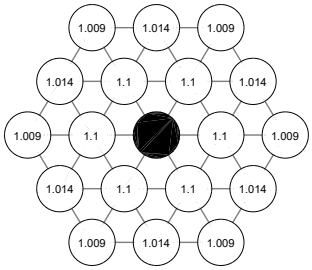

(e) Hexagonal packing with $G = 1$GPa and $\tau^{u} = \infty$.

Figure 4.7: Stress concentrations in the intact fibre surrounding a broken fibre.

redistribution process is not imposed in the model, but it is directly obtained from the equilibrium equations. For comparison purposes the stress concentration factors of an hexagonal packing are shown in Figure 4.7e, from which is possible to see that the maximum SCF is lower than that obtained using random packing.

As mentioned before, the effect of limiting the maximum shear stress in the matrix elements not only changes the stress concentrations in the plane of the fracture, but also the stress redistribution within the ineffective length. To better understand this redistribution process, the stress along the intact fibres that surround a broken one are shown in Figure 4.8, for both the cases with and without matrix yield stress and with $G = 1$ GPa. When no yield stress is considered, it is possible to see that the SCF is maximum in the fracture plane and steadily decreases until the far field stress is reached. The differences in stress concentrations between the intact fibres is a consequence of the fibre arrangement and its effect on the shear stiffness of the matrix elements connecting the broken to each of the intact fibres. When $\tau^{u} = 50$ MPa is considered, it is possible to see that the shape of the stress profile in the intact fibres changes, being now linear in the regions closer to the broken fibre. This is due to the fact that the matrix elements that connect these fibres to the broken one are within the plastic zone and, therefore, their stress is independent of the applied strain, being equal to 50 MPa. Although the maximum

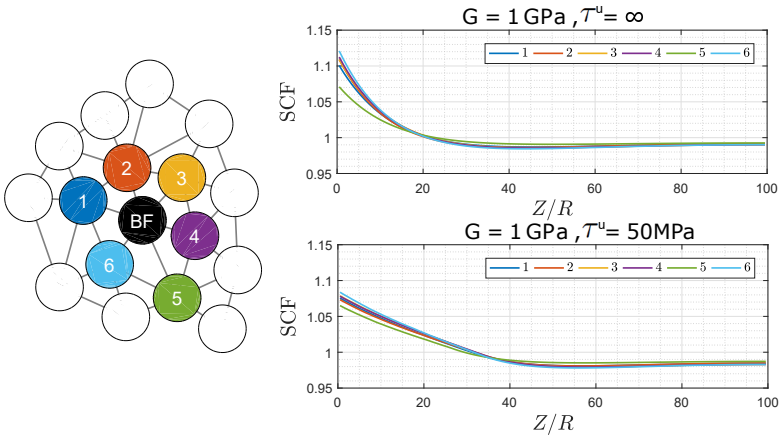

Figure 4.8: Stress concentrations in the intact fibres as a function of the distance to the fibre break plane.

stress concentration is reduced when a yield stress is considered, the intact fibres have an higher SCF away from the break plane, which may increase the failure probability of these fibres. In addition, the in-plane stress recovery region is also increased. In spite of the differences in stress redistribution being small, these effects may be amplified when more than one fibre breaks in a single cluster, being that there are more than one interacting fibre fractures. These differences in stress redistribution may affect the fracture process in composite materials leading to differences in cluster formation.

4.1.2.2 Influence of the fibre strength distribution

The longitudinal tensile failure of composite materials is a fibre dominated process, therefore, it is necessary to accurately capture the fibre's stochastic strengths. Fibres exhibit weakest-link characteristics and their strength is flaw dominated. The most used statistical distribution to describe the strength of the fibres is the Weibull distribution [35]:

$$P(\sigma) = 1 - \exp\left(-\left(\frac{L}{L_0}\right)\left(\frac{\sigma}{\sigma_0}\right)^{\rho}\right) , \tag{4.21}$$

where P is the failure probability at the applied stress σ, L is the characteristic gauge length, L_0 is the reference gauge length, σ_0 the scale parameter and ρ the shape parameter or Weibull modulus [35]. Although being the most used statistical distribution for fibre strength, it has been shown that the Weibull distribution is not the best suited for carbon and glass fibres [28, 181, 182], specially at very short gauge lengths. To better capture the experimental data different distributions have been proposed, usually based on the Weibull distribution such as the Power-Law Accelerated Weibull (PLAW) [28, 40, 183]:

$$P(\sigma) = 1 - \exp\left(-\left(\frac{L}{L_0}\right)^{\alpha}\left(\frac{\sigma}{\sigma_0}\right)^{\rho}\right) , \tag{4.22}$$

where α is an additional parameter for the distribution. A consequence of this exponent α, which is lower than one, is that for lengths smaller than the reference

L_0 the strength distribution shifts to lower strengths. This drastically changes the behaviour of the models, as usually, very small element lengths are considered and if the length scaling is not accurately captured by the statistical distribution, the element's strength can be largely over predicted.

Curtin [28] proposed another model entitled Weibull of Weibulls (WOW) that conforms with Equation (4.22) but with more solid physical background. This model assumes that the strength distribution along a fibre is a Weibull distribution with modulus ρ' and that the characteristic strength of each fibre follows a different Weibull distribution with modulus m. The different characteristic strengths of the fibres are attributed to the processing and handling of the fibres. This distribution yields Equation (4.22) if the following relations are met:

$$\rho = \frac{m\rho'}{\left(m^2 + \rho'^2\right)^{1/2}} \,, \tag{4.23}$$

and

$$\alpha = \frac{m}{\left(m^2 + \rho'^2\right)^{1/2}} \,. \tag{4.24}$$

The difference between the PLAW and WOW models is that, in the WOW model the strength along an individual fibre is highly correlated, leading to very weak and very strong fibres, while in the PLAW model there is no direct correlation in the strength of the elements within a single fibre.

The strength a an element can be generated from the shown distributions by assigning a random failure probability ($R1$) for the element and determining the corresponding strength. This is true for both the traditional Weibull distribution and the PLAW model, however, WOW model requires two random parameters ($R1$ and $R2$), corresponding to the generation of a random strength for each individual fibre and for each element within the fibre. The relations between the random generated probabilities and the element strengths are given by:

$$\text{Weibull}: \quad X_T^e = \sigma_0 \left[-\frac{L_0}{L} \ln\left(1 - R_1\right) \right]^{1/m} \tag{4.25a}$$

$$\text{PLAW}: \quad X_T^e = \sigma_0 \left[-\left(\frac{L_0}{L}\right)^{\alpha} \ln\left(1 - R_1\right) \right]^{1/m} \tag{4.25b}$$

$$\text{WOW}: \quad X_T^e = \left(\frac{L_0}{L}\right)^{1/\rho'} \sigma_0 \left(-\ln\left(1 - R_1\right)\right)^{1/\rho'} \left(-\ln\left(1 - R_2\right)\right)^{1/m} \,. \tag{4.25c}$$

Several simulations using different random distributions were performed using each of the presented strength distribution. The models used have approximately 1100 fibres, with a length of 1.05 mm, divided into 150 elements along its length. The transverse dimension of the RVEs is 260×260 μm. AS4 fibres have been considered with the properties shown in Table 4.1. The fibre volume fraction was considered to be 60%, the shear modulus of the matrix 1 GPa and the matrix elements were considered linear elastic ($\tau^{\mathrm{u}} = \infty$). For each distribution, five simulations were performed. For each simulation a new random microstructure was generated as

well as know random element strengths. For the WOW strength distribution, five simulations with a periodic hexagonal fibre arrangement was also simulated. A summary of some relevant results of the simulations are shown in Table 4.2, which include the maximum cluster size that will be defined in Section 4.1.2.4.

Table 4.1: AS4 carbon fibre properties [28].

σ_0	4275 MPa
ρ'	10.7
L_0	12.7 mm
ρ	6.4
α	0.6
m	8

Table 4.2: Maximum stress, failure strain and maximum cluster size for the AS4 composite using different strength distributions and fibre distribution.

	Sim.	1	2	3	4	5	Avg.	STDV
Weibull	X_T (MPa)	3365	3436	3370	3369	3366	3381	30.78
	ε_f (%)	2.74	2.82	2.64	2.75	2.64	2.72	0.08
	Max. cluster	23	29	14	28	19	23	6.27
PLAW	X_T (MPa)	2117	2095	2125	2137	2105	2116	16.41
	ε_f (%)	1.71	1.76	1.72	1.73	1.71	1.73	0.02
	Max. cluster	15	33	24	25	23	24	6.40
WOW	X_T (MPa)	1939	1978	1948	1928	1961	1951	19.61
	ε_f (%)	1.65	1.73	1.66	1.68	1.65	1.67	0.03
	Max. cluster	20	27	36	19	16	23	8.02
WOW hexag.	X_T (MPa)	1934	1958	1938	1930	1947	1941	11.21
	ε_f (%)	1.67	1.66	1.61	1.61	1.68	1.65	0.03
	Max. cluster	40	34	20	22	45	32	10.96

Figure 4.9 shows the results of the simulations performed using all the three strength distributions presented above. The traditional Weibull distribution leads to a higher composite strength prediction when compared with PLAW and WOW distributions. This is due to the large difference between L_0 and $L = l^z$, which leads to a higher individual tensile strength of the fibre elements. Using the PLAW or WOW model leads to lower tensile strengths, as the length scaling is affected also by the α parameter, leading to a reduction of the elements individual tensile strength and, therefore, to a reduction of predicted composite tensile strength.

Madhukar et al. [184] tested AS4 composites in an EPON 828 matrix and obtained a tensile strength for the composite material of 1890 MPa and a failure strain of 1.45% for a measured fibre volume content of 67.7%, however, according to [28], the measured Young's modulus is more consistent with an effective volume fraction

of 59%, which is consistent with the volume fraction considered in the simulations. From the results shown in Figure 4.9, it is observed that the Weibull distribution leads to an overprediction in both tensile strength and failure strain. While, the PLAW and WOW models give better results. The WOW distribution gives the results closer to the experimentally obtained, with an average tensile strength of 1951 MPa and a failure strain of 1.67%. It should be noted that size effects are present in composite materials and the size of the tested coupon and of the RVE are different.

Table 4.2 and Figure 4.9 also show the results from simulations with an hexagonal arrangement of fibres with the WOW strength distribution. Comparing the random and hexagonal fibre distributions it is possible to see that the stress-strain behaviour is not affected by the arrangement. An interesting characteristic of the stress-strain curves is that there is a high non-linearity previous to the failure of the material, which is usually not seen in the experimental results. This fact will be analysed in more depth in Section 4.1.2.4.

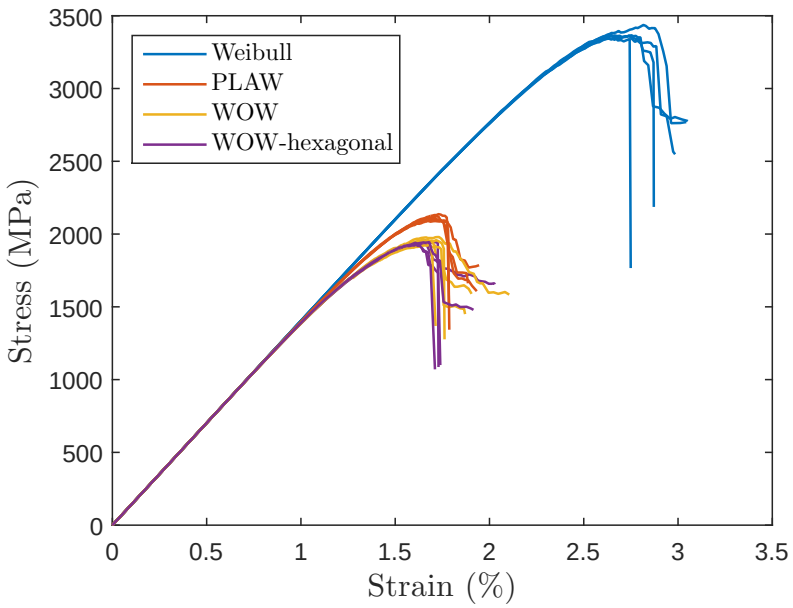

Figure 4.9: Stress-strain curves for AS4 non-hybrid composites using different strength distributions.

4.1.2.3 Influence of the matrix properties

As explained in Section 4.1.1.2 a material model was implemented for the matrix that allows to simulate and elastic-perfect plastic behaviour of the matrix. This has an effect on both stress concentrations and on the ineffective length as shown in Section 4.1.2.1 and, therefore, should also affect the failure process in a multi-fibre composite.

Figure 4.10 shows the stress-strain curves for an AS4 composite where the fibre

strength is characterized by a WOW distribution, for different yield stresses (τ^{u}), as well as different matrix shear modulus (G). Table 4.3 shows the main properties of the failure process for these simulations. From the analysis of these simulations it is possible to conclude that limiting the maximum shear stress in the matrix significantly reduces the tensile strength of the composite material, leading to an earlier failure and, therefore, also a lower failure strain. This change in the stress-strain behaviour is also accompanied by a change in the fracture process, being that the maximum cluster size determined was reduced from 23 to 18 and 14 broken fibres, which relates better with the experimental results of Scott et al.[72] and the modelling results of Swolfs et al. [73]. This can be explained by the lower maximum SCF as seen in Section 4.1.2.1 when a yield stress is considered. When comparing the results for both $\tau^{u} = 50$ MPa and $\tau^{u} = 70$ MPa it is possible to conclude that the stress-strain behaviour does not change much, leading to very similar tensile strengths, only with a slightly smaller tensile strength and critical cluster size.

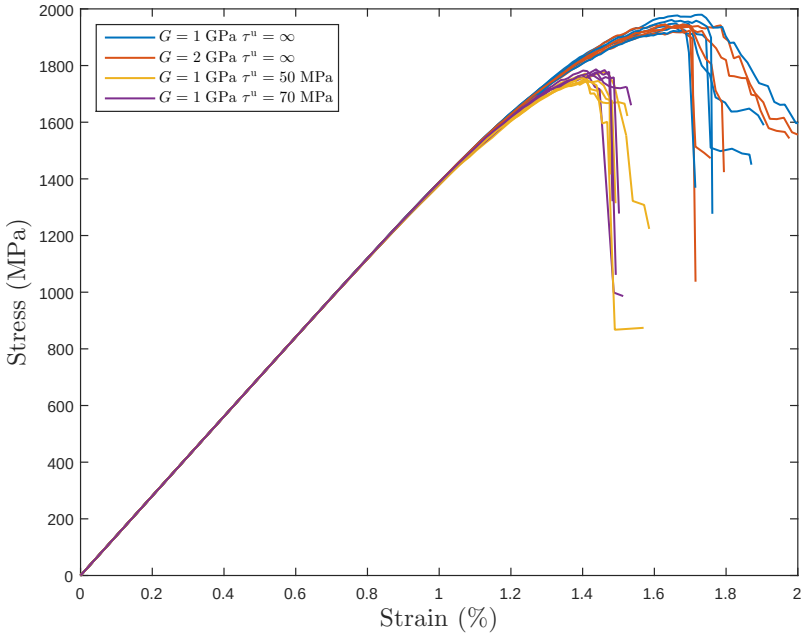

Figure 4.10: Stress-strain curves for AS4 non-hybrid composites with different matrix properties.

The results shown in Figure 4.10 and Table 4.3 enable the study of the influence of changing the matrix shear modulus from 1 to 2 MPa. It is possible to conclude that the matrix shear stiffness does not affect the stress-strain behaviour of the composite, leading to similar tensile strengths and failure strains. However, it clearly affects the maximum cluster size, which is increased from 23 to 72 broken fibres. This means that although the stress-strain curves are similar, the failure process is different, with the fibres breaking more closely with the higher matrix shear stiffness, allowing to the formation of larger clusters before the specimen dramatically looses load carrying capability.

Table 4.3: Maximum stress, failure strain and maximum cluster size for the AS4 considering different matrix properties with the WOW strength model and random fibre distribution.

	Sim.	1	2	3	4	5	Avg.	STDV
$\tau^u = \infty$ $G = 1$GPa	X_T (MPa)	1939	1978	1948	1928	1961	1951	19.61
	ε_f (%)	1.65	1.73	1.66	1.68	1.65	1.67	0.03
	Max. cluster	20	27	36	19	16	23	8.02
$\tau^u = \infty$ $G = 2$GPa	X_T (MPa)	1941	1918	1946	1945	1937	1937	11.48
	ε_f (%)	1.79	1.65	1.68	1.63	1.64	1.68	0.07
	Max. cluster	135	50	62	49	64	72	35.87
$\tau^u = 70$MPa $G = 1$GPa	X_T (MPa)	1784	1798	1848	1842	1839	1822	29.02
	ε_f (%)	1.41	1.40	1.49	1.50	1.52	1.46	0.06
	Max. cluster	12	12	25	25	18	18	6.50
$\tau^u = 50$MPa $G = 1$GPa	X_T (MPa)	1787	1774	1794	1777	1787	1784	8.22
	ε_f (%)	1.45	1.44	1.44	1.46	1.45	1.45	0.01
	Max. cluster	17	11	21	11	10	14	4.80

4.1.2.4 Analysis of cluster formation

The model proposed here can also be used to analyse the development of clusters of broken fibres during the failure process. A cluster is defined following Swolfs et al. [73]: two fibres are considered to be part of the same cluster if (i) the distance between the centres of the two fibres is lower than four times the fibre radius and (ii) the axial distance between break planes was less than ten times the fibre radius. Swolfs et al. [73] define two type of clusters: disperse clusters if the axial distance between the break planes is higher than a fibre radius and co-planar cluster if this distance is lower. In this work a cluster is considered co-planar if the break planes in the axial direction distance themselves by no more than one axial element length. The maximum cluster size for each simulation using the three different strength distributions is shown in Tables 4.2. The maximum cluster size does not significantly change with the different strength distributions, being this maximum around 23-24 fibres in average. However, there are simulations where it has gone as high as 36 fibres and as low as 14 fibres, due to the randomness of the element strength assignment. Although the cluster size does not change with the strength distribution it changes when comparing the hexagonal and random fibre packings: the mean maximum cluster size in the hexagonal packing equal to 32 while for the random packing is 23. In Section 4.1.2.3 it was seen that limiting the shear stress in the matrix elements affects not only the stress-strain behaviour but also the cluster formation, being therefore essential to consider this behaviour when analysing cluster formation.

On the previous sections the behaviour of an AS4 composite material was analysed, however, to further analyse the fibre break clustering process and to compare the numerical results and the experimental results by [4, 72] the behaviour of the T700 carbon composite material is studied. Following Watanabe et al. [38] a bimodal Weibull distribution, which assumes that there are two flaw distributions, is

used to represent the fibre strength. This distribution is characterized by two Weibull modulus and scale parameters. The parameters used are [38]: $\sigma_{01} = 5200$ MPa, $m_1 = 4.8$, and $\sigma_{02} = 6100$ MPa, $m_2 = 12$ at $L_0 = 10$ mm. The elastic modulus considered was 238 GPa and the fibre radius used was $R_f = 3.5$ μm. The matrix used in the experimental results of [4] was M21 which has a tensile modulus of 1.26 GPa. Considering Poisson's ratio of 0.4, the matrix shear modulus used was $G = 0.45$ GPa and the matrix yield stress considered was $\tau^u = 50$ MPa. The RVEs used have a fibre volume fraction of 55% and are of equal dimensions has the ones used in the previous sections.

Five simulations were performed and the results were averaged to minimize the effect of the random fibre strength. As the fibre behaviour was considered linear elastic up to failure the failure strain is overpredicted and equal to 2.61%, comparing with the 1.89%, shown in the experimental results. This large difference can be explained by the typical non-linear behaviour of T700 carbon fibres, which for an 1% increase in strain can have a 20% increase in stiffness [73, 185]. Considering that the material would fail at the same stress level, if the non-linearity was considered, the failure strain would be approximately 2%, which is in better agreement with the experimental result.

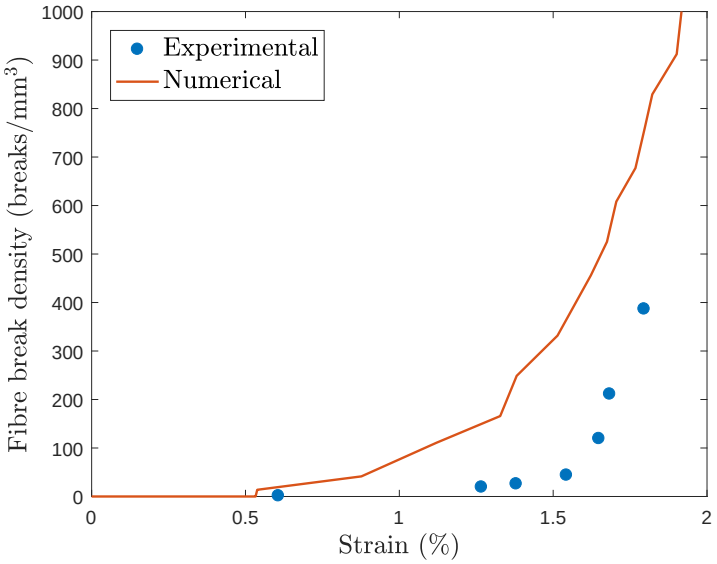

Figure 4.11: Fibre break density in the fracture process: experimental and numerical results for bimodal Weibull distribution.

The average maximum cluster size before the unstable propagation obtained in the simulations was 12.6 fibres, which is slightly smaller than the 14 observed experimentally [4]. Figure 4.11 shows the experimental and numerical comparison of the fibre break density. It can be seen that the fibre break density is clearly overpredicted. The very large discrepancy between the two results can be attributed to the inaccuracy of the Weibull distribution. Swolfs et al. [73] also attributes this difference to the in-situ defect sensitivity reduction of the fibres when surrounded by matrix, altering therefore the actual strength distribution of the fibres within the composite material. Another discrepancy between the experimental results and the

numerical ones is that the fibre break density at failure is much higher in the numerical results. While in the experimental results, before failure, less than 10% of the fibres were broken, in the numerical results this number approximately 30%. These differences in cluster formation process and a higher fibre break density prior to the failure of the material may explain the non-linearity seen in the stress-strain curves prior to failure, which usually are not present in the experimental results.

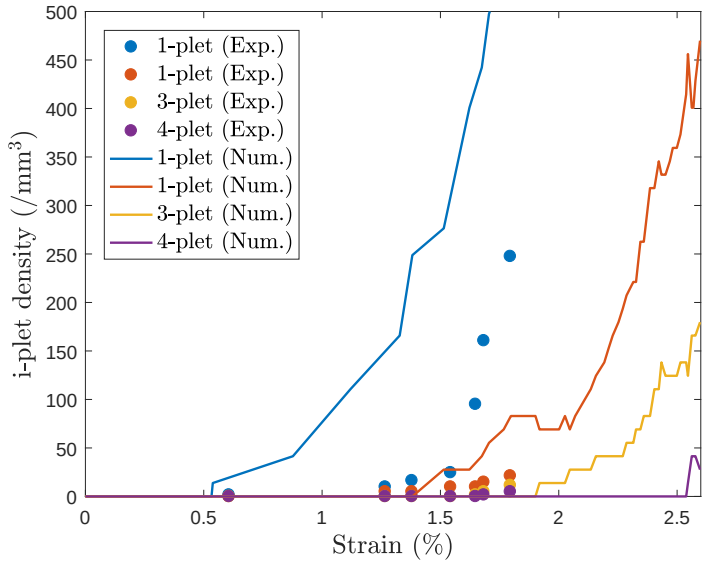

Figure 4.12: i-plet growth during the fracture process as a function of the applied strain: experimental and numerical results for bimodal Weibull distribution.

To better understand the differences in fibre break density between the model and the experimental results the cluster development needs to be analysed in more detail. Figure 4.12 shows the evolution of clusters of different sizes (i-plets) as a function of the applied strain. From the results it is possible to conclude that the singular fibre breaks (1-plet) occur at lower strains and grow rapidly, which are the main contributors for the higher fibre break density in the numerical results. The clusters of two fibres (2-plet) start appearing at similar strains in the numerical and experimental results, however, the cluster with higher number of fibres (3-plet and 4-plet) appear at higher strains in the numerical results. In the experimental results up to 50% of the breaks occurred in clusters [73], however, the model only predicts that 10-20% of the fibre breaks occur in cluster, being the majority of them singular breaks. Additionally only 30-40% of the clusters were co-planar in comparison to a value of 70% found in the experiments. It is interesting to note is that while in the experiments when a cluster was formed it remained of constant size, in the numerical results this was not the case (a cluster increases in size with the applied strain). These results show that there is an under prediction of the SCF in the surrounding fibres when a fibre breaks. Swolfs et al. [13] found that the SCFs are increased if a matrix crack surrounding the broken fibre is considered. This is not considered in the model and can be a source of underestimation of the SCFs. Additionally, it has been shown that when a fibre break there is a dynamic effect that causes an increase in the SCFs in the intact fibres [58, 77].

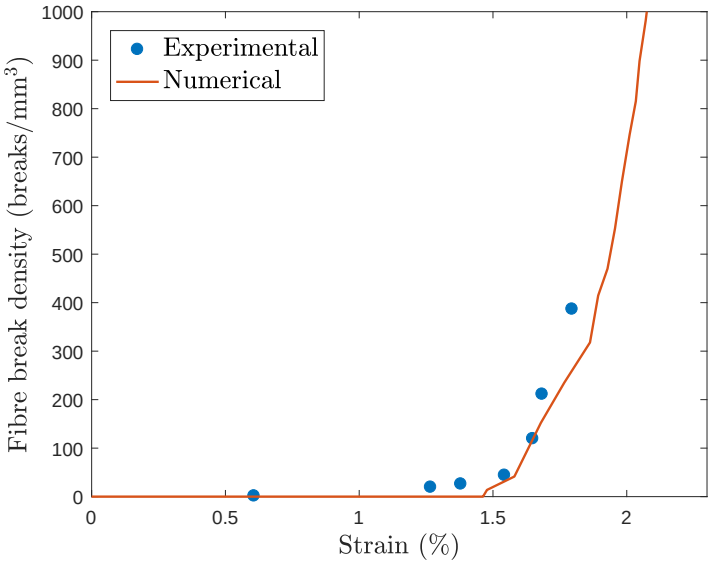

Figure 4.13: Fibre break density in the fracture process: experimental and numerical results for unimodal Weibull distribution.

To circumvent some of the issues with the bimodal Weibull distribution used, [73] fitted an unimodal Weibull distribution to the fibre break density data. A good fit was obtained for $\sigma_0 = 5200$ MPa and $m = 10$ at $L_0 = 10$ mm. Using this distribution and the same matrix properties as in the previous simulations, there was a reduction in the average failure strain to 2.37%, which is closer to the experimental value but still above. This fact may result from the non-linearity of the fibres, but also from the underestimation of the cluster formation. With the fitted Weibull distribution the fibre break density observed numerically is in better agreement with the experimental results (Figure 4.13), however, it is still observed that failure occurs at higher failure fibre break densities.

Regarding cluster formation (Figure 4.14), the results show a better agreement with the experimental results, being the single fibre breaks (1-plet) well predicted, however, there is still an underestimation of the formation of clusters of broken fibres, that only occur for higher applied strains, which causes the failure to occur at higher strains. The reasons for these underestimation of cluster formation have already been mentioned and remain valid for the present case.

To better understand the fibre fracture process and the cluster formation, the fibre break density in each section of the RVE is plotted in Figure 4.15. In this figure it is possible to see the stress-strain curve as well as the percentage of broken fibres in each section of the RVE for all the sections along the fibre direction for three different applied strains, which are marked in the stress-strain curve. The microstructures shown represent the broken fibres within 10 fibre radius in each direction of the critical section, which was at $Z = 0.34$ mm. The critical section and the 10 fibre radius distance in each direction are plotted in the fibre break density image in full and dashed lines. In the microstructure in blue it is possible to see that there are a several broken fibres forming clusters, which grow with applied strain until the

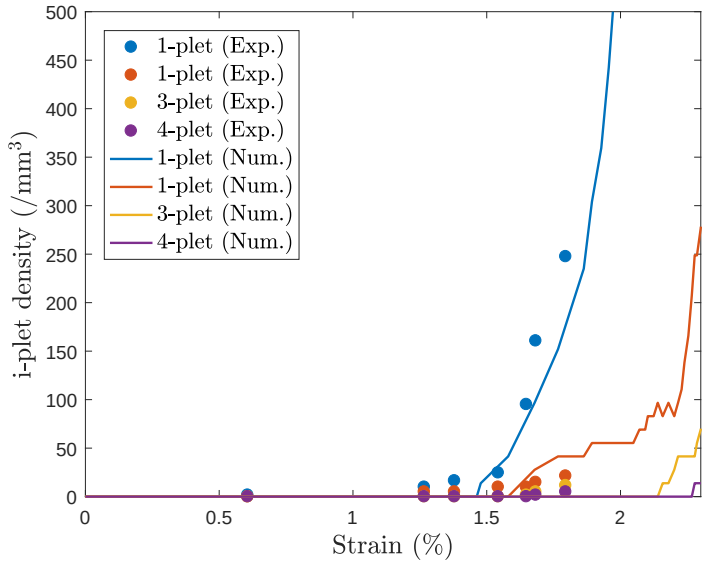

Figure 4.14: *i*-plet growth during the fracture process as a function of the applied strain: experimental and numerical results for unimodal Weibull distribution.

critical strain is achieved (figure in orange) leading to the failure of the material. After its failure (in green) it is possible to see that a large percentage of the fibres are broken and, therefore, the composite looses the load carrying capability.

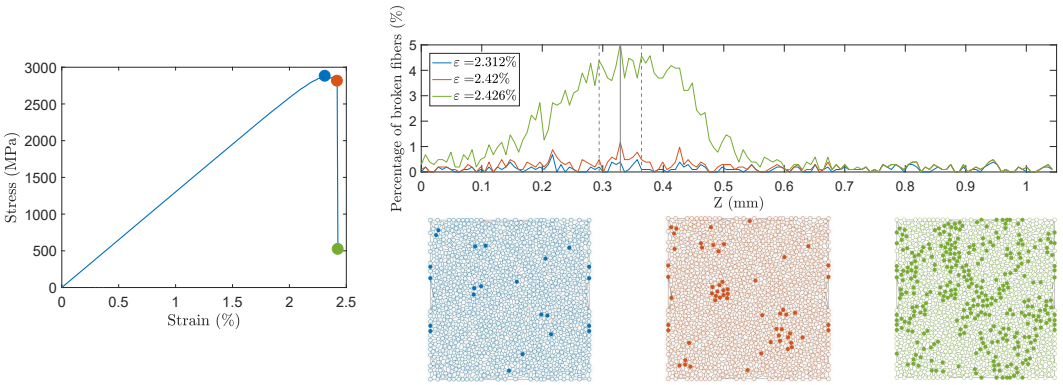

Figure 4.15: Stress-strain curve of the T700 composite with a unimodal Weibull distribution, accompanied by the fibre break density in each section of the composite and the microstructures at the critical section at different stages.

4.1.3 Summary

A spring element model that takes into account a random fibre packing was developed. The model is able to accurately capture the local stress fields surrounding a broken fibre, capturing the ineffective length of a broken fibre, as well as the stress concentrations in the intact fibres that surround a broken one. Unlike other models present in the literature, the stress redistribution resulting from a fibre break is not

enforced and the corresponding stress concentrations in the surrounding fibres arise due to the solution of the global system of equations that governs the problem.

As a fibre dominated failure, the tensile failure of unidirectional composites largely depends on the accurate representation of the strength of the fibre elements. Several statistical distributions for fibre strength are available in the literature. To study their influence on the tensile behaviour of composites several simulations were performed using the traditional Weibull, the Power Law Accelerated Weibull and the Weibull of Weibulls strength distributions. The results were compared with the available experimental data and it was concluded that the Weibull of Weibulls fibre strength distribution leads to more accurate results in terms of the maximum stress. Nonetheless, it should be noted that size effects are present in composite materials and the simulated RVE and tested specimens used for comparison have different sizes.

As the matrix plays a large role in the stress transfer procedure, a study on the effect of matrix properties on the failure process was also analysed. The shear strength has an influence on the UD strength and on the failure progression and cluster formation. The lower the interface strength is, the lower the failure strength of the composite and the maximum cluster size are.

The fibre fracture and cluster development during the failure process was also analysed and compared with existing experimental results. It is concluded that similarly to other available models there was an overprediction of the single fibre breaks while underestimating the formation of clusters of larger sizes, specially planar clusters. This difference was attributed to the fact that the model does not consider the dynamic effects present in the fracture process nor the effects of matrix cracking on the stress redistribution. Nevertheless, more insight on the cluster development and final fracture was obtained.

4.2 Comparison with analytical formulations

This section aims to provide additional insight on the damage development in unidirectional fibre reinforced composites under longitudinal tension and understanding the properties that affect this evolution. This is achieved by understanding the properties that affect the stress redistribution around a broken fibre, how the stress fields around a cluster of broken fibres evolve with the cluster size and its influence in the macro behaviour of the material. The results from the Spring Element Model (SEM), previously presented, are compared with the results from the Progressive Failure Model (PFM) developed by Guerrero et al. [63], using different functions for stress concentration and ineffective length, to understand the models' capabilities to accurately capture the stress redistribution in the tensile failure of fibre composites

4.2.1 Modelling strategies

In this work two very distinct model strategies are used. Firstly, the Spring Element Model (Section 4.1), a simplified finite element model, that inherently accounts for the effects of the different relevant fibre and matrix material properties on the longitudinal failure of composite materials. Secondly, a Progressive Failure Model [63] is used. This model is based on the chain of bundles approach [66] and uses known Stress Concentration Factor (SCF) and ineffective length functions to capture the stress redistribution around a broken fibre. The latter model is used in this work to understand if the current literature SCF and ineffective length formulations are able to accurately capture the damage process in longitudinal failure of composite materials, having the SEM as the baseline.

The SEM is able to accurately capture the stress redistribution after a fibre breaks and the effect of the different properties considered in the model, although using simplified 1D elements. Nonetheless, this model requires the solution of a system of equations at each increment, making it more computationally expensive than the PFM. The latter model uses known functions for stress redistribution and uses a superposition rule to determine the final stress redistribution profiles, which is important when there is interaction between multiple fibre breaks. This approach allows the model to be computationally efficient with reduced computational times.

To more realistically capture the stress redistribution, both models consider a random distribution of fibres. This distribution is generated using a modified version of Melro et al. [68] random fibre generator.

4.2.1.1 Progressive Failure Model

In this section the PFM [63] is briefly reviewed. The model is based on the chain of bundles approach [66] and assumes a RVE with a random distribution of fibres. Similarly to the SEM presented, the fibres are divided into elements of length l^z along their longitudinal direction. Each fibre is denoted with the subscript q, while each plane is denoted with the sub-subscript p. Furthermore, each element has a stochastic strength according to an appropriate statistical distribution. Once an element fails, a damage is distributed over the ineffective length of the broken fibre, whereas stress concentration is applied into the neighbouring intact fibre elements. The stress redistribution is performed according to different analytical formulations, presented in Section 4.2.1.1 and 4.2.1.1. The proposed approach allows to capture both fibre clustering and stiffness loss of composite materials under longitudinal tension.

The constitutive equation of the PFM which relates the stress of each element, $\sigma_{p,q}$, and the strain ε_p is

$$\sigma_{p,q} = \frac{SCF_{p,q}}{\Omega_p} E_f \left(1 - D_{p,q}\right) \varepsilon_p \ , \tag{4.26}$$

where $SCF_{p,q}$ is the stress concentration factor of element p, q and $D_{p,q}$ is the state damage variable which is equal to 1 for broken elements, equal to zero for intact

elements and in between for elements in any stress recovery region. ε_p is the strain of the plane (which is assumed to be the same for all elements of plane p) and Ω_p is a stress ratio which enforces load equilibrium by modifying the stress concentration according to the strain level. Further details on the load equilibrium scheme can be seen in Guerrero et al. [63]. The evolution of $D_{p,q}$ depends on the formulation for the ineffective length considered while $SCF_{p,q}$ depends on the stress concentration model used. In this work, different formulations for damage and SCF are used in the PFM with the objective of understanding if the current analytical formulations available in the literature can capture accurately the stress redistribution around broken fibres. These formulations are shown in the following sections.

Functions for ineffective length

The stiffness loss of the system is simulated by means of the damage variable, which is obtained using a shear-lag model. Two different possibilities arise depending on the matrix behaviour: perfectly plastic or linear elastic.

If the matrix is assumed to be plastic, the ineffective length $L^{\text{in}}_{p,q}$ of a broken fibre element is computed with the Kelly-Tyson shear-lag model:

$$L^{\text{in}}_{p,q} = \frac{E_f R_f}{2\tau^u}\varepsilon_p \ , \tag{4.27}$$

where τ^u is the shear yield strength of the matrix and R_f is the fibre radius. Another possibility is to use the modified Kelly-Tyson model as given in St-Pierre *et al.* [74], which adds a multiplier factor $H_{p,c}$ that depends on the cluster size, capturing the increase in the ineffective length with the cluster size. For the cluster scaling fractor, two fibre elements belong to the same cluster (c), if the distance between the centres of both fibres is below four times the fibre radius and both elements are in the same plane p. Thus, at each plane p, there can be several clusters represented by the subscript p, c. The subscript c ranges from 0 to the number of clusters at plane p, N^c_p. With this method, the ineffective length of a broken element belonging to cluster p, c is given by:

$$L^{\text{in}}_{p,q} = \frac{E_f R_f}{2\tau^u} H_{p,c}\varepsilon_p = \frac{n_{p,c}\pi R_f^2 E_f}{C_{p,c}\tau^u}\varepsilon_p \ , \tag{4.28}$$

where $C_{p,c} = 4s\sqrt{n_{p,c}}$, $n_{p,c}$ is the number of broken fibres on cluster p, c, and s is the mean centre-to-centre distance between each fibre and its closest neighbour, given by $s = R_f\sqrt{\pi/V_f}$, where V_f is the fibre volume fraction.

The damage along the broken fibre within a plastic matrix is simply applied assuming a gradual decrease of damage from 1 at the position of the break, to 0 at both ends of the ineffective length. As fibres may fail many times along their length, different ineffective lengths may overlap. In these cases the highest damage always prevails for each element inside overlapping stress recoveries. Hence an element p, q

is affected by each break in the fibre q at each plane i with

$$D_{p,q} = \begin{cases} \max\left(\dfrac{L_{i,q}^{\text{in}} - |i-p|\, l^z}{L_{i,q}^{\text{in}}}\right) & \forall i : (D_{i,q}=1) \cup \left(|i-p|\, l^z < L_{i,q}^{\text{in}}\right) \\ 0 & \text{otherwise.} \end{cases} . \quad (4.29)$$

If the matrix is assumed to be elastic, Cox's [166, 168] shear-lag model is adapted including the same scaling factor $H_{p,c}$ introduced earlier. The scaling factor can also be imposed to be 1, which disables its effect and leads to the original Cox's model. This parameter is added to the model to capture the influence of the cluster size on the ineffective length [7, 74]. The effective stress of a broken element at each plane p due to a break on plane i follows

$$\tilde{\sigma}_{p,q} = E_f \varepsilon_p \left(1 - \exp\left(-\frac{|i-p|\, l^z}{H_{p,c} R_f}\sqrt{\frac{2G_m R_f}{E_f(s-2R_f)}}\right)\right) , \quad (4.30)$$

where G_m is the matrix shear modulus. Because the model is exponential, the ineffective length at which the load is completely recovered approaches infinite. This would cause all elements along the length of fibre q to have damage not equal to zero but with an extremely low value. Moreover, no SCF would be applied along the fibre, as the SCF is only applied into elements with zero damage. To avoid having an infinite ineffective length it is here considered the ineffective length to be the distance at which 99.9% of the stress is recovered. Taking this into account, the ineffective length is obtained by substituting $\tilde{\sigma}_{p,q} = 0.999 E_f \varepsilon_p$ in Equation (4.30):

$$L_{p,q}^{\text{in}} = \frac{-H_{p,c} E_f \left(s-2R_f\right) \ln(0.001) \sqrt{\dfrac{2G_m R_f}{E_f\,(s-2R_f)}}}{2G_m} . \quad (4.31)$$

The damage along the ineffective length of the broken fibre can now be computed by inserting $\tilde{\sigma}_{p,q} = E_f\,(1 - D_{p,q})\,\varepsilon_p$ in Equation (4.30) resulting in:

$$D_{p,q} = \begin{cases} \max\left(\exp -\dfrac{|i-p|\, l^z}{H_{p,c} R_f}\sqrt{\dfrac{2G_m R_f}{E_f\,(s-2R_f)}}\right) & \forall i : (D_{i,q}=1) \cup \left(|i-p|\, l^z < L_{i,q}^{\text{in}}\right) \\ 0 & \text{otherwise.} \end{cases} . \quad (4.32)$$

It is worth mentioning that the ineffective length for an elastic matrix does not depend on the strain, ε_p. That is, because the stress transfer in the matrix has no upper limit, whereas it is limited by τ^u in the plastic model.

Functions for stress concentration factor

Different analytical models to predict the SCF around fibre breaks are available in the literature [41, 74, 186]. Here, the SCF is represented within two functions, one depending on the in-plane distance δ and the other which depends on the plane position along the ineffective length λ.

The first SCF function adopted in this work is the model developed by Swolfs et al. [41]. This model is based on a micro-mechanical finite element simulation assuming an elastic matrix. The SCF functions for an intact fibre element p, q, around a single broken element i, j are

$$\begin{aligned} \delta_{(q-j)} &= -6.12 \ln\left(\frac{d^{\mathrm{c}}_{q-j} - 2R_f}{R_f}\right) + 7.74 \\ \lambda_{(p-i)} &= \exp -\frac{|i-p|\, l^z}{H_{p,c} R_f}\sqrt{\frac{2G_m R_f}{E_f\,(s-2R_f)}} \quad \forall (i,j) : l^z\,|i-p| < L^{\mathrm{in}}_{i,j} \end{aligned}, \tag{4.33}$$

where d^{c}_{q-j} is the centre-to-centre distance between fibres q and j.

Similarly, Zhou et al. [186] developed a model where the broken fibre contains a debonded and a non-debonded region. For a fair comparison with the reaming models, Zhou's model is used here assuming that no debonding exists. Thus, the functions around a single break are simplified as

$$\begin{aligned} \delta_{(q-j)} &= \frac{2\varphi_{q-j}}{\pi} \\ \lambda_{(p-i)} &= \frac{\sinh \beta_j \left(L^{\mathrm{in}}_{i,j} - l^z\,|i-p|\right)}{\sinh \beta_j L^{\mathrm{in}}_{i,j}} \quad \forall (i,j) : l^z\,|i-p| < L^{\mathrm{in}}_{i,j} \\ \beta_j^2 &= \frac{2}{R_f^2 E_f E_{\mathrm{m}}}\left(\frac{E_f \frac{R_f^2}{s^2} + E_{\mathrm{m}}\left(1 - \frac{R_f^2}{s^2}\right)}{\frac{1}{4G_f}\left(1 - \frac{R_f^2}{s^2}\right) + \frac{1}{2G_{\mathrm{m}}}\left(\frac{s^2}{s^2 - R_f^2}\ln\left(\frac{s^2}{R_f^2}\right) - \frac{1}{2}\left(3 - \frac{R_f^2}{s^2}\right)\right)}\right) \end{aligned}, \tag{4.34}$$

where G_f is the broken fibre shear modulus and $\varphi_{q-j} = \arcsin\left(r_j / d^{\mathrm{c}}_{q-j}\right)$. This model also assumes that the matrix is elastic. This model was developed for a 2D composite, however, it is used in a 3D RVE with a random fibre distribution within the PFM framework. This fact may lead to an overestimation of the SCFs, which is further explored in the following sections.

An alternative model was developed by St-Pierre et al. [74] where the $SCF_{p,q}$ of an intact fibre around cluster c, located at plane i, is given by:

$$\begin{aligned} \delta_{(q-c)} &= I_{i,c}\left(\frac{R_{i,c}}{d^{c}_{q-c}}\right)^{\alpha} \\ \lambda_{(p-i)} &= \begin{cases} \exp -\frac{|i-p| l^z}{H_{p,c} R_f}\sqrt{\frac{2G_m R_f}{E_f\left(s-2R_f\right)}} & \text{Elastic matrix} \\ \dfrac{L^{\mathrm{in}}_{i,c} - l^z\,|i-p|}{L^{\mathrm{in}}_{i,c}} & \text{Plastic matrix} \end{cases} \quad \forall (i,c) : l^z\,|i-p| < L^{\mathrm{in}}_{i,c} \end{aligned}, \tag{4.35}$$

where

$$I_{i,c} = \begin{cases} \dfrac{1}{2\ln(R_t/R_{i,c})} & \text{for } \alpha = 2 \\ \dfrac{(2-\alpha) R_{i,c}^{2-\alpha}}{2(R_t^{2-\alpha} - R_{i,c}^{2-\alpha})} & \text{otherwise.} \end{cases}, \tag{4.36}$$

and $R_{i,c} = s\sqrt{n_{i,c}/\pi}$, $R_t = s\sqrt{N_q/\pi}$ and d^c_{q-c} is the in-plane distance between the centre of the intact fibre p, q and the centre of coordinates of the cluster i, c, whilst $L^{\text{in}}_{i,c}$ is the ineffective length of the cluster, which is equal to the ineffective length of any of the broken elements belonging to the cluster. $n_{i,c}$ is the number of broken fibres in the cluster and N_q is the total number of fibres in the RVE. The value of α is an input parameter of the model, however, according to St-Pierre et al. [74], a value of 2 leads to an excellent agreement between the predicted SCF and finite elements when using a plastic matrix.

As there can be multiple breaks or clusters in the model, a superposition rule is considered. The total SCF for an intact fibre is obtained by linear superposition of all broken elements when using the Swolfs and Zhou models, or by linear superposition of the contribution of all clusters when using the St-Pierre model. However, the SCF in a fibre element is bounded according to the capacity of transferring load to the fibre by shear-lag. This limitation enforces a stress continuity between elements inside any ineffective length (elements where $0 < D_{p,q} < 1$) that are not affected by the SCF, and subsequent intact element ($D_{p,q} = 0$) which can be over loaded by the SCF. Thus, the total SCF of an intact element is

$$SCF_{p,q} = \begin{cases} \min\left(SCF^0_{p,q}, SCF^L_{p,q}\right) & \forall p, q : D_{p,q} = 0 \\ 1 & \text{otherwise,} \end{cases} , \tag{4.37}$$

where $SCF^0_{p,q}$ is the SCF predicted by the linear superposition of the contribution of all breaks using the interacting functions as

$$\begin{aligned} SCF^0_{p,q} &= 1 + \sum_{i=1}^{N_p} \sum_{j=1}^{N_q} \delta_{(q-j)}\, \lambda_{(p-i)}\, [D_{i,j} = 1] && \text{Swolfs or Zhou models} \\ SCF^0_{p,q} &= 1 + \sum_{i=1}^{N_p} \sum_{c=1}^{N^c_i} \delta_{(q-c)}\, \lambda_{(p-i)} && \text{Pierre model} \end{aligned} , \tag{4.38}$$

where here $[\bullet]$ are the Iverson brackets and define 1 if $\bullet$ is true, and 0 if it is false. $SCF^L_{p,q}$ is the SCF limit calculated as the slope defined by the stress gradient of the nearest ineffective length:

$$SCF^L_{p,q} = \min\left(\tfrac{1}{L^{\text{in}}_{i,q}}\, |i - p|\, l\right) \quad \forall i : D_{i,q} = 1 \,. \tag{4.39}$$

4.2.2 Methodology

In this study, both the SEM and the PFM use the same representative volume element (RVE) when computing the same problem. The RVE has a dimension of $75 \times 75 \times 300$ fibre radius and considers a random distribution of fibres. A fibre element size of two times the fibre radius was considered in all cases.

For the SEM all the material properties in study are input directly into the model, making it a robust tool, although more computationally expensive.

For the PFM different functions for SCF and ineffective length are used depending on the model properties. Two methods to determine the ineffective length and fibre

damage variables are available, depending if the matrix behaviour is plastic or elastic. In the case where a plastic matrix is considered Equations (4.28) and (4.29) are used, while for the elastic case Equations (4.31) and (4.32) are used. In any of the cases, $H_{p,c}$ can be a function of the cluster size or equal to 1 if this effect is to be ignored. When $H_{p,c}$ is different than 1, the ineffective length scales with the cluster size. Thus, the larger the cluster the larger the ineffective length. However, when $H_{p,c} = 1$, the ineffective length does not scale with the cluster size. This leads to four possible combinations: plastic matrix ($\tau^u \neq \infty$) with cluster scaling ($H_{p,c} \neq 1$) and without cluster scaling ($H_{p,c} = 1$), and elastic matrix ($\tau^u = \infty$) with and without cluster scaling.

As for the SCF, three analytical formulations were presented in Section 4.2.1.1. Zhou's and Swolf's formulations for the SCF consider the matrix to be elastic and are, therefore, used only with the elastic formulation for ineffective length, i.e. with Equations (4.31) and (4.32). With St-Pierre's model it is possible to change the SCF function by changing the parameter α. The original authors of the model [74] found a good agreement between the formulation and FEM simulations with a plastic matrix for $\alpha = 2$. This value of α is used in this work for the cases where $\tau^u \neq \infty$, in combination with the plastic formulation for the ineffective length (with or without cluster scaling). To be able to use the latter model with an elastic matrix, the authors adjusted the α parameter to obtain a similar stress redistribution profile to the one obtained with SEM with an elastic matrix. For this case, $\alpha = 3.8$ was found to be a good approximation for an elastic matrix. In the cases where $\alpha = 3.8$ is considered, the elastic formulation for the ineffective length is always used.

To understand the properties that affect the stress redistribution around a broken fibre, an in-depth study is done. This study focuses on the effects of material properties, such as fibre elastic modulus and matrix shear modulus, on the stress fields around broken fibres. To quantify the stress redistribution profile three metrics are studied. Firstly, the SCFs in the intact fibres that surround a broken one are analysed. The SCF is defined here as the ratio of the actual stress in an intact fibre over the stress if there were no breaks, given by $E_f\varepsilon$, where ε is the applied strain. To have a comparable metric between the cases in study, the maximum SCF (SCF_{max}) is analysed, which is the maximum of the SCFs in all the intact fibres that surround the broken one. Secondly, the ineffective length (L^{in}), which is the region of the broken fibre that looses stress carrying capacity after that fibre breaks, is also analysed. The ineffective length is here considered to be the distance from the break plane that the broken fibre regains 90% of its stress carrying capacity. Lastly, the radial influence length (R^{inf}) is also analysed. This is defined as the maximum distance in the break plane between the broken fibre and an intact fibre that has a stress concentration higher than 1% (SCF$>$ 1.01). In the presented results, both the ineffective length and radial influence length are normalized by the fibre radius R_f.

To understand the influence of the different parameters on the tensile behaviour of the material, different cases are simulated under fibre tensile loading. For this purpose, randomly generated strength, based on the Weibull distribution [35], is assigned to each fibre element, using the element size for length scaling. This is done by generating a random failure probability for each element, which is then converted

into a respective element strength. Different metrics are proposed to compare the results between cases and models. These metrics are the strength (defined as the maximum stress reached by the material), the cluster size at maximum stress and the fibre break density at maximum stress.

The following sections are organized as follows. Firstly the stress fields around a single break are analysed. The SEM is used to understand what are the main properties affecting the stress redistribution and these results are then compared with the analytical formulations presented. Afterwards, cluster growth is analysed and its effect on the stress redistribution metrics is studied. Finally, the material's tensile behaviour is analysed for the different models and the results are correlated with the different stress redistribution profiles.

4.2.3 Stress fields around a single broken fibre

In this section the stress fields around a single broken fibre are analysed, with focus in understanding the material properties that affect the stress redistribution and how the analytical formulations accurately capture these fields.

4.2.3.1 Factorial design definition

In the spring element model, the stress redistribution depends not only on the elastic and strength properties of the constituents, but also on the actual random arrangement of fibres. To study the effect of each individual property on the stress redistribution, as well as eventual interactions between them, a factorial design of experiments is made.

After a preliminary analysis on the main influencing factors on the stress redistribution, the factors that are considered in this study are the fibre elastic modulus (E_f), the matrix shear modulus (G_m) and strength (τ^u), the fibre volume fraction (V_f) and the fibre radius (R_f). As the SEM is able to take into account all these factors, the factorial analysis will be done in that model and later compared with the analytical stress distribution functions used in the PFM.

To study the effects of the different parameters it is necessary to define levels for these parameters. For all the parameters, with exception of the matrix shear strength, it was decided that two levels are enough for this study. For the matrix shear strength it was decided that three levels would be used, two finite levels and a third considering the matrix to be elastic ($\tau^u = \infty$). Table 4.4 shows the different parameters and the levels that were assigned to them.

With the proposed factors and respective levels, there are forty-eight ($48 = 3^1 2^4$) cases to study. Due to the random nature of the fibre distribution, that affects the stress redistribution around a broken fibre, ten calculations, with different geometries, were done for each case that were averaged to get the necessary parameters for the sensitivity analysis. The results presented are obtained considering a remote applied strain of 2%.

Table 4.4: Parameters and respective levels used in this study

Factor		Level		
		0	1	2
A	E_f (GPa)	70	230	-
B	G_m (MPa)	450	1050	-
C	τ^u (MPa)	50	100	∞
D	V_f	0.4	0.6	-
E	R_f (μm)	3.5	7.0	-

4.2.3.2 Spring element model results

Table 4.5 shows the average results and coefficients of variation for the factors and metrics in study. The values presented are the average of all the cases at each level of the respective factor. This means that any effects of all other factors on this average are disregarded. The coefficients of variation are also shown in this table. It should be noted that both the ineffective length (L^{in}) and the radial influence length (R^{inf}) are in the normalised form, as they are divided by the fibre radius (R_f).

Table 4.5: Average results obtained with the proposed factorial design.

Factor	Level	SCF_{max}		L^{in}		R^{inf}	
		Avg. (-)	CoV (%)	Avg. (-)	CoV (%)	Avg. (-)	CoV (%)
E_f (GPa)	70	1.134	6.3	13.775	27.8	4.299	11.8
	230	1.127	8.2	31.475	34.9	4.247	17.2
G_m (MPa)	450	1.141	7.2	24.742	49.8	4.204	14.0
	1050	1.119	7.3	20.508	57.1	4.342	15.2
τ^u (MPa)	50	1.079	2.4	27.138	45.5	4.474	13.2
	100	1.080	2.5	26.650	45.3	4.455	13.2
	∞	1.232	4.6	14.088	46.5	3.890	13.7
V_f	0.4	1.157	7.8	25.075	47.6	4.723	9.5
	0.6	1.104	5.8	20.175	59.4	3.822	10.7
R_f (μm)	3.5	1.138	8.3	21.850	54.6	4.024	14.2
	7	1.123	6.0	23.400	53.2	4.521	12.9

Figures 4.16 and 4.17 show, respectively the influence of each parameter, at each level, on the maximum SCF and the Pareto front for standardized effects on the maximum SCF. The Pareto chart shows the effect that each factor has on the analysed property. The ones whose standardized effect is larger that 2.05 (red line) are considered statistically representative. From the analysis of the data it is concluded that the main factors affecting the maximum SCF are the fibre volume fraction (V_f), the matrix shear strength (τ^u) and the matrix shear modulus (G_m). Similarly to what was shown in the work of Swolfs et al. [34] for an elastic matrix, an increase in the fibre volume fraction leads to a reduction in the maximum SCF. It is interesting to note that the fibre elastic modulus (E_f) has a small effect on the maximum

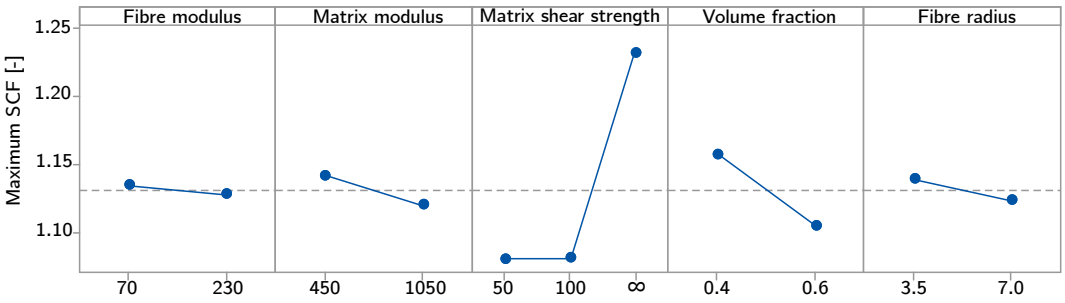

Figure 4.16: Main effects plot for the maximum SCF.

SCF. Another point to note is that the matrix shear strength not only affects directly the SCF but also has a combined effect with other properties such as the fibre modulus (AC) and the fibre radius (CE). This makes the matrix shear strength the most important factor affecting the SCF. Analysing Figure 4.16 it is possible to see that changing the matrix shear strength from 50 to 100 MPa doesn't have an important effect on the SCF. On the other hand, considering the matrix to be linear elastic ($\tau^u = \infty$) has a large effect on the maximum SCF: from $SCF_{max} = 1.08$ for $\tau^u = 50$ MPa to $SCF_{max} = 1.23$ for $\tau^u = \infty$. This high difference between considering the matrix elastic perfectly plastic and linear elastic also occurs in the combined factors AC and CE, which underlines the importance of the matrix shear stress on the predicted stress concentration factors.

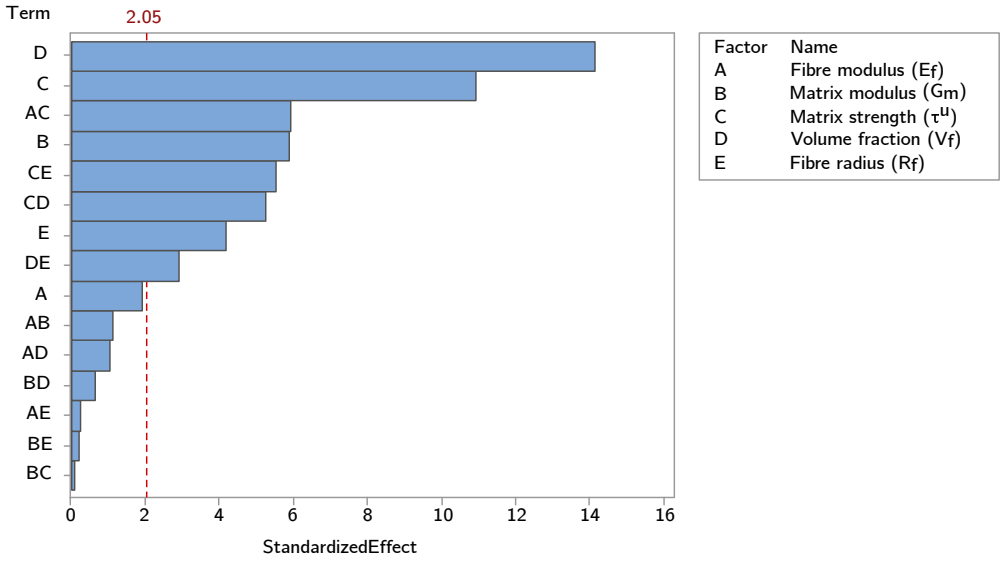

Figure 4.17: Pareto chart of the standardized effects on the maximum SCF.

Regarding the ineffective length, the most influential factor is the fibre elastic modulus. This can be explained by the fact that, with a higher fibre modulus, the stress that needs to be transferred back to the fibre by shear in the matrix is

higher and, therefore, so will be the ineffective length. It should be noted that for this analysis a constant applied strain of 2% was used and, therefore, different fibre stress depending on the fibre modulus. If a constant fibre stress was considered, the higher fibre modulus would lead to higher shear stress in the matrix and, therefore a reduced ineffective length[75]. The ineffective length is affected by the ability of the matrix to transfer the stress back to the broken fibre. This means that it will also be affected by the matrix modulus and the matrix shear strength. The matrix shear modulus directly affects the ineffective length, however, the matrix shear strength affects the ineffective length not only directly but also as a combination with the fibre elastic modulus, similarly to what occurred in the SCF analysis. The fibre volume fraction also has an important effect on the ineffective length, being the second parameter that most affects this property. With a higher fibre volume fraction the ineffective length is reduced, as the homogenized stiffness of the material that surrounds the broken fibre is higher and, therefore, it is easier for the broken fibre to recover its load carrying capacity. This is specially true if $\tau^u = \infty$ as there is no limit in the shear stress that the matrix can withstand. Nevertheless, it should be noted that fibre-matrix debonding was not considered in any of the presented models, which has been shown to increase the ineffective length [44].

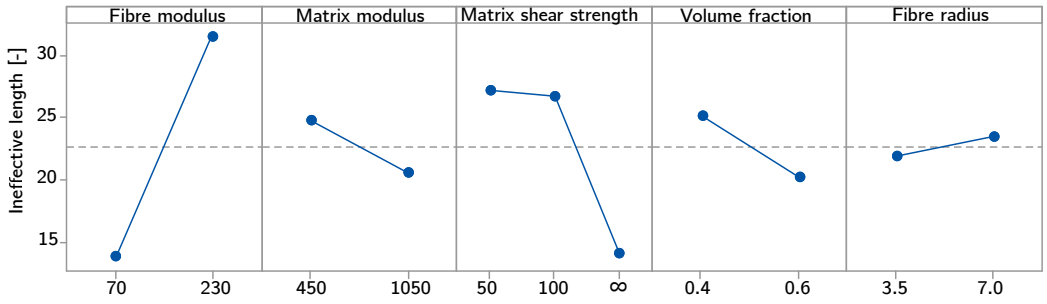

Figure 4.18: Main effects plot for the ineffective length.

The radial influence length (R^{inf}) is a factor that measures the radial distance in the break plane that is affected by the broken fibre. This distance is highly dependent on the actual fibre arrangement that surrounds the broken fibre. The radial influence length is a parameter that strongly depends on the local fibre arrangement. It was seen that for the same case there was a very high variability of this metric, which makes it difficult to conclude about the most influencing factors. Nonetheless, it is seen that the radial influence length depends more on the volume fraction and on the matrix shear strength, being higher when the matrix is considered linear elastic ($\tau^u = \infty$), as the maximum SCF is also higher.

4.2.3.3 Model comparison

In Section 4.2.1.1 different analytical models for the stress concentration factor and ineffective length have been presented. In this section the results from the SEM are compared with the analytical formulations and the validity of each approach is discussed. The RVEs used in the SEM and PFM are the same as in the previous study. The values shown are for a fibre volume fraction of 60%, a fibre radius equal

to 3.5 μm and an applied strain equal to 2%.

Ineffective length

Table 4.6 shows a comparison between the results obtained using the SEM and the respective analytical formulations. Regarding the analytical formulations, when $\tau^u = \infty$, the ineffective length is computed using Equation 4.31, else it is done so using Equation 4.28. Note however, that Equation 4.28 returns the ineffective length at 100% of load recovery while Equation 4.31 returns the ineffective length at 99.9% of load recovery. Here the results shown are for 90% of load recovery. If cluster scaling is considered, the ineffective length is multiplied by the factor $H_{p,c}$ that, for a single fibre break, $V_f = 60\%$ and $R_f = 3.5$ μm, is equal to 0.7625. The results for the ineffective length are shown in the normalized form, therefore, the ineffective length is divided by the fibre radius.

Table 4.6: Ineffective length comparison of the SEM and the various PFM analytical formulations. The average of 10 realisations is shown.

E_f (GPa)	G_m (MPa)	τ^u (MPa)	SEM	PFM	
				$H_{p,c}=1$	$H_{p,c}\neq 1$
70	450	50	15.0	12.6	8.6
		100	15.0	6.3	4.3
		∞	9.6	10.9	7.5
	1050	50	13.0	12.6	8.6
		100	12.4	6.3	4.3
		∞	6.8	7.1	4.9
230	450	50	38.4	41.4	28.4
		100	37.4	20.7	14.2
		∞	16.4	19.8	13.6
	1050	50	35.2	41.4	28.4
		100	34.8	20.7	14.2
		∞	11.2	12.9	8.9

The analytical formulations overall capture similar ineffective lengths as the SEM, if no cluster scaling is considered ($H_{p,c} = 1$). However, if $\tau^u \neq \infty$ is considered, while the SEM results depend on the matrix shear modulus, the analytical formulations do not. In the case of an elastic matrix ($\tau^u = \infty$) this dependency is well captured, being the results from the SEM very similar to the analytical formulation. If cluster scaling is considered, then the ineffective length is reduced, but the variances are the same as if no scaling is considered. It is interesting to note that for $E_f = 70$ GPa and $\tau^u = 50$ and 100 MPa, the ineffective length for the SEM does not change, while it changes using the analytical formulations. This difference is attributed to the fact that the analytical models considered the matrix to be perfectly plastic, while the SEM considered the matrix elastic perfectly plastic.

Stress concentration factor

In Section 4.2.1.1 different analytical formulations for the SCF in the intact fibres that surround a broken one were presented. These formulations are based on different assumptions and, therefore, will result in different SCFs. Table 4.7 shows the maximum SCF results of the different analytical formulations as well as results using SEM for different cases. These cases were formulated taking into account the most influencing factors in Section 4.2.3.2. For the SEM, results are shown for different matrix shear strengths. Similarly, using St-Pierre's model, different values for α are used. $\alpha = 2$ for a plastic matrix [74], while $\alpha = 3.8$ was chosen for an elastic matrix as the SCF distribution function has a good agreement with the SEM with $\tau^u = \infty$.

Table 4.7: Maximum stress concentration factor of the SEM and the various PFM analytical formulations. The average of 10 realisations is shown.

V_f	E_f (GPa)	G_m (MPa)	SEM			PFM			
			50	$\tau^u =$ 100	∞	Swolfs	Zhou	St-Pierre $\alpha =$ 2	3.8
0.4	70	450	1.127	1.127	1.315	1.205	1.309	1.082	1.287
		1050	1.095	1.096	1.285	1.205	1.309	1.082	1.287
	230	450	1.093	1.093	1.341	1.237	1.319	1.087	1.319
		1050	1.071	1.072	1.324	1.237	1.319	1.087	1.319
0.6	70	450	1.083	1.083	1.193	1.26	1.324	1.056	1.155
		1050	1.061	1.061	1.168	1.26	1.324	1.056	1.155
	230	450	1.060	1.061	1.218	1.252	1.322	1.0558	1.152
		1050	1.044	1.044	1.202	1.252	1.322	1.0558	1.152

The SEM captures the changes in stress redistribution from all the parameters that affect the model. On the contrary, the analytical formulations are not able to do so. For instance, none of the models captures the changes in the SCF with the matrix shear modulus. Regarding the effect of the fibre volume fraction on the SCF, all models capture some change with this parameter. In the case of Swolfs and Zhou's models, this effect is captured due to a change in the distance between the fibres, however, St-Pierre's model directly depends on the fibre volume fraction. On average, the lower the volume fraction, the higher the SCF should be [34]. This is captured by the SEM as well as St-Pierre's formulation. However, with Swolfs and Zhou's models the SCF increases with increasing the volume fraction, as the fibres are closer together and, therefore, the distance between them is smaller. This difference in trend can be explained by the fact that Zhou's and Swolfs' models consider that there is a direct dependency between the inter fibre distance with the volume fraction, which is not the case in randomly distributed fibres. For lower volume fractions, the stress from the broken fibre is redistributed mainly to the closest fibre, as the fibres are further apart, while for higher volume fractions the stress is more evenly redistributed among the neighbouring intact fibres. Regarding the effect of the fibre elastic modulus, it was shown in Section 4.2.3.2 that this parameter did not highly influence the SCF, but did so when combined with the matrix shear strength. None of the analytical formulations capture directly this

effect. From the results, it is possible to see that Swolfs and Zhou's formulations give similar results to the SEM with $\tau^u = \infty$ and St-Pierre's model with $\alpha = 3.8$, which represent an elastic matrix. For the case of a plastic matrix, the results from SEM and St-Pierre's model are in good agreement, disregarding the changes in the SCF with the value of the matrix shear modulus. It should be noted that, although Swolfs' and St-Pierre's models do not capture directly the effects of several parameters, finite element simulations can be used to calibrate the SCF functions for each material.

The radial influence length was not included in this study as it was similar in all the presented models.

4.2.4 Multiple fibre break analysis

In this section, the effects of fibre break clustering on the stress redistribution are studied. As the interaction between the fibre breaks and cluster formation is considered to be the basis of the failure of composite materials, it is important to understand how the stress redistribution changes with an increase in cluster size. To understand this effect, the models presented were used to study the effects of cluster size on the maximum SCF, ineffective length and radial influence length. To do so, a RVE with a random distribution of fibres with radius equal to 3.5 μm and a fibre volume fraction of 60% was considered. The fibres were considered to have a modulus equal to 230 GPa, which is representative of carbon fibres. From this RVE 10 fibres were selected randomly to initialize the cluster formation. A remote tensile strain of 2% is applied. To simulate the cluster formation, after each break, the next fibre with the higher SCF is broken, leading to an increase in the number of broken fibres in the cluster and changes in the stress redistribution. It should be noted that the path of cluster growth is not known a priori and different models may lead to different cluster shapes with the same number of broken fibres.

The ineffective length of a cluster was considered to be the largest ineffective length of the individual broken fibres that are part of that cluster, being here considered the length at which the fibre recovers 90% of its load carrying capacity. The analytical formulations presented in section 4.2.1.1 were used in the PFM, and are independent on the model for SCF used. The results for the ineffective length are shown in the normalized form the ineffective length is divided by the fibre radius.

As shown in Figure 4.19, the formulations for the ineffective length that use the base Kelly-Tyson (plastic $H_{p,c} = 1$) and Cox (elastic $H_{p,c} = 1$) models do not scale with the number of broken fibres. This drawback can, however, be solved by using the size cluster scaling proposed by St-Pierre et al. [7, 74], i.e. $H_{p,c} \neq 1$. For both cases, elastic and plastic matrix, the scaling trend is similar to that obtained with the SEM. The ineffective lengths obtained with the SEM are, however, always larger than those predicted by the analytical simulations, being the difference larger for larger cluster sizes. Nonetheless, it should be noted that some differences in the ineffective length may be due to the different cluster shapes formed with the different models.

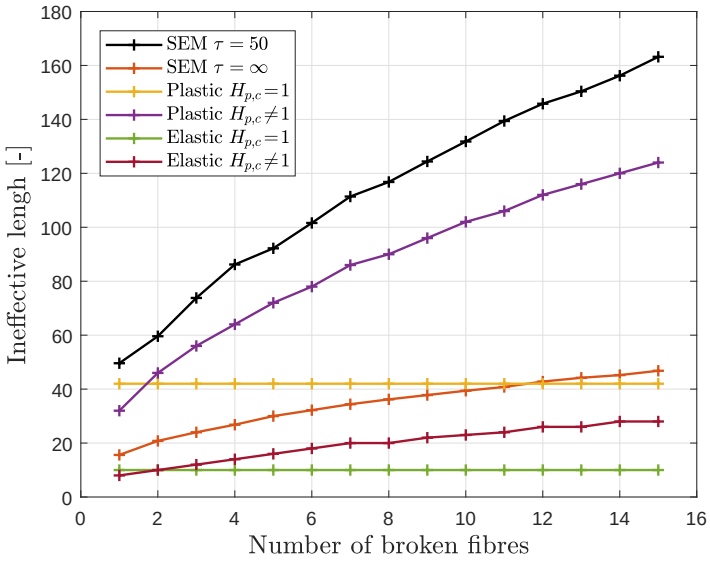

Figure 4.19: Effect of the cluster size on the ineffective length. The average of 10 realisations is shown.

Figure 4.20 shows the scaling of the maximum SCF as a function of the number of broken fibres within a cluster. In addition to the results from the SEM and PFM models, the analytical solutions proposed by Hedgepeth [75] for 2D and Hedgepeth and Van Dyke [86] for a 3D hexagonal fibre arrangement are also shown.

As expected, all models are able to capture the increase in SCF due to the increase in the number of broken fibres. This can be expected as there is additional stress that needs to be redistributed due to the increase in the number of broken fibres. Nonetheless, the different models have different trends. Zhou's model predicts the highest SCF for a single break, a trend that scales with the increase in broken fibres, reaching values of maximum SCF over 3. This value is considered too high as unstable propagation of the cluster should occur before this SCF level is reached. Nonetheless, it should be noted that this model is based on a 2D planar fibre arrangement and, therefore, leads to an overestimation of the SCFs in a 3D composite. The remaining models have a much lower scaling with the number of broken fibres, being that for St-Pierre's model, the SCF functions directly depend on the number of broken fibres. Comparing the models that consider the matrix plastic (SEM $\tau^u = 50$, SEM $\tau^u = 100$ and St-Pierre $\alpha = 2$), it is possible to see that all the models give very similar results, with a low scaling of the maximum SCF. The moderate increase in the maximum SCF is due to the fact that the matrix is not able to transfer more stress to the closest fibres, due to the shear stress limit, therefore, this stress needs to be redistributed to fibres further away from the cluster, not affecting the maximum SCF. When the matrix is considered elastic (SEM $\tau^u = \infty$, Swolfs, Zhou and St-Pierre $\alpha = 3.8$), the stress redistribution is more local and, therefore, the maximum SCF has a more pronounced increase with the number of broken fibres. In this case, the SEM has a similar trend as Swolfs' model, being that the SEM has lower SCF for small clusters and higher for the larger clusters (see Figure 4.20). St-Pierre's model, in this case, predicts a large increase on the

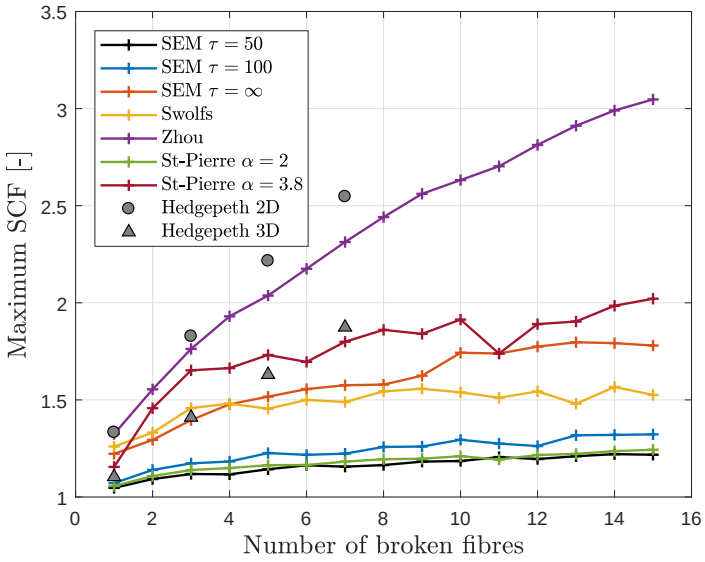

Figure 4.20: Effect of the cluster size on the maximum SCF. The average of 10 realisations is shown.

SCF from a single broken fibre to a cluster of two broken fibres, being the increase in SCF with each additional fibre reduced for larger clusters. Interestingly, there is a decrease in the maximum SCF for a cluster of 11 fibres. For different models, it is possible to see that there is a decrease in SCF when the number of broken fibres increases. This should be a consequence of the random fibre arrangement. Comparing the results from the SEM and PFM with the analytical solutions by Hedgepeth [75, 86], it is possible to see that Zhou's model is in good agreement with Hedgepeth as both are based in a 2D planar arrangement of fibres. The 3D solution shows a similar scaling as the remaining models, however, it should be noted that while the analytical formulation is for a periodical hexagonal arrangement of fibres, the results from the SEM and PFM are for a random distribution of fibres.

The radial influence length is the distance in the failure plane that is affected by more than 1% of stress concentration. This distance, for the cases with more than one broken fibre, was measured to the geometrical centre of the cluster. Figure 4.21 shows the scaling of the radial influence length with the number of broken fibres within a cluster. All models predict an increase in the radial influence length with an increase in cluster size, as expected. Zhou's model has a much higher radial influence length that scales less with the cluster size. This is due to the nature of the SCF function, whose shape causes a large region surrounding the broken fibres to have a SCF higher than 1%, which was the value used to limit the radial influence length. The other models have a very similar radial influence length for a single broken fibre, between 3.8 and 4.8 times the fibre radius. However, the models scale different with the increased cluster size. Swolfs' model predicts a lower scaling in radial influence length as the matrix is considered elastic. Similarly, the SEM and St-Pierre models show a lower increase in radial influence length for the elastic case ($\tau^u = \infty$ and $\alpha = 3.8$). Both the SEM and St-Pierre models show very similar scaling of the radial influence length with the cluster size for both the elastic and

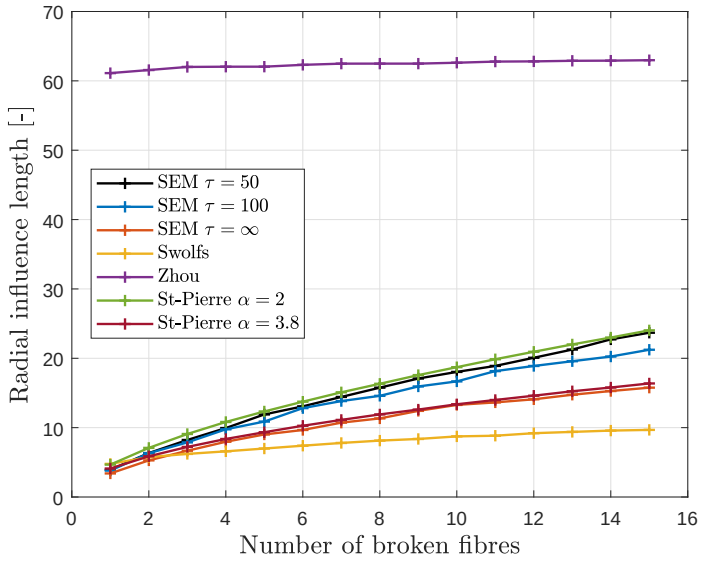

Figure 4.21: Effect of the cluster size on the radial influence length. The average of 10 realisations is shown.

plastic cases. The similarity between these two models can also be observed for the other parameters studied, namely the maximum SCF.

4.2.5 Tensile behaviour

In this section, a comparison between the several models is done at the RVE scale with the objective of understanding how the differences in the local stress fields affect the tensile behaviour and cluster formation.

To understand these effects, the same study was done in two types of fibres, one carbon fibre and one glass fibre. The variance of three factors was studied for each type of fibre. The factors selected are the matrix shear modulus (G_m), the matrix shear strength (τ^u) and the fibre volume fraction (V_f), as they affect the stress redistribution the most (Section 4.2.3.2). For the matrix shear modulus and volume fraction the same levels as in Section 4.2.3.2 were explored, however, for the matrix shear strength only two levels were considered: $\tau^u = 50$ MPa and $\tau^u = \infty$. The third level was removed as the effects of changing the shear strength from 50 to 100 MPa were reduced. A full factorial study was performed with a total of eight cases for each type of fibre. For each case five simulations were performed. The fibre strength is assigned to each fibre element randomly with a Weibull distribution. The Weibull properties (σ_m, m and L_0) and the remaining material parameters are shown in Table 4.8.

Table 4.9 shows the summary of the average results of 10 simulations for the different models with distinct input parameters. In this section, and similarly to other works in the literature [73, 187], two fibres are considered to be in the same cluster if their centres are within four times the fibre radius and the fibre break

Table 4.8: Fibre properties used for RVE study [21, 29].

Fibre	R_f (μm)	E_f (GPa)	σ_0 (MPa)	m	L_0 (mm)
Carbon	3.5	234	4275	10.7	12.7
Glass	7.0	70	1550	6.34	24

planes are within ten times the fibre radius in the longitudinal direction. The tensile strength (X_t) is calculated by means of the rule of mixtures.

Table 4.9: Carbon RVE simulation results for different models and parameters. The average of 10 realisations is shown.

				SEM		St-Pierre			Swolfs			Zhou		
V_f	τ^u (MPa)	G_m (MPa)	X_t (MPa)	Max. cluster	Break density (/mm^3)	X_t (MPa)	Max. cluster	Break density (/mm^3)	X_t (MPa)	Max. cluster	Break density (/mm^3)	X_t (MPa)	Max. cluster	Break density (/mm^3)
0.4	50	450	1784	5.4	2228	1923	11.2	5045	-	-	-	-	-	-
		1050	1802	6.0	2809	1954	18.4	5169	-	-	-	-	-	-
	∞	450	1844	9.8	3184	1646	2.4	586	1963	20.0	7151	1810	4.4	1833
		1050	1921	11.2	4708	1778	4.0	1200	2050	43.2	9291	1834	3.6	1706
0.6	50	450	2698	4.4	3696	2843	8.2	6925	-	-	-	-	-	-
		1050	2718	5.8	4600	2856	18.4	7328	-	-	-	-	-	-
	∞	450	2911	11.4	6994	2695	7.8	2482	2859	14.2	5440	2585	2.8	1526
		1050	2952	6.6	7331	2828	13.6	3630	2978	20.6	8229	2598	3.2	1446

Figure 4.22 shows the results for the different models and cases where the matrix is considered linear elastic ($\tau^u = \infty$). For a constant fibre volume fraction the difference in strength predicted by the different models is small and all of them predict accurately the increase in strength (X_t) with the increase in fibre content. The change in the matrix shear modulus has only a small effect in the predicted strength, but all models predict an increase in the strength with the increase in matrix shear stiffness. It should be noted that all predicted strengths are high, compared to typical composite material strengths. This is due to the fact that the Weibull distribution is scaled to very small lengths (7 μm) which leads to very high element strengths. This leads to an overprediction of the strengths, as seen in Section 4.1. Additionally, the RVE analysed has a small volume compared to that of a typical specimen used to characterize composite material strengths. Due to the size effects present in composite materials [44, 64], care must be taken when comparing the numerical results with experimental ones. Nonetheless, the comparison between the results of the different models should not be affected by this fact, as similar strategies to generate the strength of the elements were used.

Regarding the maximum cluster size, with exception of Swolfs' model, all models predict similar critical cluster sizes in all cases. In Swolfs' model, the maximum predicted cluster size is 43 fibres, which is a very high value compared with the data available in the literature [72, 73, 187]. Similarly, the models predict a very high fibre break density at peak stress, which is not seen in the available experimental data [72, 73].

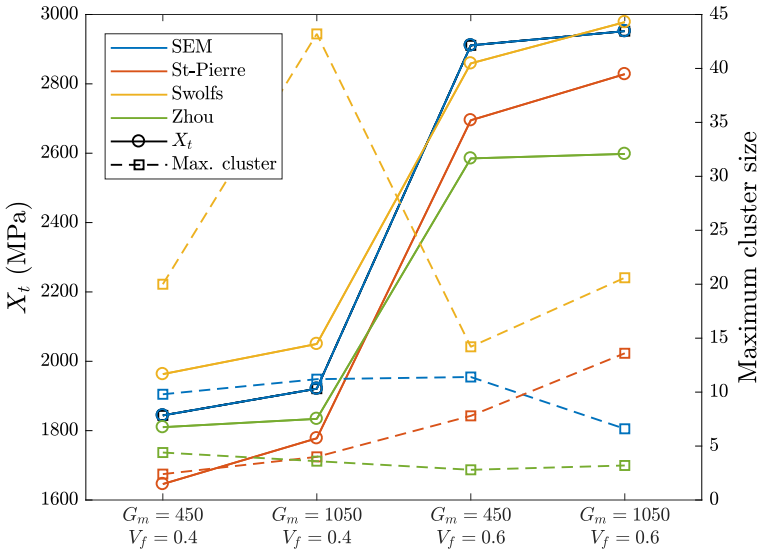

Figure 4.22: Tensile strength and maximum cluster size for the elastic matrix cases ($\tau^u = \infty$) for carbon fibre. The average of 10 realisations is shown.

Figure 4.23 shows the predicted strength and maximum cluster size for the cases where the matrix is considered plastic. These results are only available for the SEM and St-Pierre's model. Both the SEM and the PFM with St-Pierre's SCFs have the same trends, being the predicted cluster size higher for St-Pierre's model.

It is interesting to note that the trends observed, in moving from an elastic to a plastic matrix, with the SEM and St-Pierre's models are very distinct (Table 4.9). While for the SEM the maximum cluster size and the strength are lower when the matrix is considered plastic ($\tau^u = 50$ MPa), with the other model the opposite happens. With PFM it is seen that the material strength obtained is lower in the elastic case than in the plastic case and so is the predicted maximum cluster size. Similarly, the fibre break density at peak stress is lower in the elastic cases for St-Pierre's model, while it is lower in the plastic cases for the SEM.

Analysing the evolution of the SCFs as a function of the cluster size (Figure 4.20) it is possible to see that for St-Pierre's model the SCF increases rapidly for a small cluster size when the matrix is considered elastic. This rapid increase leads to the earlier formation of clusters of higher dimensions. In addition the authors observed that the formation of cluster of 3-4 fibres leads to the failure of the material, therefore, resulting in a lower strength and failure strain. With the SEM this increase is more gradual and always with lower SCF, for clusters with more than a broken fibre. This explain the premature failure predicted by St-Pierre's formulation when $\alpha = 3.8$, e.g. elastic matrix, is considered. Nonetheless, it should be noted that this can be avoided by adjusting α for several cluster sizes instead of adjusting it to accurately capture the stress fields around a single break, as was done for $\alpha = 3.8$.

Similarly to what was done for carbon fibre, Table 4.10 shows the influence of

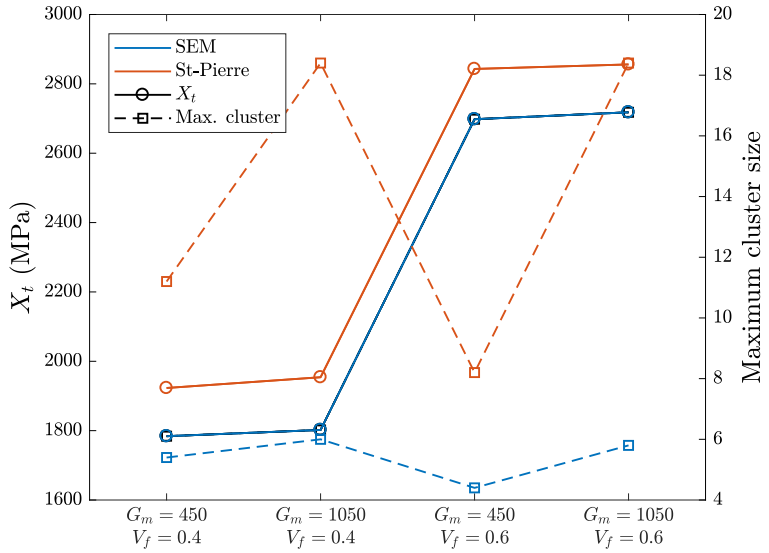

Figure 4.23: Tensile strength and maximum cluster size for the plastic matrix cases ($\tau^u =$ 50) for carbon fibre. The average of 10 realisations is shown.

several material parameters on the tensile behaviour of composite materials. In this case glass fibres are used, whose properties are shown in Table 4.8. Similar trends are found between the glass and carbon cases. All modelling strategies are able to capture the increase in tensile strength with the volume fraction. For the SEM there is also a increase in the tensile strength if the matrix is considered elastic and if the matrix shear modulus is increased. The same effect of the matrix shear modulus is seen in the remaining models. However, similarly to what occurred for the carbon cases, with St-Pierre's model, there is a decrease in the strength in the cases where the matrix is considered linear elastic. Again this is in contrast with the results obtained with the SEM. However, in this case the maximum cluster size predicted with St-Pierre formulation is higher in the elastic cases than in the plastic cases.

Table 4.10: Glass RVE simulation results for different models and parameters. The average of 10 realisations is shown.

			SEM			St-Pierre			Swolfs			Zhou		
G_m (MPa)	τ^u (MPa)	V_f	X_t (MPa)	Max. cluster	Break density (/mm^3)	X_t (MPa)	Max. cluster	Break density (/mm^3)	X_t (MPa)	Max. cluster	Break density (/mm^3)	X_t (MPa)	Max. cluster	Break density (/mm^3)
0.4	50	450	810	14.8	2387.0	938	24.4	2550.1	-	-	-	-	-	-
		1050	817	29.8	2637.8	974	61.8	2590.8	-	-	-	-	-	-
	∞	450	917	517.2	7694.4	909	291.2	3503.0	1010	247.0	5329.5	870	11.4	1344.8
		1050	964	1311.2	10240.3	968	450.4	4529.3	1108	1018.6	7631.5	921	17.0	1444.3
0.6	50	450	1233	57.6	3566.6	1350	103.0	3598.4	-	-	-	-	-	-
		1050	1241	56.0	3479.5	1375	78.0	3436.0	-	-	-	-	-	-
	∞	450	1471	62.5	4870.7	1462	585.6	7004.0	1507	733	7294	1280	23.8	1744.3
		1050	1524	70.0	5477.6	1549	1017.6	9252.1	1616	2109	10223	1329	20.0	1734.6

Regarding the maximum cluster size it is seen that the predicted cluster size is overall higher than for the carbon cases, which is expected as there is a higher dispersion in the strength of glass fibres (lower Weibull modulus m). However, for the cases where the matrix is elastic the values for the maximum cluster size are very high, sometimes higher than the total number of fibres in the RVE. In these simulations two fibres were considered to be in the same cluster if their in-plane distance was lower than four times the fibre radius and the break plane distance lower than ten times the fibre radius. As the fibre radius of the glass fibres was considered twice the one from carbon, the volume considered for two fibres to belong in the same cluster is larger. On the contrary, the ineffective length of the glass fibres are lower due to the lower fibre elastic modulus. This makes it possible for the same fibre to break more than once in the region considered for the cluster and, therefore, overpredicting the cluster size. This factor makes it necessary to have a better definition of a cluster of broken fibres, as in some cases, the current definition [72, 73, 187] leads to erroneous results.

4.2.6 Summary

In this section an extensive analysis on the stress fields and stress redistribution due to fibre failure in fibre reinforced composites under longitudinal tension was performed. The results from the SEM were compared with the results from a progressive damage model, also with a random fibre distribution, with different ineffective length and stress concentration factor formulations.

An analysis of the effects of the main model input parameters on the stress fields around a broken fibre was performed using the SEM. From this study it was possible to conclude that different materials with different input parameters, such as fibre modulus, matrix shear stiffness and matrix yield strength, leads to very distinct stress redistribution profiles. In this study three parameters were analysed: maximum stress concentration factor, ineffective length and radial influence length. These parameters were considered to define the stress field surrounding a broken fibre. It was observed that the maximum SCF depends on different input parameters, the most critical being the fibre volume fraction. In addition, it was observed that the matrix yield strength has a large influence on the maximum SCF, mainly when the matrix is considered elastic or plastic. Interestingly, it was seen that the fibre modulus did not have a high effect on the SCF, however, the combination between the fibre modulus and the matrix yield strength affects the SCF. As for the ineffective length, it was seen that the fibre modulus as well as the matrix yield strength were the most influencing factors on this property. Regarding the radial influence length, it was observed that there was a small variation with different input parameters, however, it was found that there was a large variation depending on the local fibre arrangement.

Comparing the results from the SEM with the results from the analytical formulations used within the progressive failure model framework, it is concluded that most models do not capture the dependency of the input parameters on the stress redistribution profile. In most cases, fitting is necessary to obtain accurate stress

redistribution functions and, therefore, care must be taken when considering the same SCF function for different materials. It was also seen that there is a large difference between considering the matrix linear elastic or elasto-plastic.

The stress fields that surround a cluster of broken fibres were also analysed. The different models have different evolutions of the maximum SCF, ineffective length and radial influence length as a function of the cluster size. In general, in the models where the matrix was considered linear elastic, the maximum SCF increases more rapidly with the number of broken fibres and the ineffective length has a smaller increase, when compared with the models that consider the matrix plastic. It should be noted that several models do not consider the increase in ineffective length with the cluster size, however, it was seen that the cluster size has a large effect on the ineffective length, as previously shown in St-Pierre et al. [7, 74]. Adding a factor that scales with the cluster size leads to similar results between the analytical formulations and SEM.

For the representative volume element simulations it was shown that the different presented models predicted different strengths. The main difference is between models considering the matrix elastic or elasto-plastic. Using St-Pierre's model for the SCF functions when the matrix was considered elastic ($\alpha = 3.8$) the predicted strength was lower than when the matrix was considered plastic ($\alpha = 2$). However, the results predicted by the spring element model showed the opposite trend. Regarding cluster formation, it was shown that the maximum cluster size is highly dependent on the input properties of the models. Furthermore, it was seen the current used definition for cluster [15, 187] can lead to erroneous results. In the glass cases, there were clusters with more breaks than the number of fibres in the RVE, meaning that the same fibre was broken more than once in the same cluster.

This work aimed at further developing the understanding of the damage propagation and cluster formation in unidirectional composites. It was shown that more understanding on the phenomena that control failure of unidirectional composites under longitudinal tension and more experimental data are needed. Nonetheless, it is important that the models take into account the real material input parameters as well as an accurate representation of the microstructure to better capture the material behaviour. Therefore, care should be taken when using stress concentration factor functions from a different material system.

4.3 Dynamic model

As previously mentioned, there are several models available in the literature to predict longitudinal tensile failure of composite materials [7, 29, 58, 63, 66, 73–75, 84, 85, 87, 89, 95]. Although being able to predict the tensile stress-strain behaviour of these materials, there are still some gaps between the actual mechanisms that occur in the failure of process composite materials [188] and those predicted by the models [41, 73], as was seen in the previous sections. The state of the art models consider static equilibrium to redistribute the stress of the broken fibre into the surrounding intact ones. However, fibre failure is a dynamic process where the

strain energy of the fibre is converted into kinetic energy. Fibre failure causes a stress wave that propagates along the broken fibre, as well as in the surrounding intact ones [75–77, 79]. This dynamic phenomenon causes a transient increase in the stress concentration of the fibres that surround a broken one, thus increasing the probability of failure of these fibres. According to several authors [73, 79], the inclusion of the dynamic phenomenon in the models to predict the longitudinal tensile failure of composites can help to bridge the gap between the experimental and numerical results. Hedgepeth [75] first pointed out the importance of dynamic stress concentration and found that for a 2D array of parallel fibres the maximum dynamic Stress Concentration Factor (SCF) is higher than the static. This model, based on shear lag assumptions, was later extended for out of plane SCFs by Ji et al. [77], which confirmed that the highest SCF occurs in the fracture plane. Recently, Ganesh et al. [79] presented a 2D FEM that lead to similar results to Hedgepeth's formulation [75]. The authors also showed that the models that consider shear lag assumptions tend to over predict the maximum SCF. In the current literature, there is a lack of data on the dynamic effects on fibre failure and, to the best of the authors knowledge, there is no 3D model that takes this phenomenon into account.

In this section the previously developed Spring Element Model is modified to incorporate dynamic effects, and is used to study how considering fibre fracture a dynamic problem affects the tensile behaviour and cluster formation in the longitudinal failure of fibre reinforced composites.

4.3.1 Micro-structure generation and finite element discretization

As this model builds on the previously presented SEM (section 4.1), the microstructure and RVE generation strategies are the same and is explained in Section 4.1.1.1. Additionally, there is no change in the longitudinal and shear elements used, therefore, the stiffness matrices previously developed are carried on to the present model.

Due to the dynamic nature of the model it is necessary to determine the mass matrices of the the longitudinal fibre elements and the transverse shear matrix elements. Additionally, and to stabilize the dynamic model it is necessary to add damping to the model. This ensures the stability of the model and avoids large reflections of the stress waves, caused by fibre failure, on the boundaries of the RVE, which would lead to an unstable model.

4.3.1.1 Mass matrices

The mass matrix $\mathbf{M}_f^e$ of longitudinal fibre elements is given by:

$$\mathbf{M}_f^e = \int_0^{l^z} A_f^e \boldsymbol{\mathcal{N}}_f{}^T \rho_f^e \boldsymbol{\mathcal{N}}_f dz \ , \tag{4.40}$$

where ρ_f is the density of the fibres. As A_f^e and ρ_f^e are constant, within each element, and considering the shape functions given in Equation (4.3), the mass matrix of the

fibre elements is given by:

$$\mathbf{M}_f^e = A_f^e \rho_f^e l^z \begin{bmatrix} 1/3 & 1/6 \\ 1/6 & 1/3 \end{bmatrix} . \tag{4.41}$$

A similar procedure can be done for the matrix elements:

$$\mathbf{M}_m^e = \int_0^d A_m(r) \boldsymbol{\mathcal{N}}_m{}^T \rho_m \boldsymbol{\mathcal{N}}_m dr , \tag{4.42}$$

where

$$\boldsymbol{\mathcal{N}}_m(r) = \begin{bmatrix} \mathcal{N}_1(r) & \mathcal{N}_2(r) \end{bmatrix} = \begin{bmatrix} 1 - \frac{r}{d} & \frac{r}{d} \end{bmatrix} , \tag{4.43}$$

and $A_m(r)$ is the area of the matrix element (see Figure 4.2). The following mass matrix can then be computed:

$$\mathbf{M}_m^e = \rho_m d \begin{bmatrix} 1/12 \left(3A_m^{(1)} + A_m^{(2)}\right) & 1/12 \left(A_m^{(1)} + A_m^{(2)}\right) \\ 1/12 \left(A_m^{(1)} + A_m^{(2)}\right) & 1/12 \left(A_m^{(1)} + 3A_m^{(2)}\right) \end{bmatrix} , \tag{4.44}$$

with $A_m^{(1)}$ and $A_m^{(2)}$ given by Eq. (4.6). To solve the equation of motion, it is necessary to invert the mass matrix. To improve the computational efficiency of the model, it is desirable to have a diagonal mass matrix, therefore, the row sum method [189] is used. This method operates on the global mass matrix such as:

$$M_{ij} = \begin{cases} \sum_k M_{ik} & i = j \\ 0 & i \neq j \end{cases} , \tag{4.45}$$

where M_{ij} are the individual elements of the global mass matrix.

4.3.1.2 Damping matrix

To avoid dynamic instability of the system it is necessary to introduce damping in the model. Mass and stiffness proportional damping, normally referred to as Rayleigh damping [190], is used in the present work. The damping matrix is assumed to be proportional to the mass and stiffness matrices as follows:

$$\mathbf{C} = \alpha_d \mathbf{M} + \beta_d \mathbf{K} , \tag{4.46}$$

where α and β are, respectively, the mass- and stiffness-proportional damping coefficients. The damping coefficients can be determined based on two natural frequencies of the system (ω_1 and ω_2) and on two damping ratios (ζ_1 and ζ_2) associated with that frequency:

$$\begin{bmatrix} \xi_1 \\ \xi_2 \end{bmatrix} = \frac{1}{2} \begin{bmatrix} \frac{1}{\omega_1} & \omega_1 \\ \frac{1}{\omega_2} & \omega_2 \end{bmatrix} \begin{bmatrix} \alpha_d \\ \beta_d \end{bmatrix} . \tag{4.47}$$

In this work, the two damping rations are considered equal ($\zeta_1 = \zeta_2 = \zeta$) and the associated frequencies are considered to be the minimum and maximum frequencies of the fibre and matrix elements of the RVE.

Similarly to the static SEM (Section 4.1) fibre failure is modelled using a maximum stress criterion where the strength of each element is randomly determined with one of the available stochastic distributions for fibre strength. The matrix can be considered either linear elastic or elastic perfectly plastic. Behaviour implemented using sequentially linear analysis (see Section 4.1.1.2). Other material behaviours can be used with the current modelling strategy but have not been used in this work.

4.3.2 Numerical implementation and parallelization

The major difference between the quasi-static and the transient dynamic solution of the single break phenomenon within a composite lies in the consideration of the inertial term in the governing equation of motion:

$$\mathbf{M}\ddot{\mathbf{u}} + \mathbf{C}\dot{\mathbf{u}} + \mathbf{K}\mathbf{u} = \mathbf{f}^{\text{ext}} \,, \tag{4.48}$$

where $\mathbf{u}$, $\dot{\mathbf{u}}$ and $\ddot{\mathbf{u}}$ are, respectively, the displacement, velocity and acceleration fields. $\mathbf{M}$ is the mass matrix, $\mathbf{C}$ the damping matrix and $\mathbf{K}$ the stiffness matrix. $\mathbf{f}^{\text{ext}}$ is the external force vector. As the system of equations is now time dependent, it is necessary to implement a time integration scheme. In this work an explicit integration scheme is used, based on the central difference method [191]. Let us consider that the simulation is divided into equal time steps such that:

$$t_{n+1} = t_n + \Delta t \,, \tag{4.49}$$

where the subscripts indicate the time step, and Δt is the time increment. The central difference formula for the velocity is:

$$\dot{\mathbf{u}}_{t+\Delta t/2} \approx \frac{\mathbf{u}_{t+\Delta t} - \mathbf{u}_t}{\Delta t} \,. \tag{4.50}$$

This difference formula can be converted to an integration formula by rearranging the terms:

$$\mathbf{u}_{t+\Delta t} = \mathbf{u}_t + \Delta t \dot{\mathbf{u}}_{t+\Delta t/2}. \tag{4.51}$$

Similarly, the acceleration is approximated by:

$$\ddot{\mathbf{u}}_t \approx \frac{\dot{\mathbf{u}}_{t+\Delta t/2} - \dot{\mathbf{u}}_{t-\Delta t/2}}{\Delta t} \,, \tag{4.52}$$

with the corresponding integration formula

$$\dot{\mathbf{u}}_{t+\Delta t/2} = \dot{\mathbf{u}}_{t-\Delta t/2} + \Delta t \ddot{\mathbf{u}}_t \,. \tag{4.53}$$

As it can be seen from the above, the velocities are defined at the midpoints of the time intervals, or at half-steps. The time integration of the equations of motion, at time step t, is given by:

$$\mathbf{M}\ddot{\mathbf{u}}_t = \mathbf{f}_t^{\text{ext}} - \mathbf{f}_t^{\text{int}} \,, \tag{4.54}$$

where $\mathbf{f}^{\text{int}} = \mathbf{C}\dot{\mathbf{u}} + \mathbf{K}\mathbf{u}$ is the internal force vectors. It should be noted that that the mass matrix does not depend on time.

The proposed model is implemented in Fortran language and parallelized with Message Passing Interface (MPI). Due to the simplicity and periodicity of the model, the domain decomposition of the proposed RVE is simple (see Figure 4.24). The RVE is constituted by extruding the 2D geometry (see Figure 4.1) in the fibre direction, being connected by fibre elements. This creates a 3D RVE that is a repetition of layers of matrix and fibre elements. To minimize the communications between subdomains, the RVE is divided perpendicularly to the fibre direction (see Figure 4.24). This division ensures that each subdomain communicates, at maximum, with two others, as well as ensuring a good load balance between the CPUs.

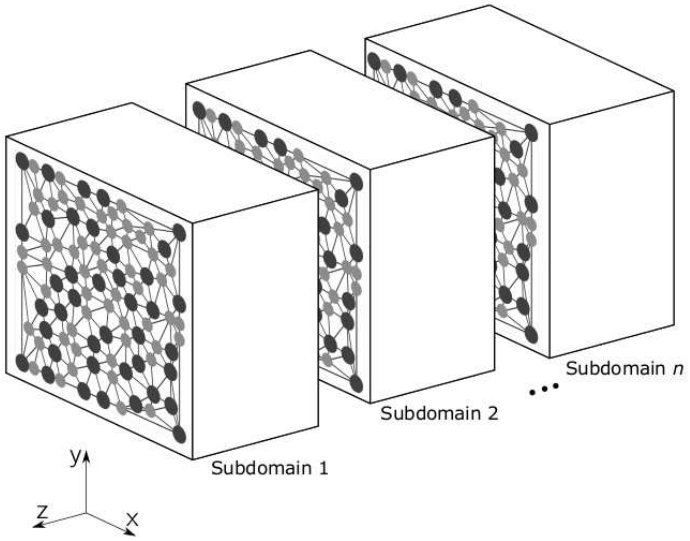

Figure 4.24: 3D RVE domain decomposition strategy.

In the proposed domain decomposition scheme, the mesh is partitioned by nodes (see Figure 4.25). Each node belongs to a subdomain while fibre elements can belong to more than one subdomain (grey elements in Figure 4.25), in this case a maximum of two subdomains. Due to the geometry of the RVE, the shared elements are always fibre elements. Nodes belonging to a given subdomain are denoted as local nodes. This partitioning scheme requires the creation of ghost nodes that have their equivalent local nodes in the neighbour subdomain (see Figures 4.25b, 4.25c and 4.25d). With this domain decomposition scheme the amount of communications between CPUs is optimized and only the nodal information of the local nodes need to be shared with the ghost nodes from the neighbouring subdomain. The number

of subdomains is equal to the number of CPUs being used for the simulation, being the number of spring elements in each subdomain variable, depending on the RVE size and the number of CPUs in use.

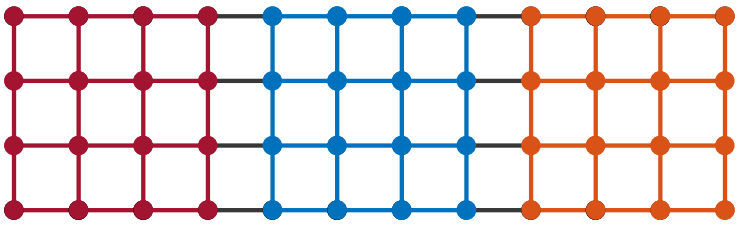

(a) Mesh Partition. Nodes are assigned a subdomain. Grey elements are duplicated in several subdomains.

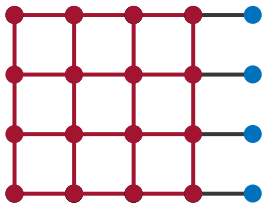

(b) Red subdomain: Local nodes (red) and ghost nodes (blue).

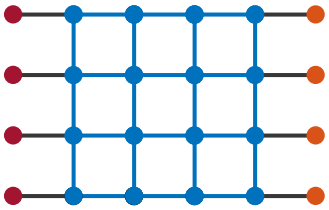

(c) Blue subdomain: Local nodes (blue) and ghost nodes (red and orange).

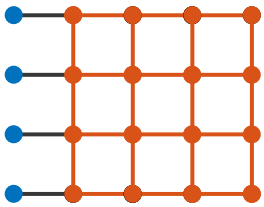

(d) Orange subdomain: Local nodes (orange) and ghost nodes (blue).

Figure 4.25: Mesh partition scheme.

After the domain decomposition has been defined, ensuring a good load balancing between CPUs, each CPU generates their respective nodal coordinates and nodal connections based on the predefined 2D geometry and fibre element size. At this stage, a random strength is also assigned to each fibre element, according to an appropriate statistical distribution. To ensure a correct definition of the model, for the elements that are shared between domains, the strength is only generated by one of the domains and is later communicated to the other domain, ensuring that the same element has the same strength in both domains.

As prior to the failure of a fibre element the model is linear elastic, a first static step is performed to reduce the computational time. The minimum strain that can be applied before fracturing a fibre element is determined within each domain. The global minimum of the computed strains is determined and applied to all subdomains to obtain the displacement and stress fields in the model. At this stage, a linear velocity field is also applied, where the velocity is zero at the blocked end and maximum at the other end where the displacement is being applied. The accelerations are, at this stage, initialized as zero.

After the static step, the dynamic explicit time integration is used. The algorithm for the integration scheme is shown in Algorithm 1.

This algorithm only requires the communication of the accelerations of the local nodes to the ghost nodes, therefore requiring a low number of communications per iteration. Additionally, and due to geometrical characteristics of the model, constituted by a repletion of layers of matrix and fibre elements, which have the same

Algorithm 1 Flowchart for explicit time integration.

1: Time update $t_{n+1} = t_n + \Delta t$
2: First partial nodal velocity update $\dot{\mathbf{u}}_{t+\Delta t/2} = \dot{\mathbf{u}}_t + \frac{\Delta t}{2}\ddot{\mathbf{u}}_t$
3: Enforce velocity boundary conditions
4: Update nodal displacements $\mathbf{u}_{t+\Delta t} = \mathbf{u} + \Delta t \dot{\mathbf{u}}_{t+\Delta t/2}$
5: Compute internal and external forces
6: Compute accelerations $\ddot{\mathbf{u}}_{t+\Delta t} = \mathbf{M}^{-1}\left(\mathbf{f}^{\text{ext}}_{t+\Delta t} - \mathbf{f}^{\text{int}}_{t+\Delta t}\right)$
7: Communicate accelerations to ghost nodes
8: Second partial nodal velocity update $\dot{\mathbf{u}}_{t+\Delta t} = \dot{\mathbf{u}}_{t+\Delta t/2} + \frac{\Delta t}{2}\ddot{\mathbf{u}}_{t+\Delta t}$
9: Compute kinetic and internal energies
10: Output; if stop criterion not met, go to 1

geometric properties, the computation and assembly of the global stiffness matrix can be simplified to improve computational efficiency. This allows the computation of the internal force vector to be done elementwise, therefore avoiding the assembly of the global stiffness and damping matrices. This results in an increase in computational speed while decreasing the memory necessary to solve the problem.

4.3.3 Model scalability

Due to the parallel implementation of the model it is important to understand how increasing the processing power affects the performance of the code. To understand this, strong and weak scalability analysis were performed. In the strong scalability, the same problem, with the same number of degrees of freedom, is considered for increasing number of cores. In the weak scalability, an increasing number of cores is considered but, at the same time, the size of the model increases proportionally to the increase in the number of cores. The analysis were performed in Curie supercomputer thin nodes, composed of 8-cores SandyBridge CPUs at 2.7GHz. The baseline was considered to be one node of the computer, which is composed of two 8-core CPUs. A maximum of 600 nodes (9600 cores) was used. For each case the average of two runs was considered.

For the strong scalability tests a RVE with a total of 470 fibres with a length of 134 mm was used. The considered fibre element length was 3.5 μm, leading to a total of 69.7 million elements. The results for the strong scalability tests are shown in Figure 4.26. The efficiency was calculated as the ratio between the actual running time and the time considering a linear scalability based on the time of one node (16 cores).

The results show that the model scales very efficiently with increasing number of CPUs. This is a result of the good parallelization scheme and domain subdivision. It is interesting to note that for 2400 cores the efficiency is maximum, being reduced for a higher number of cores. This reduction comes due to the fact that for very high number of CPUs the ratio between boundary and internal degrees of freedom increases and, therefore, the communications start playing a larger role on the computational time. Figure 4.26 shows that scalability is optimal, supraoptimal results

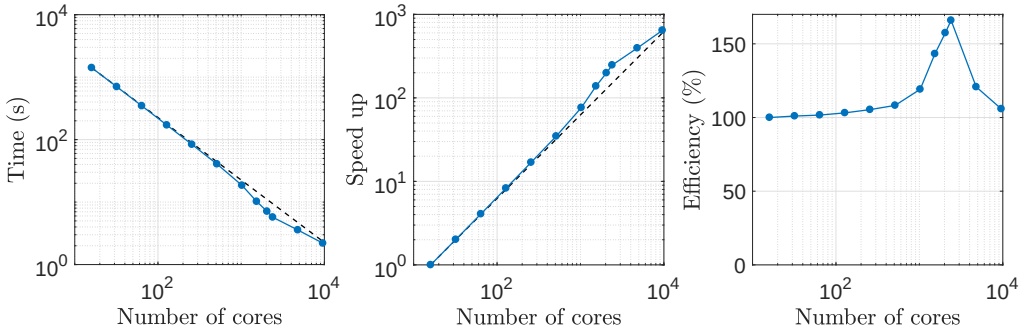

Figure 4.26: Strong scalability results: Time to solve 1000 increments as a function of the number of cores (left), along with the respective speed up (middle) and efficiency (right).

were obtained for some particular number of processors, probably due to details of the configuration of the supercomputer which the authors had no control on.

For the weak scalability test a RVE with 470 fibres and a length of 0.42 mm was user for each core (subdomain), resulting in 217920 elements per core. This RVE is repeated for each core, being the lower number of elements in this study equal to 3486720 for 16 cores and a maximum of 2092 million elements for 9600 cores. The results for the weak scaling tests are shown in Figure 4.27. In this figure it is seen that the model has a good weak scalability, being the minimum efficiency of the model around 80% for 4800 cores. As the efficiency increases from 4800 to 9600 cores, it might be possible that for the cases with 4800 cores some slower cores were used, which might affect the results.

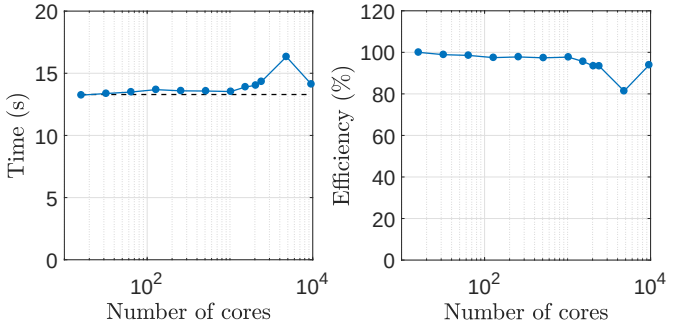

Figure 4.27: Weak scalability results: Time to solve 1000 increments as a function of the number of cores (left) and respective efficiency (right).

4.3.4 Dynamic effects on a single fibre fracture

To understand the effect of the model parameters on the stress redistribution around a broken fibre a full factorial design with $36 = 3^2 2^2$ cases was considered. For each case 10 simulations with different fibre arrangements were performed and a fibre strength of 2 GPa was considered in all cases. The factors considered for this study were the fibre modulus (E_f), the matrix shear modulus (G_m), the ma-

trix shear strength (τ^u) and the fibre volume fraction V_f. For the fibre modulus and matrix shear strength three levels were considered, where for the remaining factors only two levels were considered. Table 4.11 shows the average results for each level of each factor, disregarding the effects of the other factors. The results are shown for the maximum dynamic stress concentration factor (SCF_{max}^{Din}) and the maximum static stress concentration factor (SCF_{max}^{Stat}). The increase in SCF when considering a dynamic problem is also shown. This increase is defined as $SCF_{Inc} = \left(SCF_{max}^{Din} - 1\right) / \left(SCF_{max}^{Stat} - 1\right) - 1$. The results for all the cases are shown in Appendix A. The main effects plot for the increase in SCF is shown in Figure 4.28.

Table 4.11: Average results obtained with the proposed factorial design.

Factor	Level	SCF_{max}^{Din}		SCF_{max}^{Stat}		SCF_{Inc}	
		Avg.	CoV (%)	Avg.	CoV (%)	Avg. (%)	CoV (%)
E_f (GPa)	70	1.206	12.75	1.123	6.61	52.47	55.19
	230	1.257	11.48	1.155	6.22	58.36	31.66
	480	1.289	10.41	1.177	5.69	58.83	27.85
G_m (MPa)	450	1.268	11.12	1.164	6.12	57.70	31.96
	1050	1.232	12.11	1.140	6.49	55.40	44.65
τ^u (MPa)	50	1.129	4.92	1.089	2.86	39.55	37.45
	100	1.192	5.71	1.130	3.93	46.88	10.66
	∞	1.430	4.12	1.235	3.04	83.23	7.35
V_f	0.4	1.291	11.61	1.176	6.40	58.83	30.34
	0.6	1.210	10.74	1.127	5.53	54.27	46.08

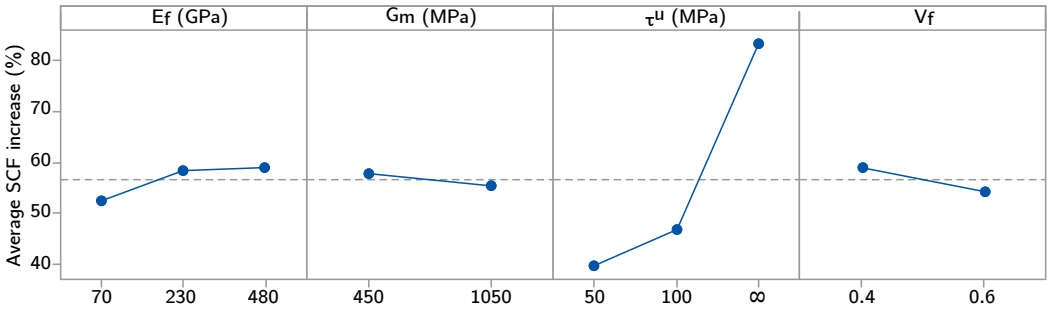

Figure 4.28: Main effects plot for the dynamic increase in SCF.

From the analysed parameters it is possible to see that the fibre volume fraction, matrix shear stiffness and the fibre modulus do not have a large effect on the SCF increase due to the dynamic effects, although the actual SCFs (static and dynamic) vary with these properties. The main factor affecting the dynamic SCF and the increase in SFC compared with the static case is the matrix shear strength. Nonetheless, depending on the chosen material parameters the SCF_{Inc} can vary from 11.8% for case 8 to 110.3% for case 12 (see Annex A). Both cases consider a fibre modulus of 70 GPA, a volume fraction of 0.6 and a matrix shear stiffness of

1050 MPa, however, case 8 considers a matrix shear strength of 50 MPa while case 12 considers the matrix elastic ($\tau^u = \infty$). If all cases are considered, the average SCF_{Inc} is 56.55%. If only the cases where the matrix is elasto-plastic are considered, the average SCF_{Inc} is 43.21%, while if only the elastic cases are considered it is 83.23%. In addition to the fact that in the static cases the SCF is higher when the matrix is considered elastic, the increase in SCF due to dynamic effects is also higher in these cases, leading to very high SCFs, which will change the cluster formation process in the material and, therefore, the material's behaviour.

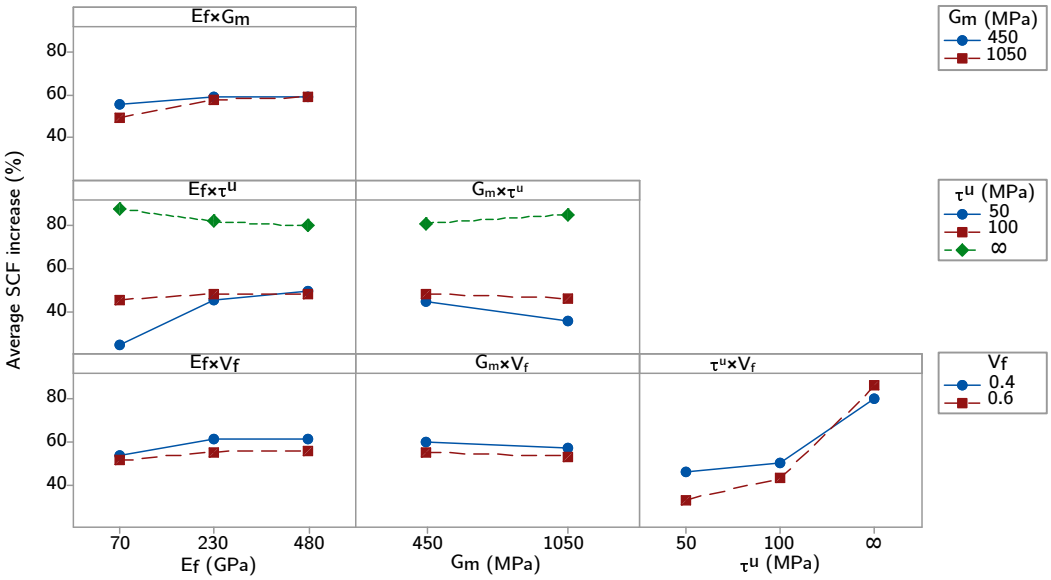

Figure 4.29: Interaction plot for the dynamic increase in SCF.

Figure 4.29 shows the interaction plot of the factors in study. It is interesting to note that the fibre elastic modulus affects more the dynamic increase in SCF when the matrix shear strength is equal to 50 MPa when compared to the other matrix shear strengths. Other than this interaction, there is no other special interaction between the factors in study. Nevertheless, it is seen that the dynamic failure of the fibres clearly increases the SCF on the surrounding intact fibre, which will affect the cluster formation and macro behaviour of the material.

To understand the effect of damping on the mechanics of fibre fracture, the value of the damping ratio ξ was changed from 0 to 0.04. The results are shown in Table 4.12.

Table 4.12: Effect of the damping parameter on the maximum SCF.

ξ	SCF_{max}^{Din}	Error (%)
0	1.395	-
0.01	1.385	0.69
0.02	1.376	1.35
0.04	1.359	2.59

It is possible to see that damping has a small effect on the maximum dynamic SCF, marginally reducing it when increasing the damping ratio. However, for $\xi = 0.01$ there is only a 0.69% difference between the maximum dynamic SCF in this case and when no damping is considered. The introduction of damping is necessary to stabilize the numerical simulation. In addition, damping is introduced so that the stress waves are damped before reaching the boundary to avoid the bounce back of these stress waves.

To better understand the stress redistribution, Figure 4.30 shows the dynamic fibre failure phenomenon for a material with $E_f = 230$ GPa, $G_m = 450$ MPa, $\tau^u = \infty$ and $V_f = 0.6$. In Figure 4.30 a) the local fibre arrangement that surrounds the broken fibre (BF) is shown. The evolution of the in-plane SCF on each intact fibre with time is shown Figure 4.30 b). It is possible to see that the SCF is significantly higher for the two closest fibres to the broken one, Fibre 1 (blue) and Fibre 2 (orange). In addition, the SCF varies with time, as the stress wave due to the fibre break progresses in the longitudinal direction, being that the maximum SCF, which is more likely to cause fibre failure, occurs during the first peak. Figures 4.30 c), d) and e) show snapshots of the stresses in the fibres affected by the break, including the broken one, at distinct time steps. In Figure 4.30 c), where the maximum SCF occurs, it is possible to see that the stress is maximum in the break plane and decreases away from the break plane (increase in Z/R). In addition, the stress in the broken fibre is lower than the remote stress (2000 MPa). In Figure 4.30 d), in the minimum of the SCF in Fibre 1, it is possible to see that while the in-plane SCF is lower, there is a stress peak away from the fibre break plane. Additionally, it is seen that there is an increase in stress of the broken fibre, which may cause additional fractures on this fibre, leading to its fragmentation. Finally, Figure 4.30 e) shows the final part of the dynamic effect where most of the stress waves have subsided and the static equilibrium is achieved. At this stage there are still some oscillations, that should be damped when damping is considered.

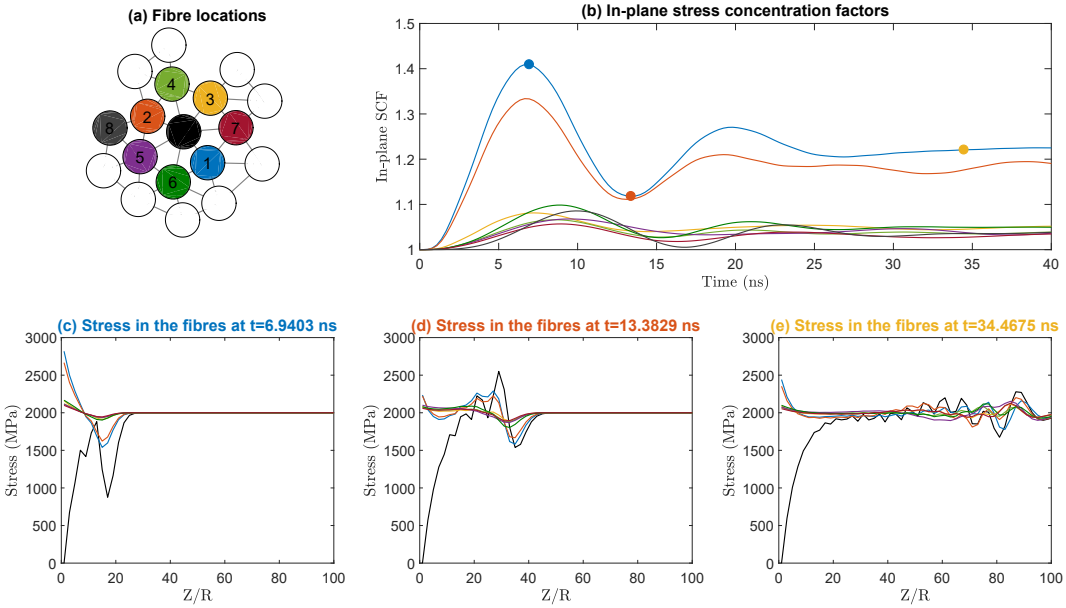

Figure 4.30: Dynamic effects due to a fibre failure.

4.3.5 Dynamic effects on multiple fibre breaks

The previous section focused on the analysis of the dynamic effects on a single fibre fracture, however, multiple fibre breaks and cluster formation are the mechanisms responsible for the failure of composite materials under longitudinal tension. An analysis on the dynamics of multiple fibre breaks is performed in this section. This analysis is simplified to the consideration that the interacting breaks occur in the same break plane, therefore, creating a fully planar clusters. Furthermore, it is considered that all the fibre fractures occur in the same time instant, which might not occur in a real simulation. Nevertheless, for this study simultaneous failure is considered. For each cluster size five simulations were performed to minimize local geometrical effects. This simulations were performed considering a fibre elastic modulus of 230 GPa, a matrix shear stiffness of 450 MPa and a fibre volume fraction of 0.6, as in the previous section. Similarly, the fibres were considered to break with a strength of 2 GPa. Regarding the matrix shear strength, two cases values were considered: elastic matrix with $\tau^u = \infty$ and elasto-plastic matrix with $\tau^u = 50$ MPa. The SCF results are shown in Figure 4.31 as a function of the cluster size.

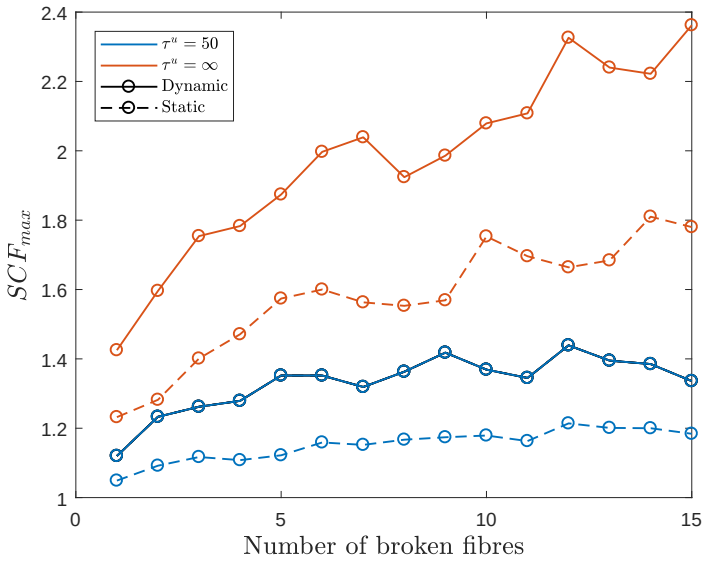

Figure 4.31: Evolution of the maximum SCF with the number of the cluster size.

The maximum SCF is seen to increase with cluster size for both the dynamic and static cases, as previously shown in Section 4.2. It is possible to see that there is a large variation in the increase in SCF due to dynamic effects, for both, elastic and plastic cases. Nevertheless, it is seen that, for the analysed cases, the increase in SCF due to the dynamic effects is, usually, larger in the plastic cases than in the elastic one. However, the SCFs for an elastic matrix are higher than the ones with an elasto-plastic matrix, even when dynamic effects are considered in the latter. The increased maximum SCF will lead to changes in the cluster formation, eventually leading to the formation of more co-planar clusters. This is a feature that was seen to be lacking in most of the models that do not take into account dynamic effects [73].

4.3.6 Tensile behaviour and cluster formation

In the previous sections the dynamic effects were analysed at a local level, analysing its influence on the stress redistribution around a single or multiple fibre breaks. The objective of capturing the local dynamic effects in fibre failure is to analyse how it affects the global stress-strain behaviour and cluster formation on composite materials. In this section, a RVE with a size equal to $75 \times 75 \times 300$ fibre radius and a volume fraction of 55% is considered and is subjected to longitudinal tension. the model as around 1800 fibres that are considered to be T700 carbon fibres with $R_f = 3.5$ μm, $E_f = 238$ GPa and a standard Weibull distribution is considered, with $\sigma_0 = 5200$, $m = 10$ at $L_0 = 10$ mm [73]. The simulations were performed with and without dynamic effects and the either with an elastic matrix ($\tau^u = \infty$) or with an elasto-plastic matrix ($\tau^u = 50$ MPa).

Table 4.13 shows some metrics obtained from the mentioned simulations. Both the strength (X_t) and failure strain (ε_f) are shown, as well as metrics from the fibre breakage: maximum cluster size, percentage of planar clusters and fibre break density at peak stress. The respective stress-strain curves for these simulations are shown in Figure 4.32.

Table 4.13: Average results obtained with the proposed factorial design.

		X_t		ε_f		Max. cluster		Planar clusters		Break dens.	
		Avg. (MPa)	CoV (%)	Avg. (%)	CoV (%)	Avg.	CoV (%)	Avg. (%)	CoV (%)	Avg. (/mm^3)	CV (%)
$\tau^u =$ 50 MPa	Static	2946	0.71	2.37	1.26	3.8	28.8	45	22.0	3430	11.0
	Dynamic	2956	1.12	2.32	1.54	5.6	32.4	38	22.8	4362	21.7
$\tau^u =$ ∞	Static	3243	0.70	2.56	0.94	28.6	87.8	44	10.8	8873	15.3
	Dynamic	2971	0.77	2.34	1.03	21.4	34.0	40	21.2	7806	15.8

Analysing the results from the simulations with an elastic matrix ($\tau^u = \infty$), the strength predicted by the dynamic model is clearly lower than the static one, being reduced from 3243 to 2971 MPa. This reduction in strength is also accompanied by a reduction in failure strain, from 2.56% to 2.34%. This reduction in the failure strain leads to a reduction of the fibre break density at peak stress, as a lower amount of fibre elements have failed at that strain. The large differences seen in the simulations with an elastic matrix due to dynamic effects are not present in the simulations with an elasto-plastic matrix. It is seen that, in this case, both the strength and failure strain are very similar. However, it is interesting to note the fibre break density at peak stress is higher for the dynamic case. This might be explained by the fact that the dynamic stress wave propagates in the broken fibre as well as in the intact fibres which increases the probability of failure of these fibres, causing the multiple fragmentation of the fibres and, therefore, increasing the fibre break density.

Figure 4.33 shows the evolution of the fibre break density as a function of the strain. It is possible to see that, although there is a good agreement between the experimental results [72] and the numerical results at lower strains, the fibre break density at failure is clearly overpredicted by the models, both dynamic and static.

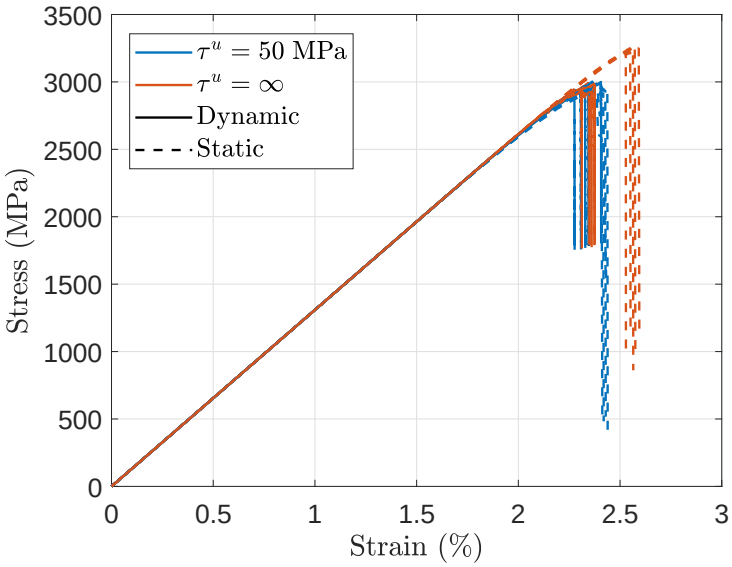

Figure 4.32: Stress-strain curves for the dynamic and static cases with $\tau^u = 50$ MPa and $\tau^u = \infty$.

To better understand the damage evolution, the formation and development of clusters of broken fibres is shown in Figures 4.34 and 4.35, for elastic and elasto-plastic matrix, respectively. It is considered that two fibres belong in the same cluster if the radial distance between their centres is lower than 4 times the fibre radius and the breaks occur in planes that are less than 10 times the fibre radius apart. In addition, a cluster is considered planer, if all the breaks in that cluster occur in a longitudinal distance lower than twice the fibre radius. Analysing the results for cluster formation shown in Table 4.13 it is possible to see that there is no clear change in the maximum cluster size or the percentage of planar clusters in the dynamic model, however, there is a clear difference in the maximum cluster size between an elastic and an elasto-plastic matrix.

Figure 4.34 shows the evolution of cluster with different sizes (1, 2, 3, ..., >6 fibre elements) as a function of the strain, when $\tau^u = \infty$, and the experimental results from Scott et al. [72]. Comparing the cluster evolution from the dynamic and static models, it is concluded that the number of singular fibre breaks relates well in both cases with the experimental results, which accounts for the majority of the fibre breaks, specially at lower strains. However, the formation of clusters with multiple fibre breaks is delayed in the numerical results compared to the experiments. Nevertheless, it is seen that in the dynamic model the larger clusters are created at lower strains, specially the clusters with more than 4 fibres, compared to the static model. This in turn leads to the failure of the material at lower strains, as shown in Table 4.13. Figure 4.35 shows a similar analysis, but for an elasto-plastic matrix ($\tau^u = 50$ MPa). In this case the differences seen between the dynamic and static models are smaller and, therefore, there is no change in the material's failure strain. Nevertheless, it is seen that larger clusters form at slightly lower strains. However, as these clusters are smaller when compared with the elastic cases and do not lead to the earlier failure of the material.

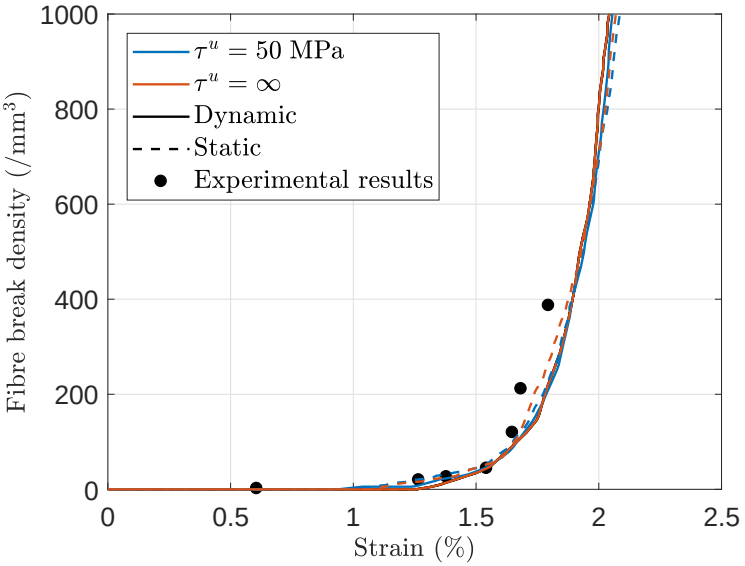

Figure 4.33: Fibre break density for the dynamic and static cases with $\tau^u = 50$ MPa and $\tau^u = \infty$.

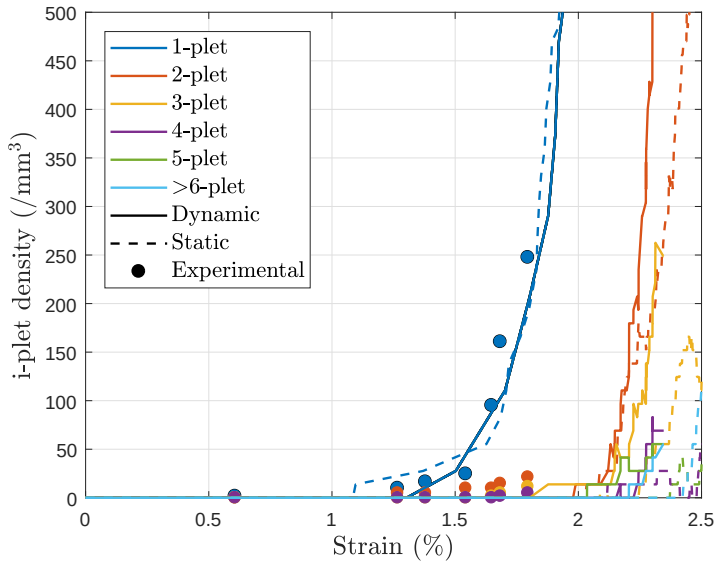

Figure 4.34: Cluster evolution for static and dynamic cases with $\tau^u = \infty$.

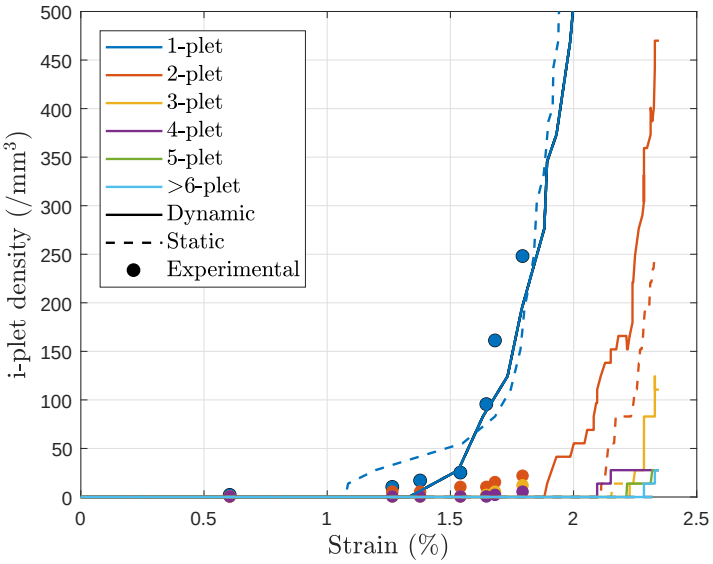

Figure 4.35: Cluster evolution for static and dynamic cases with $\tau^u = 50$ MPa.

Although there is an increase in the SCFs when a fibre breaks due to the dynamic effects, as seen in Section 4.3.4 and 4.3.5, there is still a large discrepancy between the numerical results in terms of fibre breaks and cluster formation, as the failure is predicted to occur at much larger fibre break densities and the formation of large clusters of broken fibres occurs at higher strains. Nevertheless, it should be noted that the available experimental data is still limited and more experimental data should shed light on the shortcomings of the available models and help improve them. Nonetheless, the inclusion of dynamic effects on the model is seen as an improvement over the previous modelling strategies and has been shown to lead to reduction of the strain at which larger clusters of broken fibres are formed.

4.3.7 Summary

In this section the spring element model is extended to a dynamic formulation to study fibre fracture as a dynamic process. When a fibre fractures, the strain energy previously stored is transformed into kinetic energy. This causes a stress wave to propagate in the broken fibre and surrounding intact fibres, leading to a transient increase in the stress concentration and therefore increasing the failure probability of the fibres. The model proposed is able to capture this transient effect. It was observed that there is always an increase in the maximum SCF in the dynamic model over the static one. However, this increase is highly dependent on the material parameters considered. There is a large discrepancy in the results depending on the behaviour considered for the matrix, being the increase of the maximum SCF more pronounced when an elastic matrix is considered. This increase in SCF due to dynamic effects was also seen to be present when multiple fibre breaks are considered, which will affect the cluster formation process.

In addition to the study of the effects of dynamics in the local stress redistribution

around a broken fibre, a study on the tensile behaviour of fibre reinforced materials was also performed. This analysis lead to the conclusion that the dynamics have a large effect on the tensile behaviour of the material if the matrix is considered elastic, leading to a reduction in both strength and failure strain of the material. However, this was not seen in the results obtained in the simulations that represent plastic deformation of the matrix, where the results were very similar. As for the analysis of cluster formation and damage development, it was seen that considering the dynamic effects lead to an earlier formation of larger clusters that, for the elastic case, lead to the earlier material failure. It is interesting to note that the fibre break density at peak stress was higher in the dynamic cases than in the static ones for an elasto-plastic matrix. This was considered to be due to the fact that the stress waves that propagate around a broken fibre leads to the multiple fragmentation of these fibres, therefore, leading to higher fibre break densities.

4.4 Hybridization analysis

The static (Section 4.1) and the dynamic (Section 4.3) Spring Element Models, were developed with the aim of being used for hybrid composite materials. In this section, the dynamic SEM is used to analyse the behaviour of hybrid composite materials as well as understand damage development and fibre break clustering. Additionally, the effect of fibre dispersion in different hybrid configurations is analysed.

The fibres chosen for this study were the AS4 and M50S carbon fibres. These fibres were seen to lead to a non-brittle behaviour in Chapter 3. The relevant fibre properties used in the model are shown in Table 4.14. For both fibre types the Weibull of Weibulls strength distribution was used, however, as the value of the α parameter of the M50S fibres is not available, the value of 0.6 was used.

For these analysis, a fibre volume fraction of 50% and a matrix with a shear modulus of 1 GPa and yield strength of 50 MPa were used. The RVEs are $75 \times 75 \times 300$ the maximum fibre radii and an element size of twice the maximum fibre radii was used. As the fibres chosen have different radii, the number of fibres in the model will depend on the hybrid volume fractions used. For each material system five runs were performed to avoid erroneous results due to the random fibre distribution and fibre strength.

The volume fraction of each fibre type has a large influence on the behaviour of the hybrid material, as the stress redistribution as well as the damage development changes. In Figure 4.36, RVE microsructures of materials with different hybrid volume fractions are shown. For these configurations a random fibre dispersion was used, meaning that no constraints were imposed on the positions of the fibres of each type.

The different hybrid volume fractions lead to very different material behaviours, as shown in Figure 4.37, where a representative curve of each hybrid volume fraction, as well as for the non-hybrid AS4 and M50S composites, is represented. The

Table 4.14: Carbon fibre properties used in the hybrid study [27, 28].

Material property	AS4	M50S
Fibre radius		
R (μm)	3.5	2.65
Young's moduli		
E_1 (MPa)	234000	480000
Weibull parameters		
σ_0 (MPa)	4275	4600
m	6.4	9
α	0.6	0.6
l_0 (mm)	12.7	10

behaviour of the non-hybrid composites, as expected, leads to a catastrophic failure, however, some non-linear behaviour due to fibre failure is observed prior to peak stress for the AS4 material. The M50S shows a linear behaviour up to failure. The three tested hybrid volume fractions (25, 50 and 75% of M50S fibres), show very distinct behaviours. The materials with lower AS4 content have a brittle behaviour, as the failure of the lower elongation M50S fibres lead to the failure of the material while the material with 25% M50S volume fractions leads to a non-brittle failure, with a stress plateau. Table 4.15 shows some relevant metrics to characterize the tensile curve of the analysed materials. X_T is the maximum stress, ε_f the strain at peak stress, ε_d the pseudo-ductile strain, as defined in Chapter 2.2, *Cluster max.* and *Break dens.* are, respectively, the maximum cluster size and fibre break density at peak stress. For these metrics, both the average and the standard deviation are shown, as five simulations were performed for each material.

Table 4.15: Properties of the AS4-M50S random hybridization.

VF_{M50S} (%)	X_T (MPa)		ε_f (%)		ε_d (%)		Cluster max.		Break dens. (/mm^3)	
	Avg.	STDV	Avg.	STDV	Avg.	STDV	Avg.	STDV	Avg.	STDV
0	1537.47	16.95	1.41	0.03	0.13	0.02	30.20	20.34	14570.52	565.02
25	1350.53	11.07	1.20	0.02	0.30	0.02	159.60	44.75	43056.43	1829.92
50	1407.40	12.33	0.81	0.01	0.04	0.01	15.80	9.68	8790.41	1776.57
75	1594.42	17.25	0.79	0.01	0.03	0.01	42.00	23.21	10266.54	1420.56
100	1803.13	3.67	0.77	0.00	0.03	0.01	27.60	13.78	11087.53	1019.53

To better understand the influence of the hybrid volume fraction on the behaviour of the hybrid materials, a plot of the strength, strain and pseudo-ductile strain as function of the volume fraction of M50S fibres is shown in Figure 4.38. It is interesting to note that, although being a non-hybrid material, the AS4 composite has a pseudo-ductile strain of 0.13%, which is due to the non-linear behaviour observed prior to peak stress. This value is higher than that of the 50% and 75% M50S materials, however, the highest pseudo-ductile strain occurs for the 25% M50S fibre composite, which shows a plateau in the stress-strain curve. Regarding failure strain, adding M50S to the baseline AS4 material always results in a lower failure strain. In terms of strength, the lowest strength is for the hybrid material with

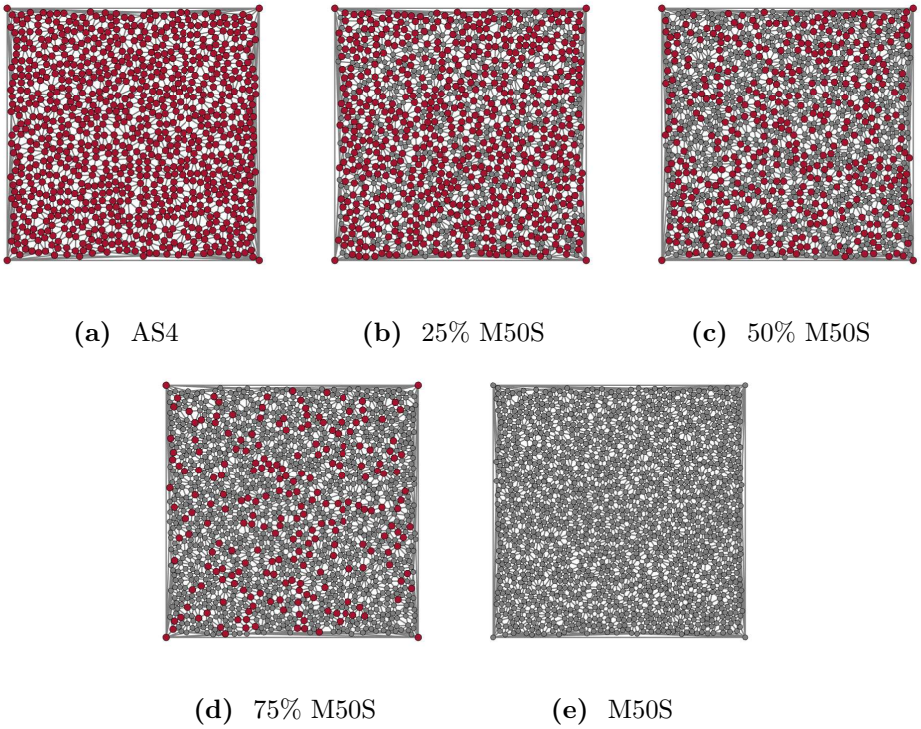

(a) AS4 **(b)** 25% M50S **(c)** 50% M50S

(d) 75% M50S **(e)** M50S

Figure 4.36: Representative microstructures of the AS4-M50S hybridization for different hybrid volume fractions.

25% M50S fibres, which has the highest pseudo-ductile strain and failure strain of the hybrid materials. This reinforces the idea that there is always a compromise between strength and ductility. Nevertheless, the reduction in strength might be acceptable in the hybrid materials as this results in a non-brittle behaviour and a non-catastrophic failure. It is interesting to note the differences in the fibre clustering process. The material with 25% M50S fibres, which has a non-brittle failure, shows a much higher break density at peak stress as well as a larger maximum cluster size. This shows that the material allows the failure and multiple fragmentation of the M50S fibres without catastrophic failure, which in turn results in the shown pseudo-ductile behaviour.

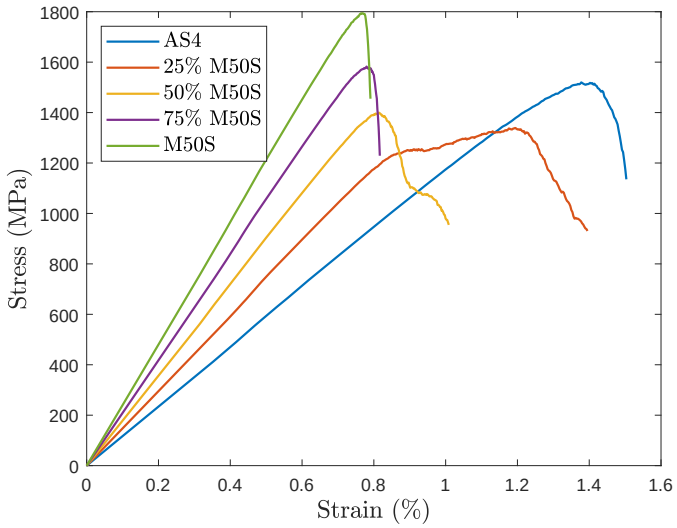

Figure 4.37: Stress-strain curves for different hybrid volume fractions for the AS4-M50S hybridization.

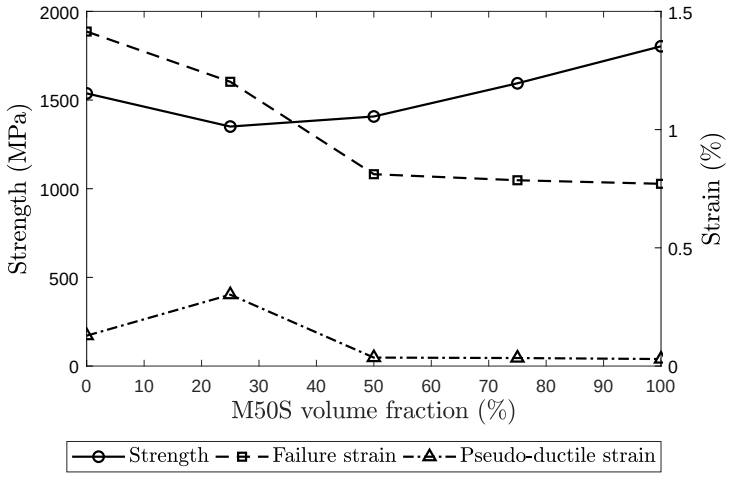

Figure 4.38: Influence of the volume fraction of M50S on the properties of the hybrid material.

As discussed in Chapter 2.2, the type of fibre hybridization used changes the behaviour of the material. This is, in part, result of the different fibre dispersions obtained with the different methods. Fibre dispersion is a measure of how well mixed are the two types of fibres used in the hybrid material. In this work, the metric used to characterize fibre dispersion is based on the one proposed by Conde et al. [192]. Having a hybrid microstructure such as the numerical ones shown in Figures 4.36, 4.39 or 4.41, or even experimental ones such as shown in Figure 6.3, it is possible to generate connections between the fibres using a Delaunay triangulations mesh [177]. This algorithm is already used in the case of the SEM to generate the matrix elements, however, the same scheme can be used for the experimental results, if the centres of the fibres, as well as the type of fibres is known. Having the mesh generated it is possible to distinguish between two types of connections, the ones that connect fibres of the same type and the ones that connect fibres of different types. It is then possible to use the Dispersion Degree (DD) as a metric for fibre dispersion, defined as:

$$DD = \frac{N_{12}}{N_{11} + N_{22} + N_{12}} \, , \tag{4.55}$$

where N_{12} is the total number of connections between different fibres and N_{11} and N_{22} are the number of connections between fibres of the same type (type 1 and 2). It should be noted that this metric for fibre dispersion not only depends on the type of hybrid configuration but also is affected by the hybrid volume fraction, as this will affect the number of connections of each type. For instance, for 25% of M50S and a random distribution the average DD is equal to 45.25%, while the one for 50% M50S is 47.45%.

As the fibre dispersion changes the behaviour of the hybrid material, an analysis on the effects of this parameter in the behaviour of the AS4-M50S hybrid material with 25% M50S fibres is done. This analysis focuses on two types of non-random microstructures: a fibre arrangement composed of tows or bundles of M50S is used (Figure 4.39) and a layer-by-layer type of hybridization (Figure 4.41).

For the tow hybridization, distinct microstructures were generated based on different number of tows as, increasing the number of tows, increases the fibre dispersion (Figure 4.39). A representative stress-strain curve for each of the microstructures is shown in Figure 4.40, as well as the reference material with a random microstructure. Table 4.16 shows the relevant metrics of the hybrid behaviour, as well as the DD for each configuration. The material behaviours for the different configurations is very different, taking into account that the hybrid volume fraction is kept constant.

In Figure 4.40 it is shown that, as the number of tows increases, thus the dispersion degree, there is a reduction in the load drop between the the failure of the LE fibres (M50S) and the HE fibres (AS4). Additionally, there is an increase in maximum stress (X_T), failure strain (ε_f) and pseudo-ductile strain (ε_d) with increasing number of tows. Comparing with the results for the random microstructure, the maximum stress of the tow-by-tow hybridizations is always lower than the random, however, both the pseudo-ductile strain and the failure strain are higher for the microstructures with higher number of tows. Analysing the fibre failure data, it is

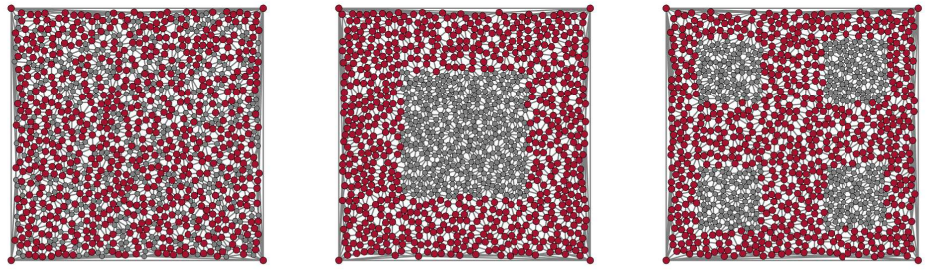

(a) Random **(b)** 1 Tow **(c)** 4 Tows

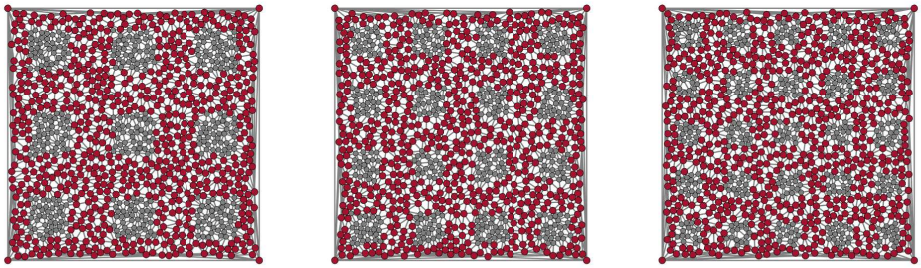

(d) 9 Tows **(e)** 16 Tows **(f)** 25 Tows

Figure 4.39: Representative microstructures of the AS4-M50S tow-by-tow hybridizations with 25% volume fraction of M50S fibres.

interesting to note that increasing the dispersion degree, the fibre break density at failure increases, being for the material with 25 tows, very similar to that of the random material. Interestingly, the maximum cluster size reduces with increasing dispersion, however, this may be related with the geometry of the microstructure, as increasing the number of tows reduces the number of M50S fibres together which should reduce the maximum possible cluster size.

Table 4.16: Properties of the AS4-M50S tow-by-tow hybridization.

	DD (%)	X_T (MPa)		ε_f (%)		ε_d (%)		Cluster max.		Break dens. (/mm^3)	
		Avg.	STDV	Avg.	STDV	Avg.	STDV	Avg.	STDV	Avg.	STDV
Rand.	45.25	1350.53	11.07	1.20	0.02	0.30	0.02	159.60	44.75	43056.43	1829.92
1 tow	4.66	1234.22	47.31	1.09	0.09	0.27	0.06	1210.40	228.55	23322.23	4733.52
4 tows	9.18	1281.08	36.80	1.17	0.07	0.32	0.05	334.40	104.40	31205.96	5011.23
9 tows	13.44	1306.09	24.94	1.20	0.06	0.33	0.04	163.40	67.55	35637.10	3634.62
16 tows	17.86	1338.51	13.43	1.24	0.03	0.35	0.02	156.40	83.93	40131.82	2461.42
25 tows	21.77	1338.68	10.14	1.25	0.03	0.36	0.02	97.20	17.91	43531.89	1298.57

A distinct strategy to create the microstructure is considering a layer-by-layer hybridization. For this type of hybridization, layers of each material are stacked on top of each other (Figure 4.41). Using the SEM to simulate this type of microstructure is an approximation as no interface between the layers is considered, and therefore, delamination cannot occur, which was observed to be an important mechanisms in this type of material. Nevertheless, the elasto-plastic behaviour used for the matrix

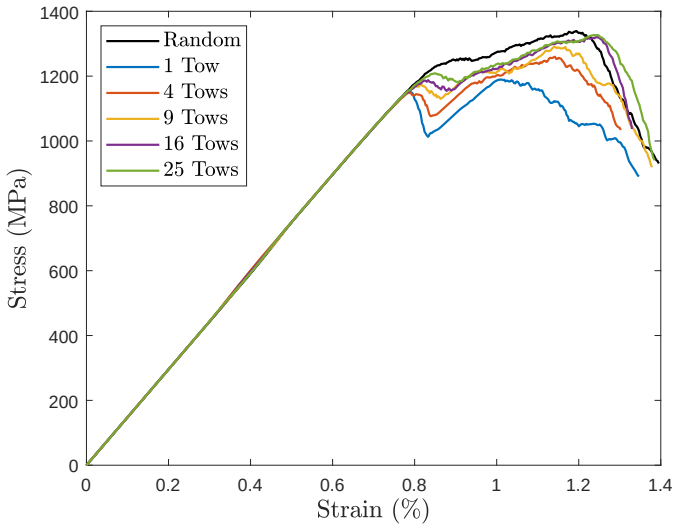

Figure 4.40: Stress-strain curves for different tow-by-tow hybridizations in 25% volume fraction of M50S fibres.

should capture some of the effects of having layers of distinct materials. In this work the RVE microstructure was defined in number of layers in the RVE and, in order to ensure that the RVE is symmetric, the middle layer (considered to be of M50S fibres) has double thickness, therefore counting as two layers. Four layer-by-layer configurations were considered, ranging from a minimum of 4 layers to the maximum of 32 layers, which results in layers of M50S fibres with a single fibre in the thickness.

In Figure 4.42 a representative stress-strain curve of each material is shown, with the addition of the baseline material with a random microstructure. Additionally, the main metrics that characterize the materials tensile behaviour are shown in Table 4.17.

Table 4.17: Properties of the AS4-M50S layer-by-layer hybridization.

	DD (%)	X_T (MPa)		ε_f (%)		ε_d (%)		Cluster max.		Break dens. (/mm^3)	
		Avg.	STDV	Avg.	STDV	Avg.	STDV	Avg.	STDV	Avg.	STDV
Rand.	45.25	1350.53	11.07	1.20	0.02	0.30	0.02	159.60	44.75	43056.43	1829.92
4 layers	5.11	1280.57	37.48	1.14	0.07	0.29	0.05	945.80	165.39	21318.13	3583.23
8 layers	14.53	1293.25	26.47	1.16	0.05	0.30	0.03	426.20	296.05	32615.74	2983.89
16 layers	32.27	1338.52	19.59	1.23	0.05	0.34	0.04	243.80	111.99	43675.63	3914.98
32 layers	50.67	1355.92	13.84	1.20	0.07	0.30	0.06	162.00	154.46	42658.37	6209.57

Analysing the DD values for the ply-by-ply hybridizations it is noted that the 32 layer material has a higher value than the random materials. This shows that the fibres are better mixed in this type of material than in the random one, has the number of connections between fibres of different types is higher, which should lead to an improved material response. Nevertheless, creating one fibre thick laminas is not feasible in a real world application. Yet it is interesting too see that the 32 layer materials has a higher strength than the random baseline. Analysing the remaining

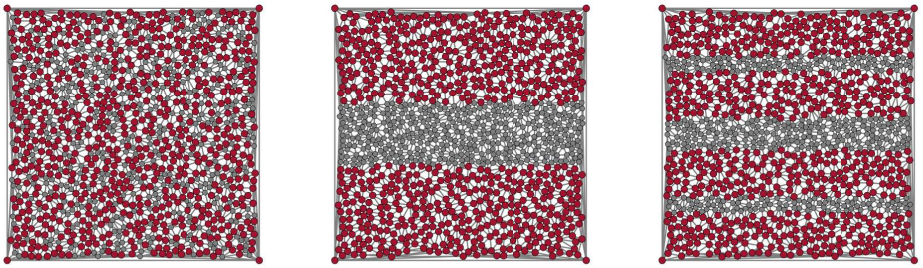

(a) random **(b)** 4 Layers **(c)** 8 Layers

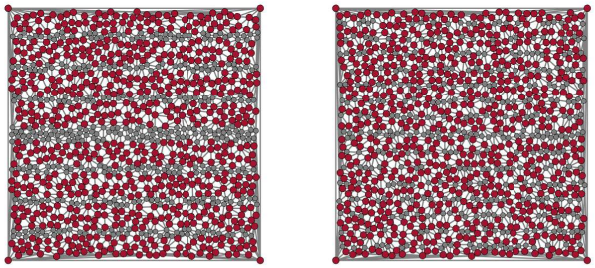

(d) 16 Layers **(e)** 32 Layers

Figure 4.41: Representative microstructures of the AS4-M50S layer-by-layer hybridizations with 25% volume fraction of M50S fibres..

materials, the same trends observed for the tow hybridization can be seen, increasing the DD increases material's strength and reduces the load drop in the non-linear region of the stress-strain curve. Additionally, a decrease in the maximum cluster size and an increase in the fibre break density at peak stress are also observed. However, the maximum break density is observed for the 16 layer material, which also has the highest pseudo-ductile strain ($\varepsilon_d = 0.34\%$) of the analysed materials, reinforcing the relation between the pseudo-ductile behaviour and the higher fibre break density.

To better understand the changes in behaviour for the different layer-by-layer hybridizations the details of fibre break clustering are analysed in Figures 4.43 and 4.44.

Figure 4.43 shows the evolution in fibre break density as a function of strain until the peak stress. It is interesting to see that the different microstructures lead to very distinct fibre break evolutions, taking into account that the same strength distributions were used. Thus, the changes in the break process are only due to the changes in microstructure and in the fibre stress redistribution that occurs after the fibres fail. Analysing the results for the 4 layer material, a large increase in the fibre break density is observed at a strain of 0.8%, which corresponds to the failure of the M50S carbon fibres. Due to the nature of this microstructure, it is observed that most of the fractures of the M50S fibres occur in a very narrow strain band, as the stress concentration due to the fracture of a M50S fibre affects mainly other M50S fibres, causing them to fracture. This large increase in the fibre break density

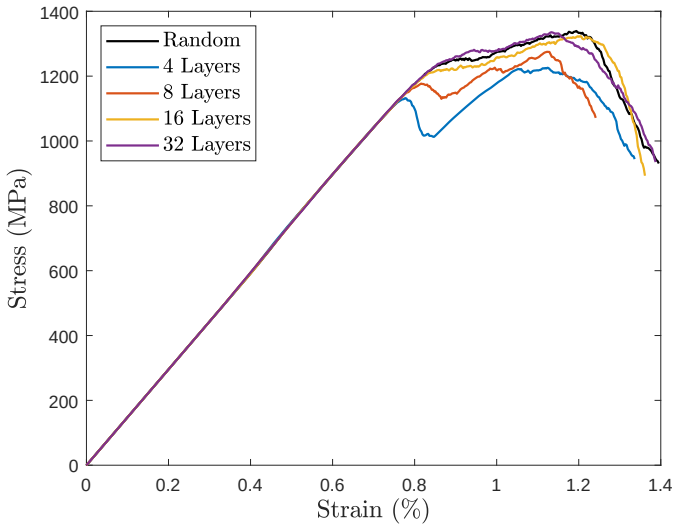

Figure 4.42: Stress-strain curves for different layer-by-layer hybridizations in 25% volume fraction of M50S fibres.

is responsible for the load drop observed in the stress-strain curve for this material (Figure 4.42). As the number of layers in the material increases, thus increasing the fibre dispersion, the fibre break density increases in a less drastic way, as the rupture of a single M50S fibre is less likely to cause the fracture of other M50S fibres. This leads to the more gradual failure of the low elongation fibres, which leads to the more gradual failure of the hybrid materials, increasing the measured pseudo-ductile strain.

In Figure 4.44, the cluster formation evolution for the hybrid material with a random fibre distribution is compared with two materials with a layer-by-layer type hybridization: 4 layers and 32 layers. It is observed that there are clear differences in the distribution of clusters. While for the 4 layer material, there is an early increase in the number of cluster with 2 fibres and more than 3 fibres at low strains, for the remaining materials there is higher number of single breaks with reduced multiple break clusters. After the first increase in fibre break density, and respective load drop, there is no significant increase in the number of clusters for the 4 layer material. On the other hand, in the 32 layer and random materials, that have a pseudo-ductile behaviour, a steady increase in the number of clusters is observed up to failure. Additionally, the 32 layer material that has a higher strength than the random material, is seen to have the highest percentage of single fibre breaks. This reinforces the conclusion that the fibre dispersion is a key factor in the behaviour of hybrid composites and a higher fibre dispersion leads to better material performance.

4.4.1 Summary

In this section, a study on the behaviour of hybrid materials using the dynamic spring element model developed in Section 4.3 was performed. The fibres chosen for such study were the AS4 and M50S fibres, that were seen to lead to a pseudo-ductile

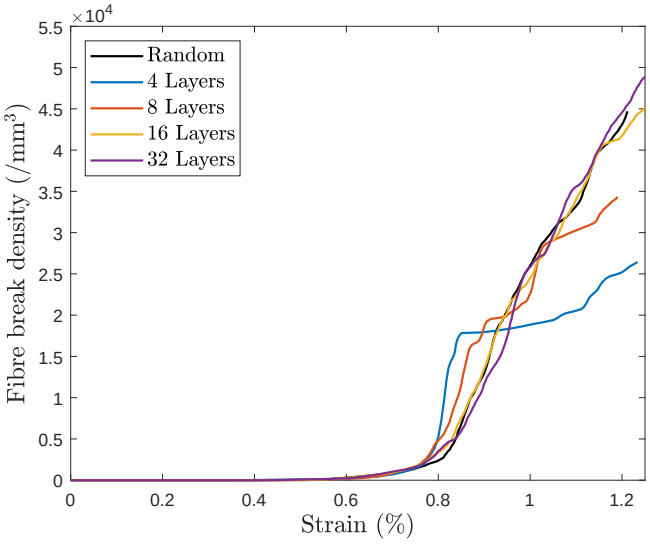

Figure 4.43: Fibre break density evolution for different layer-by-layer hybridizations in 25% volume fraction of M50S fibres.

behaviour for certain hybrid volume fractions in previous studies [58]. Different types of hybridization have been analysed to and the effects of the hybrid volume fraction , and of the fibre dispersion in the behaviour of the material were studied.

Different hybrid volume fractions were analysed using the same types of fibres and the behaviour of the material was observed to be highly dependent on this property. Depending on the volume fraction the material failure can be dominated by the failure of the low elongation or the high elongation fibres, however, the strength of the hybrid materials was seen to always be lower than the reference non-hybrid materials. Nevertheless, the objective of this hybridization was to achieve a non-brittle failure for the composite material, which was possible for a volume fraction of M50S fibres equal to 25%, which resulted in a 0.3% pseudo-ductile strain with a very gradual failure of the material.

The analysis on the hybrid volume fraction were conducted for random microsctructures, were no control over the position of each fibre type was used. However, the positioning of each fibre type and the fibre dispersion affect the behaviour of the hybrid material. To better understand, this effect two types of microstructures were considered: tow-by-tow hybridization, where the M50S were grouped in bundles was analysed for different number of bundles in the microstructure and layer-by-layer hybridization, where the fibres were grouped in layers. To characterize the fibre dispersion, the Dispersion Degree metric, previously proposed by [192], was used. As expected the fibre dispersion increases with the increased number of bundles as well with the increase in number of layers. It was interesting to note that for 32 layers, the Dispersion Degree was higher than that of a random microsctructure. The 16 layer material shows a very similar behaviour to that of the random material, making it an interesting configuration as the layers of the low elongation fibres are 16 μm thick, which is close to the ply thickness limit currently commercially available (20 μm).

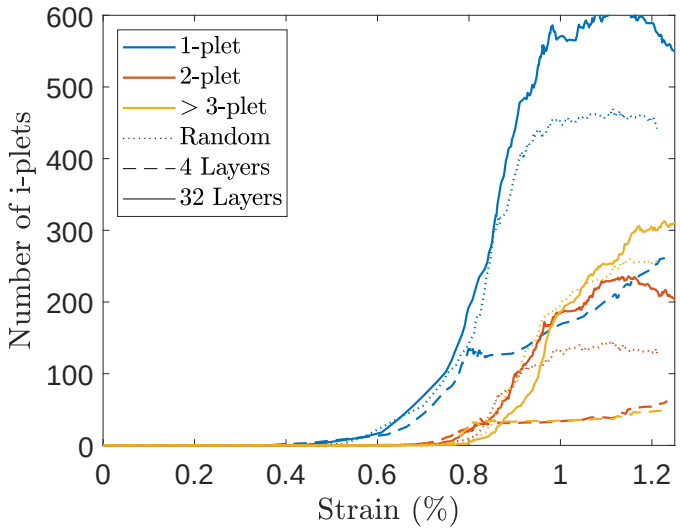

Figure 4.44: Fibre break cluster evolution.

The changes in fibre dispersion lead to very distinct material behaviours. While for the materials with lower dispersions, the M50S fibres tend to fail in a very narrow range of strain, leading to a load drop in the stress-strain curve, for higher dispersions the failure of the low elongation fibres is more gradual, thus leading to a progressive failure of the material.

This study reinforces the fact that for hybrid materials, the control of the fibres to hybridized as well as the hybrid ratio are important, however, controlling the actual microstructure of the material to ensure a good fibre dispersion is equally important to achieve a material with a non-brittle failure.

4.5 Conclusions

In this chapter a computationally efficient model to predict tensile fibre dominated failure in composite materials is proposed. The proposed Spring Element Model uses a random fibre distribution, which better relates to the real microstructures of composite, as well as being able to be used for fibre hybrid composites, whose fibres can have different geometrical and material properties.

In Section 4.1, the baseline model is presented and used to further understand the mechanisms that affect fibre dominated tensile failure. The results for the stress fields that surround a broken fibre are analysed and it is seen that the model is able to capture both the stress concentration in the intact fibres and the ineffective length of the broken fibre. The usage of different statistical distributions for fibre strength was also analysed and it was concluded that the traditional Weibull distribution leads to an overprediction of the strength of the fibre elements, thus leading to an overprediction of the composite's strength. To circumvent this problem, two additional statistical distributions are also studied: the Power Law Accelerated Weibull

and the Weibull of Weibulls. It is observed that both of these distributions allow a more accurate computation of the composite's strength as the fibre element strengths has a lower scaling with the length. The influence of the matrix properties is also analysed and it is concluded that considering the matrix linear elastic leads to an increased tensile strength, when comparing to the elasto-plastic case. To understand the mechanisms dominating fibre dominated failure, an extensive analysis of cluster formation is performed. The results from the SEM are compared with experimental data in the literature and it is concluded that, similarly to other models present in the literature [63, 73, 193], the SEM overpredicts the fibre break density at failure and underpredicts the formation of clusters with multiple broken fibres. Additionally, it is observed that the model predicts a higher percentage of diffuse clusters while experimentally a higher percentage of planar clusters are observed.

The developed SEM is then compared with a Progressive Damage Model developed by Guerrero et al. [63], using different functions for both the ineffective length and the stress concentration. An analysis on both the local stress fields that surround a broken fibre and the RVE behaviour is performed. It is seen that the analytical formulations lack the representation of the effects of some material parameters when comparing to the SEM, however, these formulations allow faster models, as no equilibrium equations need to be solved. The stress fields around clusters composed of multiple fibres is also analysed and it is observed that the scaling of both the ineffective length and the maximum stress concentration as a function of the number of broken fibres is important as this will lead to significant changes to the cluster formation process. For the RVE simulations the models different models were seen to lead to different material behaviour, mainly regarding cluster formation, where the input material parameters have a large influence of this process. Additionally, it is seen that considering a static definition for cluster analysis leads to erroneous results and, therefore, the cluster definition should change for different materials.

In Section 4.3, the previously developed SEM is extended to the dynamic case. This modification is done in order to overcome some shortcomings of the model, namely the underprediction of the number of planar clusters. This improvement is done by considering the inertial terms on the equilibrium equation. To improve the its computational time, the model was parallelized using Message Passing Interface, which allows the usage of multiple CPUs, to solve the same problem. Similarly to the static SEM, analysis on the local stress fields and RVE behaviour were performed as with the static model. As expected, it was observed that including dynamic effects for fibre failure has a large impact on the stress redistribution process when a fibre breaks. It is observed that there is an increase of the maximum stress concentration on the surrounding intact fibres, which increases their failure probability. Additionally, an stress wave that propagates in the fibres' longitudinal direction is observed, potentially causing the fibre s to fracture in more than one plane. The relation between the maximum dynamic stress concentration factor and the static one is seen to be highly dependent on the material's property, being that for some cases an increase of 300% is observed. For the RVE simulations the effect of dynamic fibre failure is reduced and it is seen to be more relevant if the matrix is considered linear elastic. Nevertheless, the dynamic effects are seen to lead to an earlier forma-

tion of higher dimension clusters, a prediction that better relates to experimental results.

The dynamic spring element model was used in Section 4.4 to study the behaviour of hybrid materials. In this work not only the effect of the hybrid volume fraction was analysed for a random microstructure, but also the effect of the material's microstructure was evaluated. It was observed that the microstructure of the material, particularly the fibre dispersion, characterized by the Dispersion Degree metric, is important in obtaining a gradual failure of the material, as such behaviour was only achieved for the higher fibre dispersions.

In this chapter more insight on the fibre clustering phenomenon, and the factors affecting it, was gained, specially for hybrid composites. It is also important to note that the available experimental data on fibre clustering is lacking and more results will help guide the improvement of such models.

Part IV

Experimental study on the mechanics of failure of fibre hybrid composites

Chapter 5

Interply hybrids experimental campaign

5.1 Introduction

Interply hybridization, as seen in Section 2.2, is an hybridization strategy that consists in combining layers of different materials into a single composite laminate. This is the hybridization strategy that leads to the lowest dispersion of fibres, however, it is the less challenging to manufacture, as traditional hand layup methods combined with autoclave curing can be used. This hybridization strategy can be combined with the use of thin-ply layers, enabling the control of the failure mechanisms. Several authors have used this strategy to achieve a ductile failure of the hybrid composite materials [11, 123, 129–131]. In this chapter interply hybridization is explored having as a basis the work done by Danzi [32]. This works focuses on the analysis of the effects of interply hybridization in structural details manufactured using multidirectional laminates.

Danzi [32] studied interply hybridization by combining thin-ply T800 and HR40 carbon fibre layers. In addition to analysing the behaviour of the inter-ply hybrid materials, Danzi [32] also reported the stochastic strength of the fibres in study, which are shown in Table 5.1, where σ_0 is the Weibull scale parameter at a reference length L_0, ρ is the Weibull shape parameter and α is the modified Weibull length scaling parameter.

Table 5.1: T800 and HR40 carbon fibre properties [30, 31].

Fibre	R_f (μm)	E_f (GPa)	Tensile strength (MPa)	Failure strain (%)	Density (g/cm^3)	σ_0 (MPa)	L_0 (mm)	ρ	α
T800	2.5	294	5880	2.0	1.80	10679	1	4.69	0.75
HR40	3.0	375	4410	1.18	1.82	6044	1	4.09	0.44

Danzi [32] performed an extensive experimental campaign on both non-hybrid T800 and HR40 materials, as well as three different hybrid materials. Both T800

and HR40 materials were acquired from NTPT using the ThinPreg™80EP-736 resin system. The T800 material has an areal weight of 50 g/m^2, resulting in a thickness of 53 μm, and the HR40 material has an areal weight of 20 g/m^2, which results in a thickness of 23 μm. The non-hybrid laminas were used to create three different hybrid materials with the following sublaminate building blocks:

- **H1**: [$T800/HR40/T800$] - 120 g/m^2;
- **H2**: [$2T800/HR40/2T800$] - 220 g/m^2;
- **H3**: [$3T800/2HR40/3T800$] - 340 g/m^2.

These configurations were selected based on the predictions of the model developed by Jalavand et al. [11]. The chosen configurations promote stable fragmentation and delamination leading to an non-brittle failure of the material. The material properties obtained by Danzi [32] are shown in Table 5.2. The missing properties were not measured in the work from Danzi [32].

Table 5.2: Material properties obtained for the interply hybridization [32].

		T800	H1	H2	H3	HR40
Elastic properties						
E_1	[GPa]	148.36	154.72	144.26	144.71	192.60
ν_{12}	[-]	0.304	0.307	0.310	0.317	0.290
E_2	[GPa]	8.01	8.2	-	-	6.55
G_{12}	[GPa]	4.73	4.42	-	-	3.70
Strength properties						
X_T	[MPa]	2923.8	2369.1	2640.4	2587.1	2157.6
Y_T	[MPa]	63.76	58.27	-	-	37.52
S_{12}	145.74	131.39	-	-	-	95.20
Fracture properties						
R_0	[KJ/m^2]	191.74	250.69	371.16	751.40	24.69
l_{fpz}	[mm]	2.17	2.60	2.33	5.42	0.015
γ	[mm^{-1}]	0.3912	0.3236	0.3635	0.1503	60.99
β	[-]	3.585	3.622	3.595	3.785	3.393

Danzi [32] concluded that although there is a reduction in the tensile strength of the hybrid materials, when comparing to the baseline T800 material, there is a large increase in their intralaminar fracture toughness. The tensile tests on the hybrid materials suggest the occurrence of stable fragmentation of the HR40 plies, specially on the H2 and H3 materials. This was concluded by a post-mortem analysis of the tensile specimens. As for the Double Edge Notched Specimens (DENT) used to determine the fracture toughness, a large difference in the failure mechanisms was observed when comparing the hybrid to the non-hybrid baseline materials.

Figure 5.1 shows the post-mortem x-ray images of the DENT specimens of largest size (50 mm wide). It is observed that mechanisms that occur in the failure of

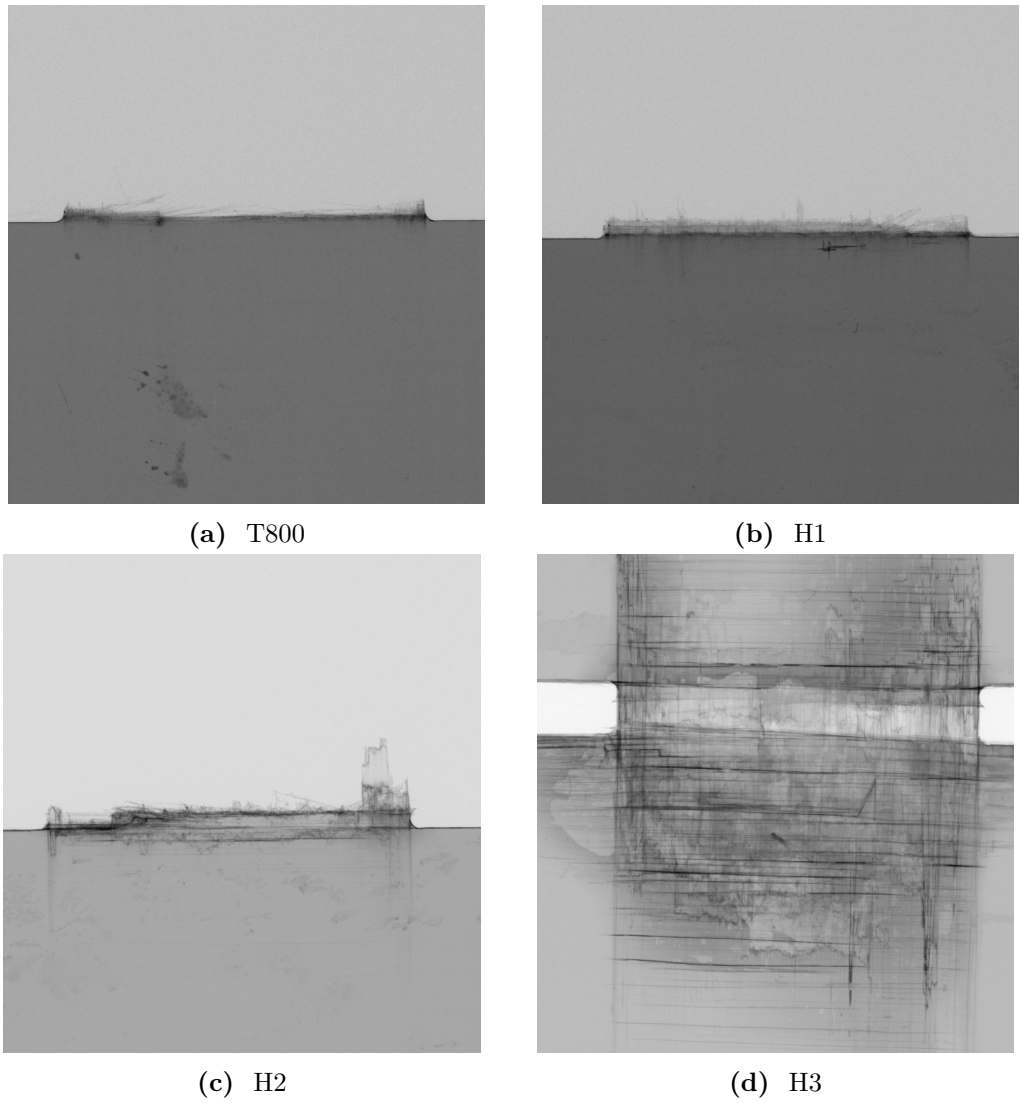

(a) T800 **(b)** H1

(c) H2 **(d)** H3

Figure 5.1: Post failure X-ray images of the interply double edge notch specimens.

these specimens changes with hybridization. The T800 materials shows a very clean crack propagating in the notched section with almost no fibre pull-out and no split cracking. With the addition of the HR40 plies it is possible to see an increase in disperse damage surrounding the main crack. The H1 material, although presenting an increased fracture toughness when compared to the baseline T800 material, shows very similar damage mechanisms, with a slight increase in fibre pull-out. The H2 material shows splitting in the notch tip and increased fibre pull out. Additionally, multiple cracks seem to originate from the notch tip, leading to the increased fracture toughness. The H3 material shows very dissimilar damage patterns when compared to the other materials. It is possible to see that large splits develop in the notch tips. Additionally, it is possible to see that multiple cracks develop before the failure of the specimen, both in the 90° and in the 0° plies. It is also possible to observe very large pull-outs and delaminations. These damage mechanisms are responsible for the increase of the notched strength of this material, which leads to the measured

increase in the fracture toughness. It should be noted that, in composite materials, there is a ply thickness effect on the measured fracture toughness of the laminate [194–198], this may contribute to the increase in the fracture toughness observed in the hybrid materials. Nevertheless, the observed increase (from 192 to 371 KJ/m^2) and change in damage mechanisms, including multiple fragmentation and cracking, can't be solely justified by the ply thickness effect.

In this chapter interply hybridization is explored focusing on the analysis of the effects of interply hybridization in structural details manufactured using multidirectional laminates.

5.2 Materials

Taking into account the work previously done by Danzi [32], reviewed in the previous section, an experimental campaign on structural detail coupons is performed. From the materials considered in [32] only three were selected to be tested at this stage. Due to the lower tensile strength and fracture toughness of the HR40 material, this composite was not tested and, therefore, the comparisons with the baseline non-hybrid composite will be done with the T800 material. The H3 material, with an areal weigh of 340 g/m^2 is considered too thick for typical aeronautical application, restricting the number of layers that can be stacked in a multidirectional laminate for a given thickness. This material was, therefore, not considered in this campaign. For the multidirectional laminates of the T800 material an areal weigth of 100 g/m^2 was used.

Hard multidirectional laminates similar to the industry defined baseline were selected based on previous work developed. Due to the different areal weights and thicknesses of the materials two different layups were defined, which are shown in Table 5.3.

Table 5.3: Laminate definition for interply hybrid level two testing.

Material	Layup	Thickness (mm)
T800	$[45/-45/0/45/-45/90/0]_{\$}$	1.404
H1	$[45/-45/0/45/-45/90/0]_{\$}$	1.690
H2	$[45/-45/0/90]_{\$}$	1.687

Note that each layer of the hybrid materials represent the hybrid sublaminate: [T800/HR40/T800] for the H1 material and [2T800/HR40/2T800] for the H2 material. The elastic properties of each material are shown in Table 5.4. These properties were determined based on the measured properties in Table 5.2 using classical laminate theory. For the H2 material, if a lamina property was not measured directly, it was assumed to be equal to that of the H1 material.

For each of the defined layups, plain strength tension and compression, and open-hole tension and compression tests were performed.

Table 5.4: Elastic properties of the multidirectional materials.

Material		T800	H1	H2
E_x	[MPa]	53473	55078	58501
E_y	[MPa]	44334	45602	41680
ν_{xy}	[-]	0.44	0.44	0.44
ν_{yx}	[-]	0.36	0.37	0.31
G_{xy}	[MPa]	25244	26112	23079

5.3 Plain strength tension

Unnotched specimens with a nominal width (W) of 25 mm and a nominal length (L) of 250 mm were tested in tension, following the ASTM D3039/D3039M – 14 test standard [199]. 50 mm long aluminium tabs were bonded to the specimens, resulting in a gauge length of 150 mm. The tests were performed under displacement control, at a speed of 1.0 mm/min, in an Instron 4208 electro-mechanical universal testing machine equipped with a 200 kN load cell. The test data was acquired directly by the testing machine commands module, with an acquisition frequency of 5.0 Hz. Hydraulic grips were used with a hydraulic clamping pressure of 200 bar.

The stress vs displacement curves for the three tests materials are shown in Figure 5.2 and the maximum stress and normalized maximum stress (normalized by the longitudinal elastic modulus (E_x)) are presented in Table 5.5. The behaviour of both the T800 non-hybrid material and the H1 hybrid material is linear elastic up to failure, however the H2 material shows some non-linearity before peak stress.

Comparing the strengths of the materials it is interesting to see that the H1 material has a significantly lower strength than the T800 material, which follows the trend observed in the UD material characterization done by Danzi [32]. The earlier failure of the material is caused by the rupture of the lower elongation fibres (HR40) which reduces the strength. On the contrary, the H2 material has a higher maximum stress than the T800 baseline. However, if we analyse the normalized strength, obtained by dividing the maximum stress by the laminate's elastic modulus, the H2 material shows a lower normalized strength when compared to the T800 material. This reduction in the normalized strength for the hybrid materials leads to the conclusion that, in fact, adding the HR40 layers to the T800 material leads to an earlier failure of the material and that the higher maximum stress observed for the H2 material is due to this configuration having an higher percentage of layers aligned with the loading direction than the T800 material (28.6% vs 23%). In addition, the H2 material is seen to have some non-linear behaviour prior to peak stress, which is accompanied by acoustic emission. This leads to the conclusion that there is damage developing in the material before the maximum stress. In addition, delaminations were observed prior to the failure of the specimen

Figure 5.3 shows the post-mortem photos of representative plain strength tension specimens. In all the materials the fracture is very complex with different interacting damage mechanisms. The T800 and H1 specimens show similar fracture patterns,

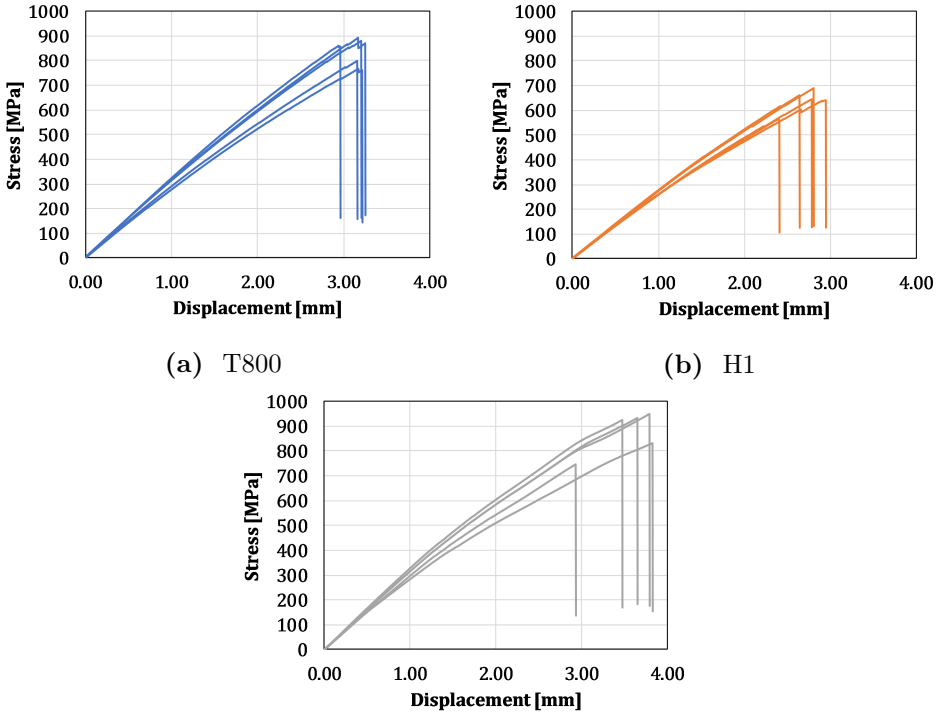

(a) T800 **(b)** H1

(c) H2

Figure 5.2: Stress vs displacement curves of the plain strength tension tests.

Table 5.5: Plain strength tension results.

Material	X_T^L [MPa]		E_x [MPa]	X_T^L/E_x [MPa/GPa]
	avg.	stdev.		
T800	839.6	53.4	53472.69	15.70
H1	640.8	46.8	55078.03	11.63
H2	875.8	86.1	58501.16	14.97

with split cracks and fibre pull-out, but limited delamination. The H1 material appears to have a more brittle fracture with less fibre pull-out, which is related with the addition of the more brittle HR40 material. The H2 material shows a very complex fracture. This material was seen to delaminate at the middle plane prior to peak stress (see Figure 5.4), delamination that extended towards the ends of the specimen resulting in extensive delamination as seen in Figure 5.5. Figure 5.4 also shows the presence of matrix cracks emanating from the free edges prior to the peak stress, feature that was not seen in the remaining materials. Additionally, the fractured area of the H2 specimens is more extensive than in the other materials, with multiple fractures occurring and extensive fibre pull out and shear cracks.

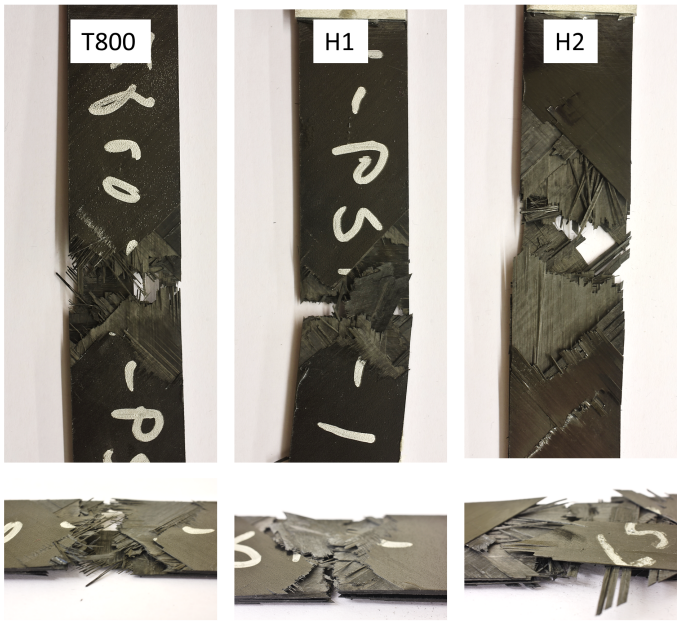

Figure 5.3: Post-mortem photos of the PST specimens.

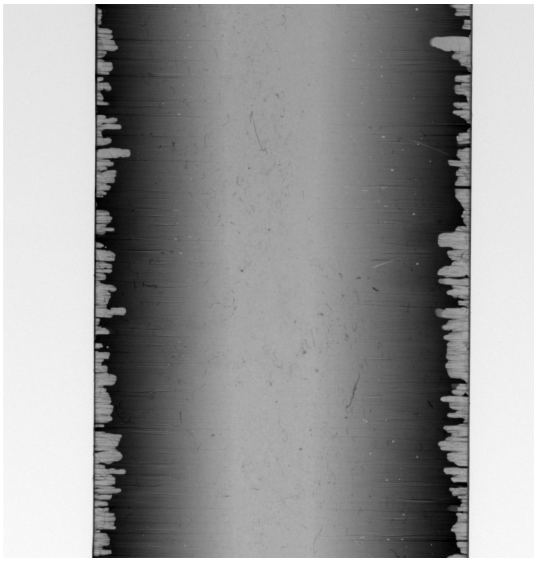

Figure 5.4: X-ray image of an H2 plain strength tension specimen at 90% of the peak load.

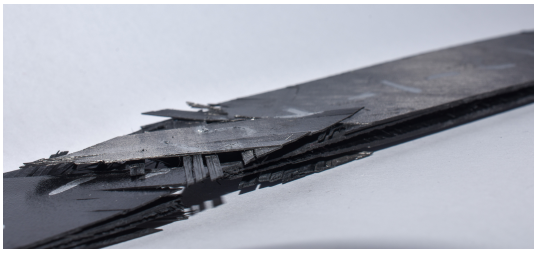

Figure 5.5: Delamination detail on a post-mortem H2 plain strength tension specimen.

5.4 Plain strength compression

Unnotched specimens with a nominal width (W) of 25 mm and a nominal length (L) of 305 mm were tested, following the ASTM D6484/D6484M [200] test standard. The compression rig was clamped using M8 bolts fastened with a torque of 8 Nm. The tests were performed under displacement control, at a controlled speed of 1.0 mm/min, in a servo-hydraulic MTS 810 testing machine with a load capacity of 250 kN.

Table 5.6: Plain strength compression results.

Material	X_C^L [MPa]		E_x [MPa]	X_C^L/E_x [MPa/GPa]
	avg.	stdev.		
T800	569.7	39.7	53472.69	10.65
H1	456.9	32.7	55078.03	8.30
H2	536.8	37.8	58501.16	9.18

Figure 5.6 shows the stress vs displacement curves the plain strength specimens tested. The strengths and strengths normalized by the elastic modulus of the laminates are shown in Table 5.6.

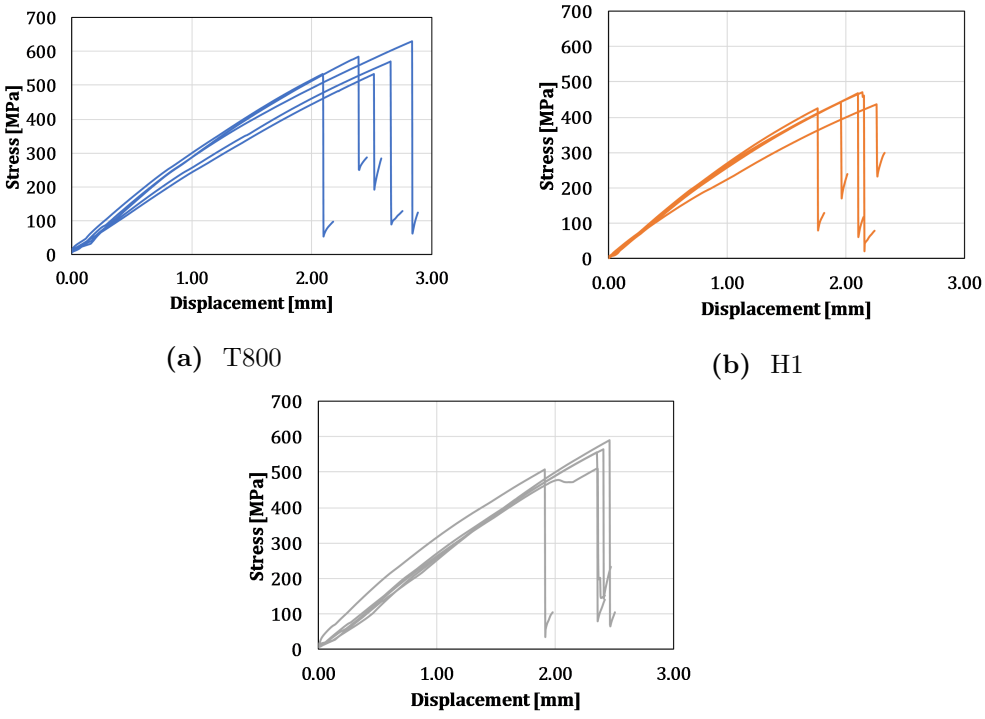

(a) T800

(b) H1

(c) H2

Figure 5.6: Stress vs displacement curves of the plain strength compression tests.

In compression the hybrid materials present a lower strength when compared with the non-hybrid material configuration, being lowest for the H1 material. This

can be explained by the addition of the HR40 plies and the fact that there is no synergy between the two materials in a compressive stress state. Figure 5.7 shows the post-mortem images of representative plain strength compression tests of the three materials analysed. The compressive failure of the laminates is characterized by a combination of complex damage mechanisms including fibre kinking, wedge transverse fracture, delamination and surface split cracking on the outer 45° plies, however, there differences between the fractures in the different materials are minor.

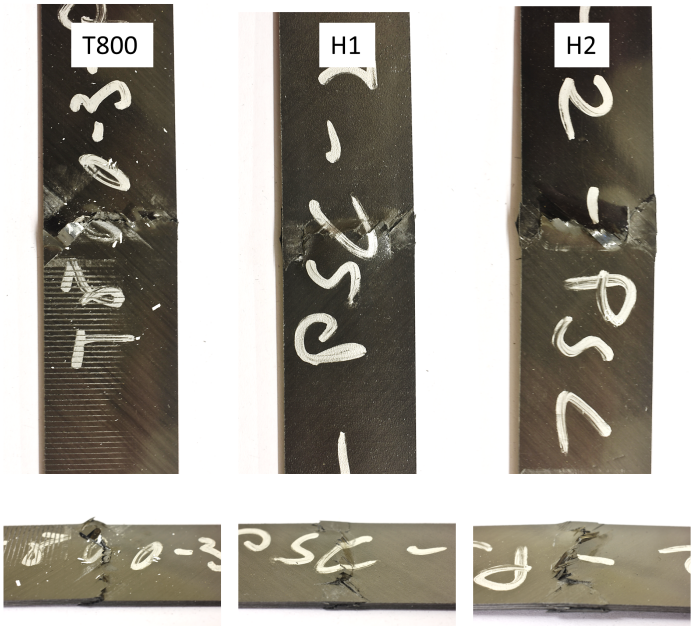

Figure 5.7: Post-mortem photos of the PSC specimens.

5.5 Open-hole tension

Open-hole specimens were tested in tension, following the ASTM D5766/D5766M – 02A test standard [201]. The tests were performed under displacement control, at a speed of 1.0 mm/min, in an Instron 4208 electro-mechanical universal testing machine equipped with a 200 kN load cell. The test data was acquired directly by the testing machine commands module, with an acquisition frequency of 5.0 Hz. Hydraulic grips were used with a hydraulic clamping pressure varying from 50 to 200 bar depending on the specimen's size. Specimens with a constant diameter to width ration ($2W/R$) equal to 1/6 and different widths were tested to determine the size effect of theses materials for this notched configuration. Three widths were tested 12, 36 and 72 mm, resulting in holes with diameters equal to 2, 6 and 12 mm, respectively. The failure stress of the Open-Hole Tension (OHT) specimens was calculated as:

$$\bar{\sigma}^{\infty} = \frac{P}{WT} \,, \tag{5.1}$$

where P is the failure load, and W and T are the specimen's width and thickness, respectively.

Figure 5.8 shows the stress vs displacement curves of the tested open-hole tension specimens. For each material three specimens sizes were tested. In Figure 5.9 the maximum stress of the all the materials is shown, together with the elastic modulus of each laminate, which is higher for the H2 material. The behaviour of the T800 material is linear elastic up to failure, however, both hybrid materials show non-linearity prior to failure, although only in some specimens. Overall, the H2 material has a higher notched strength, being it higher than the non-hybrid baseline material. The H1 material has a notched strength lower than the T800 material, which was already true for the unnotched tensile strength.

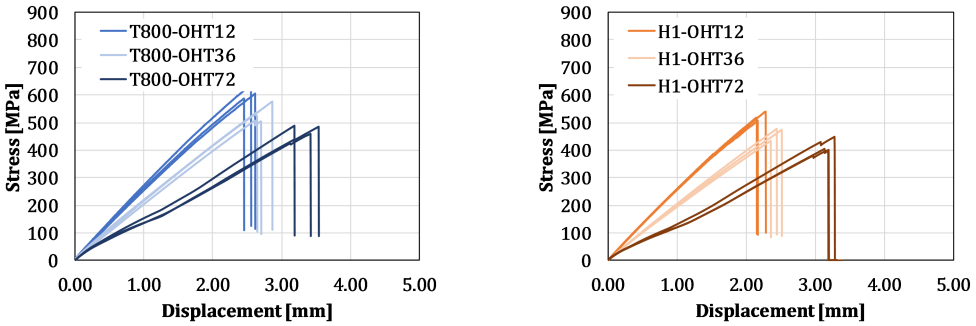

(a) T800

(b) H1

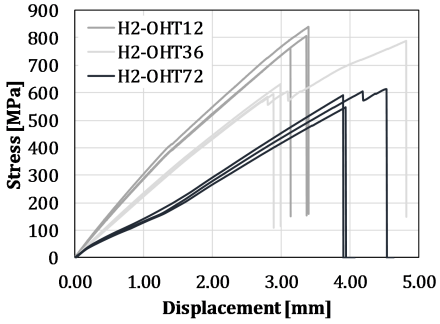

(c) H2

Figure 5.8: Stress vs displacement curves of the open-hole tension tests.

Post-mortem images of the fracture of 36 mm wide open-hole specimens are shown in Figure 5.10. It is possible too see that the extension of damage increases in the hybrid materials. The T800 material shows a fibre dominated pull-out failure mode after testing, where fibre/matrix splitting and triangular shaped delaminations are present. The hybrid materials show a much more complex type of failure with extensive delamination and fracture zone. The H1 material has a single fracture zone, as does the T800, however it is more fibre pull-out and shear cracks are observed. The H2 material has the most complex fracture, where multiple cracks appear with extensive delamination. This material showed the highest variability in behaviour, due to the more complex failure behaviour. Figure 5.11 shows details of the fracture of one of the H2 open-hole specimens with a 36 mm length. This

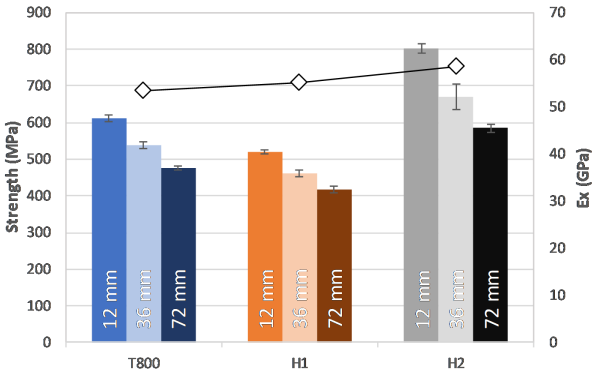

Figure 5.9: Maximum stress for the open-hole tension tests for the different materials and geometries.

particular specimen had a very interesting behaviour, with a plateau like behaviour on the stress-displacement curve before the peak load and final failure. The plateau occurred at approximately 600 MPa, which is similar to the peak stress of the remaining H2 open-hole specimens with 36mm width. For the specimen shown in Figure 5.11, failure did not occur at this point, however, acoustic emission was observed at this stage and delamination could be observed. Nevertheless, the specimen only failed at a stress of 800 MPa and it failed in a region away from the notch. This behaviour only occurred for one specimen out of the nine specimens tested (of different sizes) of the H2 material, however, some non-linear behaviour can be observed for the specimens that are 72 mm wide.

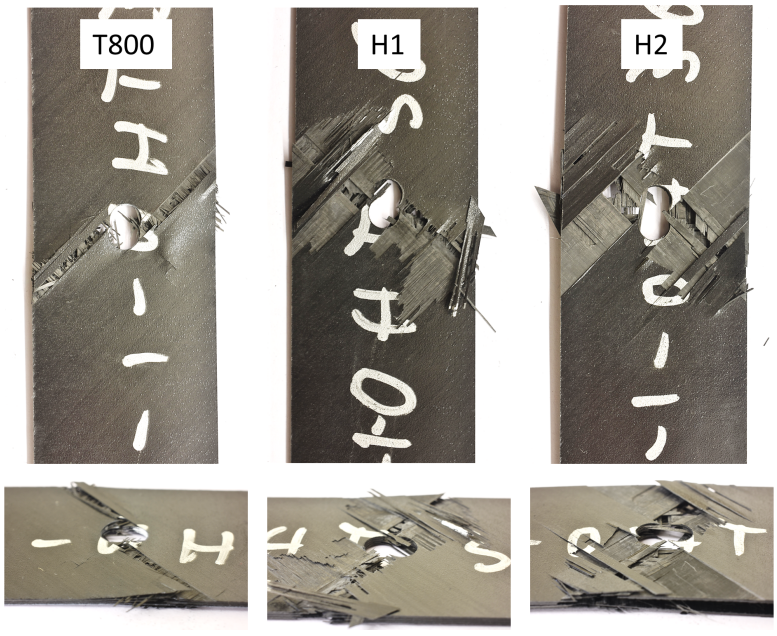

Figure 5.10: Post-mortem photos of the OHT specimens with 36mm width.

Figure 5.12 shows the x-ray images of the 12mm and 72mm wide open-hole tension specimens post-failure and at 90% of the failure load (the test was interrupted prior

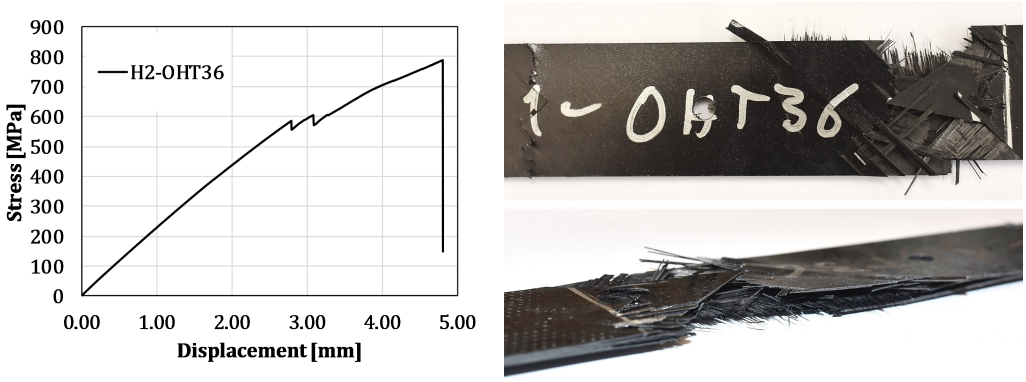

(a) Stress-displacement curve.

(b) Post-mortem failure detail.

Figure 5.11: Stress-displacement curve and failure detail of a H2 open-hole tension specimen with 36mm width. Note that this specimen failed outside the notched section.

to failure). The fracture behaviour of the T800 and H1 materials is very similar, with cracks appearing in the 45° direction as well as the perpendicular to the load direction, with triangular delaminations. At 90% of the peak stress these materials show delaminations emanating from the free edges, however, no damage can be seen surrounding the hole. The H2 material has a more complex behaviour. Specially for the 12mm wide specimen, at 90% of the load free edge delamination can be observed, as well as split cracks near the hole. In addition, transverse cracks can also be observed, which are believed to occur in the 90° layers. Post failure, the complex damage mechanisms occurring in this material can be observed. Large splits around the hole can be observed as well as shear and transverse cracks initiating from the split. This leads to a complex crack with a very large damage area with the appearance of multiple cracks, that are not limited to the notched section. This multiple cracking explain why the specimen in Figure 5.11 failed outside of the notched area. The combination of delamination with multiple cracks growing from the longitudinal splits, make it possible for this behaviour to occur, however, it only occurred in some specimens.

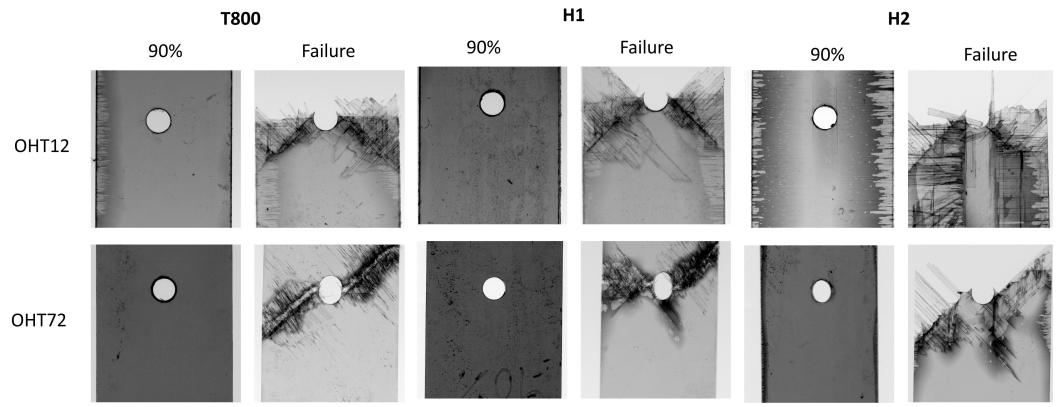

Figure 5.12: X-ray images of the open-hole tension specimens: 12 mm and 72 mm wide specimens at 90% of the failure load and post-mortem.

5.5.1 Notch sensitivity analysis

To better understand the effects of notches in the behaviour of the materials and to better compare them, an analysis on the notch sensitivity is performed [202–204]. The notch sensitivity can be determined using the normalized notched strength [202]:

$$\bar{\sigma}_N = \frac{\bar{\sigma}^{\infty}}{X_T^L} \,, \tag{5.2}$$

where $\bar{\sigma}^{\infty}$ is the notched strength and X_T^L is the unnotched strength of the laminate. The response of a notched specimen is bound between two opposite behaviours: notch sensitive and notch insensitive.

Notch sensitive behaviour

A material is considered notch sensitive when it has a brittle behaviour and the strength of the notched coupon is function only of the stress concentration factor (K_T) at the notch tip. For this scenario the normalized notch strength reads:

$$\bar{\sigma}_S = \frac{1}{K_T} \,. \tag{5.3}$$

For an finite plate with a width W and a centre hole width radius R, K_t can be written as:

$$K_T = K_T^{\infty} R_K \tag{5.4}$$

where K_T^{∞} is the stress concentration a plate of an infinite plate with a centre hole

$$K_T^{\infty} = 1 + \sqrt{2\left(\sqrt{\frac{E_x}{Ey}} - \nu_{xy}\right) + \frac{E_x}{G_{xy}}} \,, \tag{5.5}$$

where E_x, E_y and G_{xy} are the elastic properties of the laminate and R_k is the width correction factor

$$R_K = \left\{ \frac{3\left(1 - 2R/W\right)}{2 + \left(1 - 2R/W\right)^3} + \frac{1}{1}\left(\frac{2R}{W}M\right)^6 \left(K_T^{\infty} - 3\right)\left[1 - \left(\frac{2R}{W}M\right)^2\right] \right\}^{-1} \,, \tag{5.6}$$

with

$$M^2 = \frac{\sqrt{1 - 8\left[\frac{3(1-2R/W)}{2+(1-2R/W)^3}\right] - 1} - 1}{2\left(1 - 2R/W\right)^2} \,. \tag{5.7}$$

Notch insensitive behaviour

The other end of the spectrum the material behaviour can be considered notch insensitive if the strength of the material is not affect by the presence of the notch.

This corresponds to a ductile behaviour and the notched strength only depends on the notch section and reads:

$$\bar{\sigma}_{IS} = 1 - \frac{2R}{W} \,. \tag{5.8}$$

The notch sensitivity analysis for the tested materials is shown in Figure 5.13. In this figure, the normalized notched strengths are plotted versus the specimen's width. The lines in black represent the notch sensitive and insensitive limits, given, respectively by Equations (5.3) and 5.7. As expected, the T800 material has the highest notch sensitivity, which is reduced for the hybrid materials. This reduction is related to the more complex and less brittle type of failure that occurs for the hybrid materials. It is interesting to note that the H2 material has a normalized notched strength higher than the notch insensitive value for the 12 mm wide specimens. This represents an interesting behaviour and results from the complex damage mechanisms and multiple cracking and delamination that occur in the hybrid materials. In addition, the failure of the 36 mm wide specimen in an unnotched region (Figure 5.11) helps understanding this notch insensitive behaviour. The H1 material shows a notch sensitiveness in between the H2 and T800 materials, nevertheless, this material has a lower unnotched tensile strength and thus a lower notched tensile strength.

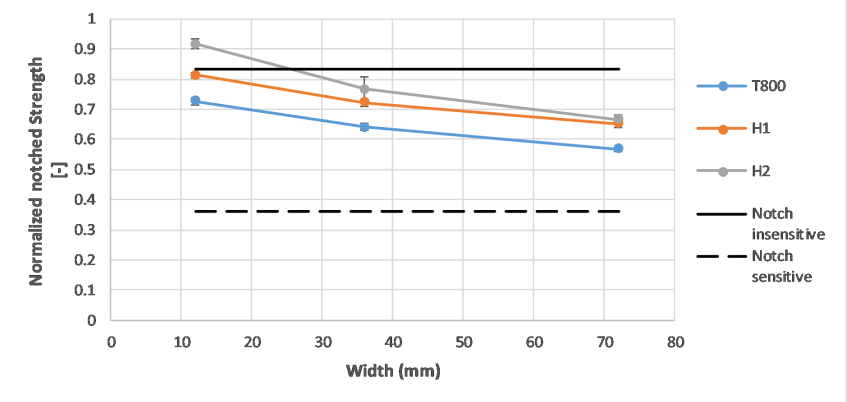

Figure 5.13: Notch sensitivity of the open-hole tension tests.

5.6 Open-hole compression

Open-hole specimens were tested, following the ASTM D6484/D6484M [200] test standard. The compression rig was clamped using M8 bolts fastened with a torque of 8 Nm. The tests were performed under displacement control, at a controlled speed of 1.0 mm/min, in a servo-hydraulic MTS 810 testing machine with a load capacity of 250 kN. As for the the open-hole tensile tests, three different geometries with the same diameter to width ration were tested ($2W/R = 1/6$) and widths equal to 18, 24 and 36 mm and holes with 3, 4 and 6 mm of diameter.

The stress-displacement curves of all the tested Open-Hole Compression (OHC) specimens are shown in Figure 5.14 and the notched compression strengths are shown

in Figure 5.15. In addition, a notch sensitivity analysis, using the framework derived in Section 5.5.1 is shown in Figure 5.16.

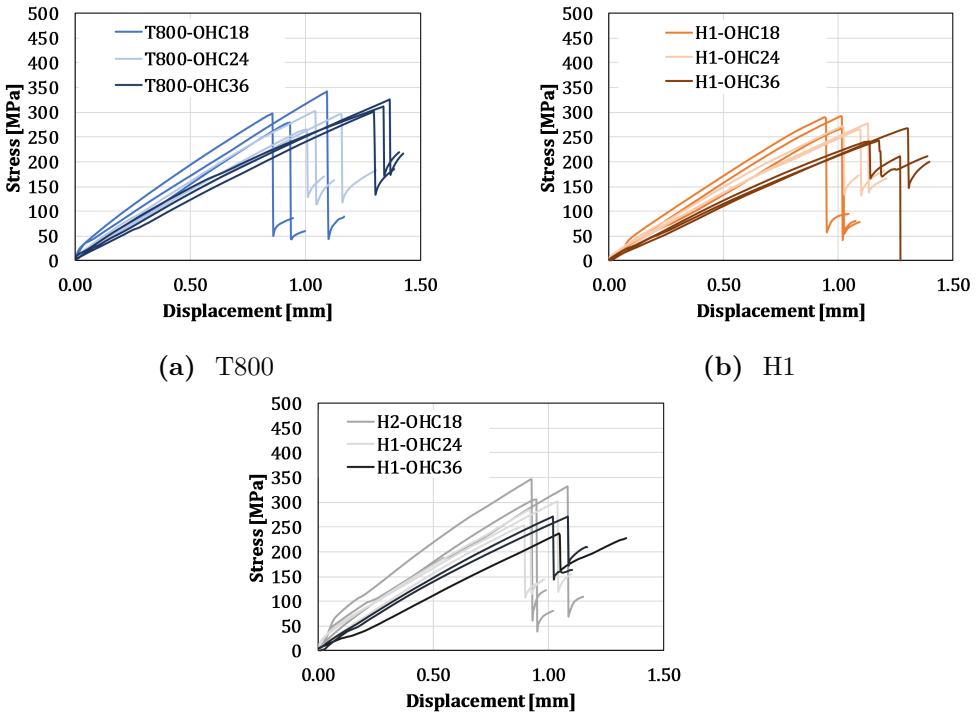

(a) T800 **(b)** H1

(c) H2

Figure 5.14: Stress vs displacement curves of the open-hole compression tests.

The behaviour of the three materials is very similar, being that the hybrid materials have comparable notched compressive strengths to that of the T800 material. Nevertheless, a noticeable size effect is observed for the hybrid materials, while the T800 material shows barely any size effect. The notch sensitivity analysis reinforces the similarity in behaviour of the tested materials. Although the unnotched strength of the hybrid materials is lower than that of the T800 material, the normalized notched strengths are very similar, leading to very similar notch sensitivities. The behaviour of all the materials in neither fully notch insensitive nor notch sensitive, having an intermediate behaviour, which is typical of composite materials [202–204].

Post-mortem photographies and X-ray images are shown, respectively, in Figures 5.17 and 5.18. Similarly to the notched strengths, there is no clear difference in the damage mechanisms observed in the specimens. For this test case no specimens were tested at 90% of the failure load and, therefore, is impossible to analyse if damaged occurs at earlier stages for any of the tested materials. Nevertheless, no non-linearities prior to peak stress were detected in the stress-displacement curves shown in Figure 5.14. For all the materials the specimens exhibited a net-section failure mode failure dominated by fibre kinking. Some delamination is observed in the X-ray images, being it more marked for the smaller 18 mm wide specimens.

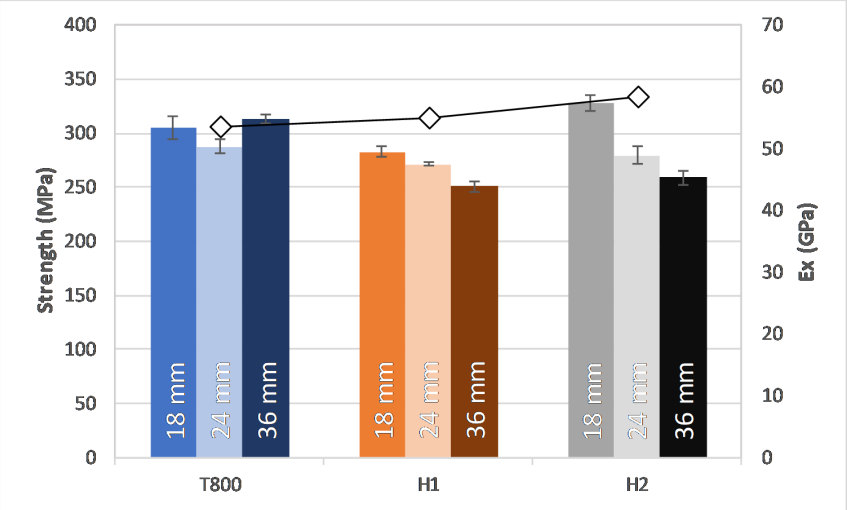

Figure 5.15: Maximum stress for the open-hole compression tests for the different materials and geometries.

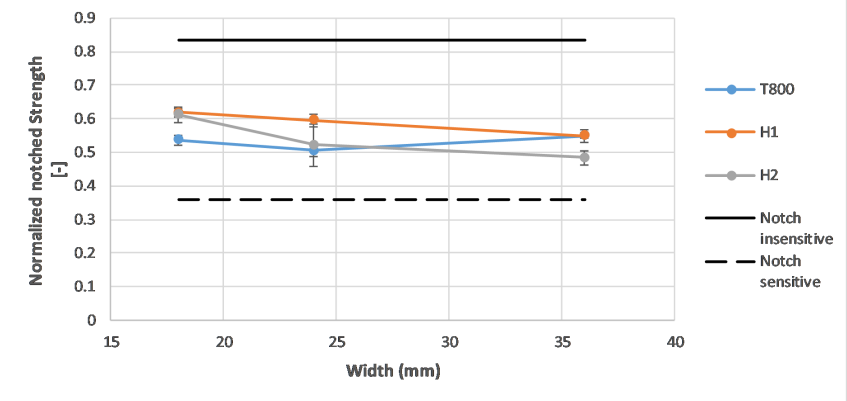

Figure 5.16: Notch sensitivity of the open-hole compression tests.

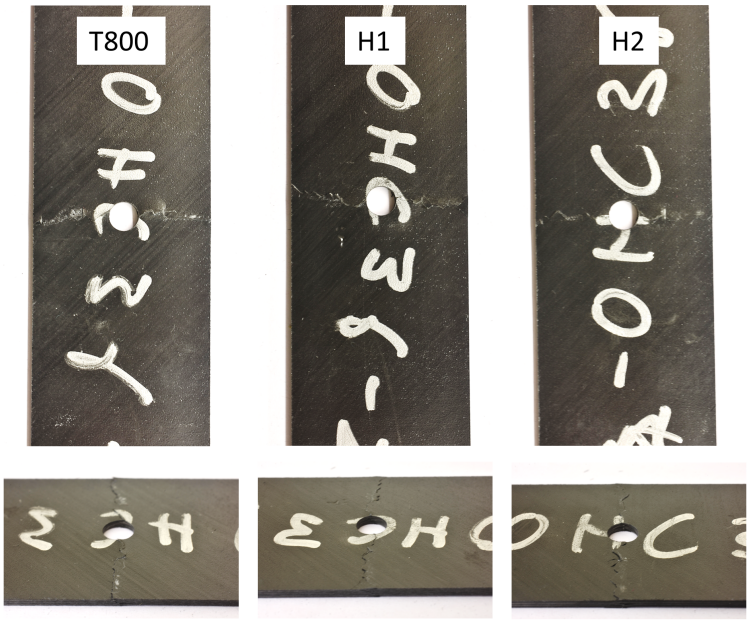

Figure 5.17: Post-mortem photos of the OHC specimens with 36 mms width.

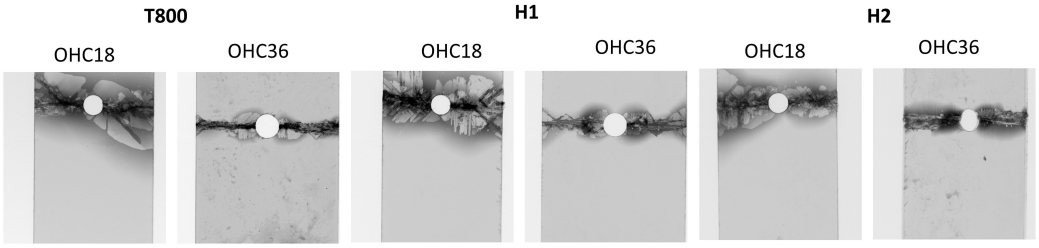

Figure 5.18: X-ray images of the open-hole compression specimens: 18 mm and 36 mm wide specimens post-mortem.

5.7 Conclusions

In this chapter the ply-by-ply or interply hybridization concept was used to design and test multidirectional laminates at coupon level. This work was built upon the previous work developed by Danzi [32], where the author used the interply hybrid concept at the lamina level to determine its effects on key material properties such as longitudinal strength and intralaminar fracture toughness.

Three materials were chosen to be tested: a baseline T800 non-hybrid material with 100 g/m^2 and two hybrids H1- $[T800/HR40/T800]$ and H2- $[2T800/HR40/2T800]$, where the HR40 has an areal weight of 20 g/m^2 and the T800 has an areal weight of 50 g/m^2. Two hard laminates were manufactured: for the T800 and H1 materials a $[45/-45/0/45/-45/90/0]_{\$}$ layup was chosen, while for the H2 material, due to its higher sublaminate thickness the $[45/-45/0/90]_{\$}$ layup was used. Plain strength tension and compression as well as open-hole tension and compression tests were conducted to compare the performance of the materials.

The plain strength tension tests it is concluded that the H2 material has the highest unnotched strength, however, this material has a higher percentage of 0° layers than the remaining two materials. If we considered the strength normalized by the laminate's longitudinal elastic modulus, the T800 non-hybrid material has the highest normalized strength, meaning that the addition of the brittle HR40 layers to the T800 material leads to a lower unnotched normalized strength of the material. Nevertheless, a clear distinction in the fracture mechanisms can be seen in the materials tested. The H2 material shows a less brittle fracture with multiple cracks and extensive delamination and pull-out, while the H1 and T800 material show a smaller, more localized fracture region.

The results of the open-hole tensile tests performed show a very interesting behaviour of the hybrid materials. Notched tensile tests are not only dominated by strength or toughness, but both properties interact and affect the notched strength of the material. In these tests, the lowest strength of the hybrid materials (Table 5.2) will compete with their higher toughness. Open-hole tensile tests were performed for different hole sizes (12, 36 and 72 mm) to determine analyse the size effect. It was concluded that the H2 material had the highest notched strength, higher than the non-hybrid T800 baseline, however, the H1 material showed the lowest strength. Additionally, a notch sensitivity analysis was performed. The results of this analysis are specially interesting for the H2 material, that shows a very notch insensitive behaviour, being the normalized strength of the 12 mm wide specimens higher than the theoretical notch insensitive limit. The H1 material, although having lower unnotched and notched strengths than the baseline T800, also shows a high notch intensive behaviour, which can be explained by the complex failure mechanisms that occur in the hybrid materials. Specially for the H2 material, X-ray images showed that the material failed with large splits and multiple cracks emanating from the split, with the addition of large delaminations. This notch insensitive behaviour was specially observed in an open-hole test with a 36 mm width (Figure 5.11), where the specimen started to fracture in the notch section, however, the final fracture occurred in an unnotched section of the specimen.

In the compression tests, both plain strength and open-hole, no clear synergy was found due to hybridization. Both hybrid materials showed a lower compression strength than the non-hybrid T800, with no difference in the fracture mechanisms observed in the post-mortem specimens. In the open-hole compression tests all the materials showed very similar notched strengths as well as notch sensitive behaviours. In addition, very similar fracture mechanics were observed in the post-mortem X-ray analysis.

The study performed in this chapter showed that interply hybridization can lead to interesting behaviour in notched specimens, especially under tensile loadings. This is a promising technology, particularly in damage tolerance applications. Nevertheless, a more extensive analysis on the damage progression in these materials, as well as detection of damage initiation is necessary. In addition, fatigue analysis should be done to understand how hybridization affects the hybrid material's behaviour under cyclic loadings, as it was observed that the hybrids develop damage at lower stresses.

Chapter 6

Intraply hybrids experimental campaign

6.1 Introduction

As demonstrated in Chapter 2.2 the behaviour of hybrid composites depends on the degree of dispersion of the hybridized fibres. In this chapter the spread tow technology is used to manufacture intra-ply hybrid composite materials with different hybrid volume fractions. An experimental campaign focused on fibre fibre dominated properties is performed and the behaviour of the materials is analysed.

6.2 Manufacturing

6.2.1 Material selection

The objective of this work is to analyse the effect of dispersion on the behaviour of hybrid composites. Danzi [32] analysed the behaviour of inter-ply hybrid composites composed of T800 and HR40 carbon fibres. The author demonstrated the potential of this hybridization in creating composites with a pseudo-ductile behaviour and increased fracture toughness. The author observed that for some combinations there was stable fragmentation of the HR40 plies leading to a gradual failure of the material with an increase in dissipated energy in the failure process. Following Danzi's [32] work, Chapter 5 focused on the analysis of interply hybridization at the structural detail level. An increase in the open-hole strength was observed for a hybrid material, with clear changes in the damage mechanisms and fracture process.

In this work the same fibres are used: T800 carbon fibres as the high elongation fibres and HR40 as the low elongation fibres. The T800 carbon fibres were acquired from Toray Carbon Fibres Europe in 24K (1030 tex) tows [30]. The HR40 carbon fibres were acquired from Mitsubishi Chemical Carbon Fiber and Composites in 12K (600 tex) tows [31]. The manufacturer properties for these carbon fibres is shown in Table 5.1.

The resin used for the composite materials in study was MTC510 epoxy resin from SHD composites.

6.2.2 Tow-spread hybridization

To produce the tape necessary for the hybrid composite materials the spread tow technology was used. The spread tow technology consists in continuously spreading fibre tows to a flat, thinner tape. Currently there three different basic spreading method: mechanical spreading, air spreading and ultrasonic spreading. The mechanical spreading process is considered a passive process, as it only uses tension and continuous movement for spreading, while the air and ultrasonic are considered active spreading processes as energy is used in the spreading process [205]. Mechanical spreading is the oldest and most basic process and has the disadvantage of being limited in the terms of production speed. Additionally, as the spreading is dependent on the tension acting on the fibres, the maximum spreading is limited as, for high levels of tension, the fibres are damaged. Air spreading is a technology that allows the maximum spreading without inducing damage in the fibres, as in this processes the friction is reduced. Ultrasonic spreading combines mechanical spreading bars with with ultrasounds that cause the filaments to vibrate, helping the spreading process, reducing the mechanical tension required for the same spreading ratio.

In this study, an UD500 spreading machine from LIBA (now Karl Mayer Technische Textilien GmbH, Naila), at the Airbus Group Innovations Munich, Germany was used. The machine can produce UD tapes up to 500mm wide and combines coated spreading bars with the possibility of adding vibration and temperature to spread the fibres. The machine is divided in several units, that allow the transformation of rolled tows of fibres to a winded unidirectional tape with binder for stabilization. The machine is composed of the following units [205]:

1. Fibre creel and guiding bars.
2. Spreading units.
    - Unit 1: 9 spreading bars (5 vibrating) and possibility of heating.
    - Unit 2: 9 spreading bars (5 vibrating).
    - Unit 3: 7 spreading bars (3 vibrating).
3. Transportation unit.
4. Bindering unit (includes a heating unit).
5. Winding unit.

In a standard non-hybrid material the fibres start in spools that are stored in the Fibre creel (1) whose resistance can be changed to adjust the initial tension in the fibres. The tows are then guided into the spreading machine. As the spreading

units (2) are independent, the spreading can occur in any combination of units, being that the bar deflection, vibration and heating (in unit 1) can be regulated independently. The settings on the spreading units change the behaviour of the tow and, therefore, its spreading. The tow deflection changes the deflection angle, as the spacing between bars cannot be changed within each spreading unit. The higher the deflection angle is the higher the tension in the fibres and, therefore, the more spread the tow gets. However, with increase deflection the friction also increases and as a consequence the fibre damage also increases [205]. Additionally, increasing the number of spreading bars used also increases the tension in the fibres, thus the potential for fibre damage. Due to the modular nature of the unit all the parameters can be changed depending on the fibre type, tow weight and desired tape areal weight, being necessary to make sure that limited fibre damage is introduced during the process.

After the spreading process, the spread tows must be combined to form a cohesive UD tape. This step is usually done in the third spreading unit, making sure that some overlap between the tows exists to ensure the connection between them. Afterwards, the spread tape moves into the transportation unit that is the power unit of the machine, which is responsible for pulling the fibres from the spools and into the spreaders. From this unit the spread tape passes into the bindering unit. In this unit, a regulated powder dispenser ensure that a uniform and controllable weight of binder is applied to the tape. After its application, binder is then heated up to a specific temperature, depending on the binder in use. The binder ensures that the cohesion of the material and helps in the handling of the tape in the composite manufacturing process. With the binder applied the tape is winded into spools. At this stage the material is ready to be used in any manufacturing process that requires dry tapes/fabrics, as in infusion or Resin Transfer Molding (RTM) processes.

The objective of this work is to use the previously described process and machine to commingle two types of fibres in a single UD tape. A similar process was used by Diao et al. [206] to produce a carbon/glass hybrid material, however, the authors used a air assisted spreader to successfully create an intraply carbon/glass hybrid material. The degree of hybridisation in the CF/GF tow was defined and characterized by comparing the fibre distribution obtained from a model of a composite containing randomly distributed hybrid composite and the fibre distribution determined experimentally from micrographs of the hybrid fibre tow using an image recognition program. The authors determined a degree of dispersion of 32.45% for the material, meaning only a partial hybridization of the material.

The process of spreading a intratow hybrid material is more complex than the traditional non-hybrid spreading as it is not only required that the tows are spread into a cohesive tape, but also that the two fibre types to be hybridized are commingled the best possible way. As the spreading machine used has three spreading units, the process was divided in three stages, schematically represented in Figure 6.1: (1) initial spreading, (2) comminglind and spreading and (3) tape spreading.

The spools of both fibre types are stored in the racks of the fibre creel and are guided (a) into the first spreading unit to be spread individually (b). The number of tows used of each fibre type will determine the hybrid volume fraction of the material.

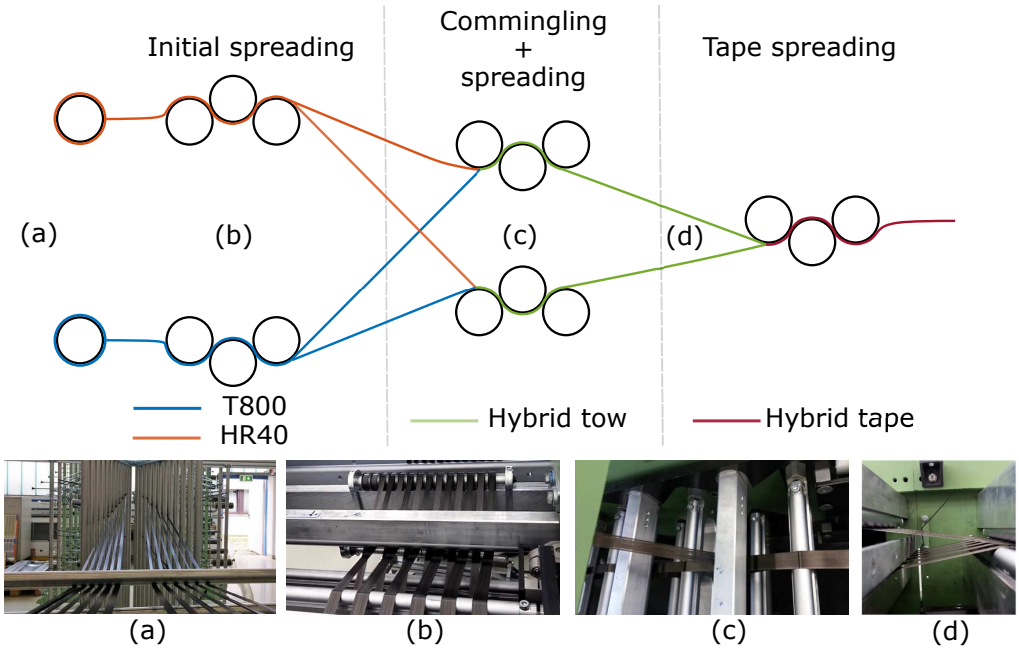

Figure 6.1: Schematic representation of the spreading process for hybrid materials and pictures of the different stages.

The first spreading stage spreading stage is used to reduce the areal weight of each tow individually and to open the tows to assist in the commingling process. At this stage the spreading parameters were controlled to ensure that a similar width of the tows of both fibre types at the end of the stage. These parameters are, however, not independent of the remaining of the process as more spreading at this stage implies reduced spreading in the later stages as extensive spreading causes fibre damage. At the second spreading unit (c) the tow hybridization is achieved. This is done by overlapping the tows of both fibre types in a single spreading lane, ensuring a good alignment between them, and spreading them together. The number of tows for each fibre type that compose the hybrid tow define the hybrid ratio. The ratio is therefore limited by the weight of the tows used in the process and by the number of tows that are used to create a single hybrid tow. At the end of this stage the tow is hybridized and the its areal weight should be close to the desired areal weight for the material. The tape spreading stage (d) is the last stage of the spreading process and is where the UD tape is created. This is done by combining several spread hybrid tows into a single UD tape. To do so the tows are combined with some slight overlap, to ensure that there are no gaps in the tape, and the tape is spread slightly to help ensure its cohesion. From this stage the process is similar to the one for non-hybrid composites and an epoxy appropriate binder is applied to the material and the UD tape is winded into spools to be used later on.

6.2.3 Hybrid materials

As seen in Section 6.2.1 the fibres chosen to be hybridized were T800 and HR40 fibres, acquired in 24k and 12k tows, respectively. As mentioned in the previous

section, the hybrid ratio is controlled by the weight of the tows and the ratio of tows of each fibre used. For this work five materials were manufactured. Two baseline non-hybrid composites and three hybrid composites with different hybrid ratios (Table 6.1). The hybrids are classified in terms of ratio of tows of each fibre type used. For instance the Hybrid 2-1 material used two tows of T800 for each tow of HR40. The spreading parameters for each material were chosen to ensure minimal damage of the final tape while achieving the maximum fibre dispersion. However, this lead to the high variability in tape areal weight, as the hybrid 2-1 and 4-1 were harder to spread without damage. For all cases it was observed that adding vibration to the spreading processes improved the spreading.

To manufacture the plates necessary for the mechanical characterization, MTC510 epoxy resin films were bought from SHD composites. The epoxy films were hand stacked in conjunction with the dry tapes of each material and the composite was cured in an autoclave. The cure cycle used was 1 hour at 120ºC with a 2 hour post cure at 130ºC with appropriate heating and cooling rates. The fibre volume fraction of each material was aimed at 50%, therefore, the resin films were acquired in 50, 75 and 100 GSM. The relevant properties of the UD tapes manufactured are shown in Table 6.1.

Table 6.1: Hybrid and non-hybrid material configurations.

Material	Tape areal weight (g/m^2)	$\%_{T800}$	$\%_{HR40}$	Resin areal weight (g/m^2)	Expected fibre volume fraction (%)	Tape width (mm)
T800	116	100	0	75	51.5	215
Hybrid 4-1	138	88	12	100	48.3	210
Hybrid 2-1	141	78	22	100	49.0	230
Hybrid 1-1	93	64	36	75	45.6	215
HR40	63	0	100	50	46.4	115

6.3 Material microstructure

As demonstrated in Chapter 2.2 the degree of dispersion of the hybridized fibres changes the behaviour of the material. With intratow hybridization the objective was maximizing the degree of dispersion within the material and improve its behaviour. The process of individually spreading the fibre tows before commingling them to produce the hybrid tape was aimed in reduce their areal weight. This should help the tows penetrating each other and, therefore, increase the homogenization of the tows, leading to a higher dispersion of fibres.

To understand the microstructure of the manufactured materials micrographs were performed using an optical microscope and a 20× magnification (Figure 6.2).

Due to the similar radii of the fibres used, 2.5 μm and 3 μm, it is difficult to distinguish them based on their radii. Nevertheless, there is a slight difference in colour between both fibre types. Image processing utilities were used to analyse the

microstructure and distinguish the fibres based on their colouration. The analysed microstructures are shown in Figure 6.3, being each fibre type represented by one colour (HR40 fibres in blue and T800 in red).

(a) Hybrid 1-1

(b) Hybrid 2-1

(c) Hybrid 4-1

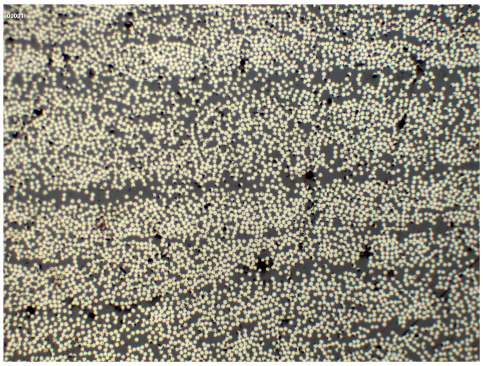

(d) T800

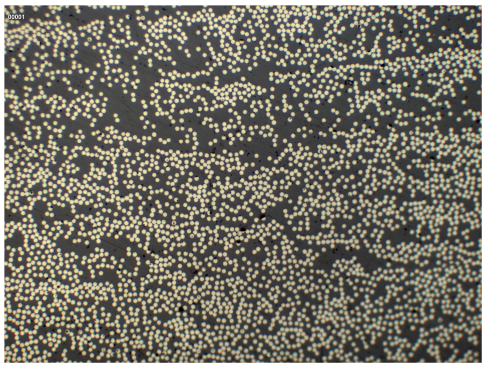

(e) HR40

Figure 6.2: Microstructures of the spread materials in study.

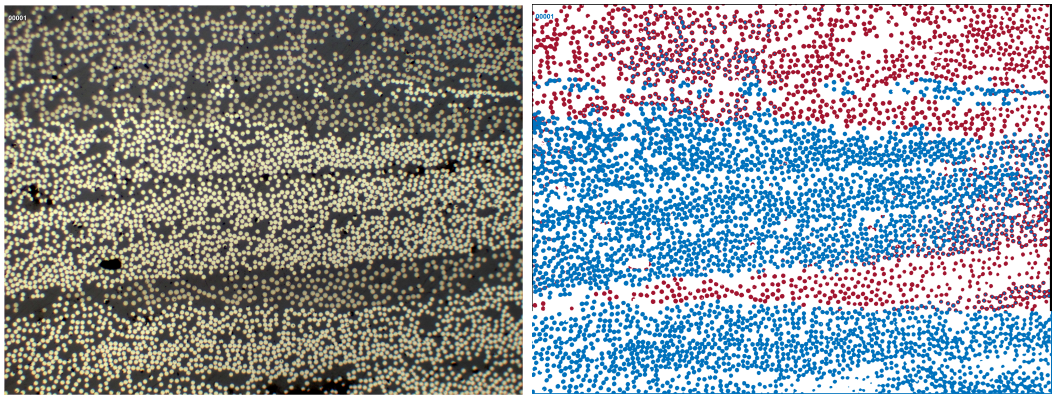

(a) Hybrid 1-1

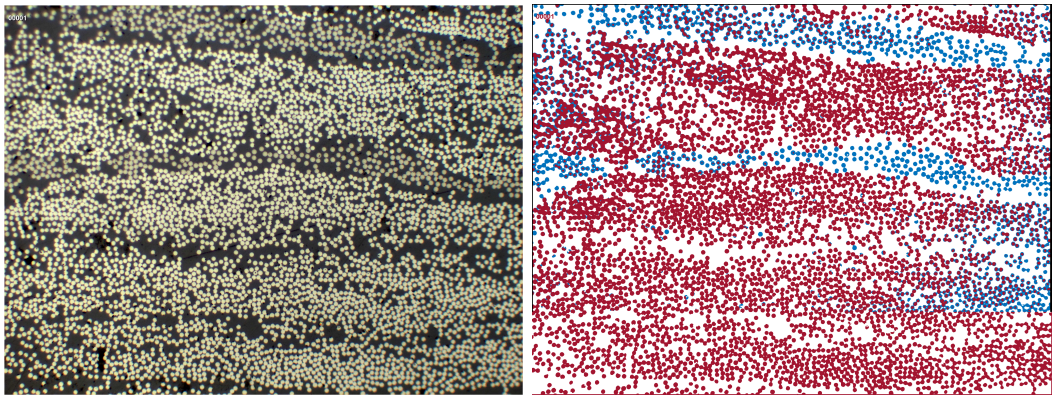

(b) Hybrid 2-1

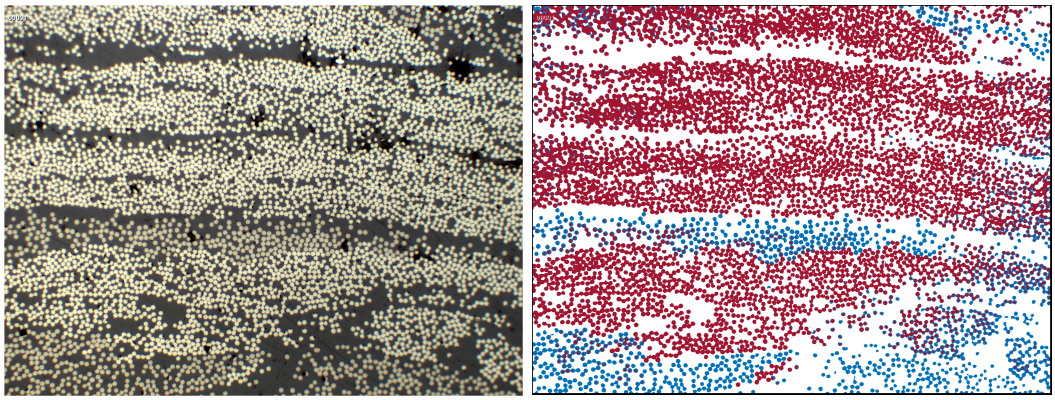

(c) Hybrid 4-1

Figure 6.3: Microstructures and analysed microstructures of the hybrid materials in study. HR40 fibres in blue and T800 in red.

Observing the microstructures it is concluded that the degree of dispersion achieved in the hybrid composites is very low as the fibres are not well commingled. At some locations in the material there is a good dispersion of both fibre types (see top of Figure 6.3a), however, generally the tows of different fibres are stacked on top of each other with very small penetration between them. The obtained micrographs are just a sample of the micrographs analysed, however, these are considered to be representative of the microstructure of the materials. The hybridizations resemble tow-by-tow hybridization, as the tows are stacked on top of each other, however, due to the spreading process there is no resin rich area between the tows, which should hinder the development of delaminations when the HR40 fails and, therefore, change the behaviour of the material in comparison to the interply hybrids. The mechanical behaviour of the materials will be analysed in the following sections.

The microstructure of the hybrid materials is influenced by the parameters used in the spreading process. For instance, Diao et al. [206] were able to achieve a higher degree of dispersion in a hybrid carbon-glass material, however, the authors used an air assisted spreading machine that allows the tows to be spread thinner helping the commingling process. In this work, a mechanical spreading machine was used, which limited the spreading of the tows prior to the commingling process, hindering the penetration of the tows and, therefore, the dispersion of the fibres.

To understand if a better dispersion was possible to be achieved for a different set of fibres, a small batch of Teijin Tenax HTS45 and IMS65 carbon fibre hybrid was manufactured. The two fibres used have different diameters 7 μm and 5 μm, therefore, the analysis of the microstructure can be done based on the fibre radii. A typical microstructure and the analysed microstructure fot the HTS45 and IMS65 material is shown in Figure 6.4.

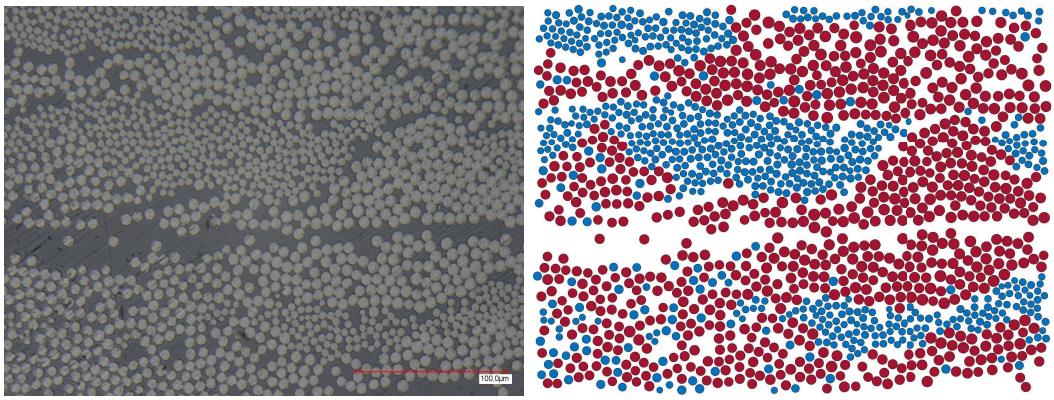

Figure 6.4: Microstructure and analysed microstructure of the HTS45-IMS65 hybrid material.

Analysing the microstructures it is concluded that there is a similar degree of dispersion as the one seen for the T800-HR40 materials. Nevertheless, for this material there are regions where the fibres dispersion is higher (bottom left corner) and regions where there is no tow penetration (top right corner).

From this analysis it is possible to conclude that to reach a higher degrees of dispersion it is necessary to change the spreading process. To improve the dispersionit

is considered that the first step of the spreading process (initial spreading) must be changed, with the aim of reaching lower thickness for the individual tows before the commingling process. Thinner tows will lead to the creation of gaps in the tows and help tow penetration, which should increase the fibre dispersion on the final material. However, this was not possible to do with the setup used, as it has to be a continuous process (from tows of fibres to hybridized tape) and higher spreading was not possible without severely damaging the fibres. One solution might be the usage of air assisted spreading, as done by Diao et al. [206], which improves tow spreadability. Other solution might be the separation of the process into a two stage process where the tows are spread individually to the maximum spreading possible and are stored in coils. The spread coils are positioned in the fibre creel and the commingling and tape spreading are performed in a separate process. The two stage process allows higher spreading ratios to be achieved in the initial spreading and higher deflections to be used in the commingling process, as both processes are separated. The issue with this solution is the stabilization of the spread tows after the initial spreading, as no binder can be used without disrupting the commingling process. Nevertheless, with more advanced techniques a higher degree of dispersion can be achieved.

In addition to the microstructure, fibre volume content tests were performed according to BS EN2564 standard [207]. To determine the fibre volume content material, samples are cut from the manufactured plates and the resin is eliminated by treating the specimen with pure H_2SO_4 at 160°C. Afterwards, the specimen is treated with H_2SO_4 30% in volume and the fibres are cleaned with distilled water. The remainder is filtered and dehydrated with acetone at 100°C. The fibres are then dried at 120°C for minimum of 45 minutes. Finally the sample and the filter are kept in a desiccator with silica gel until their total weight becomes constant. Two samples were used for each material. Table 6.2 shows the results for the volume content test with the addition of the actual ply thickness, determined dividing the average thickness of the manufactured plates by the number of layers in those plates.

Table 6.2: Volume content test results and ply thickness for the materials in study.

Material	Expected fibre volume fraction (%)	Measured fibre volume fraction (%)	Void content (%)	Ply thickness (mm)
T800	52.20	50.36	0.16	0.140
Hybrid 4-1	48.91	46.21	0.63	0.169
Hybrid 2-1	49.56	43.89	0.53	0.165
Hybrid 1-1	46.10	43.35	0.81	0.127
HR40	46.43	42.43	0.56	0.083

The overall fibre volume fractions are lower than the expected values. However, this value was estimated based on the linear weight of the tows and tape width and theoretical areal weight of the resin films. Values that are subject to variation, specially the tape width and, therefore, the areal weight of the dry tape. The maximum void content is 0.81%, which is lower than the 1% limit typically considered for aerospace applications [208]. The thickness of the plies varies significantly for

the different materials. This is a consequence of the different spreading parameters used for each material, which affects the areal weight of the dry tapes. The difference in ply thickness may affect the properties of the materials [209, 210], however, the effects of fibre hybridization can be distinguished from the effects of ply thickness.

To understand the effects of the hybridization on the mechanical properties of the manufactured materials an experimental campaign was performed. As fibre hybridization affects mostly the properties of the composite in the fibre direction, the campaign was composed of UD tensile testing in the 0° direction and Double Edge Notch Tension (DENT) specimens to determine the size effect law and characterise the fracture toughness of the materials.

6.4 UD tensile testing

Longitudinal tensile tests were performed in compliance with ASTM standards [199] on a INSTRON 4208 testing machine equipped with a 200kN load cell and hydraulic self centering grips. A gripping pressure of 150 bar was used. The specimens was monotonically loaded in tension under displacement control conditions while recording force and cross-head displacement. Strain gauges were mounted on the specimens to determine the longitudinal stress-strain behaviour. Five specimens were tested for each material and one specimen of material was equipped with a transverse strain gauge to determine the material' Poisson's ratio. The speed of testing was set in order to get a nearly constant strain rate in the gauge section. A standard head displacement rate of 1 mm/min was used and no explicit conditioning process was performed on the specimens. The test were conducted at room temperature. The specimens are 250 mm long, 15 mm wide and approximately 1 mm thick. Glass fibre tabs were used with a 65 mm length, resulting in 120 mm total gauge length.

The stress-strain behaviour of the UD tensile tests performed are shown in Figure 6.5. Table 6.3 shows the properties measured in the performed tests: tensile strength (X_t), Young's modulus (E_1), failure strain (ε_f), Poisson's ratio (ν_{12}). The normalized strength and Young's modulus for a 50% volume fraction are also presented in Table 6.3.

Table 6.3: Properties measured in the UD tensile tests performed.

Material	V_f (%)	$\%_{\text{HR40}}$	X_t (MPa)	ε_f (%)	E_1 (GPa)	ν_{12}	X_t (MPa) (V_f = 50%)	E_1 (GPa) (V_f = 50%)
T800	50.36	0.0	2191.03	1.48	127.174	0.35	2175.27	126.26
Hybrid 4-1	48.91	12.4	1702.49	1.35	120.111	0.37	1841.95	129.95
Hybrid 2-1	49.56	22.1	1338.97	1.06	120.319	0.42	1525.21	137.05
Hybrid 1-1	46.10	36.1	1335.27	1.01	124.255	0.35	1540.23	143.33
HR40	46.43	100.0	1323.35	0.88	142.723	0.34	1559.62	168.20

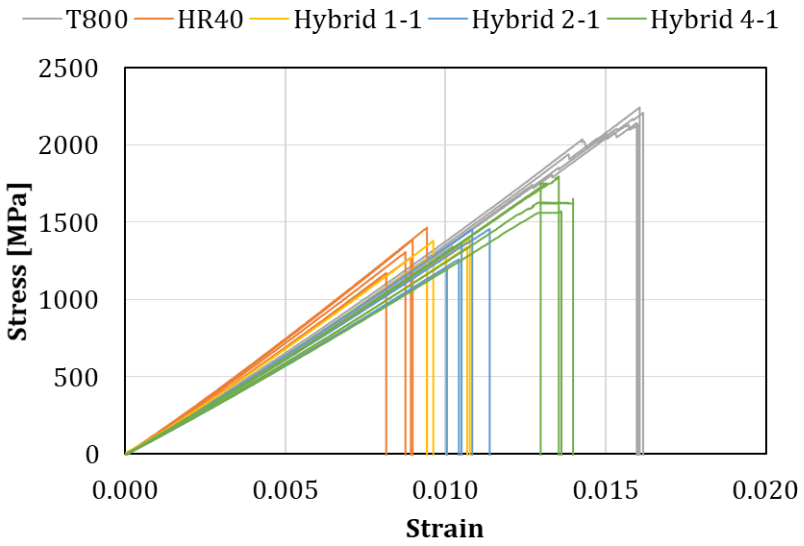

Figure 6.5: Stress-strain diagrams for the spread materials in study.

Both non-hybrid materials analysed show a linear response up to failure, although, for some specimens of the T800 material there was a some damage prior to failure, which caused load drops prior peak stress. It is observed that the T800 material presents a higher strength and a lower modulus than the HR40 material, which can be expected from the properties of the fibres in each material (Table 5.1), an effect that is enhanced by the lower fibre content of the HR40 material. The Hybrid 1-1 and Hybrid 2-1 materials also show a linear behaviour up to failure, with a strength similar to that of the HR40 material (Figure 6.6). This means that failure is being dominated by the HR40 fibres, and that when these fail the T800 fibres in the material cannot support the additional load, which leads to the failure of the material. The normalized strength of Hybrid 1-1 and Hybrid 2-1 are similar to the HR40, however, the HR40 material presents a lower failure strain.

The most interesting behaviour is that of the Hybrid 4-1 material, which has the lower content of HR40 fibres (12%). The lower content of HR40, when compared to the other hybrids, means the failure of the HR40 no longer leads to the catastrophic failure of the material, therefore, the material shows highly non-linear behaviour before failure, which can be characterized as a pseudo-ductile behaviour, as defined in Chapter 2.2. The maximum pseudo-ductile strain achieved was 0.12%, however, some specimens of these material did not have any non-linear behaviour. This might be explained by the irregular microstructure of the material. Nevertheless, it was observed that, for all the specimens, there was extensive acoustic emission prior to maximum load, which indicates fibre failure prior to the peak stress.

Fibre failure should promote other damage mechanisms such as matrix cracking and fibre matrix decohesion [58], which results in the shown non-linear behaviour and should promote energy dissipation. The energy dissipated in longitudinal fracture will be analysed in the next section using the Double Edge Notch Tension tests.

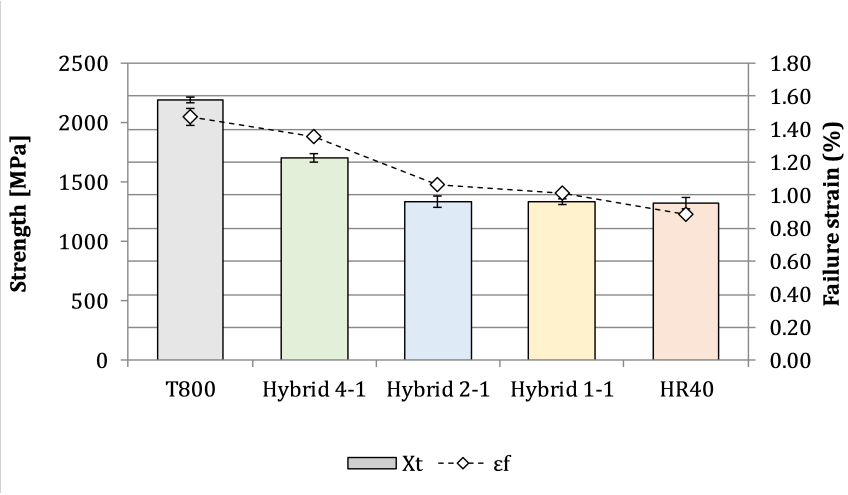

Figure 6.6: Strength and failure strain of the spread materials.

6.5 Double Edge Notch Tension tests

6.5.1 Methodology

To quantify the energy dissipated per unit area during failure, the crack resistance curves for longitudinal tension were obtained following the methodology proposed by Catalanotti et al. [20], which is based on the on the size effect law, i.e., the relation between the size of the specimens and their notched strength ($\overline{\sigma}^{\infty}(w)$).

The size effect law associated with tensile failure was determined experimentally testing geometrically similar DENT cross-ply specimens, i.e. with the same width-to-crack length ($2w/a$) ratio and different width ($2w$) as shown in Figure 6.7. The tests were performed under displacement control, at a controlled speed of 1.0 mm/min, in an Instron 4208 electro-mechanical universal testing machine with a load capacity of 300 kN, equipped with a 200 kN load cell. The hydraulic clamping pressure used ranged from 50 MPa to 150 MPa depending on the width of the specimen. Displacement was measured using the LVDT from the testing machine and the notched strength was obtained dividing the failure load by the specimen cross-section.

Table 6.4: Internal 4: Double edge crack test matrix.

Test	Length (mm)	2w (mm)	a_0 (mm)	Nr. specimens	Speed (mm/min)
$G_{1+}(\Delta a)$ 4A	250	10	3	3	1
$G_{1+}(\Delta a)$ 4B	250	20	6	3	1
$G_{1+}(\Delta a)$ 4C	250	30	9	3	1
$G_{1+}(\Delta a)$ 4D	250	40	12	3	1
$G_{1+}(\Delta a)$ 4E	250	50	15	3	1

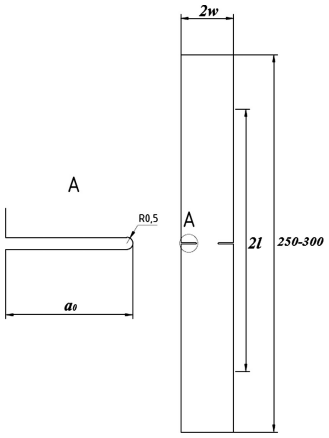

Figure 6.7: Double edge crack specimens [20] .

According to Catalanotti et al. [20], the driving force curves ($\mathcal{G}_I$) at the ultimate remote stress are tangent to the $\mathcal{R}$-curve, which means that the ultimate remote stresses ($\overline{\sigma}^{\infty}$) can be calculated solving the following: system of equations

$$\begin{cases} \mathcal{G}_I(\Delta a) = \mathcal{R}(\Delta a) \\ \frac{\partial \mathcal{G}_I(\Delta a)}{\partial \Delta a)} = \frac{\partial \mathcal{R}(\Delta a)}{\partial \Delta a} \end{cases} . \tag{6.1}$$

According to Bao et al. [211] and Chen et al. [212] the energy release rate in mode I of a two-dimensional orthotropic body for a crack propagating in the y direction (perpendicularly to the loading direction, x) is given by:

$$\mathcal{G}_I = \frac{1}{\acute{E}} \mathcal{K}_I^2 \, , \tag{6.2}$$

where $\mathcal{K}_I$ is the mode I stress intensity factor and $\acute{E}$ is the equivalent elastic modulus

$$\acute{E} = \left(\frac{1+\rho}{2E_x E_y} \right)^{-1/2} \left(\frac{E_y}{E_x} \right)^{-1/4} \, , \tag{6.3}$$

and ρ is an in-plane orthotropy parameter

$$\rho = \frac{(E_x E_y)^{1/2}}{2G_{xy}} - (\nu_{xy}\nu_{yx})^{1/2} \, . \tag{6.4}$$

For sufficient long DENT specimens with $w/L \leq 1/2$ the stress intensity factor $\mathcal{K}_I$ is given by:

$$\mathcal{K}_I = \overline{\sigma}^{\infty} \sqrt{w} \kappa(\alpha, \rho) \, , \tag{6.5}$$

where $\overline{\sigma}^{\infty}$ is the notched remote stress, w is half the width of the specimen, $2L$ the total free length,z κ is a correction factor that depends on the geometry and

orthotropy of the specimens. Following Catalanotti et al.[20], κ reads:

$$\kappa(\alpha,\rho) = \sqrt{\tan\frac{\pi\alpha}{2}} \sum_{i=1}^{M}\sum_{j=1}^{N} \Phi_{ij}\alpha^{i-1}\rho^{j-1} \ , \tag{6.6}$$

where α is the notch length-to-width ratio $\alpha = a/w$ and Φ_{ij} is the element of the matrix $\mathbf{\Phi}$ of indexes i and j, and M and N are the number of rows and columns of $\mathbf{\Phi}$, respectively:

$$\mathbf{\Phi} = \begin{bmatrix} 1.7482487564 & -0.053754159533 & 0.0040142704949 & -9.8480085881E-4 \\ -0.76896688866 & -0.0068632911438 & 0.0029984681658 & -0.00010108691939 \\ 0.85633404777 & 0.23922363475 & -0.023289123198 & 0.00062358861997 \\ -0.67470597429 & -0.25334178248 & 0.022297779266 & -0.00056784694513 \\ 0.18495379886 & 0.084067007027 & -0.0068989066533 & 0.00016783852495 \end{bmatrix} . \tag{6.7}$$

Replacing equation (6.5) in equation (6.2), the energy release rate can be written as:

$$\mathcal{G}_I(\Delta a) = \frac{1}{\acute{E}} w(\overline{\sigma}^{\infty}))^2\kappa^2(\alpha_0 + \frac{\Delta a}{w}, \rho) \ , \tag{6.8}$$

where α_0 is the initial notch length-to-width ratio $\alpha_0 = a_0/w$. Combining equation 6.2 and 6.1, $\mathcal{R}(\Delta a)$ yields

$$\mathcal{R}(\Delta a) = \frac{1}{\acute{E}} w(\overline{\sigma}^{\infty})^2\kappa^2(\alpha_0 + \frac{\Delta a}{w}, \rho) \ . \tag{6.9}$$

For a constant w/L and a_0/w and knowing that, by definition the R-curve is size independent ($\frac{\partial R}{\partial w} = 0$), differentiating equation (6.9) with respect to w yields:

$$\frac{\partial}{\partial w}(w(\overline{\sigma}^{\infty})^2\kappa^2) = 0 \ . \tag{6.10}$$

Given the size effect $\overline{\sigma}^{\infty}(w)$ is know, equation (6.10) can be solved for $w(\Delta a)$ which can then be replaced in Equation (6.9) to cumpute the $\mathcal{R}$-curve.

The size effect law is determined by testing geometrically similar double edge crack specimens, i.e. with the same crack-to-width length a_0/w ratio and different widths $2w$ and applying one of three linear regressions proposed in Ref. [213] that best fits the experimental data: i) bilogarithmic regression ii) linear regression I or iii) linear regression II. The regressions and the R-curve parameters (length of the fracture process zone, l_{fpz}, and the fracture toughness at propagation $\mathcal{R}_{ss}$) are shown in Table 6.5 ($\kappa_0 = \kappa(\alpha_0)$ and $\acute{\kappa}_0 = \partial\kappa/\partial\alpha(\alpha_0)$).

Catalanotti et al. [20] suggests that it is useful and more convenient to express the R-curve analytically and proposed the following equation:

$$\mathcal{R}(\Delta a) = \mathcal{R}_{ss}\left[1 - (1 - \gamma\Delta a)^{\beta}\right] \tag{6.11}$$

where γ and β are the parameters that best fit the R-curve. The $\mathcal{R}$-curve of the 0° plies ($\mathcal{R}_0$) only can de obtained neglecting the fracture toughness of the 90° plies

Table 6.5: Regressions and the R-curve parameters [20]

Regression	Formula	Fitting parameters	$\mathcal{R}_{ss}$	l_{fpz}
Bilogarithmic	$ln(\overline{\sigma}^{\infty}) = ln\frac{M}{\sqrt{N+w}}$	M, N	$\frac{\kappa_0^2}{E}M^2$	$\frac{\kappa(\alpha_0)}{2\acute{\kappa}_0}N$
Linear regression I	$\frac{1}{(\overline{\sigma}^{\infty})^2} = Aw + C$	A, C	$\frac{\kappa_0^2}{E}\frac{1}{A}$	$\frac{\kappa(\alpha_0)}{2\acute{\kappa}_0}\frac{C}{A}$
Linear regression II	$\frac{1}{w(\overline{\sigma}^{\infty})^2} = A\frac{1}{w} + C$	A, C	$\frac{\kappa_0^2}{E}\frac{1}{C}$	$\frac{\kappa(\alpha_0)}{2\acute{\kappa}_0}\frac{A}{C}$

using the following equation:

$$\mathcal{R}_0 = \frac{t}{t_0}\mathcal{R}_{ss} \ , \tag{6.12}$$

where t_0 is the total thickness of the 0° plies and t is the laminate's thickness.

6.5.2 Results

For the DENT specimens centre symetric $[90/0]_{n\$}$ laminates were manufacture of the T800, Hybrid 1-1, Hybrid 2-1 and Hybrid 4-1 materials. A target 2 mm thickness was chosen and the layups were varied accordingly. The HR40 material was not tested, however, Danzi [32] tested a HR40 composite system and determined that it was a very brittle material with a fracture toughness of 24.69 N/mm. This material has, however, a different matrix system. Nevertheless, this results can be used for comparison with the hybrid materials.

Figures 6.8, 6.9, 6.10 and 6.11 show the stress vs displacement curves for the different specimens for all the tested materials.

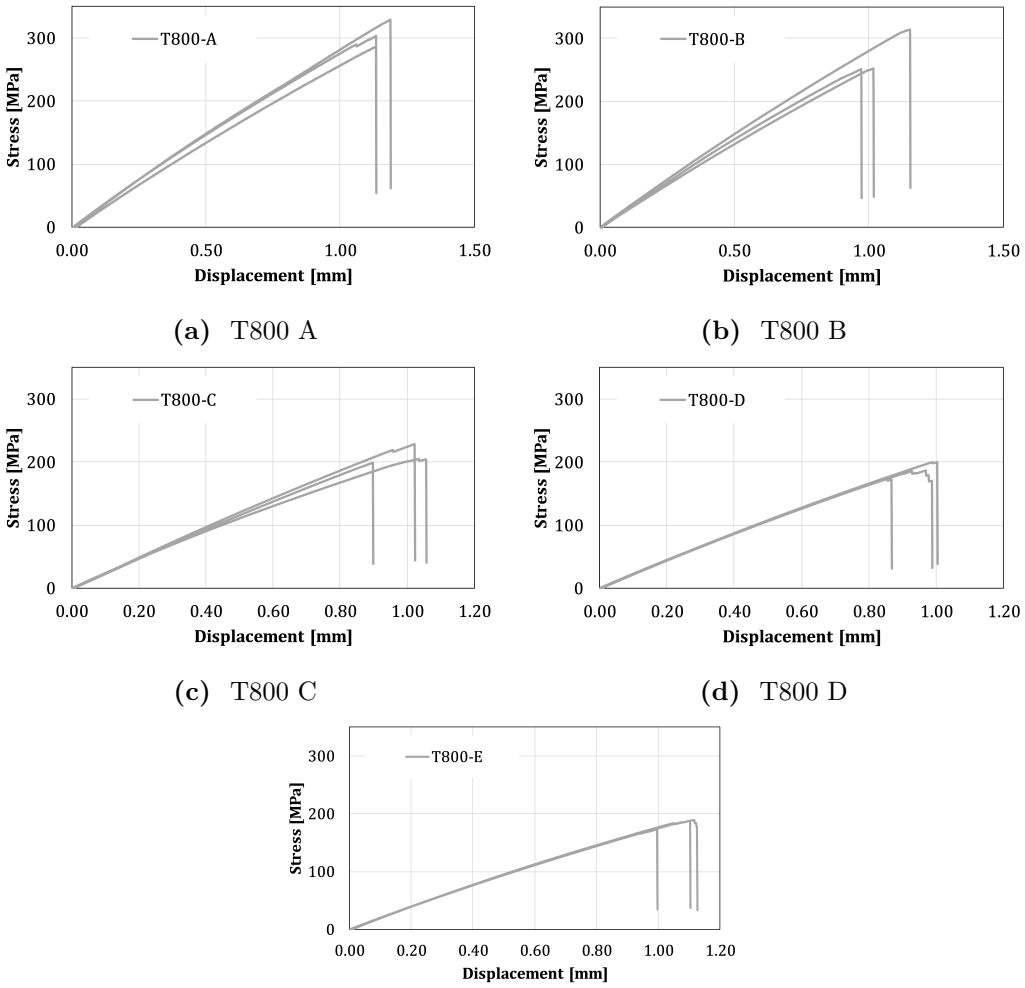

(a) T800 A

(b) T800 B

(c) T800 C

(d) T800 D

(e) T800 E

Figure 6.8: Stress versus displacement of the different geometries of the DENT tests on the T800 material.

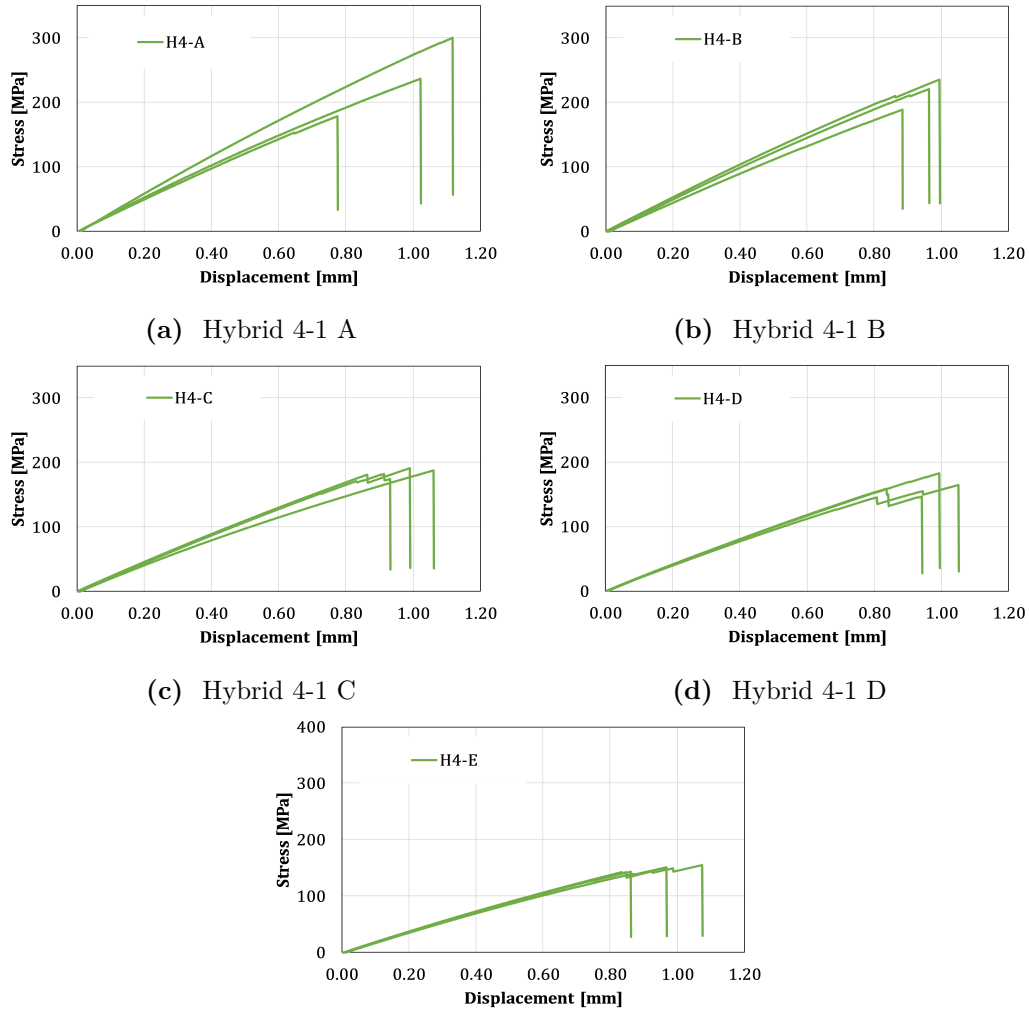

(a) Hybrid 4-1 A

(b) Hybrid 4-1 B

(c) Hybrid 4-1 C

(d) Hybrid 4-1 D

(e) Hybrid 4-1 E

Figure 6.9: Stress versus displacement of the different geometries of the DENT tests on the Hybrid 4-1 material.

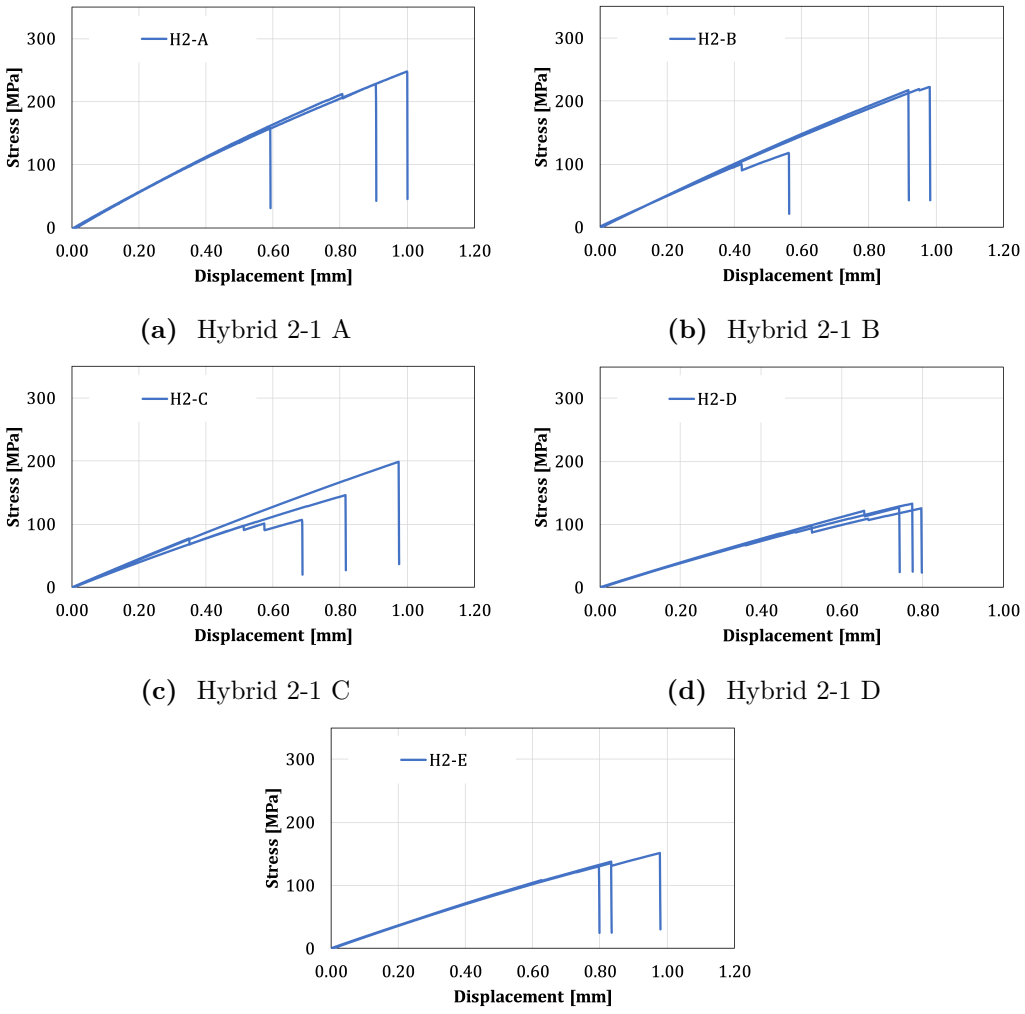

(a) Hybrid 2-1 A

(b) Hybrid 2-1 B

(c) Hybrid 2-1 C

(d) Hybrid 2-1 D

(e) Hybrid 2-1 E

Figure 6.10: Stress versus displacement of the different geometries of the DENT tests on the Hybrid 2-1 material.

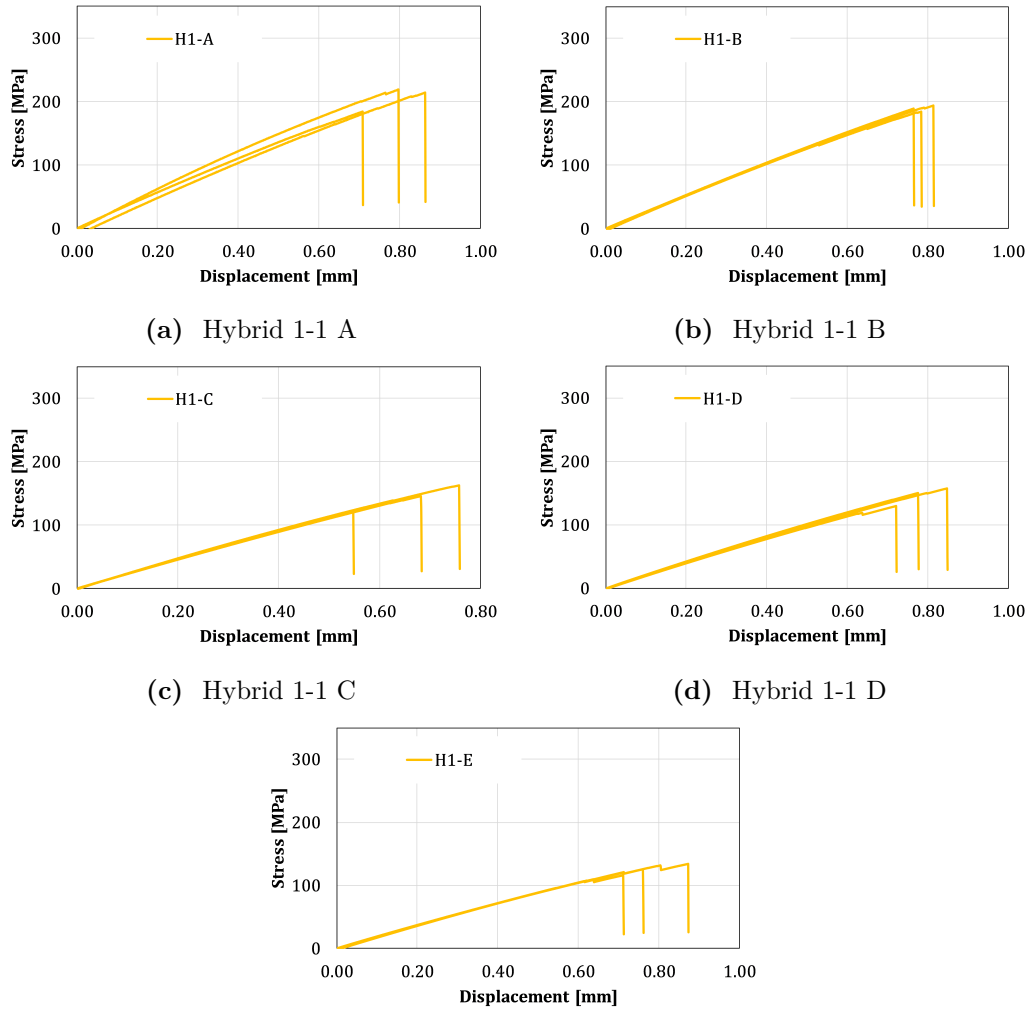

(a) Hybrid 1-1 A

(b) Hybrid 1-1 B

(c) Hybrid 1-1 C

(d) Hybrid 1-1 D

(e) Hybrid 1-1 E

Figure 6.11: Stress versus displacement of the different geometries of the DENT tests on the Hybrid 1-1 material.

The notched tensile strength is shown Figure 6.12 as a function of the specimen width ($2W$). Is is observed that the material with the highest notched strength is the T800, for all analysed specimen dimensions. Hybrid 1-1 and Hybrid 2-1 materials show a very similar behaviour, which was already true in the unnotched strength tensile tests. The Hybrid 4-1 material shows an increased notched strength in comparison with the remaining hybrid materials, however, the notched strengths are lower than the non-hybrid T800 material. A size effect is seen for all the materials, as the notched strength is seen to decrease with increased specimen size. However, it is observed that Hybrid 1-1 and Hybrid 2-1 notched strengths plateaus for geometries larger than 30 mm, effect that is not seen for the remaining hybrid material.

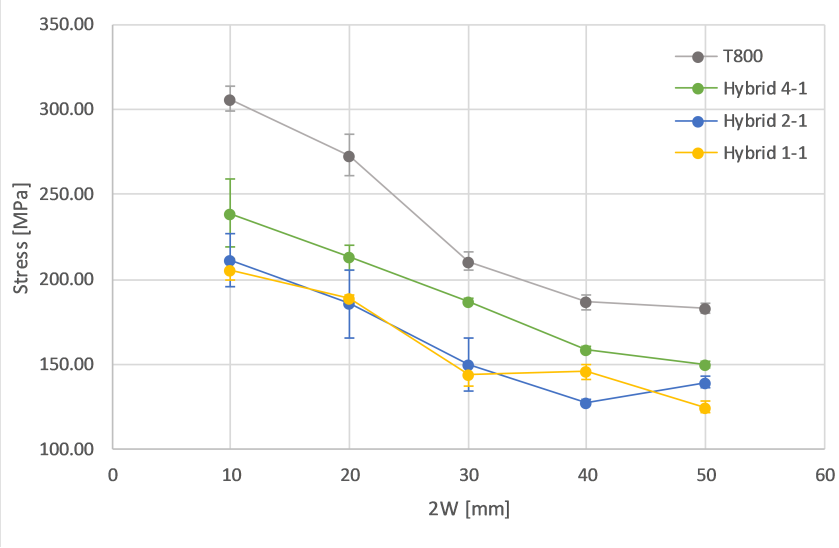

Figure 6.12: Size effect on the double edge notch tests.

It was observed that the best fitting regression for the size effect law was the bilogarithmic one, with exception of the Hybrid 4-1 material which best fitted the Linear 1 regression. Both the parameters for the size effect laws and the R-curve parameters are shown in Table 6.6 and the $\mathcal{R}$-curves are represented in Figure 6.13. Analysing the $\mathcal{R}$-curves it is concluded that all hybrid materials have a lower fracture toughness then the baseline non-hybrid T800 material, which has a fracture toughness of 171 N/mm. Similarly to that observed for the UD tensile tests, Hybrid 1-1 and Hybrid 2-1 present a very similar behaviour, which results in very similar fracture toughnesses around 100 N/mm. Hybrid 4-1 however, has a higher fracture toughness of 133 N/mm, nevertheless this is a reduction comparing to the T800 material.

The reduction of the fracture toughness of the hybrid materials in comparison with the T800 baseline is related with the lower fracture toughness of the HR40 material, which is very brittle and, therefore, compromises the fracture toughness of the hybrid material. Post-mortem X-ray analysis of the A and E geometries of the DENT specimens are shown in Figure 6.14. From the x-ray analysis it is concluded that failure occurs in the notch for all specimens, with a clear crack like behaviour, which makes the method used to determine the $\mathcal{R}$-curve valid for the

Table 6.6: Fitting parameters for the size effect law and corresponding R-curve parameters for the spread materials.

Material	Fitting parameters				R-curve parameters					
	Type	Parameter 1	Parameter 2	R^2	$\mathcal{R}$ (N/mm)	$\mathcal{R}_0$ (N/mm)	l_{fpz}	β	γ	$\mathcal{R}_0/V_f$ (N/mm)
T800	bilog	966.181	4.517	0.950	80.820	171.743	1.380	3.520	0.620	333.562
Hybrid 4-1	linear I	1.43E-06	8.97E-06	0.980	62.150	133.179	1.920	3.570	0.450	275.825
Hybrid 2-12	bilog	719.951	6.482	0.900	47.340	100.598	1.980	3.570	0.430	205.299
Hybrid 1-1	bilog	718.656	6.645	0.920	47.070	98.847	2.030	3.580	0.420	216.552

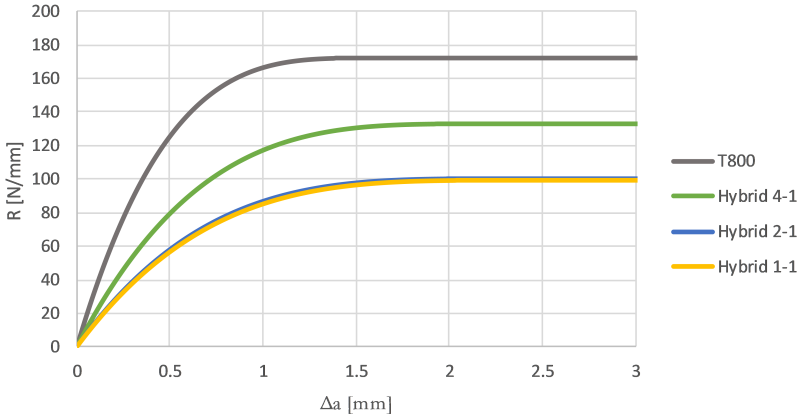

Figure 6.13: R-curves of the spread materials.

materials under investigation. None of the materials shows extensive damage in the notch tip, however, the Hybrid 4-1 material shows limited splitting at the notch tip for the smallest geometry.

Danzi [32] showed that extensive damage was observed in interply hybrid materials, leading to the formation of multiple cracks in the DENT specimens, however, the same does not occur for the manufactured intratow hybrids. These damage mechanisms lead to an increase the notched strength of the material, which results in a higher apparent fracture toughness. The suppression of these mechanisms makes fibre failure the main mechanisms for energy dissipation and, therefore, the hybridization with HR40 fibres (whose material shows a very low fracture toughness) leads to a decrease in fracture toughness of the hybrids when comparing to the T800 baseline material.

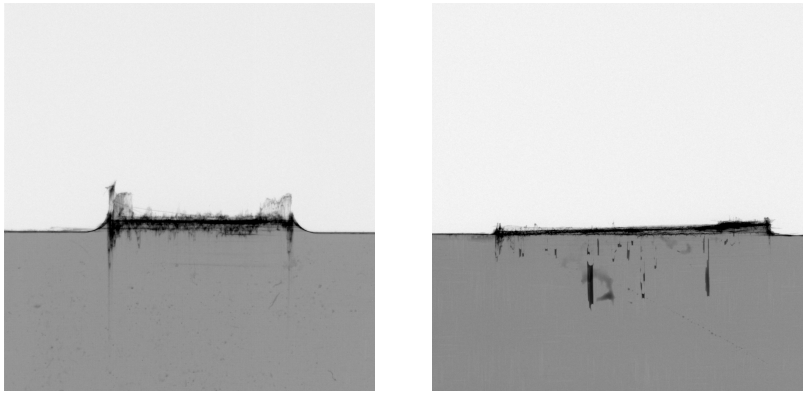

(a) T800 A

(b) T800 E

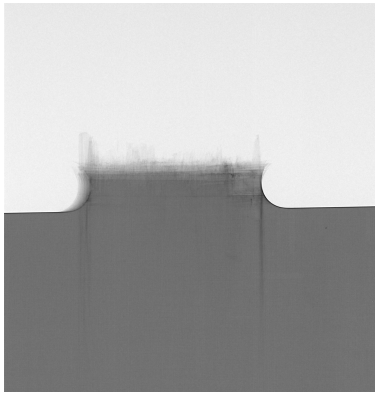

(c) Hybrid 4-1 A

(d) Hybrid 4-1 E

(e) Hybrid 2-1 A

(f) Hybrid 2-1 E

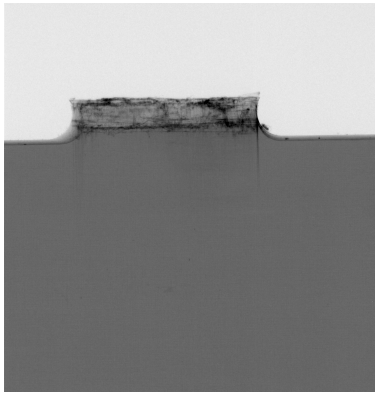

(g) Hybrid 1-1 A

(h) Hybrid 1-1 E

Figure 6.14: Post failure X-ray images of the DENT A and DENT E geometries of the studied materials.

6.6 Conclusions

In this chapter a methodology to manufacture intratow hybrid composite materials was developed. The strategy was developed resorting to the tow spreading technology and the mechanical spreading machine available at Airbus Group Innovations in Munich, Germany.

A set of three hybrid materials was manufactured with different hybrid volume fraction, using T800 and HR40 fibres, as well as the respective baseline non-hybrid materials. To understand the resulting material microstructure after the spreading process, micrographs were taken of the hybrid materials. These micrographs were treated using image processing tools to identify each fibre type in the material and characterize the dispersion of the fibres in the hybrid materials. From this analysis it was concluded that the degree of dispersion was lower than expected and that the tow-by-tow like type of hybridization was achieved, meaning that the tows of the different types of fibres could not penetrate each other. This was attributed to the low spreading ratio achieved with the mechanical spreader. Higher spreading ratio could not be achieved as it would lead to extensive fibre damage during the manufacturing process and, therefore, a lower quality material. However, no solution was found to increase spreading in the manufacturing configuration used. Nevertheless, the dispersion of these materials is higher than that of the interply hybrids, as the fibres of each type are grouped in bundles.

Although the microstructure of the materials manufactured presented a lower fibre dispersion than expected, an experimental campaign focused on tensile failure in the fibre direction was performed. Both strength and fracture toughness tests were performed for tensile loadings in the fibre direction.

From the tensile tests in the unidirectional composites, it was concluded that there was a reduction in strength for the hybrid materials when comparing to the T800 baseline. Additionally, Hybrid 2-1 and Hybrid 1-1 materials had a very similar strength as the HR40 material, being their failure dominated by the failure of the HR40 fibres. Nevertheless, an increase in failure strain was observed. The Hybrid 4-1 material with a 12.4% of HR40 fibres showed the highest strength of the hybrid materials. Additionally, a high non-linear behaviour prior to the failure was observed. This non-linearity is associated with the failure of the HR40 fibres, that have a lower failure strain and that, in this hybrid, did not lead to the failure of the material, as the T800 fibres could support the additional load, due to the higher T800 volume fraction.

Additionally, geometrically similar double edge notched specimens, with different sizes, were tested to determine the size effect law and the intraply $\mathcal{R}$-curve and steady state fracture toughness of the materials. From this analysis it was concluded that all hybrid materials had a lower fracture toughness than the baseline non-hybrid T800 material. This reduction of fracture toughness was attributed to the addition of more brittle HR40 fibres without promoting other failure mechanisms with the exception of fibre failure. The promotion of other failure mechanisms was seen to be crucial in the increase of the apparent fracture toughness of interply hybrid

materials, as demonstrated by Danzi [32].

The concept of intratow hybridization is interesting as it can lead to a higher range of composite materials available, with tailored properties for a given application. However, there are still challenges in manufacturing these materials, in particular to ensure a good material quality with a high degree of dispersion of the hybridized fibres.

Part V

Conclusions and future work

Chapter 7

Conclusions and future work

The work developed in this thesis was centred on the study of the mechanics of deformation and failure of fibre hybrid composites, focusing on the development of numerical models and detailed experimental campaigns. This chapter summarizes the main conclusions of this work, reporting the main developments and results achieved. Additionally, research topics for the continuation of the work developed in this thesis are also presented.

7.1 Conclusions

7.1.1 Numerical modelling of the longitudinal failure of composite materials

Longitudinal failure of composite material is a complex phenomenon to model. This is a fibre dominated loading condition, therefore, the taking into account the statistical nature of fibre strength in the model is extremely important. Furthermore, the correct stress redistribution after fibre fracture and the local effects of the microstructure's geometry need to be captured. Additionally, both the behaviour of the matrix and the fibre-matrix interface affect the stress redistribution and, therefore, the formation of clusters of broken fibres and the failure process.

To accurately simulate the tensile behaviour of composite materials and to be able to analyse the mechanisms and sequence of failure, it is necessary to use micromechanical numerical simulations that correctly model the behaviour of each of the constituents of the composite material. This includes not only the fibres but also the matrix and the interfaces between the two. A model for the fibre that is able to capture the statistical variability of the strength of the fibres was implemented. In addition, the model was developed with a non-linear elastic formulation to capture the non-linear behaviour of carbon fibres when loaded in tension. The matrix was modelled with an isotropic damage model with plasticity, developed by Melro et al. [142], which is able to capture the non-linear behaviour and fracture of typical epoxy systems used in composite materials. The interfaces between the matrix and the fibres were modelled using cohesive surfaces to correctly simulate the separation

between the matrix and the reinforcing material.

These material models were used to simulate simple micromechanical phenomena such as the single fibre fragmentation and fibre pushout. The modelling and analysis of these tests were used to validate not only the materials models used, but also the modelling strategies employed. It is concluded that the main failure mechanics observed experimentally are captured by the models. Additionally, the effect of the fibre-matrix interface properties was analysed, and it was concluded that the interface properties previously used for simulation of the RTM6 resin were too low and resulted in the premature failure of the specimen.

To understand the behaviour of fibre hybrid composites it is necessary to understand the behaviour and fracture process in non-hybrid composites. Using the random fibre generator developed by Melro et al, [68], extended in this work to consider fibres with different geometrical properties, different RVEs were generated and simulated. These models were used to understand the failure process in composite materials subjected to longitudinal tensile loadings. It was concluded that this is a phenomenon controlled by a population of defects as the fibres were seen to, typically, break in the locations of the most severe defects. As the developed material model for the fibres accurately captures the non-linear behaviour of carbon fibres, the influence of this effect on the tensile behaviour and failure process was analysed. It was concluded that its effect was reduced and, therefore, no changes in the fracture process were observed. Nonetheless, the non-linear behaviour of the fibres leads to a reduction of the composite material's failure strain, which better relates with experimental results. Due to the fully 3D nature of the models developed, they are able not only to capture the behaviour of composite materials in simple unidirectional loading conditions, but also under more complex scenarios such as the combination of unidirectional loading with hydrostatic pressure. An analysis on the effect of hydrostatic pressure on the longitudinal failure of composites materials was performed and it was concluded that the model captures the generalized reduction of the tensile strength with increasing hydrostatic pressure. Significant differences in the failure process were observed experimentally, moving from a disperse failure with severe fibre splitting to a more localized failure with increased pressure. In the numerical models, however, no distinction could be made, nevertheless, some changes in the fibre break density were observed. This lead to the conclusion that, to capture this changes in the fracture process, larger RVEs should be used, however, due to the computational cost of these models, that is currently not feasible without supercomputing resources.

This modelling strategy was also used to simulate the behaviour of two different hybrid material systems. It was concluded that different material behaviours can be attained by controlling the volume fraction of each type of fibre. In fact, it was possible to achieve a non-brittle, pseudo-ductile behaviour of the hybrid material in some cases. To achieve such behaviour it was concluded that the hybridized fibres had to be compatible to create a continuous failure between the low and the high elongation fibres. If this condition is not met, a load drop is observed when the low elongation fibres fail.

The 3D modelling strategy developed in this thesis is capable of capturing the

complex failure mechanisms of composite materials, however, its computational complexity and cost limit its usability. To mitigate this problem, a simplified model to predict the tensile failure of composite materials was introduced. The Spring Element Model is a geometrically 3D model with a single degree of freedom per node, that is able to correctly capture fibre failure, the stress redistribution process and cluster formation. The model is based on linear elastic springs to model the fibres, which have a maximum stress failure criterion, and shear springs connecting the fibres, which represent the elasto-plastic behaviour of the matrix. The SEM enables the use of larger RVEs, and has a much lower computational cost when compared to the micromechanical framework developed in Chapter 3.

The SEM was implemented first for the static case and used to further understand the fibre failure process and cluster formation, using not only the traditional Weibull distribution for fibre strength but also modified versions of this stochastic distribution that better relate with experimental results. It was concluded that, although, fairly accurate predictions of the strength of composite materials were achieved, the fracture process and cluster formation did not match the experimental observations. In addition, this model was compared and used to validate analytical formulations for stress redistribution typically used in fibre bundle models. It was concluded that most the analytical formulations analysed do not capture the effects of some material parameters on the stress redistribution, however, they allow a faster computational time. Furthermore, it was concluded that capturing the increase of both the maximum stress concentration and the ineffective length with the increase in cluster size is essential for an accurate representation of the stress redistribution and cluster development.

One of the shortcomings of the SEM is that, although it accurately captures the static equilibrium for stress redistribution, it does not capture the dynamic fracture of the fibres. To overcome this problem, a dynamic formulation of the Spring Element Model was proposed. This model builds upon the framework developed for the static model adding the dynamic components on the equilibrium equation. This model was implemented in a parallel computing framework for usage in computing clusters, to allow faster computing times. The framework developed is able to capture the dynamic stress wave that propagates in a broken failure due to its failure and the transient increase in the stress concentration in the fibres that surround the broken one. It was, however, observed that, although the model accurately captures the local dynamic effects, the overall material behaviour and fracture process remained unaltered, specially when a elasto-plastic matrix was considered. Additionally, it was concluded that, similarly to the static model, the dynamic model lead to an overestimation of the fibre break density at failure as well as an underestimation of the formation of clusters of multiple broken fibres.

Finally, the dynamic model was used to study and understand the longitudinal tensile failure of hybrid materials. The AS4-M50S, previously studied in Chapter 3, was further explored. The effect of the hybrid ratio and the effect of the microstructure on the failure process were analysed. As fibre dispersion is known to affect the behaviour of hybrid materials, different microstructures were generated, with different dispersions. It was observed that for lower dispersions the material was characterized by a more sudden failure of the low elongation fibres, which resulted

in a load drop in the stress-strain curve. For higher dispersions the failure of the low elongation fibres was gradual, leading to a progressive failure of the material. Interestingly, it was observed that a higher Dispersion Degree (metric used to characterize fibre dispersion) could be achieved for a layer-by-layer hybridization than that of the random material. This influence of the microstructure is important as it shows that the design of a hybrid composite depends not only on the fibres chosen and their ratios, but also on their arrangement in the microstructure.

7.1.2 Experimental study on the mechanics of failure of fibre hybrid composites

Fibre hybridization was shown to lead to interesting material behaviour, such as increased ductility and toughness, by exploiting the synergies between fibres with different mechanical properties. In this work the concept of fibre hybridization was analysed by performing detailed experimental campaigns, focusing not only on the material behaviour but also on the damage mechanisms leading to failure. Two distinct concepts of hybridization were analysed: interply or ply-by-ply and intratow hybridization.

Interply hybridization consists in combining layers of different materials, typically with the same resin system, into a single composite material. This technology associated with thin-ply technology results in interesting material behaviours, such as progressive failure of the hybrid material [8, 12, 32]. The work developed in this thesis is based on the preliminary work done by Danzi [32], where thin-ply HR40 (20 g/m^2) were combined with thin-ply T800 (50 g/m^2) layers to produce hybrid materials with improved fracture toughness.

The work presented in this thesis focused on the analysis of the effects of this type of hybridization on the material's response at the structural detail level. Two different hybrid material systems were manufactured with different layer combinations as well as the baseline T800 non-hybrid material, and were tested for tension and compression for plain-strength and open-hole specimens. The results of the plain strength tension specimens showed that the hybrid materials had a lower normalised tensile strength than their non-hybrid counterpart, thus leading to the conclusion that adding the HR40 fibres to the T800 composite materials leads to a reduction of its tensile strength. Nevertheless, a clear distinction between the failure mechanisms in the hybrid and non-hybrid composites was observed. The hybrid materials, specially the H2 material, which results of the combination of two 100 g/m^2 T800 layers with one 20 g/m^2 HR40 layer, showed a less brittle fracture with multiple cracks and extensive delamination and pull-out.

The test campaign on open-hole specimens lead to interesting results, with an increase in the notched strength of the H2 configuration. This increase was promoted by changes in the failure mechanisms in this material. Large splits were observed with multiple transverse cracks and fibre fractures emanating from the main splits. These damage mechanisms are considered to be responsible for changes in the stress fields surrounding the hole and, therefore, lead to the increased strength. Addition-

ally, a notch sensitivity study was performed, and an outstanding notch insensitivity was observed for the H2 hybrid material. The notch insensitivity of this material was further reinforced by the observation that one specimen failed outside the notched area, due to the appearance of large splits and delaminations through the width and length of the specimen. Similar studies were performed for compressive loadings and no synergies due to hybridization were observed.

The last chapter of the thesis focused on the exploration of the concept of intratow hybridization. In this work, the T800 and HR40 fibres, previously used for the interply hybridization, were used to manufacture intratow hydrid materials. These materials results in the combination of different fibres at the tow level, theoretically resulting in the highest dispersion possible and, therefore, the best hybrid behaviour.

Spread-tow technology was used to commingle the two types of fibres into a single tow and spread the hybrid tows into a tape that could be used to produce a composite material. Materials with different hybrid ratios were manufactured by controlling the ratio of the tows used of each fibre type and balancing the spreading parameters to optimize commingling and reducing tow damage. To analyse the hybridization dispersion, the microstructures of the manufactured materials were analysed. It was observed that the tows did not commingle to a high degree of dispersion. However, physical limitations of the manufacturing process prevented the production of materials with higher dispersion, as extensive tow damage would otherwise appear.

The experimental campaign performed focused on fibre dominated properties and consisted of longitudinal tensile strength tests and double-edge notched tensile specimens to derive the material's fracture toughness and $\mathcal{R}$-curve. A generalized reduction of the tensile strength of the hybrid materials was observed compared to the baseline non-hybrid materials. This lead to the conclusion that the introduction of the HR40 fibres in the T800 material lead to the premature failure of the material, which reinforces the conclusions obtained for the interply hybrid materials. Nevertheless, an increase in failure strain was observed. The Hybrid 4-1 material with 12.4% of HR40 fibres showed the highest strength of the hybrid materials and a highly non-linear behaviour prior to failure. Double edge notched tensile specimens were used to determine the $\mathcal{R}$-curve of the materials. From this analysis it was concluded that all hybrid materials had a lower fracture toughness than the baseline non-hybrid T800 material. This reduction of fracture toughness was attributed to the addition of more brittle HR40 fibres without promoting additional failure mechanisms, with the exception of fibre failure, which was seen as crucial in the increase of the fracture toughness in the interply hybrids. Nevertheless, the concept of intratow hybrid materials has a high potential for increased material performance, as shown in the numerical simulations, however, manufacturing capabilities of hybrid materials with increased fibre dispersion is necessary.

7.2 Future work

In spite of the vast number of models to predict tensile failure of composite materials available in the literature, there is still a gap between their numerical predictions and the experimental results. To help to bridge this gap, firstly, detailed bottom-up experimental campaigns should be performed. This experimental campaign should focuses on the *in-situ* determination of the properties of the constituents of the composite material, mainly the matrix properties, as it has been shown that the bulk properties are different from the *in-situ* ones [55]. Furthermore, the strength of the fibres should be address and the scaling and validity of the stochastic distribution should be studied for very short gauge lengths, similar to those used in micromechanical simulations. The interface properties should also be measured and correlated with numerical models similar to those proposed here. These analysis should be complemented with detailed experimental testing at the composite level that include not only stress-strain behaviour and strength, but also a detailed analysis on the damage process and cluster formation. The knowledge of the properties of both constituents and the fracture process should guide the improvement of the numerical models.

The usage of micromechanical models to predict strength of materials is very well established, however, one of the drawbacks of these models is the difficulty in the prediction of the fracture toughness. The determination of the fracture toughness requires the micromechanical analysis of stress states characterized by severe stress gradients, thus requiring more complex modelling strategies. One of the possible solutions is the combination of micromechanical models with meso/macro models in a multiscale formulation to be able to simulate, for instance, a compact tension test. The accurate representation of both the macro stress fields and the micromechanical failure mechanisms should allow the determination of the fracture toughness of a fibrous material, however, there is a large computational cost associated with this type of models, which can be tackled by reduced order modelling or concurrent multiscale simulations.

The topic of hybridization, particularly fibre hybridization, has been a focus of attention in the scientific community, however, this technology as yet to be fully exploited. Models for intrawtow hybridization and hybrid composite materials with high fibre dispersion have shown that these materials have a high potential to promote synergistic effects between the two hybridized fibres, however, there is no technical solution for their production. The spread-tow technology has potential to help produce these materials, however, more complex manufacturing techniques should be used, such has air spreading, as this allows higher spreading ratios, thus promoting tow penetration and fibre commingling.

Interply hybridization was shown to lead to improved properties at the structural detail level when compared to a baseline non-hybrid material, namely for tensile loadings. Nevertheless, more complex loading scenarios should be analysed so a full comparison on the advantages and drawbacks of hybrid composites can be assessed. Taking into account that this can only be done by comparing with traditional non-hybrid baseline materials. Furthermore, mesomechanical models to predict failure

of these materials should be developed. This should be address by building upon the currently state-of-the-art ply level mesomechanical models and modelling strategies for non-hybrid composites, which have shown a good correlation with experimental results [214–217].

The simulation of intraply hybrid composites is shown to be possible using the micromechanical strategies developed here. Nevertheless, further improvement on these models is possible and should be done, accompanied by detailed micromechanical testing campaigns on these materials. This should include not only the analysis of the macro behaviour of the material, but also detailed analysis on their fracture process, including computational tomography analysis of their failure. Additionally, mesoscale models for intraply hybrid materials are currently not available, but are essential to design these materials for structural applications. This should either be addressed using multiscale analysis and reduced order modelling or by developing homogenized models for intratow hybrid materials.

Additionally, it was shown that the microstructure of the hybrid material strongly affects the material's behaviour and that the developed micromechanical models are able to capture this effect. This enables the possibility of engineering hybrid composite materials by optimizing their microstructure. This should be addressed by combining micromechanical simulations with optimization techniques, however, the computationally cost of these models is still high for them to be combined with traditional methods. Therefore, more advanced strategies such as machine learning should be used, not only to support the fibre selection process but also to optimize the material's microstructure.

Bibliography

[1] Y. Swolfs, I. Verpoest, and L. Gorbatikh. A review of input data and modelling assumptions in longitudinal strength models for unidirectional fibre-reinforced composites. *Composite Structures*, 150:153–172, 2016.

[2] Y. Swolfs. *Hybridisation of Self-reinforced Composites: Modelling and Verifying a Novel Hybrid Concept*. PhD thesis, KU Leuven, 2015.

[3] M. R. Wisnom. Size effects in the testing of fibre-composite materials. *Composites Science and Technology*, 59(13):1937–1957, 1999.

[4] A. E. Scott, I. Sinclair, S. M. Spearing, A. Thionnet, and A. R. Bunsell. Damage accumulation in a carbon/epoxy composite: Comparison between a multiscale model and computed tomography experimental results. *Composites Part A: Applied Science and Manufacturing*, 43(9):1514–1522, 2012.

[5] S. Pimenta. Fibre failure modelling. In Pedro P Camanho and Stephen R Hallet, editors, *Numerical Modelling of Failure in Advanced Composite Materials*, chapter 25. Woodhead Publishing, 2015.

[6] A. Turon, J. Costa, P. Maimí, D. Trias, and J. A. Mayugo. A progressive damage model for unidirectional fibre-reinforced composites based on fibre fragmentation. Part I: Formulation. *Composites Science and Technology*, 65(13):2039–2048, 2005.

[7] S. Pimenta and S. T. Pinho. Hierarchical scaling law for the strength of composite fibre bundles. *Journal of the Mechanics and Physics of Solids*, 61(6):1337–1356, 2013.

[8] Y. Swolfs, L. Gorbatikh, and I. Verpoest. Fibre hybridisation in polymer composites: A review. *Composites Part A: Applied Science and Manufacturing*, 67(0):181–200, 2014.

[9] C. Dong, J. Duong, and I. J. Davies. Flexural properties of S-2 glass and TR30S carbon fiber-reinforced epoxy hybrid composites. *Polymer Composites*, 33(5):773–781, 2012.

[10] Z. Wu, X. Wang, K. Iwashita, T. Sasaki, and Y. Hamaguchi. Tensile fatigue behaviour of FRP and hybrid FRP sheets. *Composites Part B: Engineering*, 41(5):396–402, 2010.

[11] M. Jalalvand, G. Czél, and M. R. Wisnom. Numerical modelling of the damage modes in UD thin carbon/glass hybrid laminates. *Composites Science and Technology*, 94(0):39–47, 2014.

[12] R. Amacher, J. Cugnoni, J. Brunner, E. Kramer, C. Dransfeld, W. Smith, K. Scobbie, L. Sorensen, and J. Botsis. Toward Aerospace Grade Thin-Ply Composites. In *Proceedings ECCM-17, 17th European Conference on Composite Materials*, 2016.

[13] Y. Swolfs, L. Gorbatikh, and I. Verpoest. Stress concentrations in hybrid unidirectional fibre-reinforced composites with random fibre packings. *Composites Science and Technology*, 85(0):10–16, 2013.

[14] S. Pimenta and P. Robinson. Modelling the Tensile Response of Unidirectional Hybrid Composites. *European Conference on Composite Materials, ECCM*, 2014.

[15] Y. Swolfs, R. M. McMeeking, I. Verpoest, and L. Gorbatikh. The effect of fibre dispersion on initial failure strain and cluster development in unidirectional carbon/glass hybrid composites. *Composites Part A: Applied Science and Manufacturing*, 69(0):279–287, 2015.

[16] I. M. Djordjević, D. R. Sekulić, M. N. Mitrić, and M. M. Stevanović. Non-Hookean elastic behavior and crystallite orientation in carbon fibers. *Journal of Composite Materials*, 2010.

[17] M. Nishikawa, T. Okabe, and N. Takeda. Determination of interface properties from experiments on the fragmentation process in single-fiber composites. *Materials Science and Engineering A*, 480(1-2):549–557, 2008.

[18] M. Rodríguez, J. M. Molina-Aldareguía, C. González, and J. LLorca. A methodology to measure the interface shear strength by means of the fiber push-in test. *Composites Science and Technology*, 72(15):1924–1932, 2012.

[19] J. Jäger, M. G. R. Sause, F. Burkert, J. Moosburger-Will, M. Greisel, and S. Horn. Influence of plastic deformation on single-fiber push-out tests of carbon fiber reinforced epoxy resin. *Composites Part A: Applied Science and Manufacturing*, 71:157–167, 2015.

[20] G. Catalanotti, A. Arteiro, M. Hayati, and P. P. Camanho. Determination of the mode I crack resistance curve of polymer composites using the size-effect law. *Engineering Fracture Mechanics*, 118:49–65, mar 2014.

[21] W. A. Curtin and N. Takeda. Tensile Strength of Fiber-Reinforced Composites: II. Application to Polymer Matrix Composites. *Journal of Composite Materials*, 32(22):2060–2081, nov 1998.

[22] P. D. Soden, M. J. Hinton, and A. S. Kaddour. Lamina properties, lay-up configurations and loading conditions for a range of fibre-reinforced composite laminates. *Composites Science and Technology*, 58(7):1011–1022, 1998.

[23] A. R. Melro, P. P. Camanho, F.M. Andrade Pires, and S. T. Pinho. Micromechanical analysis of polymer composites reinforced by unidirectional fibres: Part II – Micromechanical analyses. *International Journal of Solids and Structures*, 50(11):1906–1915, 2013.

[24] A. Arteiro, G. Catalanotti, A. R. Melro, P. Linde, and P. P. Camanho. Micromechanical analysis of the in situ effect in polymer composite laminates. *Composite Structures*, 116:827–840, 2014.

[25] B. Fiedler, M. Hojo, S. Ochiai, K. Schulte, and M. Ando. Failure behavior of an epoxy matrix under different kinds of static loading. *Composites Science and Technology*, 61(11):1615–1624, 2001.

[26] J. Varna, L. A. Berglund, and M. L. Ericson. Transverse single-fibre test for interfacial debonding in composites: 2. Modelling. *Composites Part A: Applied Science and Manufacturing*, 28(4):317–326, 1997.

[27] F. Tanaka, T. Okabe, H. Okuda, I. A. Kinloch, and R. J. Young. Factors controlling the strength of carbon fibres in tension. *Composites Part A: Applied Science and Manufacturing*, 57(0):88–94, 2014.

[28] W. A. Curtin. Tensile Strength of Fiber-Reinforced Composites: III. Beyond the Traditional Weibull Model for Fiber Strengths. *Journal of Composite Materials*, 34(15):1301–1332, 2000.

[29] T. Okabe, N. Takeda, Y. Kamoshida, M. Shimizu, and W. A. Curtin. A 3D shear-lag model considering micro-damage and statistical strength prediction of unidirectional fiber-reinforced composites. *Composites Science and Technology*, 61(12):1773–1787, 2001.

[30] Toray Carbon Fibers Inc. T800S Data Sheet.

[31] Mitsubishi Chemical Carbon Fiber and Composites. PYROFIL™ HR 40 12M.

[32] F. Danzi. *Composite failure properties and non-linearity evaluation via statistical micromechanical analysis*. PhD thesis, Università di Pisa, 2018.

[33] A. S. Argon. Statistical Aspects of Fracture. In L J Broutman, editor, *Composite Materials: Fatigue and Fracture*, volume 5, chapter 4, pages 153–190. Academic Press, New York, 1974.

[34] Y. Swolfs, L. Gorbatikh, V. Romanov, S. Orlova, S. V. Lomov, and I. Verpoest. Stress concentrations in an impregnated fibre bundle with random fibre packing. *Composites Science and Technology*, 74(0):113–120, 2013.

[35] W. Weibull. A Statistical Distribution Function of Wide Applicability. *Journal of Applied Mechanics - Transactions of the ASME.*, 58(7):1001–1010, 1951.

[36] V. Calard and J. Lamon. Failure of fiber bundles. *Composites Science and Technology*, 64(5):701–710, 2004.

[37] M. R'Mili, N Godin, and J. Lamon. Flaw strength distributions and statistical parameters for ceramic fibers: The normal distribution. *Phys. Rev. E*, 85(5):51106, 2012.

[38] J. Watanabe, F. Tanaka, H. Okuda, and T. Okabe. Tensile strength distribution of carbon fibers at short gauge lengths. *Advanced Composite Materials*, 23(5-6):535–550, 2014.

[39] H. Peterlik and D. Loidl. Bimodal strength distributions and flaw populations of ceramics and fibres. *Engineering Fracture Mechanics*, 68(3):253–261, 2001.

[40] W. J. Padgett, S. D. Durham, and A. M. Mason. Weibull Analysis of the Strength of Carbon Fibers Using Linear and Power Law Models for the Length Effect. *Journal of Composite Materials*, 29(14):1873–1884, 1995.

[41] Y. Swolfs, I. Verpoest, and L. Gorbatikh. Issues in strength models for unidirectional fibre-reinforced composites related to Weibull distributions, fibre packings and boundary effects. *Composites Science and Technology*, 114:42–49, 2015.

[42] J. Andersons, R. Joffe, M. Hojo, and S. Ochiai. Glass fibre strength distribution determined by common experimental methods. *Composites Science and Technology*, 62(1):131–145, 2002.

[43] D. Sinclair. A Bending Method for Measurement of the Tensile Strength and Young's Modulus of Glass Fibers. *Journal of Applied Physics*, 21(5):380, 1950.

[44] I. J. Beyerlein and S. L. Phoenix. Statistics for the strength and size effects of microcomposites with four carbon fibers in epoxy resin. *Composites Science and Technology*, 56(1):75–92, 1996.

[45] M. Nakatani, M. Shioya, and J. Yamashita. Axial compressive fracture of carbon fibers. *Carbon*, 37(4):601–608, 1999.

[46] M. R'Mili, T. Bouchaour, and P. Merle. Estimation of Weibull parameters from loose-bundle tests. *Composites Science and Technology*, 56(7):831–834, 1996.

[47] S Feih, A Thraner, and H Lilholt. Tensile strength and fracture surface characterisation of sized and unsized glass fibers. *Journal of Materials Science*, 40(7):1615–1623, 2005.

[48] V. Pauchard, A. Chateauminois, F. Grosjean, and P. Odru. In situ analysis of delayed fibre failure within water-aged GFRP under static fatigue conditions. *International Journal of Fatigue*, 24(2–4):447–454, 2002.

[49] G. Foray, A. Descamps-Mandine, M. R'Mili, and J. Lamon. Statistical flaw strength distributions for glass fibres: Correlation between bundle test and AFM-derived flaw size density functions. *Acta Materialia*, 60(9):3711–3718, 2012.

[50] K. Naito. Tensile properties and weibull modulus of some high-performance polymeric fibers. *Journal of Applied Polymer Science*, 128(2):1185–1192, 2013.

[51] Q. Zeng, Z. Wang, and L. Ling. A study of the influence of interfacial damage on stress concentrations in unidirectional composites. *Composites Science and Technology*, 57(1):129–135, 1997.

[52] P. W. J. van den Heuvel, T. Peijs, and R. J. Young. Failure phenomena in two-dimensional multi-fibre microcomposites. Part 4: a Raman spectroscopic study on the influence of the matrix yield stress on stress concentrations. *Composites Part A: Applied Science and Manufacturing*, 31(2):165–171, 2000.

[53] Y. Swolfs, R. M. McMeeking, I. Verpoest, and L. Gorbatikh. Matrix cracks around fibre breaks and their effect on stress redistribution and failure development in unidirectional composites. *Composites Science and Technology*, 108(0):16–22, 2015.

[54] T. Hobbiebrunken, B. Fiedler, M. Hojo, and M. Tanaka. Experimental determination of the true epoxy resin strength using micro-scaled specimens. *Composites Part A: Applied Science and Manufacturing*, 38(3):814–818, 2007.

[55] J. Chevalier, P. P. Camanho, F. Lani, and T. Pardoen. Multi-scale characterization and modelling of the transverse compression response of unidirectional carbon fiber reinforced epoxy. *Composite Structures*, 209:160–176, feb 2019.

[56] A. B. de Morais. Prediction of the longitudinal tensile strength of polymer matrix composites. *Composites Science and Technology*, 66(15):2990–2996, 2006.

[57] J. P. Foreman, S. Behzadi, S. A. Tsampas, D. Porter, P. T. Curtis, and F. R. Jones. Rate dependent multiscale modelling of fibre reinforced composites. *Plastics, Rubber and Composites*, 38(2):67–71, 2009.

[58] R. P. Tavares, A. R. Melro, M. A. Bessa, A. Turon, W. K. Liu, and P. P. Camanho. Mechanics of hybrid polymer composites : analytical and computational study. *Computational Mechanics*, 57(3):405–421, 2016.

[59] F. M. M. Zhao and N. Takeda. Effect of interfacial adhesion and statistical fiber strength on tensile strength of unidirectional glass fiber / epoxy composites. Part I : experiment results. *Composites Part A: Applied Science and Manufacturing*, 31:1215–1224, 2000.

[60] T. Okabe. Size effect on tensile strength of unidirectional CFRP composites—experiment and simulation. *Composites Science and Technology*, 62(15):2053–2064, nov 2002.

[61] M. R. Wisnom, B. Khan, and S. R. Hallett. Size effects in unnotched tensile strength of unidirectional and quasi-isotropic carbon/epoxy composites. *Composite Structures*, 84(1):21–28, 2008.

[62] S. R. Hallett, B. G. Green, W. G. Jiang, and M. R. Wisnom. An experimental and numerical investigation into the damage mechanisms in notched composites. *Composites Part A: Applied Science and Manufacturing*, 40(5):613–624, 2009.

[63] J. M. Guerrero, J. A. Mayugo, J. Costa, and A. Turon. A 3D Progressive Failure Model for predicting pseudo-ductility in hybrid unidirectional composite materials under fibre tensile loading. *Composites Part A: Applied Science and Manufacturing*, 107:579–591, apr 2018.

[64] W. A. Curtin. Dimensionality and size effects on the strength of fiber-reinforced composites. *Composites Science and Technology*, 60(4):543–551, 2000.

[65] C. Landis and R. M. McMeeking. Stress concentrations in composites with interface sliding, matrix stiffness and uneven fiber spacing using shear lag theory. *International Journal of Solids and Structures*, 36(28):4333–4361, 1999.

[66] B. W. Rosen. Tensile failure of fibrous composites. *AIAA Journal*, 2(11):1985–1991, 1964.

[67] A. A. Gusev, P. J. Hine, and I. M. Ward. Fiber packing and elastic properties of a transversely random unidirectional glass/epoxy composite. *Composites Science and Technology*, 60(4):535–541, 2000.

[68] A. R. Melro, P. P. Camanho, and S. T. Pinho. Generation of random distribution of fibres in long-fibre reinforced composites. *Composites Science and Technology*, 68(9):2092–2102, 2008.

[69] G. Catalanotti. On the generation of RVE-based models of composites reinforced with long fibres or spherical particles. *Composite Structures*, 138:84–95, mar 2016.

[70] S. Bargmann, B. Klusemann, J. Markmann, J. Schnabel, K. Schneider, C. Soyarslan, and J. Wilmers. Generation of 3D representative volume elements for heterogeneous materials: A review. *Progress in Materials Science*, 96:322–384, jul 2018.

[71] Z. Wang, X. Wang, J. Zhang, W. Liang, and L. Zhou. Automatic generation of random distribution of fibers in long-fiber-reinforced composites and mesomechanical simulation. *Materials & Design*, 32(2):885–891, feb 2011.

[72] A. E. Scott, M. Mavrogordato, P. Wright, I. Sinclair, and S. M. Spearing. In situ fibre fracture measurement in carbon–epoxy laminates using high resolution computed tomography. *Composites Science and Technology*, 71(12):1471–1477, 2011.

[73] Y. Swolfs, H. Morton, A. E. Scott, L. Gorbatikh, P. A. S. Reed, I. Sinclair, S. M. Spearing, and I. Verpoest. Synchrotron radiation computed tomography for experimental validation of a tensile strength model for unidirectional fibre-reinforced composites. *Composites Part A: Applied Science and Manufacturing*, 77:106–113, 2015.

[74] L. St-Pierre, N. J. Martorell, and S. T. Pinho. Stress redistribution around clusters of broken fibres in a composite. *Composite Structures*, 2017.

[75] J. M. Hedgepeth. Stress Concentrations in Filamentary Structures. Technical report, NASA Langley Research Center; Hampton, VA United States, 1961.

[76] E. N. Sakharova and A. S. Ovchinskii. Dynamics of stress redistribution in a ruptured fiber of a composition material. *Mechanics of Composite Materials*, 15(1):45–51, 1979.

[77] J. Xing, X. Liu, and T. Chou. Dynamic Stress Concentration Factors in Unidirectional Composites. *Journal of Composite Materials*, 19(3):269–275, 1985.

[78] G. Bullegas. *Carbon fibre laminates with engineered fracture behaviour*. PhD thesis, Imperial College London, 2017.

[79] R. Ganesh, S. Sockalingam, B. Z. (Gama) Haque, and J. W. Gillespie. Dynamic effects of single fiber break in unidirectional glass fiber-reinforced composites. *Journal of Composite Materials*, 51(9):1307–1320, apr 2017.

[80] M. Ibnabdeljalil and W. A. Curtin. Strength and reliability of fiber-reinforced composites: Localized load-sharing and associated size effects. *International Journal of Solids and Structures*, 34(21):2649–2668, 1997.

[81] D. R. Aroush, E. Maire, C. Gauthier, S. Youssef, P. Cloetens, and H. D. Wagner. A study of fracture of unidirectional composites using in situ high-resolution synchrotron X-ray microtomography. *Composites Science and Technology*, 66(10):1348–1353, 2006.

[82] W. Na, D. Kwon, and W. Yu. X-ray computed tomography observation of multiple fiber fracture in unidirectional CFRP under tensile loading. *Composite Structures*, 188:39–47, mar 2018.

[83] L. Mishnaevsky Jr. and P. Brøndsted. Micromechanical modeling of damage and fracture of unidirectional fiber reinforced composites: A review. *Computational Materials Science*, 44(4):1351–1359, 2009.

[84] H. E. Daniels. The Statistical Theory of the Strength of Bundles of Threads. I. *Proceedings of the Royal Society of London A: Mathematical, Physical and Engineering Sciences*, 183(995):405–435, 1945.

[85] W. A. Curtin. Theory of Mechanical Properties of Ceramic-Matrix Composites. *Journal of the American Ceramic Society*, 74(11):2837–2845, nov 1991.

[86] J. M. Hedgepeth and P. Van Dyke. Local Stress Concentrations in Imperfect Filamentary Composite Materials. *Journal of Composite Materials*, 1(3):294–309, 1967.

[87] D. G. Harlow and S. L. Phoenix. The chain-of-bundles probability model for the strength of fibrous materials I: analysis and conjectures. *Journal of composite materials*, 12(2):195–214, 1978.

[88] D. G. Harlow and S. L. Phoenix. The chain-of-bundles probability model for the strength of fibrous materials II: a numerical study of convergence. *Journal of composite materials*, 12(3):314–334, 1978.

[89] T. Okabe, H. Sekine, K. Ishii, M. Nishikawa, and N. Takeda. Numerical method for failure simulation of unidirectional fiber-reinforced composites with spring element model. *Composites Science and Technology*, 65(6):921–933, 2005.

[90] W. A. Curtin and N. Takeda. Tensile strength of fiber-reinforced composites: I. Model and effects of local fiber geometry. *Journal of composite materials*, 32(22):2042–2059, 1998.

[91] I. J. Beyerlein and S. L. Phoenix. Stress concentrations around multiple fiber breaks in an elastic matrix with local yielding or debonding using quadratic influence superposition. *Journal of the Mechanics and Physics of Solids*, 44(12):1997–2039, 1996.

[92] C. Landis, I. J. Beyerlein, and R. M. McMeeking. Micromechanical simulation of the failure of fiber reinforced composites. *Journal of the Mechanics and Physics of Solids*, 48(3):621–648, 2000.

[93] X. Bai, M. A. Bessa, A. R. Melro, P. P. Camanho, L. Guo, and W. K. Liu. High-fidelity micro-scale modeling of the thermo-visco-plastic behavior of carbon fiber polymer matrix composites. *Composite Structures*, 134:132–141, 2015.

[94] S. Blassiau, A. Thionnet, and A. R. Bunsell. Three-dimensional analysis of load transfer micro-mechanisms in fibre/matrix composites. *Composites Science and Technology*, 69(1):33–39, 2009.

[95] A. Thionnet, H. Y. Chou, and A. R. Bunsell. Fibre break processes in unidirectional composites. *Composites Part A: Applied Science and Manufacturing*, 65(0):148–160, 2014.

[96] A. Matzenmiller, J. Lubliner, and R. L. Taylor. A constitutive model for anisotropic damage in fiber-composites. *Mechanics of Materials*, 20(2):125–152, 1995.

[97] A. K. Kaw. *Mechanics of Composite Materials*. Tayler and Francis, 2nd edition, 2006.

[98] T. Hayashi. On the improvement of mechanical properties of composites by hybrid compositon. *Proc 8th int reinforced plastics conference*, pages 149–152, 1972.

[99] G. Czél, M. Jalalvand, and M. R. Wisnom. Hybrid specimens eliminating stress concentrations in tensile and compressive testing of unidirectional composites. *Composites Part A: Applied Science and Manufacturing*, 2016.

[100] G. Kretsis. A review of the tensile, compressive, flexural and shear properties of hybrid fibre-reinforced plastics. *Composites*, 18(1):13–23, 1987.

[101] G. Marom, S. Fischer, F. R. Tuler, and H. D. Wagner. Hybrid effects in composites: conditions for positive or negative effects versus rule-of-mixtures behaviour. *Journal of Materials Science*, 13(7):1419–1426, 1978.

[102] Z. S. Wu, C. Q. Yang, Y. H. Tobe, L. P. Ye, and T. Harada. Electrical and Mechanical Characterization of Hybrid CFRP Sheets. *Journal of Composite Materials*, 40(3):227–244, 2006.

[103] M. G. Phillips. Composition parameters for hybrid composite materials. *Composites*, 12(2):113–116, 1981.

[104] P. W. Manders and M. G. Bader. The strength of hybrid glass/carbon fibre composites. *Journal of Materials Science*, 16(8):2246–2256, 1981.

[105] C. Zweben. Tensile strength of hybrid composites. *Journal of Materials Science*, 12(7):1325–1337, 1977.

[106] Y. Xia and C. Ruiz. Analysis of damage in stress wave loaded unidirectional composites. *Computers and Structures*, 38(3):251–258, 1991.

[107] R. Ganesh, S. Sockalingam, and J. W. Gillespie. Dynamic effects of a single fiber break in unidirectional glass fiber-reinforced polymer composites: Effects of matrix plasticity. *Journal of Composite Materials*, page 002199831773760, oct 2017.

[108] J. I. Xing, G. C. Hsiao, and T. Chou. A Dynamic Explanation of The Hybrid Effect. *Journal of Composite Materials*, 15(5):443–461, 1981.

[109] I. Taketa. *Analysis of Failure Mechanisms and Hybrid Effects in Carbon Fibre Reinforced Thermoplastic Composites*. PhD thesis, KU Leuven, Leuven, 2011.

[110] C. Wonderly, J. Grenestedt, G. Fernlund, and E. Cĕpus. Comparison of mechanical properties of glass fiber/vinyl ester and carbon fiber/vinyl ester composites. *Composites Part B: Engineering*, 36(5):417–426, 2005.

[111] C. Dong and I. J. Davies. Optimal design for the flexural behaviour of glass and carbon fibre reinforced polymer hybrid composites. *Materials and Design*, 37(0):450–457, 2012.

[112] J. W. Giancaspro, C. G. Papakonstantinou, and P. N. Balaguru. Flexural response of inorganic hybrid composites with E-glass and carbon fibers. *Journal of Engineering Materials and Technology*, 132(2):21005, 2010.

[113] M. Sayer, N. B. Bektaş, and O. Sayman. An experimental investigation on the impact behavior of hybrid composite plates. *Composite Structures*, 92(5):1256–1262, 2010.

[114] B. Z. Jang, L. C. Chen, C. Z. Wang, H. T. Lin, and R. H. Zee. Impact resistance and energy absorption mechanisms in hybrid composites. *Composites Science and Technology*, 34(4):305–335, 1989.

[115] N. K. Naik, R. Ramasimha, H. Arya, S. V. Prabhu, and N. ShamaRao. Impact response and damage tolerance characteristics of glass–carbon/epoxy hybrid composite plates. *Composites Part B: Engineering*, 32(7):565–574, 2001.

[116] F. Sarasini, J. Tirillò, M. Valente, T. Valente, S. Cioffi, S. Iannace, and L. Sorrentino. Effect of basalt fiber hybridization on the impact behavior under low impact velocity of glass/basalt woven fabric/epoxy resin composites. *Composites Part A: Applied Science and Manufacturing*, 47(0):109–123, 2013.

[117] I. M. De Rosa, F. Marra, G. Pulci, C. Santulli, F. Sarasini, J. Tirillò, and M. Valente. Post-impact mechanical characterisation of E-glass/basalt woven fabric interply hybrid laminates. *Express Polym Lett*, 5(5):449–459, 2011.

[118] R. Park and J. Jang. Effect of laminate geometry on impact performance of aramid fiber/polyethylene fiber hybrid composites. *Journal of Applied Polymer Science*, 75(7):952–959, 2000.

[119] E. V. González, P. Maimí, J. R. Sainz de Aja, P. Cruz, and P. P. Camanho. Effects of interply hybridization on the damage resistance and tolerance of composite laminates. *Composite Structures*, 108:319–331, feb 2014.

[120] A. A. Peijs and J. M. de Kok. Hybrid composites based on polyethylene and carbon fibres. Part 6: Tensile and fatigue behaviour. *Composites*, 24(1):19–32, 1993.

[121] K. D. Jones and A. T. DiBenedetto. Fiber fracture in hybrid composite systems. *Composites Science and Technology*, 51(1):53–62, 1994.

[122] H. Yu, M. L. Longana, M. Jalalvand, M. R. Wisnom, and K. D. Potter. Pseudo-ductility in intermingled carbon/glass hybrid composites with highly aligned discontinuous fibres. *Composites Part A: Applied Science and Manufacturing*, 73(0):35–44, 2015.

[123] G. Czél and M. R. Wisnom. Demonstration of pseudo-ductility in high performance glass/epoxy composites by hybridisation with thin-ply carbon prepreg. *Composites Part A: Applied Science and Manufacturing*, 52(0):23–30, 2013.

[124] M. Fotouhi, M. Jalalvand, and M. R. Wisnom. High performance quasi-isotropic thin-ply carbon/glass hybrid composites with pseudo-ductile behaviour in all fibre orientations. *Composites Science and Technology*, 152:101–110, nov 2017.

[125] Y. Liang, C. Sun, and F. Ansari. Acoustic Emission Characterization of Damage in Hybrid Fiber-Reinforced Polymer Rods. *Journal of Composites for Construction*, 8(1):70–78, 2004.

[126] G. Czél, S. Pimenta, M. R. Wisnom, and P. Robinson. Demonstration of pseudo-ductility in unidirectional discontinuous carbon fibre/epoxy prepreg composites. *Composites Science and Technology*, 106(0):110–119, 2015.

[127] G. Czél, M. Jalalvand, and M. R. Wisnom. Demonstration of pseudo-ductility in unidirectional hybrid composites made of discontinuous carbon/epoxy and continuous glass/epoxy plies. *Composites Part A: Applied Science and Manufacturing*, 72(0):75–84, 2015.

[128] Y. Swolfs, Y. Meerten, P. J. Hine, I. Ward, I. Verpoest, and L. Gorbatikh. Introducing ductility in hybrid carbon fibre/self-reinforced composites through control of the damage mechanisms. *Composite Structures*, 131(0):259–265, 2015.

[129] J. D. Fuller and M. R. Wisnom. Pseudo-ductility and damage suppression in thin ply CFRP angle-ply laminates. *Composites Part A: Applied Science and Manufacturing*, 69:64–71, 2015.

[130] J. D. Fuller, M. Jalalvand, and M. R. Wisnom. A Pseudo Ductile Angle-Ply Sub-Laminate Approach for Multidirectional Thin-Ply CFRP Laminates. In *Proceedings ECCM-17, 17th European Conference on Composite Materials*, 2016.

[131] G. Czél, T. Rev, M. Jalalvand, M. Fotouhi, M. L. Longana, O. J. Nixon-Pearson, and M. R. Wisnom. Pseudo-ductility and reduced notch sensitivity in multi-directional all-carbon/epoxy thin-ply hybrid composites. *Composites Part A: Applied Science and Manufacturing*, 104:151–164, jan 2018.

[132] A. Ortega, P. Maimí, E. V. González, J. R. Sainz de Aja, F. M. de la Escalera, and P. Cruz. Translaminar fracture toughness of interply hybrid laminates under tensile and compressive loads. *Composites Science and Technology*, 143:1–12, may 2017.

[133] D. G. Harlow. Statistical Properties of Hybrid Composites. I. Recursion Analysis. *Proceedings of the Royal Society of London A: Mathematical, Physical and Engineering Sciences*, 389(1796):67–100, 1983.

[134] J. M. Guerrero, R. P. Tavares, F. Otero, J. A. Mayugo, J. Costa, A. Turon, and P. P. Camanho. An analytical model to predict stress fields around broken fibres and their effect on the longitudinal failure of hybrid composites. *Composite Structures*, 211:564–576, mar 2019.

[135] H. Fukunaga, T. Chou, and H. Fukuda. Probabilistic strength analyses of interlaminated hybrid composites. *Composites Science and Technology*, 35(4):331–345, 1989.

[136] H. Fukuda. An advanced theory of the strength of hybrid composites. *Journal of Materials Science*, 19(3):974–982, 1984.

[137] L. Mishnaevsky Jr. and G. Dai. Hybrid carbon/glass fiber composites: Micromechanical analysis of structure–damage resistance relationships. *Computational Materials Science*, 81(0):630–640, 2014.

[138] P. W. Manders. *The strength of mixed fibre composites*. PhD thesis, University of Surrey, UK, 1979.

[139] P. Ren, Z. Zhang, L. Xie, F. Ren, Y. Jin, Y. Di, and C. Fang. Hybrid effect on mechanical properties of M40-T300 carbon fiber reinforced Bisphenol A Dicyanate ester composites. *Polymer Composites*, 31(12):2129–2137, 2010.

[140] A. R. Melro. *Analytical and numerical modelling of damage and fracture of advanced composites*. PhD thesis, Faculdade de Engenharia da Universidade do Porto, 2011.

[141] Dassault Systèmes Simulia Corp. ABAQUS 6.14 documentation, 2014.

[142] A. R. Melro, P. P. Camanho, F.M. Andrade Pires, and S. T. Pinho. Micromechanical analysis of polymer composites reinforced by unidirectional fibres: Part I – Constitutive modelling. *International Journal of Solids and Structures*, 50(11):1897–1905, 2013.

[143] G. J. Curtis, J. M. Milne, and W. N. Reynolds. Non-Hookean behaviour of strong carbon fibres. 1968.

[144] W. Van Dreumel and J. Kamp. Non Hookean behaviour in the fibre direction of carbonfibre composites and the influence of fibre waviness on the tensile properties. Technical report, Delft University of Technology, 1977.

[145] J. D. H. Hughes. Strength and modulus of current carbon fibres. *Carbon*, 24(5):551–556, 1986.

[146] L. Oliveira, D. Hitchcock, H. Behlow, R. Podila, M. J. Skove, S. M. Serkiz, and A. M. Rao. Second and third-order elastic constants of filaments of Hex-Tow IM7 carbon fiber. *Journal of materials engineering and performance*, 23(3):685–692, 2014.

[147] M. Shioya, E. Hayakawa, and A. Takaku. Non-hookean stress-strain response and changes in crystallite orientation of carbon fibres. *Journal of materials science*, 31(17):4521–4532, 1996.

[148] T. Ishikawa, M. Matsushima, and Y. Hayashi. Hardening non-linear behaviour in longitudinal tension of unidirectional carbon composites. *Journal of materials science*, 20(11):4075–4083, 1985.

[149] H. T. Hahn and S. W. Tsai. Nonlinear Elastic Behavior of Unidirectional Composite Laminae. *Journal of Composite Materials*, 7(1):102–118, jan 1973.

[150] P. Maimí, P. P. Camanho, J. A. Mayugo, and C. G. Davila. A thermodynamically consistent damage model for advanced composites. Technical report, NASA Langley Research Center; Hampton, VA, United States, 2006.

[151] Z. P. Bažant and B. H. Oh. Crack band theory for fracture of concrete. *Matériaux et Construction*, 16(3):155–177, 1983.

[152] M. L. Benzeggagh and M. Kenane. Measurement of mixed-mode delamination fracture toughness of unidirectional glass/epoxy composites with mixed-mode bending apparatus. *Composites Science and Technology*, 56(4):439–449, 1996.

[153] T. Okabe and N. Takeda. Estimation of strength distribution for a fiber embedded in a single-fiber composite: experiments and statistical simulation based on the elasto-plastic shear-lag approach. *Composites Science and Technology*, 61(12):1789–1800, 2001.

[154] V. P. Rajan and W. A. Curtin. Rational design of fiber-reinforced hybrid composites: A global load sharing analysis. *Composites Science and Technology*, 117:199–207, 2015.

[155] X. Wang, J. Zhang, Z. Wang, W. Liang, and L. Zhou. Finite element simulation of the failure process of single fiber composites considering interface properties. *Composites Part B: Engineering*, 45(1):573–580, 2013.

[156] F. P. van der Meer, S. Raijmaekers, and I. Rocha. Interpreting the single fiber fragmentation test with numerical simulations. *Composites Part A: Applied Science and Manufacturing*, 118:259–266, mar 2019.

[157] M. Kharrat, A. Chateauminois, L. Carpentier, and P. Kapsa. On the interfacial behaviour of a glass/epoxy composite during a micro-indentation test: assessment of interfacial shear strength using reduced indentation curves. *Composites Part A: Applied Science and Manufacturing*, 28(1):39–46, 1997.

[158] A. S. Wronski and T. V. Parry. Compressive failure and kinking in uniaxially aligned glass-resin composite under superposed hydrostatic pressure. *Journal of Materials Science*, 17(12):3656–3662, dec 1982.

[159] T. V. Parry and A. S. Wronski. The effect of hydrostatic pressure on the tensile properties of pultruded CFRP. *Journal of Materials Science*, 20(6):2141–2147, jun 1985.

[160] T. V. Parry and A. S. Wronski. The tensile properties of pultruded GRP tested under superposed hydrostatic pressure. *Journal of Materials Science*, 21(12):4451–4455, dec 1986.

[161] C. P. R. Hoppel, T. A. Bogetti, and J. W. Gillespie. Literature Review-Effects of Hydrostatic Pressure on the Mechanical Behavior of Composite Materials. *Journal of Thermoplastic Composite Materials*, 8(4):375–409, oct 1995.

[162] P. Zinoviev, S. Tsvetkov, G. Kulish, R. van den Berg, and L. Van Schepdael. The behavior of high-strength unidirectional composites under tension with superposed hydrostatic pressure. *Composites Science and Technology*, 61(8):1151–1161, 2001.

[163] P. J. Hine, R. A. Duckett, A. S. Kaddour, M. J. Hinton, and G. M. Wells. The effect of hydrostatic pressure on the mechanical properties of glass fibre/epoxy unidirectional composites. *Composites Part A: Applied Science and Manufacturing*, 36(2):279–289, 2005.

[164] M. J. Hinton and A. S. Kaddour. Triaxial test results for fibre-reinforced composites: The Second World-Wide Failure Exercise benchmark data. *Journal of Composite Materials*, 47(6-7):653–678, mar 2013.

[165] J. Lamon. *Mécanique de la rupture fragile et de l'endommagement: approches statistiques et probabilistes*. Études en mécanique des matériaux et des structures. Hermes Science Publications, 2007.

[166] C. Landis and R. M. McMeeking. A shear-lag model for a broken fiber embedded in a composite with a ductile matrix. *Composites Science and Technology*, 59(3):447–457, 1999.

[167] H. Fukuda. Stress concentration factors in unidirectional composites with random fiber spacing. *Composites Science and Technology*, 22(2):153–163, jan 1985.

[168] H. L. Cox. The elasticity and strength of paper and other fibrous materials. *British Journal of Applied Physics*, 3(3):72–79, 1952.

[169] A. Kelly and W. R. Tyson. Tensile properties of fibre-reinforced metals: Copper/tungsten and copper/molybdenum. *Journal of the Mechanics and Physics of Solids*, 13(6):329–350, dec 1965.

[170] C. Zweben. Tensile failure of fiber composites. *AIAA Journal*, 6(12):2325–2331, dec 1968.

[171] J. M. Hedgepeth and P. Van Dyke. Local Stress Concentrations in Imperfect Filamentary Composite Materials. *Journal of Composite Materials*, 1(3):294–309, jul 1967.

[172] S.B. Batdorf. Tensile Strength of Unidirectionally Reinforced Composites — I. *Journal of Reinforced Plastics and Composites*, 1(2):153–164, apr 1982.

[173] S. B. Batdorf and R. Ghaffarian. Tensile Strength of Unidirectionally Reinforced Composites — II. *Journal of Reinforced Plastics and Composites*, 1(2):165–176, apr 1982.

[174] Z. H. Xia and W. A. Curtin. Multiscale modeling of damage and failure in aluminum-matrix composites. *Composites Science and Technology*, 61(15):2247–2257, nov 2001.

[175] L. Mishnaevsky Jr. and P. Brøndsted. Micromechanisms of damage in unidirectional fiber reinforced composites: 3D computational analysis. *Composites Science and Technology*, 69(7-8):1036–1044, jun 2009.

[176] Tomonaga Okabe, Kensuke Ishii, Masaaki Nishikawa, and Nobuo Takeda. Prediction of Tensile Strength of Unidirectional CFRP Composites. *Journal of the Japan Society for Composite Materials*, 33(December 2014):205–212, jan 2007.

[177] B. Delaunay. Sur la sphere vide. *Izv. Akad. Nauk SSSR, Otdelenie Matematicheskii i Estestvennyka Nauk*, 7(793-800):1–2, 1934.

[178] M. J. DeJong, M. A. Hendriks, and J. G. Rots. Sequentially linear analysis of fracture under non-proportional loading. *Engineering Fracture Mechanics*, 75(18):5042–5056, dec 2008.

[179] J. G. Rots and S. Invernizzi. Regularized sequentially linear saw-tooth softening model. *International Journal for Numerical and Analytical Methods in Geomechanics*, 28(78):821–856, jun 2004.

[180] F. Otero, S. Oller, X. Martínez, and O. Salomón. Numerical homogenization for composite materials analysis. Comparison with other micro mechanical formulations. *Composite Structures*, 122:405–416, apr 2015.

[181] I. J. Beyerlein and S. L. Phoenix. Statistics for the strength and size effects of microcomposites with four carbon fibers in epoxy resin. *Composites Science and Technology*, 56(1):75–92, jan 1996.

[182] R. Gulino and S. L. Phoenix. Weibull strength statistics for graphite fibres measured from the break progression in a model graphite/glass/epoxy microcomposite. *Journal of Materials Science*, 26(11):3107–3118, 1991.

[183] A. S. Watson and R. L. Smith. An examination of statistical theories for fibrous materials in the light of experimental data. *Journal of Materials Science*, 20(9):3260–3270, sep 1985.

[184] M. S. Madhukar and L. T. Drzal. Fiber-Matrix Adhesion and Its Effect on Composite Mechanical Properties: II. Longitudinal (0°) and Transverse (90°) Tensile and Flexure Behavior of Graphite/Epoxy Composites. *Journal of Composite Materials*, 25(8):958–991, aug 1991.

[185] N. Toyama and J. Takatsubo. An investigation of non-linear elastic behavior of CFRP laminates and strain measurement using Lamb waves. *Composites Science and Technology*, 64(16):2509–2516, dec 2004.

[186] X. F. Zhou and H. D. Wagner. Stress concentrations caused by fiber failure in two-dimensional composites. *Composites Science and Technology*, 59(7):1063–1071, 1999.

[187] R. P. Tavares, F. Otero, A. Turon, and P. P. Camanho. Effective simulation of the mechanics of longitudinal tensile failure of unidirectional polymer composites. *International Journal of Fracture*, 208(1-2):269–285, dec 2017.

[188] S. C. Garcea, I. Sinclair, S. M. Spearing, and P. J. Withers. Mapping fibre failure in situ in carbon fibre reinforced polymers by fast synchrotron X-ray computed tomography. *Composites Science and Technology*, 149:81–89, sep 2017.

[189] V. Thomée. *Galerkin finite element methods for parabolic problems*. Springer, 2006.

[190] G. B. Warburton. Dynamics of structures, by Ray W. Clough and Joseph Penzien, 2nd edition, McGraw-Hill, New York, 1993. No. of pages: 738. ISBN 0-07-011394-7. *Earthquake Engineering & Structural Dynamics*, 24(3):457–462, mar 1995.

[191] T. Belytschko, W. K. Liu, B. Moran, and K. Elkhodary. *Nonlinear finite elements for continua and structures*. John wiley & sons, 2013.

[192] F. M. Conde, P. G. Coelho, R. P. Tavares, J. M. Guedes, H. C. Rodrigues, and P. P. Camanho. Optimization of Unidirectional Hybrid Polymer Composites Using a Spring Element Model. In *13th World Congress of Structural and Multidisciplinary Optimization*, 2019.

[193] A. R. Bunsell, L. Gorbatikh, H. Morton, S. Pimenta, I. Sinclair, S. M. Spearing, Y. Swolfs, and A. Thionnet. Benchmarking of strength models for unidirectional composites under longitudinal tension. *Composites Part A: Applied Science and Manufacturing*, mar 2018.

[194] M. F. da Costa Fernandes. Traslaminar fracture of thinply composite laminates. Master's thesis, Faculdade de Engenharia, Universidade do Porto, Porto, 2014.

[195] G. Bullegas, S. T. Pinho, and S. Pimenta. Engineering the translaminar fracture behaviour of thin-ply composites. *Composites Science and Technology*, 131:110–122, 2016.

[196] R. F. Teixeira, S. T. Pinho, and P. Robinson. Thickness-dependence of the translaminar fracture toughness: experimental study using thin-ply composites. *Composites Part A: Applied Science and Manufacturing*, 90:33–44, 2016.

[197] M. J. Laffan, S. T. Pinho, P. Robinson, and L. Iannucci. Measurement of the in situ ply fracture toughness associated with mode I fibre tensile failure in FRP. Part II: Size and lay-up effects. *Composites Science and Technology*, 70(4):614–621, 2010.

[198] S. Pimenta and S. T. Pinho. An analytical model for the translaminar fracture toughness of fibre composites with stochastic quasi-fractal fracture surfaces. *Journal of the Mechanics and Physics of Solids*, 66:78–102, 2014.

[199] ASTM D 3039 D 3039M-14. Standard Test Method for Tensile Properties of Polymer Matrix Composite Materials. ASTM International, West Conshohocken, PA.

[200] ASTM Standard. D6484/D6484M–04. *Standard test method for open-hole compressive strength of polymer matrix composite laminates*, 2004.

[201] ASTM D 5766 D 5766M-02a. Open hole tensile strength of polymer composite laminates. ASTM International, West Conshohocken, PA.

[202] P. P. Camanho, G. H. Erçin, G. Catalanotti, S. Mahdi, and P. Linde. A finite fracture mechanics model for the prediction of the open-hole strength of composite laminates. *Composites Part A: Applied Science and Manufacturing*, 43(8):1219–1225, aug 2012.

[203] G. H. Erçin, P. P. Camanho, J. Xavier, G. Catalanotti, S. Mahdi, and P. Linde. Size effects on the tensile and compressive failure of notched composite laminates. *Composite Structures*, 96:736–744, feb 2013.

[204] G. H. Erçin. *Stress Gradient Effects on Laminated Composites*. PhD thesis, 2013.

[205] D. Gizik, C. Metzner, C. Weimer, and P. Middendorf. Spreading of heavy tow carbon fibers for the use in aircraft structures. In *Proceeding of the 17th European Conference on Composite Materials*, 2016.

[206] H. Diao, A. Bismarck, and P. Robinson. Production of continuous intermingled CF/GF hybrid composite via fibre tow spreading technology. *Proceedings of ECCM16-*, 2014.

[207] British Standards Institution. and British Standards Institution. *Carbon fibre laminates : determination of the fibre, resin and void contents*. British Standards Institution, 1998.

[208] L. Liu, B. Zhang, D. Wang, and Z. Wu. Effects of cure cycles on void content and mechanical properties of composite laminates. *Composite Structures*, 73(3):303–309, jun 2006.

[209] S. Sihn, R. Y. Kim, K. Kawabe, and S. W. Tsai. Experimental studies of thin-ply laminated composites. *Composites Science and Technology*, 67(6):996–1008, may 2007.

[210] A. Arteiro, G. Catalanotti, J. Xavier, and P. P. Camanho. Notched response of non-crimp fabric thin-ply laminates. *Composites Science and Technology*, 79:97–114, apr 2013.

[211] G. Bao, S. Ho, Z. Suo, and B. Fan. The role of material orthotropy in fracture specimens for composites. *International Journal of Solids and Structures*, 29(9):1105–1116, jan 1992.

[212] D. L. Chen, B. Weiss, and R. Stickler. A new geometric factor formula for a center cracked plate tensile specimen of finite width. *International Journal of Fracture*, 55(1):R3–R8, may 1992.

[213] Z. P. Bažant and J. Planas. *Fracture and size effect in concrete and other quasibrittle materials*, volume 16. CRC press, 1997.

[214] P. Maimí, P. P. Camanho, J. A. Mayugo, and C. G. Dávila. A continuum damage model for composite laminates: Part II – Computational implementation and validation. *Mechanics of Materials*, 39(10):909–919, oct 2007.

[215] C. Furtado, G. Catalanotti, A. Arteiro, P. J. Gray, B. L. Wardle, and P. P. Camanho. Simulation of failure in laminated polymer composites: Building-block validation. *Composite Structures*, 226:111168, oct 2019.

[216] F. Zhuang, P. Chen, A. Arteiro, and P. P. Camanho. Mesoscale modelling of damage in half-hole pin bearing composite laminate specimens. *Composite Structures*, 214:191–213, apr 2019.

[217] F. Zhuang, A. Arteiro, C. Furtado, P. Chen, and P. P. Camanho. Mesoscale modelling of damage in single- and double-shear composite bolted joints. *Composite Structures*, 226:111210, oct 2019.

Appendices

Chapter A

Full DOE results for the dynamic SEM

Table A.1: Results of the full factorial design analysis for the stress concentration around a single broken fibre.

Case	E_f (GPa)	G_m (MPa)	τ^u (MPa)	V_f	SCF_{max}^{Din}		SCF_{max}^{Stat}		SCF_{Inc}	
					Avg.	CoV (%)	Avg.	CoV (%)	Avg. (%)	CoV (%)
1	70	450	50	0.4	1.119	1.53	1.087	0.79	36.77	27.72
2	70	450	50	0.6	1.073	0.67	1.056	0.59	29.40	40.22
3	70	450	100	0.4	1.194	3.43	1.125	1.60	54.78	28.18
4	70	450	100	0.6	1.121	1.68	1.084	0.85	43.26	35.54
5	70	450	∞	0.4	1.471	11.62	1.260	7.45	80.95	7.14
6	70	450	∞	0.6	1.363	2.26	1.194	1.38	87.40	4.20
7	70	1050	50	0.4	1.080	0.92	1.067	0.61	19.04	36.53
8	70	1050	50	0.6	1.046	0.66	1.041	0.40	11.78	80.88
9	70	1050	100	0.4	1.141	2.26	1.096	0.98	46.24	36.45
10	70	1050	100	0.6	1.086	1.38	1.063	0.70	36.24	31.88
11	70	1050	∞	0.4	1.442	11.09	1.240	6.89	83.58	7.71
12	70	1050	∞	0.6	1.336	1.62	1.168	1.10	100.25	6.21
13	230	450	50	0.4	1.195	3.44	1.122	1.46	59.22	31.79
14	230	450	50	0.6	1.117	1.70	1.084	0.83	38.42	38.01
15	230	450	100	0.4	1.263	4.17	1.178	3.24	49.23	34.37
16	230	450	100	0.6	1.179	1.94	1.122	0.78	46.19	29.22
17	230	450	∞	0.4	1.497	12.04	1.277	7.92	78.81	7.22
18	230	450	∞	0.6	1.395	2.66	1.217	1.70	81.90	3.86
19	230	1050	50	0.4	1.143	2.21	1.096	0.87	48.21	30.89
20	230	1050	50	0.6	1.087	1.13	1.064	0.69	35.05	29.08
21	230	1050	100	0.4	1.211	3.90	1.139	1.97	51.58	33.63
22	230	1050	100	0.6	1.136	1.78	1.094	0.80	44.84	33.74
23	230	1050	∞	0.4	1.480	11.76	1.266	7.62	80.21	7.22
24	230	1050	∞	0.6	1.376	2.28	1.202	1.48	86.63	3.91
25	480	450	50	0.4	1.232	4.25	1.152	2.23	52.48	44.27
26	480	450	50	0.6	1.155	1.57	1.105	0.81	47.66	30.63
27	480	450	100	0.4	1.326	5.61	1.218	4.61	51.99	21.93
28	480	450	100	0.6	1.219	1.70	1.154	0.47	42.35	22.39
29	480	450	∞	0.4	1.506	12.19	1.284	8.08	78.11	7.38
30	480	450	∞	0.6	1.407	2.91	1.226	1.85	79.66	3.67
31	480	1050	50	0.4	1.188	3.35	1.117	1.33	59.26	30.93
32	480	1050	50	0.6	1.112	1.69	1.081	0.82	37.28	39.31
33	480	1050	100	0.4	1.256	4.13	1.173	3.08	49.46	33.29
34	480	1050	100	0.6	1.174	1.97	1.119	0.81	46.37	32.30
35	480	1050	∞	0.4	1.495	12.02	1.276	7.89	79.01	7.20
36	480	1050	∞	0.6	1.393	2.65	1.216	1.68	82.25	3.98